Imperial College London

PhD Thesis

Analytical models for thermoacoustic interactions in axially varying flows

by

Saikumar Reddy Yeddula

A thesis submitted in fulfilment of the requirements for the degree of Doctor of Philosophy

in the

Department of Mechanical Engineering,
Imperial College London,
Exhibition Road, London SW7 2AZ, United Kingdom.

Submitted on 26$^{\text{th}}$ of September, 2021
Revised on 24$^{\text{th}}$ of December, 2021

Declaration

I hereby certify that the work presented in this thesis is the result of my original research, except where acknowledged in the text. The findings reported throughout this thesis have been presented at several conferences and published in scientific journals, as listed on page 40.

Saikumar Reddy Yeddula

24th of December, 2021

Abstract

Thermoacoustic instabilities are a major problem in boilers, low NO_x gas-turbine combustors, and rocket engine combustors. They occur due to positive feedback between the unsteady heat release of the combustion and the acoustic waves, which leads to self-sustained oscillations. These oscillations increase the overall noise emissions of the engine, lead the system to operate in off-design conditions, and result in premature component failure or permanent structural damage. The ability to accurately model the acoustic propagation and acoustic energy balance for given operating conditions can help identify the regions susceptible to instability during the preliminary design phase. This identification can be achieved using computationally efficient low-order acoustic network models where the equations for the mean flow and the acoustics can be solved sequentially.

Lower order models for the acoustics which employ analytical solutions have the benefit of being grid-independent (or, for the case of semi-analytical solutions, grid convergent) and are computationally fast. They also provide more physical insight into the acoustic behaviour across the various mean flow and boundary conditions and thus allow for swift parametric sweeps.

The primary objective of the present thesis is to develop simplified analytical frameworks for estimating the one-dimensional and two-dimensional acoustic fields established in axial and annular nozzles, respectively. These nozzles can (i) feature varying cross-sectional area, (ii) feature varying axial mean temperature, and (iii) sustain subcritical/supercritical mean flow, which does not have to be isentropic. These acoustic field predictions are achieved using asymptotic methods, and the resulting model estimates are validated using numerical simulations. The applicability of some of the developed models for stability analysis is shown by comparing the obtained modal solutions to in-house developed low order network model solvers based on modal expansions.

The analytical models thus developed can be of great interest to both thermoacoustic and acoustic communities.

Acknowledgements

First and foremost, I offer my sincere gratitude to my supervisor, Professor Aimee S. Morgans, for allowing me to be a part of her research group, providing support during my induction and securing funding from the European Research Council. She rendered valuable knowledge, guidance and generous help at all the stages of my research work whilst allowing me the room to work independently. She is always kind, humble and empathetic towards researchers. For someone like me with an interest in academia, she is an academic exemplar.

I am deeply indebted to the Inlaks Shivdasani Foundation for providing the required financial assistance throughout my doctoral study. Without them, I would not have been in this position. I have been blessed with a friendly and cheerful group of fellow researchers, and I sincerely thank them for their help and support. Especially I shall be grateful to my colleagues and dear friends, Dr Dong Yang, Dr Juan-Guzman Inigo, Dr Jialin Su and Dr Aswathy Surendran, for their timely discussions and generous help. They were always available to take my questions and mentored me on both professional and personal aspects, like a family. I also thank all my colleagues who were so kind, friendly and humble. Particularly the days I spent with Xiao Hu, Dr Renaud Gaudron, Faron Hesse, and Dania Ahmed will remain memorable. Renaud's enthusiasm and questioning approach in research will always remain inspirational to me.

I am grateful to my Masters Supervisor, Dr Srikrishna Sahu, who encouraged me to be a part of Imperial College London. My sincere thanks to my out-of-office friends Mohan Ananth, Ashok Reddy, Prashanth Reddy, Saiteja and Leela Vinodh for their emotional support and care.

My parents receive my deepest gratitude for their love, support and patience. My brother, the late Sai Sundeep Reddy, gave me the primary motivation and support for a PhD with Imperial College London. Thanking him can only trivialise what he has done to me; I sincerely dedicate this thesis to him.

The silent support, best wishes of my wife, and other family member's blessings have been the constant inspiration throughout my research programme. My profound debt to them, therefore, remain silent and unacknowledged.

Contents

List of Figures

List of Tables

Abbreviations

2LEEs	Two Linearised Euler Equations.
3LEEs	Three Linearised Euler Equations.
ACARE	Advisory Council for Aeronautics Research in Europe.
CFD	Computational Fluid Dynamics.
CI	Combustion Instabilities.
FDF	Flame Describing Function.
FTF	Flame Transfer Function.
GT	Gas Turbine.
LEE	Linearised Euler Equation.
LES	Large Eddy Simulations.
LNSE	Linearised Navier-Stokers Equation.
LOMTI	Low Order Modelling for Thermoacoustic Instability.
LOTAN	Lower Order Thermo-Acoustic Network solver.
LPP	Lean, Premixed, and Prevaporised.
NO_x	Nitrogen Oxides.
ODE	Ordinary Differential Equation.
OSCILOS	Open Source Combustion Instability Low Order Simulator.
PCI	Proceedings of the Combustion Institute.
PM	Particulate Matter.
TAI	Thermo-Acoustic Instabilities.
TAO	Thermo-Acoustic Oscillations.
WKB	Wentzel, Kramers, and Brillouin.

Nomenclature

Greek Symbols

Symbol	Description	Unit
α	Area gradient, $\alpha = \dfrac{1}{A_s}\dfrac{\mathrm{d}A_s}{\mathrm{d}x}$.	m^{-1}
α^*	Non-dimensional area gradient, $\alpha^* = \alpha l$.	-
β	Temperature gradient, $\beta = \dfrac{1}{\overline{\overline{T}}}\dfrac{\mathrm{d}\overline{T}}{\mathrm{d}x}$.	m^{-1}
β^*	Non-dimensional temperature gradient, $\beta^* = \beta l$.	-
Γ	$\Gamma = \dfrac{\alpha^* M^2 (\gamma - 1) - \beta^* \left(1 - M^2\right)}{1 - \gamma M^2}$.	-
γ	Adiabatic index of the fluid.	-
Δ	Acoustic absorption coefficient.	-
Δ_r	$\Delta_r = \dfrac{1}{r}\dfrac{\mathrm{d}r}{\mathrm{d}m}$.	-
δ	Ratio of scales of the area (α) or mean temperature (β) gradient to the axial wave-number (k_o).	-
ϵ	L^2 norm of the error of the analytical model compared to numerical LEEs.	-
ζ	$\zeta = 1 + \dfrac{\gamma - 1}{2} M^2$.	-
η	Order of ratio of scales of the fluctuating component to the mean component of a flow or thermodynamic variable, for example $\eta = u^{'}/\overline{u}$.	-
Θ	Ratio of the cross-sectional area at the inlet to the outlet, $\Theta = A_{s,\,1}/A_{s,\,2}$.	-

θ	Azimuthal coordinate.	rad
κ	Represents the scale of the gradient of area or mean temperature gradient, $\kappa = \dfrac{1}{\alpha^2}\dfrac{\mathrm{d}^2\alpha}{\mathrm{d}x^2}$ or $\dfrac{1}{\overline{T}^2}\dfrac{\mathrm{d}^2\overline{T}}{\mathrm{d}x^2}$.	-
λ	$\lambda = \sqrt{\left(1-\mu M_\theta\right)^2 - \mu^2\left(1-M_m^2\right)}$	-
μ	Ratio of the azimuthal wave-number to the meridional (or axial) wave-number, $\mu = \dfrac{n}{k_o r}$.	-
ν	Order of ratio of the imaginary part to the real part of the angular frequency, $\nu = \omega_I/\omega_R$.	-
Ξ	Ratio of the mean temperature at the inlet to the outlet, $\Xi = \overline{T}_1/\overline{T}_2$.	-
ξ	Ratio of the mean pressure at the inlet to the outlet, $\xi = \overline{p}_1/\overline{p}_2$.	-
ρ	Density of the fluid.	kg/m^3
σ^*	Non-dimensional entropy disturbance, $\sigma^* = s'/c_p$.	-
ϕ	Meridional flow angle, $\phi = \sin^{-1}\dfrac{\mathrm{d}r}{\mathrm{d}m}$.	rad
χ	Mode function in the Galerkin expansion.	-
$\hat{\Psi}$	Amplitude of the i^{th} mode in the Galerkin expansion.	-
$\hat{\psi}$	$\hat{\psi} = \gamma\overline{p}\hat{s}/c_p$.	Pa
Ω	Azimuthal Helmholtz number, $\Omega = \dfrac{nl}{r}$.	-
ω	Complex angular frequency.	rad/s
ω_R	Real part of the angular frequency.	rad/s
ω_I	Imaginary part of the angular frequency.	rad/s

Roman Symbols

Symbol	**Description**	**Unit**
A_s	Cross-sectional area of the quasi 1-D nozzle.	m^2

$\tilde{A}_s$	Throat area of the quasi 1-D nozzle.	m^2
A_f	Flow area of an annular nozzle, $A_f = 2\pi r h/\cos\phi$.	m^2
$\mathbf{A}$	Coefficient matrix in the first-order system of ODEs for the invariants.	-
a	Real x (or m) coordinate dependant variable in the WKB solution representing the mean gradient changes.	m^{-1}
$\breve{a}$	Area variation parameter, $\breve{a} = \dfrac{r_2 - r_1}{r_1 l}$.	m^{-1}
a^*	Non-dimensional area variation parameter, $a^* = \breve{a} l$	-
$\mathcal{B}^{\pm}$	Coefficients in the WKB acoustic velocity solution written as superposition of the upstream (-) and downstream (+) propagating wave amplitudes.	-
b	Real x (or m) coordinate dependant variable in the WKB solution representing the rapidly varying phase.	m^{-1}
$\breve{b}$	Temperature variation parameter, $\breve{b} = \dfrac{\overline{T}_2 - \overline{T}_1}{\overline{T}_1 l}$.	m^{-1}
b^*	Non-dimensional temperature variation parameter, $b^* = \breve{b} l$.	-
$\mathcal{C}^{\pm}$	Constants in the WKB acoustic solution written as superposition of the upstream (-) and downstream (+) propagating wave amplitudes.	-
$\mathbf{C}$	Coefficient matrix of the wave vector $\mathbf{W}$ in the first-order system of ODEs.	-
c	Adiabatic speed of sound, $c = \sqrt{\gamma R_g T}$.	$\mathrm{m\,s^{-1}}$
c_p	$c_p = \gamma R_g / (\gamma - 1)$.	$\mathrm{J\,kg^{-1}\,K^{-1}}$
d_a	$d_a = 1 - \kappa_\alpha$.	-
d_b	$d_b = 1 - \kappa_\beta$.	-
$\mathbf{D}$	Matrix relating the invariant vector ($\mathbf{I}$) to the non-dimensional wave-vector ($\mathbf{W}^*$.)	-
$\mathbf{E}$	Acoustic energy density.	$\mathrm{J/m^3}$
$\mathbf{E}_x$	Coefficient matrix governing the effects of axial flow in the invariant system of ODEs.	-

$\mathbf{E}_s$	Coefficient matrix governing the effects of heat transfer in the invariant system of ODEs.	-
$\mathbf{E}_\theta$	Coefficient matrix governing the effects of azimuthal flow in the invariant system of ODEs.	-
$\mathcal{F}_{p,\,u}$	Transfer functions for acoustic pressure and velocity.	-
F_1	$F_1 = (\gamma - 1)/\zeta$.	-
F_2	$F_2 = M_\theta \bar{c}_t/\bar{c}$.	-
f	Frequency.	Hz
f_{lower}	Lower frequency limit.	Hz
f_{upper}	Upper frequency limit.	Hz
$\mathbf{G}$	Acoustic energy generation rate.	$\mathrm{W/m^3}$
H	Specific enthalpy.	$\mathrm{J\,kg^{-1}}$
He	Helmholtz number, $\mathrm{He} = \omega l/\bar{c}$.	-
He_{lower}	Lower frequency limit in terms of Helmholtz number.	-
He_{upper}	Upper frequency limit in terms of Helmholtz number.	-
h	Flow width of the annular nozzle measured in the normal (n_r) direction.	m
h_t	He_1 S_b.	m
$\mathbf{I}$	Invariant vector, $I = [I_A\ I_B\ I_C\ I_D]$.	-
I_A	Normalised mass flow fluctuations, $I_A = m'/\overline{m}$.	-
I_B	Normalised stagnation temperature fluctuations, $I_B = {T_t}'/\overline{T}_t$.	-
I_C	Normalised entropy fluctuations, $I_B = s'/c_p$.	-
I_D	Specific angular momentum fluctuations, $I_D = r v_\theta^*$.	-
i	Imaginary number, $\mathrm{i} = \pm\sqrt{-1}$.	-
J'	Specific acoustic energy flux.	$\mathrm{J\,kg^{-1}}$

k	Order of the Magnus expansion.	-
k_o	Wave-number, $k_o = \omega/\overline{c}$.	m^{-1}
k_1	Wave-number at the inlet, $k_1 = \omega/\overline{c}_1$.	m^{-1}
l	Nozzle length.	m
l_m	Length of the nozzle along the meridional axis.	m
M	Flow Mach number, $M = \overline{u}/\overline{c}$.	-
M_m	Meridional flow Mach number, $M_m = \overline{v}_m/\overline{c}$.	-
M_θ	Azimuthal flow Mach number, $M_\theta = \overline{v}_\theta/\overline{c}$.	-
M_{avg}	Average of the flow Mach numbers at the inlet and outlet.	-
$\mathcal{M}$	$\mathcal{M} = 1 + 2M$.	-
m	Meridional coordinate.	m
m^*	Non-dimensional meridional coordinate, $m^* = m/l$.	-
$\dot{m}$	Mass flow rate.	
$\mathbf{N}$	Acoustic energy flux.	$\mathrm{W/m^2}$
N	Total number of segments/modules the nozzle is divided into.	-
N_t	Total mode number.	-
n	Azimuthal mode number.	-
n_r	Normal coordinate.	m
$\mathbf{P}$	Acoustic wave-vector, $\mathbf{P} = \left[\mathrm{P}^+ \ \ \mathrm{P}^-\right]^{\mathrm{T}}$.	-
$\mathbf{IP}$	Non-dimensional wave-vector for annular nozzle, $\mathbf{IP} = [p^* \ \ v_m^* \ \ s^* \ \ rv_\theta^*]^{\mathrm{T}}$.	-
$\mathcal{P}^\pm$	Upstream (-) and downstream (+) propagating wave amplitudes in the WKB acoustic solution.	Pa
$\mathrm{P}^\pm$	Upstream (-) and downstream (+) propagating Riemann invariants.	Pa

$p^{\pm}$	Upstream (-) and downstream (+) propagating non-dimensional Riemann inavariants, $p^{\pm} = p^* \mp u^* M$.	-
p	Pressure.	Pa
$\dot{Q}$	Heat release rate per unit volume.	$\mathrm{W/m^3}$
$\tilde{Q}$	Non-dimensional heat release, $\tilde{Q} = \dfrac{\bar{\dot{Q}} l}{p_{t,1} \bar{c}_{t,1}}$.	-
R	Acoustic reflection coefficient, $R = \mathrm{P}^+/\mathrm{P}^-$.	-
R_s	Entropy reflection coefficient, $R_s = \sigma^*/\mathrm{P}^-$.	-
R_g	Gas constant.	$\mathrm{J\,kg^{-1}\,K^{-1}}$
r	Mean radius of the nozzle, $r = r(x)$.	m
r_o, r_i	Outer and inner radius of the annular nozzle.	m
S_a	$S_a = (M_1 - M_2)$.	-
S_b	$S_b = \int_{x_1}^{x_2} (1 \mp M)\,\mathrm{d}\check{x}$.	-
S_c	$S_c = -M_1 \left(\dfrac{1}{\Xi} + \gamma\sqrt{1 + b^*} - (\gamma + 1) \right)$.	-
s	Entropy.	$\mathrm{J\,kg^{-1}\,K^{-1}}$
$\mathbf{T}$	Transfer matrix relating the wave vectors at the inlet to those at the outlet.	-
T	Temperature.	K
t	Time coordinate.	s
u	Axial flow velocity.	$\mathrm{m\,s^{-1}}$
v_m	Meridional flow velocity.	$\mathrm{m\,s^{-1}}$
v_θ	Azimuthal flow velocity.	$\mathrm{m\,s^{-1}}$
$\mathbf{W}$	Wave-vector, $\mathbf{W} = \begin{bmatrix} \mathrm{P}^+ & \mathrm{P}^- & \hat{\psi} \end{bmatrix}^{\mathrm{T}}$.	Pa
$\mathbf{W}^*$	Non-dimensional wave-vector, $\mathbf{W}^* = [p^+ \;\; p^- \;\; \sigma^*]^{\mathrm{T}}$.	-
x	Axial coordinate.	m

x^*	Non dimensional axial coordinate, $x^* = x/l$.	-
$\tilde{x}$	Location of the nozzle throat.	m
Z	Non-dimensional acoustic impedance.	-

Subscripts and superscripts

Symbol	**Description**
$\overline{(\ )}$	Mean time-averaged component.
$(\ )'$	Fluctuating unsteady component.
$(\ )^*$	Non-dimensional fluctuating unsteady component.
$(\ )^{\pm}$	Represents downstream (+) and upstream (-) propagating waves.
$(\ )_{1,\,2}$	Flow and thermodynamic variables at the inlet (1) or outlet (2).
$(\ )_{0,\,1}$	Iteration number for variables a, b in the WKB solution.
$(\ )_{in,\,out}$	Represents incoming (in) or outgoing (out) waves of the nozzle.
$(\ )_f$	Acoustic or entropy input forcing.
$(\ )_t$	Stagnation quantity.
$(\ )_{u,\,d}$	Represents infinitesimally upstream (u) and downstream (d) locations of the nozzle throat.

Chapter 1

Introduction

The World Health Organization estimates that ambient outdoor pollution results in around 3 million deaths every year [1]. Transport and power generation sectors alone contribute to 65% of the total harmful outdoor air pollutants like oxides of nitrogen (NO_x), oxides of sulphur (SO_x), carbon monoxide (CO), and particulate matter (PM). In particular, long term exposure to NO_x can cause decreased lung function, increase the risk of respiratory conditions. It also contributes to PM and ground-level ozone formation, which are associated with adverse health effects. NO_x emissions also lead to acid deposition and eutrophication of soil and water. The acid deposition can adversely affect the terrestrial ecosystems due to ammonia (NH_3) emissions and subsequent nitrogen accumulation in soil and water. Eutrophication, which occurs due to excess enrichment of water with minerals and nutrients of nitrogen, can gravely affect water quality with increasing toxicity levels and impacting biodiversity.

With around 700 major cities spread across the world [1] having 'unhealthy' air quality, reducing NO_x emissions is vital. In addition to air pollution, reports also support the linkage between environmental noise and adverse health effects, suggesting a loss of an estimated 1 to 1.6 million healthy life years annually in high income western European Countries. For example, aircraft noise can also negatively influence health if the exposure is long-term and exceeds certain levels [2]. Hence, the Advisory Council for Aeronautics Research in Europe (ACARE) has set stringent targets in reducing overall aircraft noise by 65% and NO_x pollutants by 90% by 2050, compared to the levels in 2000 [3].

The share of energy production and distribution (17%) and non-road transport sectors (9%) together accounts for 26% of the total $\mathrm{NO_x}$ emissions from the countries of the European Union [4]. Non-road transport constitutes aviation and maritime transport, primarily using gas-turbine (GT) based combustion engines. These GT engines are also predominantly used in the energy production sector and some specific industries like ceramics. Thus, GT engines

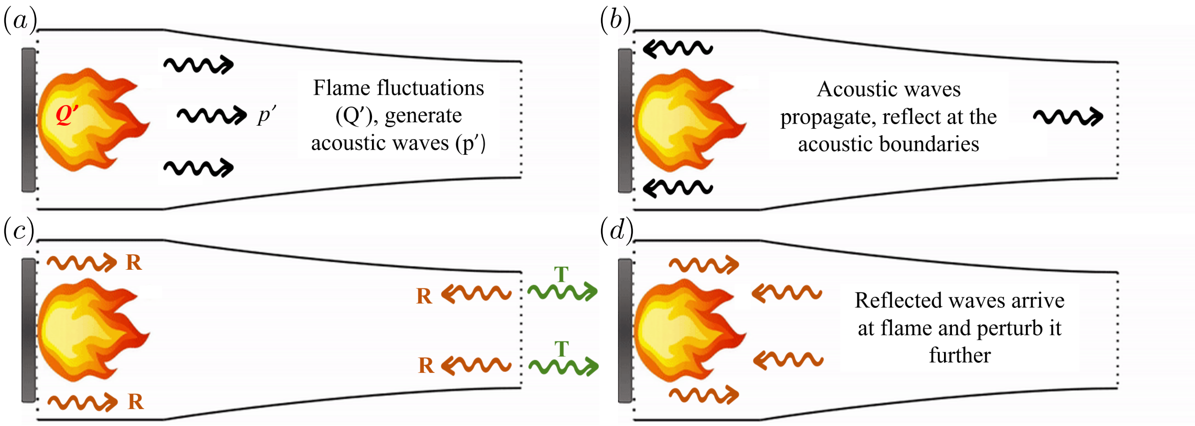

Figure 1.1: Positive feedback between the flame and the acoustic waves leading to self-sustained oscillations.

could be regarded as one of the main sources for NO_x emissions. Targeting these sources could significantly reduce the total NO_x produced in the non-road transport sectors. Thus, rising environmental concern has forced GT engine manufacturers to look for efficient ways of controlling NO_x and improving the overall efficiency of these engines.

1.1 NO_x formation in combustion engines

NO_x formation in combustion engines occurs via three modes [5]:
a) Thermal NO_x formation is mainly controlled by the molar concentrations of nitrogen, oxygen and the mean flame temperature in the combustion zone. In general, the molar concentrations of nitrogen and oxygen are fixed for engines using ambient air as the oxidiser, and only the mean combustion zone temperature can be controlled. This mode of NO_x formation accounts for around 70% of the total NO_x produced in combustion systems and is highly sensitive to the sustained temperatures in the combustors. For example, a decrease of about 400^oC in the mean flame temperature could result in almost a ten-fold reduction in the overall thermal NO_x formation [5].

b) Fuel NO_x occurs due to the oxidation of “already-ionized" nitrogen in the fuel. The contribution to total NO_x formation from this mode can be controlled by reducing the nitrogen content in the fuel.

c) Prompt NO_x is the result of nitrogen's reaction with active hydrocarbon radicals in the fuel. Its contribution is limited and is $< 5\%$ of the total NO_x formed.

Thus, GT engine manufacturers' main active reduction strategies to reduce NOx emissions have been reducing the overall combustion zone temperature. This has led to low NOx burners, such as lean, premixed, and pre-vaporised (LPP) burners. However, this results in an increased

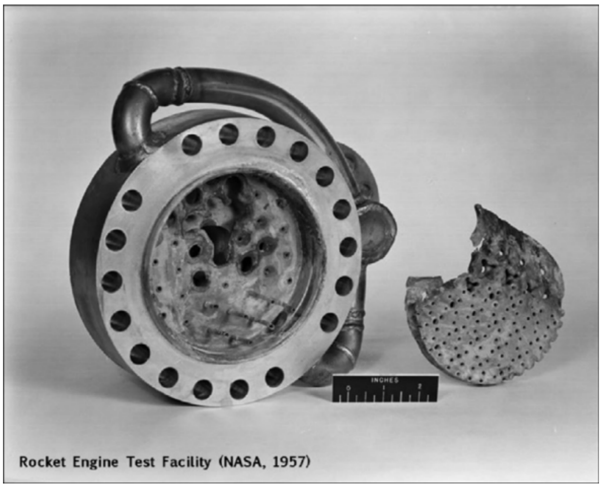

Figure 1.2: Engine burner damaged by instabilities during the testing phase of Apollo moon program (Image reproduced from [16] with permission of the rights holder, Elsevier - Appendix E).

flame unsteadiness in the combustor, increasing the potential for a problem called "thermoacoustic instabilities (TAI) [6]. Also known as Combustion Instabilities (CI), these occur due to a two-way coupling between unsteady heat release at the flame and acoustics of the combustor duct [7–9]. TAI are also turning out to be highly relevant for future combustor designs, which burn fuel blends that include carbon-free fuels, such as hydrogen [10–12]. As shown in Fig. 1.1, the acoustic disturbances produced due to the unsteady heat release (Q') in a combustor propagate, reflect at the acoustic boundaries and arrive back at the heat source. As firstly presented by Rayleigh [7, 13], these acoustic disturbances can grow in magnitude if there is a net energy gain from the unsteady heat release compared to the sum of the acoustic energy flux losses across the boundary and due to dissipation [14–16]. These growing self-sustained thermoacoustic oscillations (TAO) cause high noise and system vibration levels until the effects of acoustic non-linearities lead to limit-cycling or other non-linear oscillations. TAI result in permanent structural damage to the engine. Famously, TAI were a major problem in developing the F1 rocket engine during the Apollo moon program in the 1960s. This resulted in more than 1000 real scale engine prototype tests, costing billions of dollars [16]. Fig. 1.2 shows one such burner prototype that was damaged due to TAI during these tests. Faster ageing of the engine or making the system operate at off-design conditions are also certain side effects of TAO [17]. The failure of the engine in both power generation and aviation sectors is very costly. Hence thermoacoustic interactions need to be accurately modelled across a wide range of input flow or acoustic boundary conditions to understand and avoid/control any undesired phenomena inside the combustor.

1.2 Modelling thermoacoustic phenomena

1.2.1 Challenges

The disparity between the acoustic length scales, which are O(metre), and the flame wrinkling, O(millimetre), and flame reactions O(micrometre), makes the identification of TAO computationally costly. This is particularly the case when the sample space of flow conditions and acoustic boundary conditions is extensive. There can be scenarios where the initial set of conditions ensure stability of the combustor but it subsequently destabilises after serving a portion of the planned lifetime due to changes in component behaviour as they age. These ageing effects of the mechanical components can only be studied by a sensitivity analysis which is not feasible to be implemented using high fidelity numerical simulations. Also, considering an extensive range of input flow or acoustic boundary conditions during the design stage involves too many calculations. These conditions cannot all be implemented using numerical simulations owing to the involved computational costs. Thus, although Computational Fluid Dynamics (CFD) simulations for the entire combustor domain are possible [18–22], they are impractical as an industry analysis tool. Laboratory level experiments [22] could demonstrate the on-set of TAI for canonical cases. However, these models cannot capture the complexity of a real scale combustor. For example, real engine combustors often sustain two-dimensional (2-D) or three-dimensional (3-D) flow and disturbance effects, intricate geometries, indirect noise effects from flow inhomogeneities (entropy or vortical or compositional inhomogeneities) passing into the downstream turbine [23]. Though possible, full-scale experimental test rigs are incredibly costly.

1.2.2 Decoupling treatment

Computational methods that employ coupling of separate treatments for the acoustic waves and the flame have been shown to have much promise in the accurate prediction of thermoacoustic behaviour [15, 24–32]. These decoupling treatment approaches utilise the fact that the thermoacoustic oscillations have relatively long wavelengths compared to the flame features, meaning that the flame can be treated as “acoustically compact" and represented by an infinitesimally thin flame sheet [33]. The acoustics is then amenable to a simplified treatment. For some GT combustors and rocket engine combustors, this allows using a linear framework to solve the wave propagation. This linear analysis assumes the acoustic pressure fluctuations to be much lesser than the mean pressure. For a fluid flow comprising of a mean (denoted by $\overline{(\,)}$) and a fluctuating component, (denoted by $(\,)'$) this reads $p' < 0.1\overline{p}$ [34]. As the acoustic waves are central to the cause of TAO, the unstable frequencies mostly remain close to the acoustic resonant frequencies of the combustors and the deviation caused by combustion interaction is typically small [15]. Hence, accurate acoustic propagation solutions are vital and form the primary step in a full-scale thermoacoustic analysis.

The Galerkin method [35–38] is one of the several acoustic modelling methods where the acoustic solution is approximated as a summation of multiple normal modes using the mode function, $\chi_i\left(x\right)$ with an amplitude of $\Psi_i\left(t\right)$ for each mode. Thus the acoustic solution is split into two separate time and location dependant functions. For example, the acoustic pressure is given by,

$$p'(x,\ t) = \overline{p}\sum_{i=1}^{N_t} \chi_i\left(x\right)\Psi_i\left(t\right), \tag{1.1}$$

with N_t representing the total mode number. Galerkin method is primarily used for combustors with distributed reaction zones like solid rocket engines. However, this method requires large amount of modes to accurately capture the velocity discontinuity due to $\dot{Q}'$, across the thin flame sheet present in GT combustors.

Simplified acoustic treatment using Helmholtz solvers was reported in [31, 39–42]. These solvers can capture the geometrical intricacies and any temperature variations inside the combustor, however, neglect the presence of any mean flow. This affects the accuracy of the achieved acoustic solution [43, 44] and therefore cannot be applied to combustors/nozzles sustaining high flow velocities.

The inhomogeneous wave equation governing the evolution of linear acoustic disturbance in a nozzle sustaining an isentropic flow can be represented by [15],

$$\frac{1}{\overline{c}^2}\frac{\overline{\mathrm{D}}^2 p'}{\mathrm{D}t^2} - \nabla^2 p' = \frac{\gamma - 1}{\overline{c}^2}\frac{\overline{\mathrm{D}}\dot{Q}'}{\mathrm{D}t}, \tag{1.2}$$

where $\overline{c}$ corresponds to the speed of sound, γ is the adiabatic index of the fluid and $\dot{Q}'$ represents the fluctuations of the heat release rate of the flame. The material derivative $\overline{\mathrm{D}}/\mathrm{D}t = \partial/\partial t + \bar{u}\cdot\nabla$ accounts for the non-zero flow velocity. Wave based acoustic modelling treatment involves seeking a solution for the wave equation described in Eq. (1.2) using low order network models [15, 30, 45–53]. For planar acoustic field the acoustic solution is represented as the superposition of the upstream (-) and downstream (+) travelling wave amplitudes $\mathrm{P}^{\pm}$, such that,

$$p'(x,t) = \mathrm{P}^{+} + \mathrm{P}^{-}. \tag{1.3}$$

As observed from Eq. (1.2), the heat release rate fluctuations $\dot{Q}'$ acts as the source of the acoustic waves and can potentially amplify them when they are in-phase. Solving Eq. (1.2) therefore requires capturing the flame response to acoustic excitation, which is obtained using a flame model. As suggested by Crocco [54, 55], the flame is modelled as an acoustic element in response to local fluctuations. A flame model therefore links the fluctuation in the heat release rate per unit volume, $\dot{Q}'$, to acoustic or entropy fluctuations, for example, velocity fluctuations upstream of the flame, u'_u. In the linear limit of such flame models, a "flame transfer function

(FTF)” [54, 55] is defined in the frequency domain assuming a sinusoidal dependence of the form $y' = \hat{y}\exp(\mathrm{i}\omega t)$, for the disturbances. This gives,

$$\mathcal{F}_f(\omega) = \frac{\widehat{\dot{Q}}/\overline{\dot{Q}}}{\widehat{u}_u/\bar{u}_u} = |\mathcal{F}_f(\omega)|\exp(\mathrm{i}\angle\mathcal{F}_f(\omega)) \tag{1.4}$$

where ω correspond to the complex angular frequency with $|F_f|$ and $\angle F_f$ denoting the gain and phase of the transfer function, respectively, and $\mathrm{i}^2 = -1$. The flame is also sensitive to to other types of perturbations, for example, equivalence ratio, mass flow [56, 57], temperature or pressure fluctuations [14]; all result in heat release rate fluctuations.

While FTFs assume the gain and phase of the transfer function to be a function of only the frequency, Flame Describing Functions (FDFs) account for weak non-linearity by further accounting for the dependence of the input disturbance [58, 59]. This weakly non-linear flame behaviour captured by FDFs is representative of gas turbine combustors where the amplitudes of the acoustic velocity fluctuations are generally large enough during instability to cause non-linearity. It should be noted that this non-linearity occurs for the heat release rate fluctuations in response to the large amplitude velocity fluctuation forcing while the acoustics remain linear. A model for the unsteady flame response to acoustic excitation (flame model) can be extracted from large eddy simulations (LES) [30, 32, 60–68] or experiments [58, 59, 69–73]. It should be noted that at the location of the flame, jump conditions based on conservation equations need to be applied for both the mean and fluctuating quantities, as outlined in [74]. These conditions along with the flame model forms a closure to the inhomogeneous wave equation posed in Eq. (1.2). Thus the modelling of the flame response forms a separate line of research, serving as an input to the acoustic treatment using low order network models.

Low order network models that employ analytical solutions for the acoustic field are of particular interest, as they swiftly obtain the full frequency response for a particular flow condition inside the combustor. This facilitates faster parametric sweeps and thereby aids in the early identification of frequencies susceptible to thermoacoustic oscillations. Low order models also serve as a preliminary tool in analysing the thermoacoustic behaviour of real systems. Physical insights drawn through analytical solutions employed in these models can also reduce the size of parametric sample space.

1.2.3 Analytical modelling

The low order network models and the Helmholtz solvers separate the primary source of non-linearity - the flame response to the flow perturbations - from the acoustic models, thus enabling a linear acoustic framework [15]. Network models further facilitate separating simple acoustic propagation regimes from the more intricate geometries, such as zones where the premix ducts/burners interact with the plenum and combustor, leading to the potential for a non-linear phenomenon called modal coupling [75].

It is beneficial for network models to represent the acoustic field as a superposition of the upstream and downstream propagating acoustic wave components, this offering physical insight, facilitating the connection to other modules and enabling acoustic damping estimates for any attached dampers. Numerical methods based on finite-difference techniques or other higher-order schemes can capture the acoustic propagation in axially varying flows. However, analytical solutions are computationally fast, offering guaranteed convergence irrespective of the grid size. This makes parametric studies much easier and, therefore, aide in quickly identifying efficient ways of altering the system to attenuate TAO during the design stage. These analytical solutions also serve as a preliminary industry analysis tool and help to reduce the generally large sample space for the CFD simulations.

1.2.4 The planar acoustic field in axially varying flows

To accurately capture the acoustic field sustained in a combustor geometry at industrial complexity, the analytical solutions need to account for the effects of the area variation, non-isentropic effects such as heat transfer, three-dimensional mean flow and perturbed flow, and be applicable over a wide range of frequencies. However, a model in the literature that accounts for all these effects does not exist. For example, analytical solutions for the one-dimensional acoustic field in a nozzle (a varying area duct) are broadly divided into exact and semi-analytical solutions. Exact solutions for a nozzle with sub-critical and super-critical flow configuration were firstly derived for acoustically compact geometries by Marble and Candel [76]. This compact analysis assumes negligible frequency and, therefore, the acoustic wavelength is much larger than the length scale of the nozzle area-change so that the nozzle appears as a 'step' to the incident acoustic wave. This approach was later extended to non-zero higher frequencies using Magnus expansion based method by Duran and Moreau [77], but assumed an isentropic mean flow. Using the Dyson expansion-based method, Magri [78] solved for the acoustic field sustained in a multi-component nozzle, thereby accounting for the compositional-acoustic coupling; however, the mean flow was assumed to be isentropic. Acoustic wave propagation in variable area ducts with stationary media can be traced to Webster [79]. For nozzles with a non-zero isentropic flow, Eisenberg and Kao [80] determined the acoustic field for specific area profiles that lead to constant coefficients for the considered ordinary differential equations, governing the evolution of the flow perturbations. The mean flow was assumed to be subsonic, and it was observed that the momentum exchange between the mean flow and the acoustics causes the acoustic amplitude to vary differently from that caused by area variation alone. For incompressible, isentropic mean flows with very low subsonic flow Mach numbers ($M < 0.2$), Easwaran and Munjal [81] presented exact solutions of the acoustic field in terms of transfer matrix for conical and exponential shaped nozzles. It was observed that the mean flow affects the transfer matrix components of the conically and the exponentially shaped nozzles differently.

Combustors often encounter heat exchange to the surroundings and the dilution air, affecting the temperature distribution along its length. The temperature gradients due to heat transfer affect the acoustic energy balance [82] inside the nozzles, and hence the acoustic models need to account for this non-isentropic effect. Munjal and Prasad [83] derived the acoustic transfer matrix using a first-order perturbation method for a uniform area duct, sustaining a mean flow and a linear temperature gradient. Sujith *et al.* [84] obtained exact solutions describing the one-dimensional (1-D) acoustic behaviour in a constant area duct with linear, exponential temperature profiles in the presence of a negligible mean flow. This analysis was later extended to low subsonic flow Mach numbers by Karthik *et al.* [85]. In these approaches, a transformation is sought for the governing equations into a single hypergeometric differential equation. Subrahmanyam and Sujith [86] obtained exact travelling wave-type solutions for specific area and temperature profiles in the absence of any mean flow.

Although these solutions are exact and capture the acoustic wave propagation for particular cases, an acoustic solution for the general case of a nozzle - with both substantial mean-flow and a temperature gradient (due to steady heat transfer), has not been found. For this reason, semi-analytical solutions came into prominence, these combining good accuracy with high computational efficiency.

Approximate wave-like solutions for second-order differential equations with variable coefficients were traditionally solved in wave-mechanics using the WKB approximate method, named after Wentzel, Kramers, Brillouin [87][1]. This method predates the method of multiple scales but works similarly. It essentially assumes the phase to vary more rapidly than the amplitude of the wave. These WKB method based solutions include integrals of rapidly varying phase terms, leading to higher computational time compared to an exact solution.

A slightly modified WKB method was used by Cummings [88] with separate amplitude and phase factors leading to the acoustic field solution for uniform area ducts sustaining a temperature gradient with negligible mean flow. This approach assumes the axial length scale of the temperature (or density) variation is much larger than the acoustic wavelength and hence requires sufficiently high frequencies. Li and Morgans [89] extended this analysis to include the non-zero mean flow effects using an adaptive WKB method. The final solution thus obtained accurately predicts the acoustic field for uniform area ducts with temperature gradients and can consider up to flow Mach numbers of ~ 0.6.

Using the framework of a WKB method, Dokumaci [43] presented a semi-analytical solution

[1]This method is named after physicists Gregor Wentzel, Hendrik Anthony Kramers, and Léon Brillouin. However, mathematician Harold Jeffreys had developed a generalised method of approximating solutions to linear, second-order differential equations earlier. Hence often the solution is referred to as WKBJ or JWKB method.

for a nozzle (has a varying area) sustaining isentropic mean flow. The governing perturbation equations are written in terms of the upstream and downstream travelling wave components, and only the off-diagonal terms in the state-space matrix are retained. This requires the wave components to be independent and hence valid only at sufficiently high frequencies. This high-frequency requirement is specified in terms of limiting frequency criteria which were derived assuming negligible mean flow. The final solution requires increased computational effort [90] to evaluate the integral terms in the state-space matrix compared to an analytical solution, making the final solution depend on the thermodynamic and flow properties of the entire nozzle. Rani and Rani [91] presented approximate (WKB and WKB2) solutions to the acoustic field in a nozzle with isentropic mean flow. The achieved solution consists of complicated parameters, increasing the computational effort and with unclear frequency limits. All the existing WKB-based models assume either uniform area and/or isentropic mean flow, with the final solution being a function of the upstream thermodynamic and flow properties, require numerical evaluation.

For nozzles sustaining non-isentropic mean flows, Umurhan [82] numerically studied the effect of different spatial heating distributions, with no heat release fluctuations, on thermoacoustic stability. Dokumaci also developed a numerical framework to solve the linearised Euler equations and obtain the acoustic response of nozzles sustaining a non-isentropic mean flow. However, an analytical/semi-analytical solution for the planar acoustic field in these nozzles with axially varying non-isentropic mean flows is so far lacking and is the topic of Chapter 2 of this thesis.

The above WKB method based solutions neglect the effect of the entropy disturbance [92] on the acoustic field [93]. This simplification is justified by the low subsonic flow Mach number assumption considered in this analysis in the context of gas-turbine combustors. At these flow Mach numbers, the acoustic-entropy coupling was observed to be weak and hence negligible [44, 94]. Also, at the sufficiently high frequencies considered for the WKB analysis, the wavelength of entropy disturbances, given as $\overline{u}/f$ (with f as frequency), is smaller than the largest turbulent length scales. This results in enhanced turbulent mixing and diffusion, leading to the decay of the entropy fluctuations [95]. Even in the mid-frequency range, the amplitude of the advecting entropy wave is strongly attenuated due to shear dispersion [95–101]. The effect of the acoustic-entropy coupling is most relevant at the low-frequencies where most unstable thermoacoustic modes (fundamental modes) often exist and hence the effect cannot be neglected.

Recently Weilenmann *et al.* [101] conducted experimental investigation of indirect noise generated by entropy waves convecting in a super-critical nozzle. The indirect noise was found to be 60% lower than isentropic compact limit calculations. The observed difference was due to the three dimensional deformation of the entropy waves and turbulent mixing. Rodrigues *et al.* [102] also analysed the effect the of shear dispersion on entropy and compositional inhomogeneities. While the dispersion effects on the compositional waves are seen to be insignificant the entropy waves were again found to be strongly attenuated.

The effect of shear dispersion, local turbulent mixing primarily results in different convection velocities to the entropy wave and there-by different resident times resulting in a two-dimensional effect on the entropy field. These 2-D (or 3-D) non planar effects can significantly change the thermoacoustic behaviour in nozzles. Emmanuelli *et al.* [103, 104] and Huet *et al.* [105, 106] developed numerical acoustic models that can accurately account for the non-planar entropy wave effects.

All these studies emphasize that the effect of entropy disturbances is less relevant for mid to sufficiently high frequencies in practical nozzle like configurations.

Semi-analytical solutions derived from truncation of an infinite series expansion have also been used to determine the acoustic field. For example, Duran and Moreau [77] used a Magnus expansion based method to obtain the acoustic response of a nozzle sustaining isentropic mean flow. These methods are applicable over a wide range of frequencies and can fully account for acoustic-entropy coupling. Hence these models are of interest to the thermoacoustic research communities due to their excellent low-frequency behaviour. To apply the Magnus expansion method, the Euler equations need to be linearised and recast in terms of flow invariants, for example, the fluctuations of mass flow rate, stagnation temperature, and entropy fluctuations for the one-dimensional acoustic field. The resulting system of first-order differential equations (ODEs) is solved by expanding the invariant formulation around the frequency. The methodology presented in Duran and Moreau [77] applies only to nozzles with an isentropic mean flow and cannot account for flows with steady heat transfer. The heat transfer effect on the acoustic field and entropy generation for both zero and non-zero frequencies needs to be investigated.

Non-isentropic sources other than heat transfer can also affect the thermoacoustic behavior, for example, De Domenico *et al.* [107, 108] analysed the effects of flow separation and friction on the acoustics. It was observed that these effects can strongly influence acoustic and entropy transfer functions of nozzles. The effect of dissipation (flow re-circulation and wall friction) was modelled from conservation laws by Jain and Magri [109], who computed acoustic transfer functions for any Helmholtz number and Mach-number regime and analysed the effect that dissipation has on thermoacoustic stability.

1.2.5 Acoustic energy analysis

The effect of the steady heat transfer on the acoustic response of nozzles can be further revealed using acoustic energy analysis. The interaction between the acoustics and the flow in terms of energy balance was first investigated by Cantrell and Hart [110] for irrotational, isentropic, subsonic mean flows. Formal definitions for the acoustic energy flux and acoustic energy density were also first presented in their work. The acoustic energy balance was later extended to non-uniform flows by Morfey [111]. For one-dimensional flow, the model was further improved to include the effects of steady (mean) and unsteady heat addition by Bloxsidge *et al.* [112]. Bechert [113] using a multipole analysis demonstrated that jet flows, flows through apertures or through blade rows absorb acoustic energy and can potentially be used as mufflers.

For arbitrary steady flows, a general disturbance energy corollary was first proposed by Myers [114], which included both acoustic and non-acoustic disturbance energy terms. Giauque *et al.* [115, 116] further extended Myers energy corollary to flows with gaseous combustion by including species and heat release terms. Karimi *et al.* [117] analysed the acoustic and disturbance energy contributions for straight ducts with steady (mean) and fluctuating heat release. A frequency limit called the 'entropic corner frequency' was proposed, above which the effect of acoustic-entropy coupling is negligible. At frequencies larger than this limit, the total disturbance energy can be approximated as acoustic energy [117]. Although acoustic energy balance studies exist, they are generalised and do not explicitly consider duct flows with area and mean temperature variations.

Characterisation of the acoustic energy balance with minimal parameters reduces the computational effort in analysing the entire sample space of frequencies, mean flow conditions and acoustic boundary conditions for identifying regions susceptible to TAO. This characterisation of the acoustic energy generation or dissipation is achieved in nozzles by a single parameter Δ, called the acoustic absorption coefficient [111].

$$\Delta = 1 - \frac{\left|\mathbf{N}_2^+\right| + \left|\mathbf{N}_1^-\right|}{\left|\mathbf{N}_1^+\right| + \left|\mathbf{N}_2^-\right|} \tag{1.5}$$

where $\mathbf{N}$ denotes the acoustic energy flux for the downstream $(+)$ and upstream (-) propagating waves at the inlet (1) and outlet (2) of the nozzle. It quantifies the loss of the acoustic energy flux across the nozzle; for instance, $\Delta > 0$ (respectively $\Delta < 0$) implies acoustic energy absorption (respectively generation), while $\Delta = 0$ corresponds to no change in the acoustic energy inside the nozzle. This characterisation of the acoustic energy balance using Δ was first investigated in the context of nozzle/duct thermoacoustic stability analysis by Gaudron *et al.* [118, 119]. The simplified expression for Δ was shown to be a function of only a few mean flow parameters and the wave amplitudes at the inlet and outlet of the nozzle. The acoustic wave amplitudes can be obtained using numerical simulations, experiments or analytical models.

1.2.6 The two-dimensional acoustic field in axially varying flows

Many modern gas-turbine engines use annular combustors, with their advantages of uniform combustion and exit temperatures, lower stagnation pressure loss and compact design [120, 121]. Several lower order models exist for annular geometries that capture the acoustic propagation in burner-combustor and plenum-burner-combustor configurations [45, 50, 122, 123]. These models tend to geometrically simplify the combustor geometry, approximating it as a straight annular duct with an isentropic mean flow in the axial direction. Aguilar *et al.* [124] showed that thermoacoustic stability is sensitive to geometrical changes for annular geometries. Hence, the acoustic models that correctly account for key aspects of practical flow configurations in annular combustors remain a work in progress.

Annular combustors generally constitute axial and swirling (azimuthal) mean flows, along with a temperature gradient in the axial direction due to the heat exchange with the dilution air and heat loss through conduction and radiation [120]. Analytical and numerical models that capture the acoustic propagation in such annular combustors are quite limited. Marble and Candel's [76] acoustically compact solution for 1-D nozzles was extended to choked thin-annular nozzles by Stow [125]. An asymptotic low frequency analysis was used to estimate the reflection coefficient in terms of an equivalent annular nozzle length. Recently, Li *et al.* [126, 127] developed semi-analytical solutions extending the WKB method for the two-dimensional acoustic field in annular geometries. While [126] considers the two-dimensional acoustic field in a straight annular duct with arbitrary temperature gradient, [127] considers a conical-shaped annular nozzle with an axial, isentropic mean flow with negligible temperature variation. In both the models, the mean flow is assumed to have no azimuthal component, and one of either heat exchange with the surroundings or the area variation is neglected. Further, the assumed linearly varying area in [127] is restrictive and may impact the predicted stability if approximating a more complex area variation [124]. Although a piece-wise linear approximation could be applied, this reduces the simplicity and increases the computational cost of the analytical models. Hence an acoustic model that accurately captures the two-dimensional acoustic field in an annular geometry, accounting for geometric complexities in the form of varying mean radius and flow width, and mean flow complexities in the form of an azimuthal mean flow component and non-isentropic mean flow does not exist and is presented in Chapter 5. This model based on WKB method estimates the two-dimensional acoustic field in an annular nozzle (shown in Fig. 5.1) with arbitrary area profile, sustaining both azimuthal and axial mean flows. The mean flow can also consider a steady heat transfer in the form of an arbitrary temperature profile. This WKB model again suffers from restricted flow Mach numbers, requires sufficiently high frequencies and neglects the effect of the entropy disturbance on the acoustic field.

Duran and Morgans [128] developed a more powerful approach for annular geometries using the Magnus-expansion based method. This semi-analytical method can describe the acoustic propagation in annular isentropic nozzles for a wide range of frequencies for both sub-critical and super-critical annular nozzle configurations, and can fully account for acoustic-entropy coupling. However, it requires both an isentropic mean flow and the mean radius of the annular geometry to remain constant axially. A two-dimensional acoustic field solution that can account for this mean radius variation can be applied for supersonic air-intake diffusers, turbine blades and nozzles sustaining an isentropic mean flow, and is described in Chapter 5 of this thesis extending the Magnus expansion based model of [128].

1.3 Thermoacoustic solvers

The acoustic models thus developed can be combined with the flame models (Eq. (1.4)) in a "thermoacoustic solver" and used for the stability analysis. "Low Order Thermo Acoustic Network solver" (LOTAN) by Stow *et al.* [129], "Low Order Modelling for Thermoacoustic Instability" (LOMTI) solver by Campa *et al.* [130], "Open Source Combustion Instability Low Order Simulator" (OSCILOS) developed by the Morgans group [52, 53] are a few thermoacoustic solvers that can be applicable for both longitudinal and annular nozzle geometries. Using an axial segmentation approach [30, 131], these solvers divide the geometry into cylindrical or straight annular segments, apply jump conditions at the interfaces and boundary conditions at the ends and solve for the eigenmodes of the system. This work uses the WKB method based analytical solutions to estimate the eigenmodes in quasi 1-D (Chapter 2) and 2-D (Chapter 5) nozzles and compare with the in-house developed $\text{OSCILOS}_{\text{long}}$ and $\text{OSCILOS}_{\text{ann}}$ thermoacoustic solvers, respectively.

1.4 Organisation of this work

The limitations of the above mentioned acoustic models are sequentially accounted for in this thesis. This work is therefore organised as follows:

- Chapter 2 of this thesis presents WKB method based analytical solutions for the planar acoustic field in nozzles with an axially varying mean flow that can be non-isentropic. The mean flow can have a temperature gradient, and the solutions thus achieved depend only on the local thermodynamic and flow properties. Hence these solutions offer some physical insight and are computationally simple. For validation, conical and exponentially shaped nozzles sustaining a linear temperature gradient are considered, and simplified analytical solutions are reported. However, these simplified solutions are limited to sufficiently high frequencies and low subsonic flow Mach numbers. A general semi-analytical solution applicable to nozzles with an arbitrary area, temperature profile, and sustaining increased subsonic flow Mach number is also presented at the expense of increased computational effort.

- Chapter 3 of this thesis shows that non-isentropicity in the mean flow due to wall heat losses affects the acoustic energy absorption or generation in combustors. The WKB solution in Chapter 2 is further used to estimate the acoustic response of the nozzle, and a detailed investigation on the effects of frequency and various mean flow conditions of the acoustic absorption coefficient, Δ, is discussed.

- Chapter 4 of this thesis presents a novel approach in using the Magnus expansion method to account for the non-isentropic effects. The first-order system of ODEs governing the flow invariants is expanded around both temporal (non-dimensional frequency) and non-temporal (non-dimensional heat transfer) parameters. This allowed the model to capture “non-acoustically compact" and “non-isentropic" effects simultaneously. The effect of heat transfer on entropy disturbance generation is also investigated.
- Chapter 5 presents models to estimate the two-dimensional acoustic field in a thin annular nozzle (shown in Fig. 5.1) with arbitrary area profile, sustaining both azimuthal and axial mean flows using both the WKB method and Magnus expansion method. The WKB model can also consider a steady heat transfer in the form of an arbitrary temperature profile but requires lower flow Mach numbers, sufficiently high frequencies and neglects the effect of the entropy disturbance on the acoustic field. The Magnus expansion based method relaxes these requirements but is restricted to isentropic mean flows in this study.

1.5 Related publications

1. Journal publications during the course of the work:
   (a) Yeddula SR, Morgans AS. “A semi-analytical solution for acoustic wave propagation in varying area ducts with mean flow”. Journal of Sound and Vibration. 2021 Feb 3;492:115770.
   (b) Yeddula SR, Gaudron R, Morgans AS. “Acoustic absorption and generation in ducts of smoothly varying area sustaining a mean flow and a mean temperature gradient”. Journal of Sound and Vibration. 2021 Sep 116437.
2. Conference publications during the course of the work:
   (a) Yeddula SR, Morgans AS. “A semi-analytical solution for acoustic wave propagation in varying area ducts with mean flow”. In: Proceedings of the 23rd International Congress on Acoustics (ICA2019). Sept. 2019, pp. 1–9.
   (b) Yeddula SR, Gaudron R, Morgans AS. “Acoustic absorption and generation in varying area ducts with non-isentropic mean flow”. In: eForum Acusticum 2020. Dec 2020, pp. 785-790.
   (c) Yeddula SR, Morgans AS. “The two-dimensional acoustic field in an annular duct with axially varying area, sustaining an isentropic mean flow”. In: Proceedings of ICSV 27-International Congress on Sound and Vibration. July 2021, pp. 1–8.

Chapter 2

WKB method based semi-analytical solution for planar acoustic wave propagation in nozzles with low subsonic mean flow

A semi-analytical model solution, developed for the propagation of plane acoustic waves in a quasi 1-D nozzle sustaining a low subsonic mean flow with a temperature gradient, is discussed in this chapter. The mean flow considered can be non-isentropic due to steady heat transfer, such that the axial variations of the area and the mean temperature can be independently prescribed. For the validation of the model, conically and exponentially shaped nozzles with a linear temperature gradient are considered. Further simplified analytical solutions depending only on local spatial coordinates and inlet conditions are presented for these cases. The analytical solutions are based on the WKB method [87] and hence require sufficiently "high" frequencies. Therefore, the frequencies considered must be both low enough for a predominantly one-dimensional acoustic field considered and large enough for the validity of the solutions. Within the frequency ranges of the model's validity, the semi-analytical model estimates, applicable for any geometry and temperature profiles, were found to be accurate up to flow Mach-numbers of 0.5 *while the simplified analytical predictions perform well up to flow Mach-numbers of around* 0.3. *The model's applicability to stability analysis is shown by accurately predicting the eigenmodes sustained in a conical-shaped nozzle.*

2.1 Introduction

The analytical solutions for the planar acoustic field sustained in a combustor geometry need to consider the effects of the area variation, steady heat transfer, non-zero mean flow and be applicable over a wide range of frequencies. The thermoacoustic behaviour in combustors is highly sensitive to geometry [124] and heat transfer effects [82]. However, all the existing analytical/semi-analytical solutions do not account for either heat transfer or area variation. This chapter considers a semi-analytical solution using the WKB method for the 1-D acoustic field in a nozzle which (i) has a varying cross-sectional area, (ii) sustains a low subsonic mean flow and (iii) exhibits an axial temperature variation, as shown diagrammatically in Fig. 2.1.

This work extends the Li and Morgans [89] WKB solution, applicable to uniform area ducts sustaining a temperature gradient, to nozzles with an arbitrary area variation. This approach assumes the axial length scale of the mean flow variation is much larger than the acoustic wavelength and hence requires sufficiently high frequencies.

2.2 Analysis - non-isentropic flows

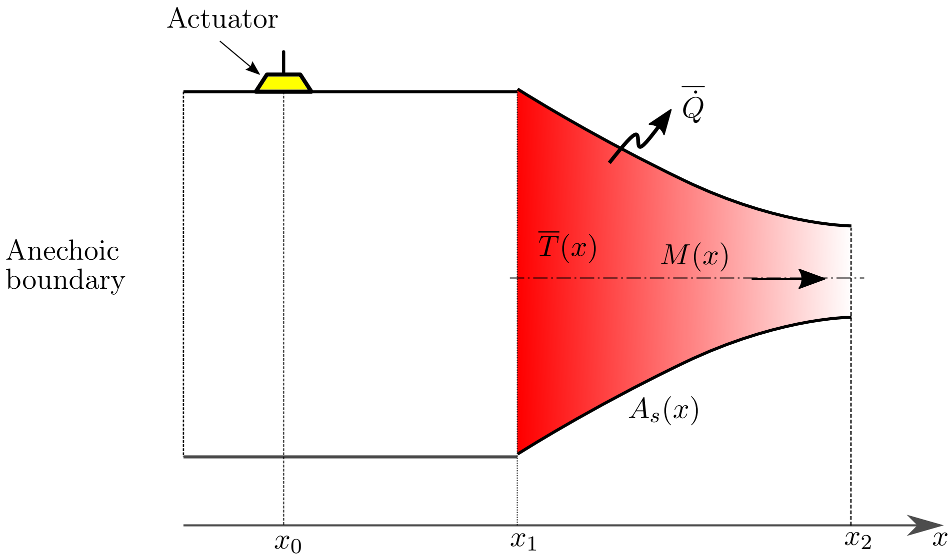

Figure 2.1: Sketch of a nozzle (x_1 to x_2) with varying mean temperature predominantly due to steady heat transfer ($\overline{\dot{Q}}$). $A_s(x)$, $M(x)$, and $\overline{T}(x)$ represent the nozzle cross-sectional area, flow Mach number and mean-temperature for given x. The validation test cases consider actuation far upstream of the nozzle with an anechoic boundary further upstream of actuation.

A solution will be derived by considering firstly non-isentropic nozzle flows exchanging heat with the surroundings, and hence the axial temperature and area gradients can be prescribed independently. The acoustic solution is then also presented for isentropic nozzle flows (with $\overline{\dot{Q}} = 0$), in which the axial temperature and area gradients are inter-related.

As shown in the schematic (Fig 2.1), the analysis assumes that the wave fronts are far from their source, behaving as planar 1-D waves. Thus the acoustic field depends only on the coordinate in the direction of propagation (x). The frequencies assumed are sufficiently large that WKB methods can be used, yet low enough to ensure that higher-order acoustic modes are not cut-on. Higher-order flow Mach number terms are neglected in this analysis - a reasonable assumption for combustors and after-burners, which require low flow Mach numbers to keep the flame attached.

Non-isentropic mean flow was observed to have a strong bearing on the acoustic field [107–109, 124, 132]. For example, the heat loss from the walls of a combustor causes a mean temperature drop which can profoundly affect the acoustic energy balance and there-by the thermoacoustic behaviour. The conservation equations for a one-dimensional perfect inviscid flow in a nozzle with mean temperature variation read,

$$A_s\frac{\partial \rho}{\partial t}+\frac{\partial(\rho A_s u)}{\partial x}=0, \quad \frac{\partial u}{\partial t}+u\frac{\partial u}{\partial x}+\frac{1}{\rho}\frac{\partial p}{\partial x}=0, \quad \frac{\partial s}{\partial t}+u\frac{\partial s}{\partial x}=\frac{R_g}{p}\dot{Q} \quad \text{with} \quad p=\rho R_g T \tag{2.1a $-$ d}$$

where ρ, p, T, u, s, R_g, denote density, pressure, temperature, axial velocity, entropy and universal gas-constant, respectively. The flow variables are linearised to retrieve the time dependant flow dynamics in the presence of small amplitude disturbances. The linearisation principle allows separating the flow variables into a mean time-averaged component, denoted by $\overline{(\ )}$, and a fluctuating component, denoted by $(\ )'$. For example, for the axial flow velocity, $u(x,\ t)=\overline{u}(x)+u'(x,\ t)$. The net heat interaction per unit volume to the surroundings is denoted by $\overline{\dot{Q}}$, assuming no heat fluctuations inside the nozzle ($\dot{Q}'=0$). Any effects of the heat fluctuations can be modelled as jump conditions at the module interfaces in the network solvers [74]. Hence these effects are neglected in this work as it primarily focuses on the disturbance propagation regimes. This simplification results in flow conservation equations, given as,

$$A_s\frac{\partial}{\partial t}\left(\overline{\rho}+\rho'\right)+\frac{\partial}{\partial x}\left(\overline{\rho}+\rho'\right)A_s\left(\overline{u}+u'\right)=0; \tag{2.2}$$

$$\frac{\partial}{\partial t}\left(\overline{u}+u'\right)+\left(\overline{u}+u'\right)\frac{\partial}{\partial x}\left(\overline{u}+u'\right)+\frac{1}{\overline{\rho}+\rho'}\frac{\partial}{\partial x}\left(\overline{p}+p'\right)=0; \tag{2.3}$$

$$\frac{\partial}{\partial t}(\overline{s}+s')+(\overline{u}+u')\frac{\partial}{\partial x}\left(\overline{s}+s'\right)=\frac{R_g}{\overline{p}+p'}\overline{\dot{Q}}. \tag{2.4}$$

We now consider the quantity η to be of the order of the ratio of fluctuating time-dependent component to the mean time-averaged component of any flow variable, for example, $\eta\approx u'/\overline{u}$. The linearisation process assumes that the fluctuating terms are much smaller than the mean time-averaged quantities, that is $\eta\ll 1$. The contributions of the mean time-averaged conservation equations can then be separated from the fluctuating flow conservation equations. This gives:

$$\frac{\mathrm{d}\left(\overline{\rho}A_s\overline{u}\right)}{\mathrm{d}x}=0, \quad \overline{\rho}\,\overline{u}\frac{\mathrm{d}\overline{u}}{\mathrm{d}x}+\frac{\mathrm{d}\overline{p}}{\mathrm{d}x}=0, \quad \overline{u}\frac{\mathrm{d}\overline{s}}{\mathrm{d}x}=\frac{R_g}{\overline{p}}\overline{\dot{Q}}. \tag{2.5a – c}$$

The area and mean-temperature gradients are normalised, and are represented by α and β defined as,

$$\alpha=\frac{1}{A_s}\frac{\mathrm{d}A_s}{\mathrm{d}x}; \qquad \beta=\frac{1}{\overline{T}}\frac{\mathrm{d}\overline{T}}{\mathrm{d}x}. \tag{2.6a – b}$$

Using the thermodynamic relation $\mathrm{d}\overline{H}=\overline{T}\mathrm{d}\overline{s}+\mathrm{d}\overline{p}/\overline{\rho}$ (with H denoting the specific enthalpy of the fluid) and Eq. (2.5 c), the steady (or mean) heat-transfer rate (per unit volume) is expressed in terms of the mean flow gradients as,

$$\overline{\dot{Q}}=\overline{\rho}\,\overline{u}\left(c_p\frac{\mathrm{d}\overline{T}}{\mathrm{d}x}+\overline{u}\frac{\mathrm{d}\overline{u}}{\mathrm{d}x}\right). \tag{2.7}$$

where, $c_p=\gamma R_g/\left(\gamma-1\right)$ with γ as the adiabatic index of the fluid. Similarly, the linearised equations are written by considering only the terms of order $\mathrm{O}(\eta)$ and neglecting $\mathrm{O}\big(\eta^2\big)$ and higher-order terms. The obtained linearised equations in the time domain are converted to the frequency domain by assuming a harmonic time-dependence. For example, the velocity disturbance is represented as $u'=\hat{u}\mathrm{e}^{\mathrm{i}\omega t}$ where ω is the complex angular frequency and $\mathrm{i}^2=-1$. This conversion gives,

$$\left(\mathrm{i}\omega+\gamma^2M^2\frac{\mathrm{d}\overline{u}}{\mathrm{d}x}+\beta\gamma\overline{u}\right)\hat{p}+\overline{u}\frac{\mathrm{d}\hat{p}}{\mathrm{d}x}+\left(\frac{\mathrm{d}\overline{p}}{\mathrm{d}x}\left(\frac{1}{M^2}+1-\gamma\right)+\gamma\overline{p}\frac{1}{\overline{T}}\frac{\mathrm{d}\overline{T}}{\mathrm{d}x}\right)\hat{u}+\gamma\overline{p}\frac{\mathrm{d}\hat{u}}{\mathrm{d}x}=0, \tag{2.8}$$

$$\left(\mathrm{i}\omega+\frac{\mathrm{d}\overline{u}}{\mathrm{d}x}\right)\hat{u}+\overline{u}\frac{\mathrm{d}\hat{u}}{\mathrm{d}x}+\overline{u}\frac{\mathrm{d}\overline{u}}{\mathrm{d}x}\frac{\hat{p}}{\gamma\overline{p}}+\frac{1}{\overline{\rho}}\frac{\mathrm{d}\hat{p}}{\mathrm{d}x}=\cancelto{\sim 0}{\overline{u}\frac{\mathrm{d}\overline{u}}{\mathrm{d}x}\frac{\hat{s}}{c_p}} \tag{2.9}$$

$$\mathrm{i}\omega\frac{\hat{s}}{c_p}+\overline{u}\frac{\mathrm{d}\left(\hat{s}/c_p\right)}{\mathrm{d}x}=\overline{u}\left(\frac{\alpha M^2\left(\gamma-1\right)-\beta\left(1-M^2\right)}{1-\gamma M^2}\right)\left(\frac{\hat{u}}{\overline{u}}+\frac{\hat{p}}{\overline{p}}\right). \tag{2.10}$$

In the above equations, the density perturbation, $\hat{\rho}$, is eliminated in favor of the pressure, $\hat{p}$, and normalised entropy, $\hat{}/c_p$, fluctuations, obtained using thermodynamic relations. This reads,

$$\frac{\hat{s}}{c_p}=\frac{\hat{p}}{\gamma\overline{p}}-\frac{\hat{\rho}}{\overline{\rho}}. \tag{2.11}$$

The effect of the entropy disturbance on the acoustic field, implied by the right-hand side of the momentum equation in Eq. (2.9), is neglected. This simplification is justified by the low subsonic flow Mach number assumption considered in this analysis in the context of gas-turbine combustors [44, 94]. Also, the WKB analysis requires sufficiently high frequencies, where the wavelength of entropy disturbances, given as $\overline{u}/f$, is smaller than the largest turbulent length scales. Hence, the amplitude of the advecting entropy wave is strongly attenuated due to shear dispersion [95–100, 102]. Furthermore, at the high frequencies considered, the total disturbance energy can be approximated by the acoustic energy [117]. The effect of neglecting the entropy disturbances' impact on the acoustic field is investigated in Section 2.7, by comparing the analytical results with the numerical solution of Eqs. (2.8) - (2.10) which fully account for the acoustic-entropy coupling. A lower value of normalised entropy fluctuation ($\hat{s}/c_p \sim 0.01$) is considered for this investigation in Section 2.7.

In this chapter, numerical simulations of the linearised Euler equations that neglect the effect of the entropy disturbance on the acoustic field are referred to as 2LEEs (two linearised Euler equations). In comparison, simulations that account for this effect are referred to as LEEs or 3LEEs (three linearised Euler equations).

Simplifying the time-averaged conservation equations (Eqs. (2.5)) allows various mean flow gradients to be expressed in terms of α and β as,

$$\frac{1}{\overline{u}}\frac{\mathrm{d}\overline{u}}{\mathrm{d}x} = \frac{\beta-\alpha}{1-\gamma M^2}; \quad \frac{1}{\overline{p}}\frac{\mathrm{d}\overline{p}}{\mathrm{d}x} = \frac{-\gamma M^2\left(\beta-\alpha\right)}{1-\gamma M^2}; \quad \frac{1}{\overline{\rho}}\frac{\mathrm{d}\overline{\rho}}{\mathrm{d}x} = \frac{-\left(\beta-\alpha\gamma M^2\right)}{1-\gamma M^2}; \quad \frac{1}{\overline{c}}\frac{\mathrm{d}\overline{c}}{\mathrm{d}x} = \frac{\beta}{2}, \tag{2.12 - 2.15}$$

where $\overline{c} = \sqrt{\gamma R_g \overline{T}}$, is the adiabatic speed of sound and $M = \overline{u}/\overline{c}$ is the flow Mach number. The linearised energy equation, Eq. (2.10) for the considered non-isentropic flows, has a source term that depends on temperature and area gradients. This dependence implies that the magnitude of the entropy disturbance can vary as it is transported. It can also be observed that entropy disturbance transport will be more strongly influenced by the temperature gradient, β, than to the area gradient, α, at low subsonic flow Mach numbers as the latter has a multiplication factor of M^2.

On dividing Eq. (2.8) by $\gamma\overline{p}$, and Eq. (2.9) by $\overline{u}$, coefficients of $\mathrm{d}\hat{u}/\mathrm{d}x$ are normalised, and the equations become,

$$A\hat{p} + B\frac{\mathrm{d}\hat{p}}{\mathrm{d}x} + C\hat{u} + \frac{\mathrm{d}\hat{u}}{\mathrm{d}x} = 0; \qquad D\hat{p} + E\frac{\mathrm{d}\hat{p}}{\mathrm{d}x} + F\hat{u} + \frac{\mathrm{d}\hat{u}}{\mathrm{d}x} = 0, \tag{2.16, 2.17}$$

where the coefficients A, B, C, D, E, F, are functions of x and wave-number, $k_o = \omega/\overline{c}$, and are given by,

$$\begin{aligned} A &= \frac{1}{\overline{\rho}\overline{c}}\left(\mathrm{i}k_o + \gamma^2 M^2 \frac{1}{\overline{u}}\frac{\mathrm{d}\overline{u}}{\mathrm{d}x} + \gamma\beta\right), \; B = \frac{\overline{u}}{\gamma\overline{p}}, \; C = \frac{1}{\gamma\overline{p}}\left(\frac{\mathrm{d}\overline{p}}{\mathrm{d}x}\left(\frac{1}{M^2} + 1 - \gamma\right) + \beta\right), \\ D &= \frac{1}{\gamma\overline{p}}\frac{\mathrm{d}\overline{u}}{\mathrm{d}x}, \; E = \frac{1}{\overline{\rho}\overline{u}}, \; F = \frac{\mathrm{i}k_o}{M} + \frac{1}{\overline{u}}\frac{\mathrm{d}\overline{u}}{\mathrm{d}x}. \end{aligned} \tag{2.18a - f}$$

Equations (2.16) and (2.17) are used to eliminate $\mathrm{d}\hat{u}/\mathrm{d}x$, so that $\hat{u}$ is expressed in terms of $\hat{p}$ and $\mathrm{d}\hat{p}/\mathrm{d}x$ as,

$$\hat{u} = G\hat{p} + H\frac{\mathrm{d}\hat{p}}{\mathrm{d}x}; \quad \text{where } G = \left(\frac{D-A}{C-F}\right) \text{ and } H = \left(\frac{E-B}{C-F}\right). \tag{2.19}$$

Eq. (2.19) and its differential with respect to x then replace $\hat{u}$ and $\mathrm{d}\hat{u}/\mathrm{d}x$ in Eq. (2.16), giving a second order differential equation (ODE) in $\hat{p}$:

$$H\frac{\mathrm{d}^2\hat{p}}{\mathrm{d}x^2} + \left(G + \frac{\mathrm{d}H}{\mathrm{d}x} + CH + B\right)\frac{\mathrm{d}\hat{p}}{\mathrm{d}x} + \left(CG + \frac{\mathrm{d}G}{\mathrm{d}x} + A\right)\hat{p} = 0. \tag{2.20}$$

On using the steady time-averaged relations from Eqs. (2.12) - (2.15) and the coefficients of the linearised Euler equations given by Eq. (2.18), Eq. (2.20) is simplified. Further assuming β is of the order α and defining parameters $\delta \sim \dfrac{\mathrm{O}(\alpha)}{k_o}$ or $\dfrac{\mathrm{O}(\beta)}{k_o}$, $\kappa = \dfrac{1}{\alpha^2}\dfrac{\mathrm{d}\alpha}{\mathrm{d}x}$ or $\dfrac{1}{\beta^2}\dfrac{\mathrm{d}\beta}{\mathrm{d}x} \sim \mathrm{O}(1)$, and neglecting terms of order δ^3, M^3 and higher, the ODE takes the following form:

$$\begin{aligned}
&\left[1 - M^2 + \overbrace{(\beta - 2\alpha)\frac{\mathrm{i}M}{k_o}}^{\mathrm{O}(\delta M)} - \overbrace{(\beta - 2\alpha)^2\frac{M^2}{k_o^2}}^{\mathrm{O}(\delta^2 M^2)}\right]\frac{\mathrm{d}^2\hat{p}}{\mathrm{d}x^2} \\
&-k_o\left[2\mathrm{i}M - \overbrace{\frac{\alpha+\beta}{k_o}}^{\mathrm{O}(\delta)} + \overbrace{\frac{\alpha M^2(1+\gamma) + \beta M^2}{k_o}}^{\mathrm{O}(\delta M^2)} - \overbrace{\frac{2\mathrm{i}\beta(\beta - 2\alpha)M}{k_o^2} - \frac{\mathrm{i}M}{k_o^2}\left(\frac{\mathrm{d}\beta}{\mathrm{d}x} - 2\frac{\mathrm{d}\alpha}{\mathrm{d}x}\right)}^{\mathrm{O}(\delta^2 M)}\right]\frac{\mathrm{d}\hat{p}}{\mathrm{d}x} \\
&+k_o^2\left[1 - \overbrace{\frac{\mathrm{i}\beta M}{k_o}(1+\gamma)}^{\mathrm{O}(\delta M)} + \overbrace{\frac{3\alpha^2 M^2}{k_o^2}(1-\kappa_\alpha) - \frac{\alpha\beta M^2}{k_o^2}(8-\gamma) + \frac{\beta^2 M^2}{k_o^2}(2-\gamma)(2+\kappa_\beta)}^{\mathrm{O}(\delta^2 M^2)}\right]\hat{p} = 0.
\end{aligned} \tag{2.21}$$

where $\kappa_\alpha = \dfrac{1}{\alpha^2}\dfrac{\mathrm{d}\alpha}{\mathrm{d}x}$ and $\kappa_\beta = \dfrac{1}{\beta^2}\dfrac{\mathrm{d}\beta}{\mathrm{d}x}$. Eq. (2.21) is the differential equation governing the acoustic pressure propagation in a nozzle with an arbitrary temperature gradient and non-isentropic mean flow. The main assumptions underpinning its derivation are: (*i*) the acoustic field is one-dimensional, (*ii*) $|\delta| \ll 1$ and $\kappa \sim \mathrm{O}(1)$, (*iii*) constant gas properties γ, R_g, (*iv*) low subsonic flow Mach numbers, such that terms of $\mathrm{O}(M^3)$ and higher are negligible and (*v*) negligible effect of the entropy disturbance on the acoustic field. The coefficients of the resultant ODE are functions only of spatial coordinate, x, and wave-number, k_o. The ODE simplifies to better-known forms under more restrictive assumptions:

- When the mean flow is negligible ($M \approx 0$), Eq. (2.21) simplifies to:

$$\frac{\mathrm{d}^2\hat{p}}{\mathrm{d}x^2} - (\alpha + \beta)\frac{\mathrm{d}\hat{p}}{\mathrm{d}x} + k_o^2\hat{p} = 0, \tag{2.22}$$

  consistent with [86].

- For a uniform area nozzle without mean-temperature variation ($\alpha = 0,\ \beta = 0$) but sustaining a mean flow, Eq. (2.21) simplifies to:

$$\left(1-M^2\right)\frac{\mathrm{d}^2\hat{p}}{\mathrm{d}x^2}-2\mathrm{i}Mk_o\frac{\mathrm{d}\hat{p}}{\mathrm{d}x}+k_o^2\hat{p}=0. \tag{2.23}$$

This is consistent with the forms in [8, 133].

- For a uniform area nozzle ($\alpha = 0$) with zero mean-temperature gradient ($\beta = 0$) and negligible mean flow ($M \approx 0$), Eq. (2.21) simplifies to the classic one-dimensional Helmholtz equation [79]:

$$\frac{\mathrm{d}^2\hat{p}}{\mathrm{d}x^2}+k_o^2\hat{p}=0. \tag{2.24}$$

2.2.1 Semi-analytical solution using an iterative WKB method

The iterative WKB method described in Li and Morgans [89] is now applied to the considered quasi 1-D nozzle sustaining non-isentropic mean flow due to steady heat transfer with the acoustic pressure solution expressed as,

$$\hat{p}\left(x,\omega\right)=I\exp\int_{x_1}^{x}\left(a^{\pm}\left(\breve{x}\right)+\mathrm{i}b^{\pm}\left(\breve{x}\right)\right)\mathrm{d}\breve{x} \tag{2.25}$$

where, I is an arbitrary constant, $\breve{x}$ is a dummy variable and a and b are two real x-dependant variables determined by substituting Eq. (2.25) in the ODE given by Eq. (2.21). The parameter b represents the rapidly varying phase of the wave, while a is related to the slowly varying amplitude, and hence it is assumed that $b \gg a$ to apply the WKB method. Therefore the length scale of the area change considered exceeds the acoustic wavelength. At sufficiently high frequencies, this assumption allows the pressure solution to be represented by independent upstream and downstream propagating plane wave amplitudes. In the context of thermoacoustics, the imaginary part of the complex wave-number k_o corresponds to the growth rate and is typically much smaller than the real part corresponding to the frequency [8, 15, 30, 71] for modes of interest. Hence the wave-number is assumed to be real for the WKB analysis presented. It will also be shown in Section 2.8 that using the analytical model to calculate the modes of the conical-shaped nozzle with isentropic mean flow (shown on the left of Fig. 2.2), led to minor errors in growth rate. A noticeable deviation was found only at the lowest frequency fundamental mode (error $\sim$ 10%) while other modes are accurately captured (error <1%) on comparison with the in-house developed modal expansion based network solver $\text{OSCILOS}_{\text{long}}$ [53]. In the final solution however, k_o is still regarded complex such that it can be used for stability analysis.

A mathematical analysis was furthermore performed, considering the angular frequency ω to be a complex quantity such that $\omega = \omega_R + \mathrm{i}\omega_I$, where ω_R and ω_I correspond to the real and imaginary parts of the angular frequency. The iterative WKB solution is expanded around ν (defined as $\nu = \omega_I/\omega_R$) up to first-order, with the final results presented in Appendix C. It can be observed that considering the angular frequency to be either real or complex leads to the same expression for the case of a planar acoustic field sustained in a quasi 1-D nozzle.

Substituting Eq. (2.25) into Eq. (2.21) gives,

$$
\begin{aligned}
&\left[1 - M^2 + \overbrace{(\beta - 2\alpha)\frac{\mathrm{i}M}{k_o}}^{\mathrm{O}(\delta M)} - \overbrace{(\beta - 2\alpha)^2 \frac{M^2}{k_o^2}}^{\mathrm{O}(\delta^2 M^2)}\right]\left(a^2 - b^2 + \mathrm{i}2ab + \frac{\mathrm{d}a}{\mathrm{d}x} + \mathrm{i}\frac{\mathrm{d}b}{\mathrm{d}x}\right) \\
&-k_o\left[2\mathrm{i}M - \overbrace{\frac{\alpha+\beta}{k_o}}^{\mathrm{O}(\delta)} + \overbrace{\frac{\alpha M^2(1+\gamma) + \beta M^2}{k_o}}^{\mathrm{O}(\delta M^2)} - \overbrace{\frac{2\mathrm{i}\beta(\beta - 2\alpha)M}{k_o^2} - \frac{\mathrm{i}M}{k_o^2}\left(\frac{\mathrm{d}\beta}{\mathrm{d}x} - 2\frac{\mathrm{d}\alpha}{\mathrm{d}x}\right)}^{\mathrm{O}(\delta^2 M)}\right](a + \mathrm{i}b) \\
&+k_o^2\left[1 - \overbrace{\frac{\mathrm{i}\beta M}{k_o}(1+\gamma)}^{\mathrm{O}(\delta M)} + \overbrace{\frac{3\alpha^2 M^2}{k_o^2}(1-\kappa_\alpha) - \frac{\alpha\beta M^2}{k_o^2}(8-\gamma) + \frac{\beta^2 M^2}{k_o^2}(2-\gamma)(2+\kappa_\beta)}^{\mathrm{O}(\delta^2 M^2)}\right] = 0.
\end{aligned}
\tag{2.26}
$$

To determine the values of a and b an iterative procedure is used with the initial values, denoted as a_0, b_0, set by the case of negligible mean flow [43, 88]. Therfore $a_0^{\pm} = -\frac{\alpha}{2} - \frac{\beta}{4}$, and hence a is of the order, O (α) or O (β) and b_0 is of the order k_o ($b_0/k_o \sim \mathrm{O}(1)$). Equating the real part of Eq. (2.26) to zero and dividing by k_o^2 results in,

$$
1 - \frac{b_0^2}{k_o^2}\left(1 - M^2\right) + 2M\frac{b_0}{k_o} + \overbrace{\frac{1}{k_o^2}\left[a_0^2 + a_0(\alpha+\beta) + \frac{\mathrm{d}a_0}{\mathrm{d}x}\right]}^{\textbf{Terms 1 -}\ \mathrm{O}(\delta^2)} - \tag{2.27}
$$

$$
\overbrace{\frac{M}{k_o^3}\left[\left(2ab_0 + \frac{\mathrm{d}b_0}{\mathrm{d}x} + 2b_0\beta\right)(\beta - 2\alpha) + b_0\left(\frac{\mathrm{d}\beta}{\mathrm{d}x} - 2\frac{\mathrm{d}\alpha}{\mathrm{d}x}\right)\right]}^{\textbf{Terms 2 -}\ \mathrm{O}(\delta^2 M)} + \cancelto{0}{\mathrm{O}(\delta^2 M^2, \delta^4 M^2)} = 0. \tag{2.28}
$$

The WKB method requires the frequency to be large; however, the frequency must also be small enough for the higher order acoustic modes to be cut-off. Thus, a heuristic lower frequency limit above which the WKB approximate solution is valid is discussed. The upper frequency limit is given by the threshold frequency above which higher order acoustic modes cut-on. These frequency limits are presented in detail in Section 2.3.

The WKB method assumes the slowly varying wave amplitude, represented by a, and the rapidly varying phase of the wave, represented by b, to be differently scaled. Hence in Eq. (2.27), terms of order O $\left(\delta^2 M^2\right)$ and higher are neglected. For the first iteration, Terms 1, 2 which are of the order O $\left(\delta^2\right)$ and O $\left(\delta^2 M\right)$, respectively, are also neglected (but considered for the second iteration). These assumptions lead to the quadratic equation given by,

$$1-\frac{b^2}{k_o^2}\left(1-M^2\right)+2M\frac{b}{k_o}\approx 0. \tag{2.29}$$

Solutions for the above equation yield updated values of b, given by $b_1{}^{\pm}=\dfrac{\mp k_o}{1\pm M}$. Similarly on equating the imaginary part of Eq. (2.26) to zero and dividing by k_o^2,

$$\begin{aligned}
&\overbrace{\frac{2ab_1}{k_o^2}+\frac{1}{k_o^2}\frac{\mathrm{d}b_1}{\mathrm{d}x}+\frac{b_1\left(\alpha+\beta\right)}{k_o^2}}^{\textbf{Terms 1 -}\ \mathrm{O}(\delta)}\overbrace{-M\left[\frac{b_1^2\left(\beta-2\alpha\right)}{k_o^3}+\frac{2a}{k_o}+\frac{\beta\left(1+\gamma\right)}{k_o}\right]}^{\textbf{Terms 2 -}\ \mathrm{O}(\delta M)}\\
&-M^2\overbrace{\left[\frac{2ab_1}{k_o^2}+\frac{1}{k_o^2}\frac{\mathrm{d}b_1}{\mathrm{d}x}+\frac{b_1\alpha\left(1+\gamma\right)}{k_o^2}+\frac{b_1\beta}{k_o^2}\right]}^{\textbf{Terms 3 -}\ \mathrm{O}(\delta M^2)}+\\
&M\overbrace{\left[\frac{a^2}{k_o^2}\frac{\left(\beta-2\alpha\right)}{k_o}+\frac{1}{k_o^2}\frac{\mathrm{d}a}{\mathrm{d}x}\frac{\left(\beta-2\alpha\right)}{k_o}+\frac{2a}{k_o}\frac{\beta\left(\beta-2\alpha\right)}{k_o^2}+\frac{a}{k_o}\frac{1}{k_o^2}\left(\frac{\mathrm{d}\beta}{\mathrm{d}x}-\frac{\mathrm{d}\alpha}{\mathrm{d}x}\right)\right]}^{\textbf{Terms 4 -}\ \mathrm{O}(\delta^3 M)}+\mathrm{O}(\delta^3M^2)=0;
\end{aligned} \tag{2.30}$$

an equation with leading order term as $\mathrm{O}\left(\delta\right)$ is obtained. Neglecting terms of order $\mathrm{O}\left(\delta^3M\right)$ and higher, and solving for $a^{\pm}$ gives,

$$a^{\pm}=\overbrace{-\frac{\alpha}{2}-\frac{\beta}{4}}^{\textbf{Terms 1}}\mp\overbrace{\left(\frac{\beta}{2}-\alpha\right)M+\left(\frac{\beta}{2}-\alpha\right)M^2}^{\textbf{Terms 2}}+\overbrace{\frac{\alpha\gamma M^2}{2}\mp\frac{\beta\gamma M}{2}}^{\textbf{Terms 3}}+\cancelto{0}{\mathrm{O}(\alpha M^3,\beta M^3)}. \tag{2.31}$$

This updated solution for $a^{\pm}$ (Eq. (2.31)) gives updated solution for $b^{\pm}$. A new quadratic equation is obtained for $b^{\pm}$ using Eq. (2.27) and considering terms of order up to $\mathrm{O}\left(\delta^2M\right)$ (Terms 1 and 2 included). This gives,

$$\frac{b^{\pm}}{k_o}=\frac{M\mp\sqrt{1-\dfrac{\Phi_{NI}^{\pm}\left(1-M^2\right)}{k_o^2}}}{1-M^2}+O\left(\delta^2M^2\right), \tag{2.32}$$

where $\Phi_{NI}^{\pm}$ is given by,

$$\begin{aligned}
\Phi_{NI}^{\pm}&=-(a^{\pm})^2-a^{\pm}\left(\alpha+\beta\right)-\frac{\mathrm{d}a^{\pm}}{\mathrm{d}x}-\frac{M}{k_o}\left[\left(2a^{\pm}b^{\pm}+\frac{\mathrm{d}b^{\pm}}{\mathrm{d}x}+2b^{\pm}\beta\right)\left(\beta-2\alpha\right)+b^{\pm}\left(\frac{\mathrm{d}\beta}{\mathrm{d}x}-2\frac{\mathrm{d}\alpha}{\mathrm{d}x}\right)\right]\\
&=\frac{\alpha^2}{4}+\frac{3\beta^2}{16}+\frac{\alpha\beta}{2}\mp M\left(\alpha^2+\frac{\beta^2}{2}\left(1-\gamma\right)-\frac{\alpha\beta}{2}\left(3-\gamma\right)\right)+\frac{\mathrm{d}\alpha}{\mathrm{d}x}\left(\frac{1}{2}\pm M\right)+\frac{1}{2}\frac{\mathrm{d}\beta}{\mathrm{d}x}\left(\frac{1}{2}\pm M\left(\gamma-1\right)\right).
\end{aligned} \tag{2.33}$$

The fraction $\dfrac{\Phi_{NI}^{\pm}}{k_o^2}$ is of the order δ^2 ($|\delta| \ll 1$) and hence using the binomial expansion for the terms in Eq. (2.32) gives,

$$\frac{b^{\pm}}{k_o} = \frac{\mp 1}{1 \pm M} \pm \frac{\Phi_{NI}^{\pm}}{2k_o^2} + \cancelto{\ll 1}{O\left(\delta^2 M^2\right)}. \tag{2.34}$$

The final analytical solution for acoustic pressure (Eq. (2.25)) requires the integrals to be evaluated. Integration of Terms 1 and 2 in $a^{\pm}$ (Eq. (2.31)) is straightforward, while for Terms 3 it depends on the nozzle shape and the temperature profile. For Terms 1:

$$\int_{x_1}^{x} \left(-\frac{\alpha}{2} - \frac{\beta}{4}\right) \mathrm{d}\breve{x} = \frac{-1}{2} \ln\left(\frac{A_s}{A_{s,\,1}} \sqrt{\frac{\overline{T}}{\overline{T}_1}}\right), \tag{2.35}$$

where $A_{s,\,1}$, and T_1 represent the nozzle area and temperature at the inlet ($x = x_1$), respectively and $\breve{x}$ is a dummy variable. For the evaluation of the integral of Terms 2, the Mach number gradient obtained from Eqs. (2.12), (2.15) is used:

$$\frac{1}{M}\frac{\mathrm{d}M}{\mathrm{d}x} = \left(\frac{\beta}{2} - \alpha\right) + (\beta - \alpha)\gamma M^2 + \cancelto{0}{O(M^4)} \Rightarrow \left(\frac{\beta}{2} - \alpha\right) M = \frac{\mathrm{d}M}{\mathrm{d}x}; \;\; \left(\frac{\beta}{2} - \alpha\right) M^2 = M\frac{\mathrm{d}M}{\mathrm{d}x}. \tag{2.36}$$

Using the final expressions for $a^{\pm}$, $b^{\pm}$, and the definition of acoustic pressure given by Eq. (2.25), the principle of superposition allows the overall analytical solution for the acoustic pressure to be written as,

$$\hat{p}\,(x,\,\omega) = \mathcal{C}^{+}\mathcal{P}^{+}\,(x,\omega) + \mathcal{C}^{-}\mathcal{P}^{-}\,(x,\omega)\,, \tag{2.37}$$

with constants $\mathcal{C}^{+}$ and $\mathcal{C}^{-}$ determined by applying the boundary conditions and,

$$\mathcal{P}^{\pm} = \left(\frac{A_{s,\,1}}{A_{s,}}\right)^{1/2} \left(\frac{\overline{T}_1}{\overline{T}}\right)^{1/4} \left[\frac{\exp\left(\dfrac{M^2}{2} \mp M + \dfrac{\gamma}{2}\displaystyle\int_{x_1}^{x} (\alpha M^2 \mp \beta M)\mathrm{d}\breve{x}\right)}{\exp\left(\dfrac{M_1^2}{2} \mp M_1\right)}\right] \exp\left(\int_{x_1}^{x} \mathrm{i}b^{\pm}\mathrm{d}\breve{x}\right), \tag{2.38}$$

where M_1 is the inlet flow Mach number. From the above expression for $\mathcal{P}^{\pm}$ (Eq. (2.38)), the explicit dependence of the acoustic field solution on the nozzle's area and mean-temperature profiles is apparent. Both the amplitude and phase parts of the wave-like solution have terms that remain under the integral, making the final solution at any location a function of the upstream flow properties.

Similarly, the velocity perturbation, $\hat{u}$, is determined from Eq. (2.19) and can be written as,

$$\hat{u}\,(x,\,\omega) = \frac{1}{\overline{\rho}\overline{c}}\left(\mathcal{B}^{+}C^{+}\mathcal{P}^{+} - \mathcal{B}^{-}C^{-}\mathcal{P}^{-}\right), \tag{2.39}$$

where,

$$\mathcal{B}^{\pm} = \frac{\mathrm{i}k_o\left(1-\gamma M^2\right) \pm \dfrac{\beta}{4} \pm \dfrac{\alpha}{2} - \alpha M + \dfrac{\beta M}{2}\left(1+\gamma\right) \pm \dfrac{\beta M^2}{4}\left(3\gamma-7\right) \pm \dfrac{\alpha M^2}{2}\left(3-2\gamma\right)}{\mathrm{i}k_o\left(1-\gamma M^2\right) + \left(\beta - 2\alpha\right) M}. \tag{2.40}$$

2.3 Frequency range of validity for semi-analytical solution

- **Lower frequency limit:** The WKB method based analytical solution requires sufficiently high frequencies, and this requirement can be written in terms of an analytical expression. The upstream and downstream propagating planar wave amplitudes are fully uncoupled for a uniform area duct without any temperature gradient and sustaining uniform mean flow. The coupling and axial evolution primarily arise due to the presence of axial gradients of the flow, with only secondary contributions from the mean flow [43]. Therefore the high-frequency requirement can be interpreted as a "decoupling criterion". It ensures that the effect of the upstream and downstream propagating plane wave amplitudes on each other is minimal. This high-frequency requirement there-by sets the lower frequency limit for the validity of the WKB method based solution. This limit follows from the terms that are neglected in the WKB analysis when making the high-frequency approximation. The terms neglected in the second iteration of $b^{\pm}$ in Eq. (2.32) ($\Phi^{\pm}_{NI}/k_o^2$ is $\ll 1$) set this limit, thus,

$$f_{lower} = \frac{\overline{c}_x}{2\pi}\max\sqrt{\left|\frac{\alpha^2}{4}\left(1+2\kappa_\alpha\right) + \frac{\beta^2}{16}\left(3+4\kappa_\beta\right) + \frac{\alpha\beta}{2} \mp M\left(\alpha^2 d_a + \frac{\beta^2}{2}\left(1-\gamma\right)d_b - \frac{\alpha\beta}{2}\left(3-\gamma\right)\right)\right|}, \tag{2.41}$$

  where the "max" function gives the maximum value of the lower frequency limit evaluated for the nozzle, $\pm$ corresponds to downstream and upstream propagating plane wave amplitudes respectively, $\overline{c}_x$ is the local speed of sound and $d_a = (1-\kappa_\alpha)$, $d_b = (1-\kappa_\beta)$.

- **Upper frequency limit:** The analytical solution derived is only valid for planar acoustic waves, meaning higher-order acoustic modes such as circumferential and radial modes must be cut-off. This requirement then sets an upper limit on the considered frequency. For a nozzle with a circular cross-section, the frequency at which the first non-planar radial modes cut-on at any given x is provided by,

$$f_{upper} = \frac{0.293\overline{c}_x}{r_x}, \tag{2.42}$$

  where, r_x is the radius of the nozzle at x.

To summarise, the expressions given by Eq. (2.38) and Eq. (2.39) are used to determine the acoustic pressure and acoustic velocity, and are an important result of this work. Beyond the assumptions outlined in the derivation of governing ODE for acoustic pressure, (i) terms of order $O(\delta^2 M^2)$ are further neglected, and (ii) the wave-number (k_o) is assumed real, neglecting the imaginary part. The expression for $\mathcal{P}^{\pm}$ given by Eq. (2.38) is applicable for nozzles of any shape/area variation and temperature profiles. A simplified analytical solution can be developed for given area and temperature profiles by evaluating the integrals in Eq. (2.38). For example, analytical solutions depending only on the local mean flow and thermodynamic properties, for simple conical and exponentially-shaped nozzles with a linear temperature variation are presented in Section (2.4) and Section (2.5), respectively, derived at the cost of restricted Mach numbers ($M^2 \ll 1$).

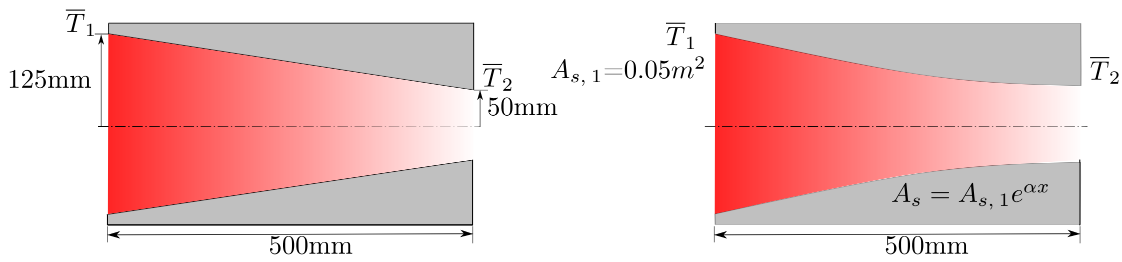

	Inlet	Outlet		Inlet	Outlet
$M = \dfrac{\overline{u}}{\overline{c}}$	0.05	0.27	$M = \dfrac{\overline{u}}{\overline{c}}$	0.06	0.28
$\lvert\alpha\rvert$	2.5	6	$\lvert\alpha\rvert$	3	3
$\overline{T}$	1600K	1200K	$\overline{T}$	1600K	1200K
$\overline{c}$	802ms^{-1}	694ms^{-1}	$\overline{c}$	802ms^{-1}	694ms^{-1}
$f_{upper} = \dfrac{0.293\overline{c}_x}{r_x}$	1880Hz	4693Hz	$f_{upper} = \dfrac{0.293\overline{c}_x}{r_x}$	1864Hz	3882Hz
$\mathrm{He}_{upper}/(2\pi)$	1.2	2.9	$\mathrm{He}_{upper}/(2\pi)$	1.2	2.4
f_{lower}, from Eq. (2.61)	128Hz	470Hz	f_{lower}, from Eq. (2.75)	237Hz	257Hz
$\mathrm{He}_{lower}/(2\pi)$	0.08	0.3	$\mathrm{He}_{lower}/(2\pi)$	0.15	0.16

Figure 2.2: (Left) Schematic of the conical-shaped nozzle with the flow parameters and calculated frequency limits for non-isentropic mean flow. (Right) Schematic of the exponential-shaped nozzle with the flow parameters and calculated frequency limits for non-isentropic mean flow. (Frequency limits, corresponding Helmholtz numbers based on length of the duct and mean speed of sound at inlet ($\mathrm{He} = 2\pi f l/\overline{c}_1$) are also presented.)

2.4 Simplified analytical solution for non-isentropic flow in a conical-shaped nozzle

To evaluate the accuracy of the proposed semi-analytical solution it is applied to two test nozzle geometries: the conical-shaped nozzle, shown on the left of Fig. 2.2 and the exponential-shaped nozzle shown on the right. A linear temperature profile is considered for these nozzle cases, and a simplified analytical solution is reported. The analytical results are then compared to the simulation results from the two-linearised Euler equations (Eqs. (2.8), (2.9)), which neglect the effect of the entropy disturbance on the acoustic propagation.

For the conical-shaped nozzle, the radius (r_x) changes linearly with space coordinate, x, and the cross-sectional area is proportional to r_x^2. For a nozzle of length l, with inlet at $x = x_1$, inlet radius r_1, and exit radius r_2, the cross-sectional area varies as,

$$A_s\,(x) = A_{s,\,1}(1 + \breve{a}\,x)^2, \quad \text{where } \breve{a} = \frac{(r_2 - r_1)}{r_1\,l} \text{ and } x \in [x_1,\ x_1 + l]\,, \tag{2.43}$$

The normalised area gradient parameter, α, and its spatial derivative become,

$$\alpha = \frac{1}{A_s}\frac{\mathrm{d}A_s}{\mathrm{d}x} = \frac{2\breve{a}}{(1 + \breve{a}\,x)} \;\Rightarrow\; \frac{\mathrm{d}\alpha}{\mathrm{d}x} = -\frac{\alpha^2}{2}. \tag{2.44a – c}$$

Considering a linear mean-temperature variation with $\overline{T}_1$ at the inlet ($x = x_1$) and $\overline{T}_2$ at the outlet ($x = x_2$, or, $x = x_1 + l$):

$$\overline{T}\,(x) = \overline{T}_1\left(1 + \breve{b}x\right), \quad \text{where } \breve{b} = \frac{\overline{T}_2 - \overline{T}_1}{\overline{T}_1 l} \text{ and } x \in [x_1, x_1 + l]\,. \tag{2.45}$$

This gives,

$$\beta = \frac{\breve{b}}{1 + \breve{b}x} \;\Rightarrow \frac{\mathrm{d}\beta}{\mathrm{d}x} = \frac{-\breve{b}^2}{\left(1 + \breve{b}x\right)^2} = -\beta^2. \tag{2.46a – c}$$

The integrals in the phase given by $b^{\pm}$ terms can be evaluated to a reasonable accuracy by assuming the flow Mach number to have the following simplified dependence on area and mean-temperature,

$$\frac{M}{M_1} \approx \frac{A_{s,\,1}}{A_s}\sqrt{\frac{\overline{T}}{\overline{T}_1}}. \tag{2.47}$$

This simplification is obtained by neglecting higher-order flow Mach number terms and hence valid for approximately $M < 0.3$, justified by the low flow Mach number assumption to neglect the effect of entropy disturbances on the acoustic field. Using the expressions for $\dfrac{\mathrm{d}\alpha}{\mathrm{d}x}$

(Eq. (2.44)), $\frac{\mathrm{d}\beta}{\mathrm{d}x}$ (Eq. (2.46)) and $\Phi^{\pm}_{NI}$ (Eq. (2.82)), $b^{\pm}$ is evaluated as,

$$\int_{x_1}^{x} b^{\pm}\mathrm{d}x = \mp\int_{x_1}^{x}\frac{k_o}{1\pm M}\mathrm{d}\breve{x} \pm \int_{x_1}^{x}\frac{\Phi^{\pm}_{NI}}{2k_o}\mathrm{d}\breve{x} \tag{2.48}$$

$$\approx \overbrace{\int_{x_1}^{x} \mp k_o\left(1\mp M + M^2\right)\mathrm{d}\breve{x}}^{I_o^c} \pm \overbrace{\int_{x_1}^{x}\left(\frac{\alpha\beta}{4k_o} - \frac{\beta^2}{32k_o} \mp \frac{3\alpha^2 M}{4k_o} \pm \frac{\alpha\beta M}{4k_o}(3-\gamma)\right)\mathrm{d}\breve{x}}^{I_1^c \quad \textbf{to} \quad I_4^c}. \tag{2.49}$$

It then follows that,

$$\mathcal{P}^{\pm} = \left(\frac{A_{s,1}}{A_s}\right)^{1/2}\left(\frac{\overline{T}_1}{\overline{T}}\right)^{1/4}\exp\left(\frac{M^2-M_1^2}{2} \mp (M-M_1) + J_1^c \mp J_2^c \mp \mathrm{i}I_0^c \pm \mathrm{i}\sum_{j=1}^{4} I_j^c\right), \tag{2.50}$$

with J_1^c and J_2^c representing the integral of Terms 3 in $a^{\pm}$. These along with I_0^c to I_4^c read:

$$J_1^c = \int_{x_1}^{x}\frac{\alpha\gamma M^2}{2}\mathrm{d}\breve{x} = \frac{\gamma M_1^2}{12\breve{a}}\left[(\breve{b}+3\breve{a}) - \frac{4\breve{a}\breve{b}x + \breve{b} + 3\breve{a}}{(1+\breve{a}x)^4}\right], \tag{2.51}$$

$$J_2^c = \mp\int_{x_1}^{x}\frac{\beta\gamma M}{2}\mathrm{d}\breve{x} \tag{2.52}$$

$$= \frac{\breve{b}M_1}{\breve{b}-\breve{a}}\left[\frac{\breve{b}}{\sqrt{\breve{a}(\breve{b}-\breve{a})}}\left(\tan^{-1}\sqrt{\frac{\breve{a}(1+\breve{b}x)}{\breve{b}-\breve{a}}} - \tan^{-1}\sqrt{\frac{\breve{a}}{\breve{b}-\breve{a}}}\right) + \frac{\sqrt{1+\breve{b}x}}{1+\breve{a}x} - 1\right], \tag{2.53}$$

$$I_0^c = \int_{x_1}^{x} k_o\left(1\mp M + M^2\right)\mathrm{d}\breve{x} = k_1\int_{x_1}^{x}\left(\frac{1}{\sqrt{1+\breve{b}x}} \mp \frac{M_1}{(1+\breve{a}x)^2} + \frac{M_1^2\sqrt{1+\breve{b}x)}}{(1+\breve{a}x)^4}\right)\mathrm{d}\breve{x}, \tag{2.54}$$

$$= \frac{2k_1}{\breve{b}}\left(\sqrt{1+\breve{b}x} - 1\right) \mp \frac{k_1 M_1 x}{1+\breve{a}x} + \tag{2.55}$$

$$k_1 M_1^2\left[\frac{\breve{b}^3\tan^{-1}\left(\sqrt{\frac{\breve{a}(1+\breve{b}x)}{\breve{b}-\breve{a}}}\right)}{8\breve{a}^{3/2}\left(\breve{b}-\breve{a}\right)^{5/2}} + \frac{\sqrt{1+\breve{b}x}\,\left(\breve{b}(\breve{a}x+3)-2\breve{a}\right)\left(\breve{b}(3\breve{a}x-1)+4\breve{a}\right)}{24\breve{a}\left(\breve{b}-\breve{a}\right)^2(1+\breve{a}x)^3}\right]_{x_1=0}^{x} \tag{2.56}$$

$$I_1^c = \frac{1}{2}\int_{x_1}^{x} \frac{\alpha\beta}{2k_o}\mathrm{d}\breve{x} = \frac{\breve{a}\breve{b}}{k_1\sqrt{\breve{a}(\breve{b}-\breve{a})}}\left[\tan^{-1}\left(\sqrt{\frac{\breve{a}(1+\breve{b}x)}{\breve{b}-\breve{a}}}\right) - \tan^{-1}\left(\sqrt{\frac{\breve{a}}{\breve{b}-\breve{a}}}\right)\right], \quad (2.57)$$

$$I_2^c = \frac{-1}{16}\int_{x_1}^{x} \frac{\beta^2}{2k_o}\mathrm{d}\breve{x} = \frac{\breve{b}}{16k_1}\left(\frac{1}{\sqrt{1+\breve{b}x}} - 1\right), \quad (2.58)$$

$$I_3^c = \mp\frac{3}{2}\int_{x_1}^{x} \frac{\alpha^2 M}{2k_o}\mathrm{d}\breve{x} = \mp\frac{M_1}{2k_1}\left[\left(\breve{b}+2\breve{a}\right) - \frac{3\breve{a}\,\breve{b}\,x+\breve{b}+2\breve{a}}{(1+\breve{a}x)^3}\right], \quad (2.59)$$

$$I_4^c = \pm\frac{3-\gamma}{2}\int_{x_1}^{x} \frac{\alpha\beta M}{2k_o}\mathrm{d}\breve{x} = \mp\frac{(3-\gamma)\,\breve{b}\,M_1}{2k_1}\left[\frac{1}{(1+\breve{a}x)^2} - 1\right]. \quad (2.60)$$

where $k_1 = \omega/\overline{c}_1$ is the wave-number at the inlet. Therefore the acoustic field solution in a conical-shaped nozzle sustaining a non-isentropic mean flow is given by Eq. (2.37) and Eq. (2.39) with $\mathcal{P}^{\pm}$ and $\mathcal{B}^{\pm}$ obtained using Eq. (2.50) and Eq. (2.40), respectively.

2.4.1 Frequency limits

Using the expressions for $\frac{\mathrm{d}\alpha}{\mathrm{d}x}$ (Eq. (2.44)) and $\frac{\mathrm{d}\beta}{\mathrm{d}x}$ (Eq. (2.46)) in the lower frequency limit given by Eq. (2.41) gives,

$$f_{lower} = \frac{\overline{c}_x}{2\pi}\max\left(\sqrt{\left|\pm\frac{3\alpha^2 M}{2} - \frac{\beta^2}{16} + \frac{\alpha\beta}{2} \pm \frac{\alpha\beta M}{2}(3-\gamma)\right|}\right). \quad (2.61)$$

The lower and upper frequency limits are calculated at the nozzle's inlet and outlet, as shown in Fig. 2.2 (Left). It can be observed that a broad intermediate frequency range exists where both the limits are satisfied.

2.4.2 Validation of analytical solution

The presented analytical solution for conical-shaped nozzles is validated by comparing its predictions with the numerical simulation of the LEEs under the acoustic forcing and boundary conditions summarised in Fig. 2.1. Like the analytical solution, the numerical simulations of the two-linearised Euler equations (Eqs. (2.8), (2.9), denoted as 2LEEs) neglect the effect of the entropy disturbance on the acoustic field. Hence, the analytical model predictions should agree with the numerical simulations of the 2LEEs, in the frequency and flow Mach ranges of models' validity. At the nozzle inlet, x_1, the acoustic impedance, Z_1, is specified by the relation between acoustic pressure, $\hat{p}_1$, and acoustic velocity, $\hat{u}_1$, being $\hat{p}_1 = \overline{\rho}_1\,\overline{c}_1 Z_1\hat{u}_1$. Dowling's [134] method of a semi-infinite boundary condition is used for the nozzle outlet, which assumes the acoustic waves to have not reached the outlet boundary at x_2; this facilitating validation of the solution across a wide range of frequencies. Dowling's approach results in an initial value problem formulation for a prescribed frequency and hence is amenable to higher-order schemes;

the 4th order Runge-Kutta is employed for our solution. It should be noted that the acoustic boundary condition at the outlet will not influence the current problem formulation. However we can still apply the boundary conditions at both inlet and outlet to determine the eigensolutions. For example, in Section 2.8, it is shown that the model can be used to predict the acoustic modes of nozzles by arbitrarily imposing both the inlet and outlet boundary conditions - a closed inlet and open outlet are considered. The deviation was observed only at low frequencies owing to the lower frequency limit set by Eq. (2.41).

The transfer functions relating the acoustic pressure and velocity variations along the nozzle to the inlet velocity forcing read:

$$F_p(x, f) = \frac{\hat{p}(x, f)}{\bar{\rho}_1 \bar{c}_1 \hat{u}_1(f)}; \qquad F_u(x, f) = \frac{\hat{u}(x, f)}{\hat{u}_1(f)}. \tag{2.62, 2.63}$$

The deviations observed with the analytical model predictions compared to the numerical solutions are characterised with "error coefficients", which are relative L^2 norms. For N representing the total number of spatial grid points, the pressure and velocity error coefficients are given by,

$$\epsilon(F_{\mathrm{Model}}, F_{\mathrm{LEEs}}) = \left(\sum_{j=1}^{N} |F_{\mathrm{Model}}(x_j) - F_{\mathrm{LEEs}}(x_j)|^2 \Bigg/ \sum_{j=1}^{N} |F_{\mathrm{Model}}(x_j)|^2 \right)^{1/2} \tag{2.64}$$

where $F_{\mathrm{Model\ or\ LEEs}}$ denote F_p and F_u corresponding to the error coefficients ϵ_p and ϵ_u, respectively.

The analytical model predictions are compared to the numerical 2LEEs results for the conical-shaped nozzle, shown in Fig. 2.2 (Left), considered across three different inlet flow Mach numbers and three different frequencies. The frequencies are presented in terms of Helmholtz number based on the length of the duct ($\mathrm{He}_1 = 2\pi f l / \bar{c}_1$). The first two frequencies ($\mathrm{He}_1/(2\pi) = 1, 0.3$) satisfy both the lower (Eq. (2.61)) and upper (Eq. (2.42)) frequency limits, with the third frequency ($\mathrm{He}_1/(2\pi) = 0.1$) below the lower frequency limit. As the physical frequencies (f) in Hz are used to present the limits, a factor of $1/(2\pi)$ is multiplied for the Helmholtz numbers.

- **Very low Mach numbers:** For a nozzle with inlet flow Mach number of $M_1 = 0.005$ and outlet flow Mach number of $M = 0.027$, sustaining a strong temperature gradient of 800K/m, Fig. 2.3 compares the analytical model and numerical 2LEEs solutions. At these very low flow Mach numbers, the lower frequency limit given by Eq. (2.61) becomes proportional to β, which is generally smaller than the area gradient, α, and hence less restrictive. Thus for the frequencies considered, $\delta \ll 1$, and as observed from Fig. 2.3, the analytical model predictions are therefore in close agreement with the numerical results.
- **Increased low Mach numbers:** Fig. 2.3 also compares the results for the nozzle

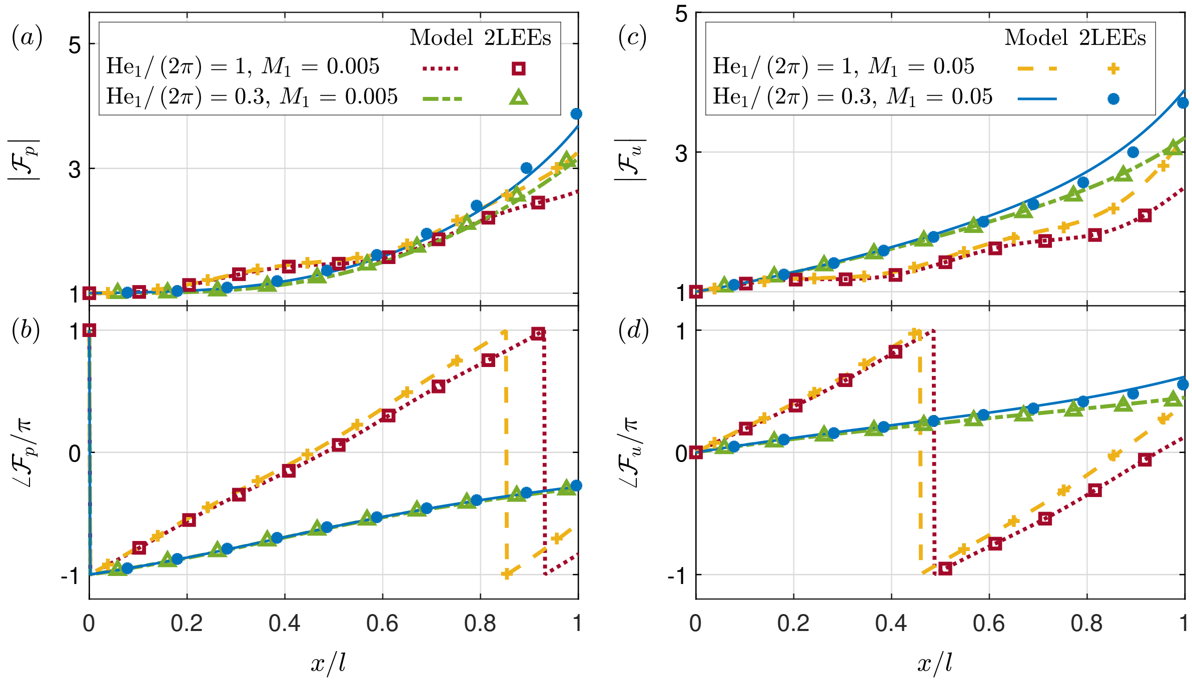

Figure 2.3: Evolution of F_p and F_u with x. $\overline{T}_1$ = 1600 K, $\overline{T}_2$ = 1200 K, M_1 = 0.005 & 0.05, M_2 = 0.027 & 0.27, $\mathrm{He}_1/(2\pi)$ = 1 & 0.3, and Z_1 = -1. (a): transfer function gain $|F_p|$. (b): transfer function phase $\angle F_p$. (c): transfer function gain $|F_u|$. (d): transfer function phase $\angle F_u$.

with an inlet flow Mach number of 0.05 and outlet Mach number of 0.27. The analytical model and numerical 2LEEs results agree close to the inlet but slightly diverge towards the exit for the case of lower frequency ($\mathrm{He}_1/(2\pi) = 0.3$). This deviation is attributed to the increased flow Mach numbers and higher α values close to the outlet.

- **Frequency below lower frequency limit:** For a frequency of 160Hz ($\mathrm{He}_1/(2\pi) = 0.1$), which lies below the lower frequency limit (Eq. (2.61)), Fig. 2.4 (plotted in red) compares the predictions. Even when the nozzle sustains very low Mach numbers, a deviation is observed in the phase of F_u, while the acoustic pressure is well-captured.

- **High subsonic Mach numbers:** For the case of high flow Mach numbers sustained in the nozzle ($\sim$ 0.73 at the outlet), Fig. 2.4 compares the predictions. The general semi-analytical solution given by Eq. (2.38) is used at the expense of slightly increased computational effort due to the simplified solutions' low Mach assumption. The model prediction is accurate, with the final solution now depending on upstream mean flow and thermodynamic properties.

- **Effect of flow temperature:** The effect of the considered frequency and the temperature distribution inside the nozzle on the model's accuracy is investigated by plotting the errors of the acoustic pressure and velocity predictions using Eq. (2.64). As observed

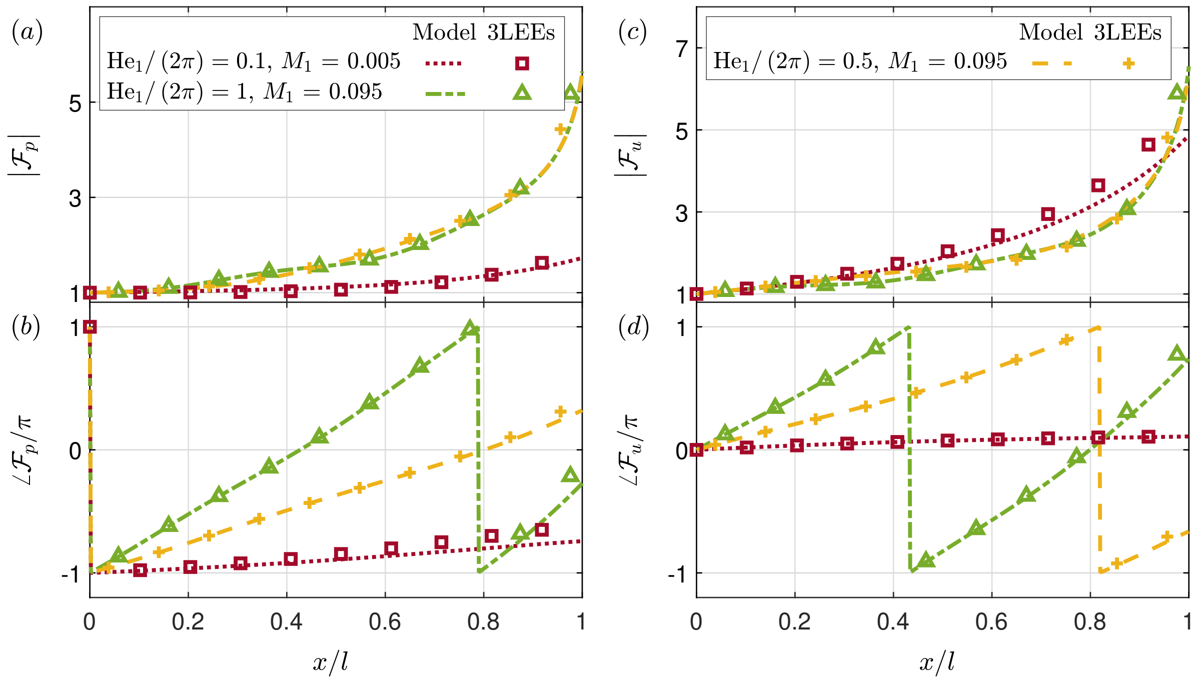

Figure 2.4: Evolution of F_p and F_u with x. $\overline{T}_1$ = 1600 K, $\overline{T}_2$ = 1200 K, M_1 = 0.005 & 0.095, M_2 = 0.05 & 0.73, Helmholtz numbers given by He_1, and Z_1 = -1. (a): transfer function gain $|F_p|$. (b): transfer function phase $\angle F_p$. (c): transfer function gain $|F_u|$. (d): transfer function phase $\angle F_u$.

in Fig. 2.5, the error remains below 10% over most conditions. Note that the flow Mach numbers at the nozzle outlet (M_2) are shown on a separate axis.

- **Effect of flow Mach number - using simplified low Mach solution:** Fig. 2.6 plots the acoustic pressure and velocity errors as a function of inlet flow Mach numbers and a range of inlet Helmholtz numbers. As observed, the error remains below 10% over most conditions; however, as the acoustic field is predicted using the simplified solution (Eq. (2.50)), valid for small Mach numbers, a deviation occurs for high flow Mach numbers and low frequencies.

- **Effect of flow Mach number - using general solution**: For nozzles with high subsonic flow Mach numbers, the errors of the acoustic field predictions using the general semi-analytical solution are shown in Fig. 2.7. The planar wave amplitudes, $\mathcal{P}^{\pm}$, are estimated using Eq. (2.38) at an increased computational effort. The errors suggest that the solution can be employed over an increased range of flow Mach numbers and frequencies while keeping the error below 10%.

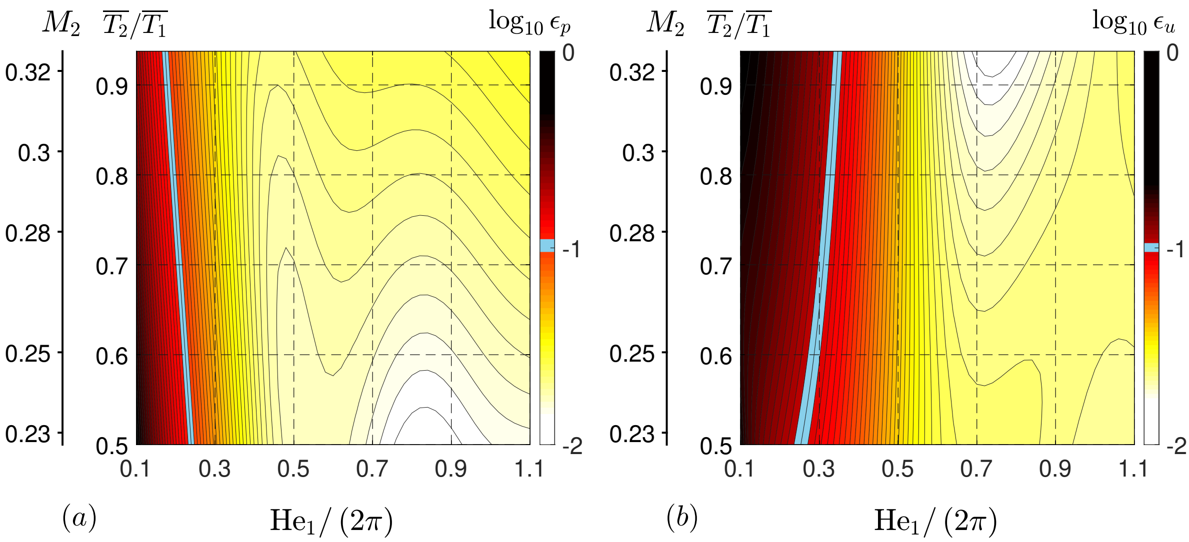

Figure 2.5: Contour maps of (a) ϵ_p and (b) ϵ_u using the proposed analytical model as functions of He_1 and $\overline{T}_2/\overline{T}_1$, in conical test-case. The dashed line represents the lower frequency limit given by Eq. (2.61) .

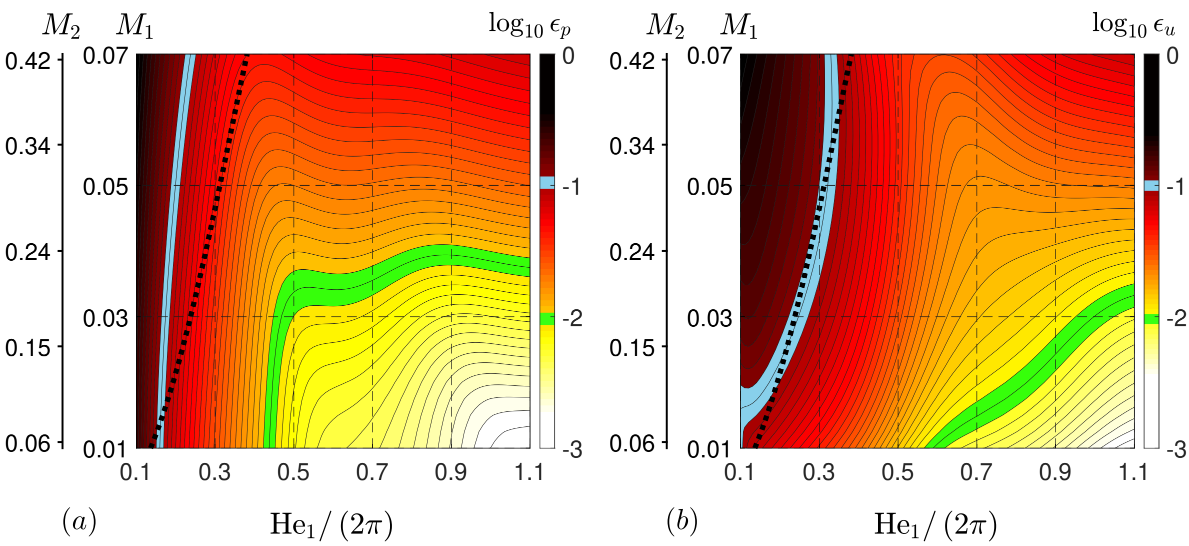

Figure 2.6: Contour maps of (a) ϵ_p and (b) ϵ_u using the proposed analytical model as functions of He_1 and M_1, in conical test-case. The dashed line represents the lower frequency limit given by Eq. (2.61).

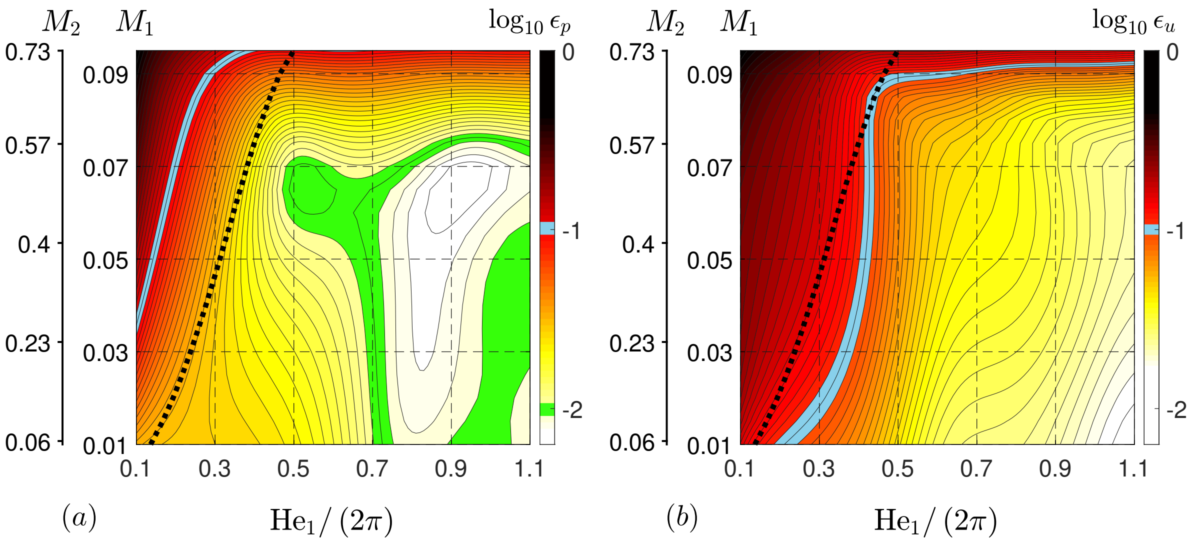

Figure 2.7: Contour maps of (a) ϵ_p and (b) ϵ_u using the general semi-analytical solution as functions of He_1 and M_1, in conical test-case. The dashed line represents the lower frequency limit given by Eq. (2.41).

2.5 Simplified analytical solution for non-isentropic flow in an exponentially-shaped nozzle

This section presents the simplified analytical solution for an exponentially-shaped nozzle with linear mean-temperature variation, as shown on the right of Fig. 2.2. For such a nozzle with area $A_{s,\,1}$ at the inlet ($x = x_1$):

$$A_s\left(x\right) = A_{s,\,1}\mathrm{e}^{\alpha x}, \quad \text{where } \alpha = \frac{1}{A_s}\frac{\mathrm{d}A_s}{\mathrm{d}x} = \text{Constant} \quad \Rightarrow \frac{\mathrm{d}\alpha}{\mathrm{d}x} = 0 \text{ and } x \in [x_1,\ x_1 + l]\,. \qquad (2.65a - b)$$

Using Eqs. (2.65), (2.46), the integrals given in $\mathcal{P}^{\pm}$ (Eq. (2.38)) are evaluated in a similar manner as for the conical-shaped nozzle.

$$\mathcal{P}^{\pm} = \left(\frac{A_{s,\,1}}{A_s}\right)^{1/2}\left(\frac{\overline{T}_1}{\overline{T}}\right)^{1/4}\exp\left(\frac{M^2 - M_1^2}{2} \mp (M - M_1) + J_1^e \mp J_2^e \mp \mathrm{i}I_0^e \pm \mathrm{i}\sum_{j=1}^{5} I_j^e\right). \quad (2.66)$$

The various terms are given by,

$$J_1^e = \int_{x_1}^{x}\frac{\alpha\gamma M^2}{2}\mathrm{d}\breve{x} = \frac{\gamma M_1^2}{8\alpha}\left[(\breve{b} + 2\alpha) - (\breve{b} + 2\alpha + 2\alpha\breve{b}x)\exp(-2\alpha x)\right], \quad (2.67)$$

$$J_2^e = \mp\int_{x_1}^{x}\frac{\beta\gamma M}{2}\mathrm{d}\breve{x} = \mp\sqrt{\frac{\pi\breve{b}}{\alpha}}\frac{\gamma M_1}{2}\exp\left(\frac{\alpha}{\breve{b}}\right)\left[\mathrm{erf}\left(\sqrt{\frac{\alpha(1+\breve{b}x)}{\breve{b}}}\right) - \mathrm{erf}\left(\sqrt{\frac{\alpha}{\breve{b}}}\right)\right], \quad (2.68)$$

$$\begin{aligned} I_0^e = \int_{x_1}^{x} k_o\left(1 \mp M + M^2\right)\mathrm{d}\breve{x} &= \frac{2k_1}{\breve{b}}\left(\sqrt{1+\breve{b}x} - 1\right) \pm \frac{M_1 k_1}{\alpha}\left(\exp(-\alpha x) - 1\right) \\ &+ \frac{k_1 M_1^2}{2\alpha}\left[\frac{1}{2}\sqrt{\frac{\pi\breve{b}}{2\alpha}}\exp\left(\frac{2\alpha}{\breve{b}}\right)\left[\mathrm{erf}\left(\sqrt{\frac{2\alpha}{\breve{b}}(1+\breve{b}x)}\right)\right]_{x=0}^{x} - \sqrt{1+\breve{b}x}\ \exp(-2\alpha x) + 1\right], \end{aligned} \quad (2.69)$$

$$I_1^e = \frac{1}{4}\int_{x_1}^{x}\frac{\alpha^2}{2k_o}\mathrm{d}\breve{x} = \frac{\alpha^2}{12\breve{b}k_1}\left((1+\breve{b}x)^{3/2} - 1\right), \quad (2.70)$$

$$I_2^e = -\frac{1}{16}\int_{x_1}^{x}\frac{\beta^2}{2k_o}\mathrm{d}\breve{x} = \frac{\breve{b}}{16k_1}\left[\frac{1}{\sqrt{1+\breve{b}x}} - 1\right], \quad (2.71)$$

$$I_3^e = \frac{1}{2}\int_{x_1}^{x}\frac{\alpha\beta}{2k_o}\mathrm{d}\breve{x} = \frac{\alpha}{2k_1}\left[\sqrt{1+\breve{b}x} - 1\right], \quad (2.72)$$

$$I_4^e = \mp\int_{x_1}^{x}\frac{\alpha^2 M}{2k_o}\mathrm{d}\breve{x} = \pm\frac{M_1}{2k_1}\left[(\alpha + \breve{b} + \alpha\breve{b}x)\exp(-\alpha x) - (\alpha + \breve{b})\right], \quad (2.73)$$

$$I_5^e = \pm\frac{(3-\gamma)}{2}\int_{x_1}^{x}\frac{\alpha\beta M}{2k_o}\mathrm{d}\breve{x} = \pm\frac{(3-\gamma)\breve{b}M_1}{4k_1}\left[1 - \exp(-\alpha x)\right]. \quad (2.74)$$

For an exponentially-shaped nozzle with a linear mean-temperature variation, the acoustic pressure, $\hat{p}$, can therefore be obtained using Eq. (2.25) with $\mathcal{P}^{\pm}$ from Eq. (2.66). Similarly, the acoustic velocity, $\hat{u}$, is obtained using Eq. (2.39) with $\mathcal{B}^{\pm}$ from Eq. (2.40).

2.5.1 Frequency limits

The lower frequency limit for the exponential-shaped nozzle is obtained using area and temperature gradient relations, Eqs. (2.65), (2.46), respectively, in Eq. (2.41). This gives,

$$f_{lower} = \frac{\bar{c}_x}{2\pi} \max \sqrt{\left| \frac{\alpha^2}{4} - \frac{\beta^2}{16} + \frac{\alpha\beta}{2} \mp M \left(\alpha^2 - \frac{\alpha\beta}{2} (3-\gamma) \right) \right|}. \tag{2.75}$$

The above equation implies a stronger dependence of the lower frequency limit on the area gradient, α, compared to the conical-shaped nozzle. For flows in the very low Mach limit, this requires $|k_o| \gg |\alpha|$ and $|k_o| \gg |\beta|$, implying the possibility for errors at even very low Mach numbers and frequencies. The lower and upper frequency limits are shown in the right of Fig. 2.2, for both the inlet and outlet of the nozzle. While the lower frequency limit for the conical-shaped nozzle suggests the considered frequency to be larger than 128Hz, the exponential-shaped nozzle requires 257Hz.

2.5.2 Validation of analytical solution

- **Very low Mach numbers:** For a Mach number of $M_1 = 0.006$ at the inlet and $M_2 = 0.027$ at the outlet, Fig. 2.8 compares the analytical model solution with the numerical 2LEEs solution. The results agree well at high frequencies but diverge for lower frequencies. This deviation is attributed to the increased lower frequency limit (shown in Fig. 2.2) for the exponential-shaped nozzle due to the strong dependence of the limit criterion (Eq. (2.75)) on the area gradient.
- **Increased low Mach numbers:** At a flow Mach number of 0.06 at the inlet and 0.28 at the outlet, the results shown in Fig. 2.8 are only subtly different to those at very low Mach numbers. At low frequencies, a slight deviation is observed throughout the length, again confirming the strong dependence of the exponential-shaped nozzles' lower frequency limit (Eq. (2.75)) on the area gradient, α.
- **Effect of flow Mach number:** The acoustic pressure and velocity prediction errors are shown in Fig. 2.9 as a function of both flow Mach number and non-dimensionalised frequency. Above an inlet Helmholtz number, $\mathrm{He}_1/(2\pi)$, of 0.3, the error remains below 10%.
- **Effect of changing duct convergence:** Fig. 2.9 shows the dependence of the model's accuracy on the area gradient parameter α. Unless both the area gradient is steep and

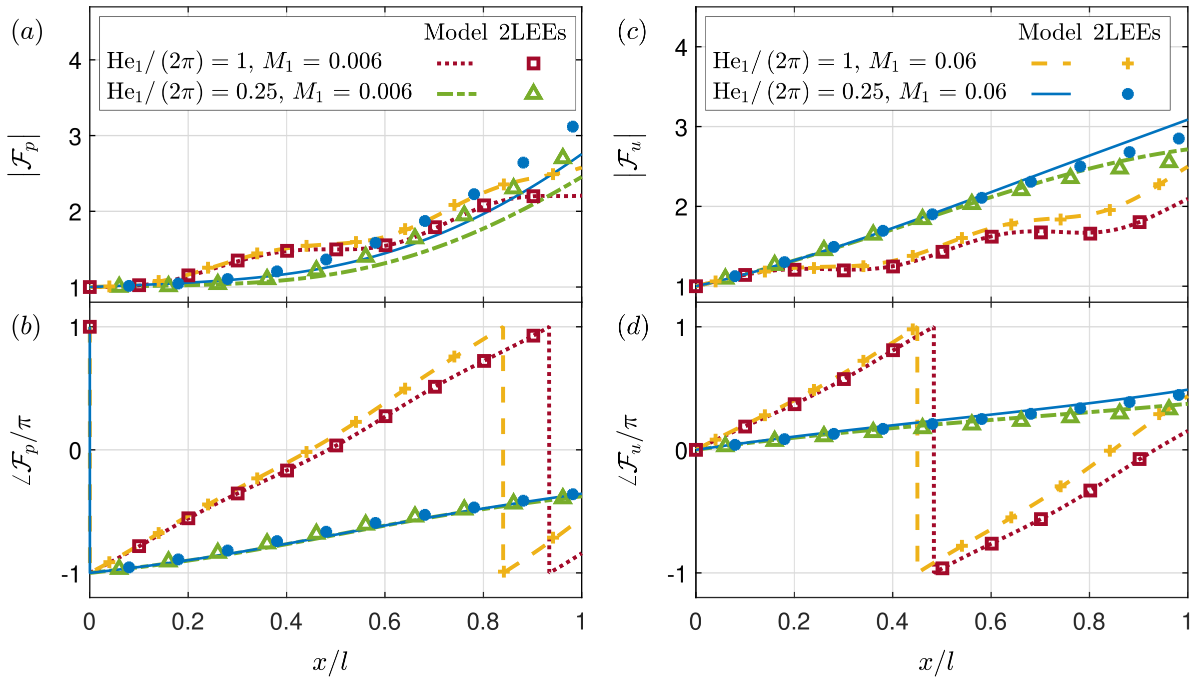

Figure 2.8: Evolution of F_p and F_u with x. $\overline{T}_1$ = 1600K, $\overline{T}_2$ = 1200K, M_1 = 0.006 & 0.06, M_2 = 0.027 & 0.28, $\mathrm{He}_1/(2\pi)$ = 1 & 0.25, and Z_1 = -1. (a): transfer function gain $|F_p|$. (b): transfer function phase $\angle F_p$. (c): transfer function gain $|F_u|$. (d): transfer function phase $\angle F_u$.

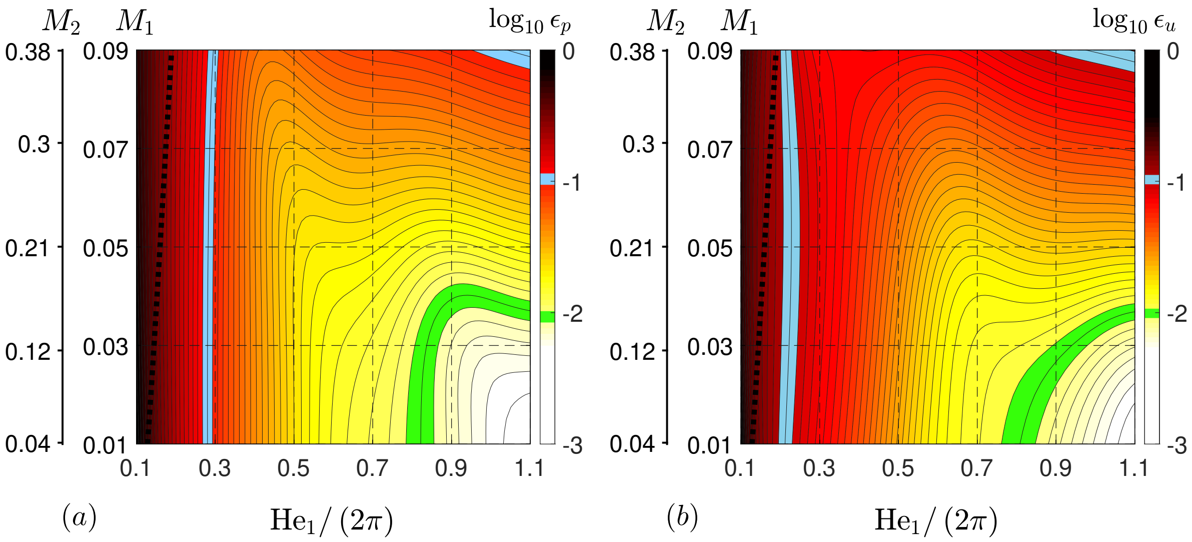

Figure 2.9: Contour maps of (a) ϵ_p and (b) ϵ_u using the proposed analytical model as functions of He_1 and M_1, in exponential test-case. The dashed line represents the lower frequency limit given by Eq. (2.75).

the frequency is low, the error remains below 10%.

To summarise, Section 2.4 and 2.5 presents simplified analytical solutions of the planar wave

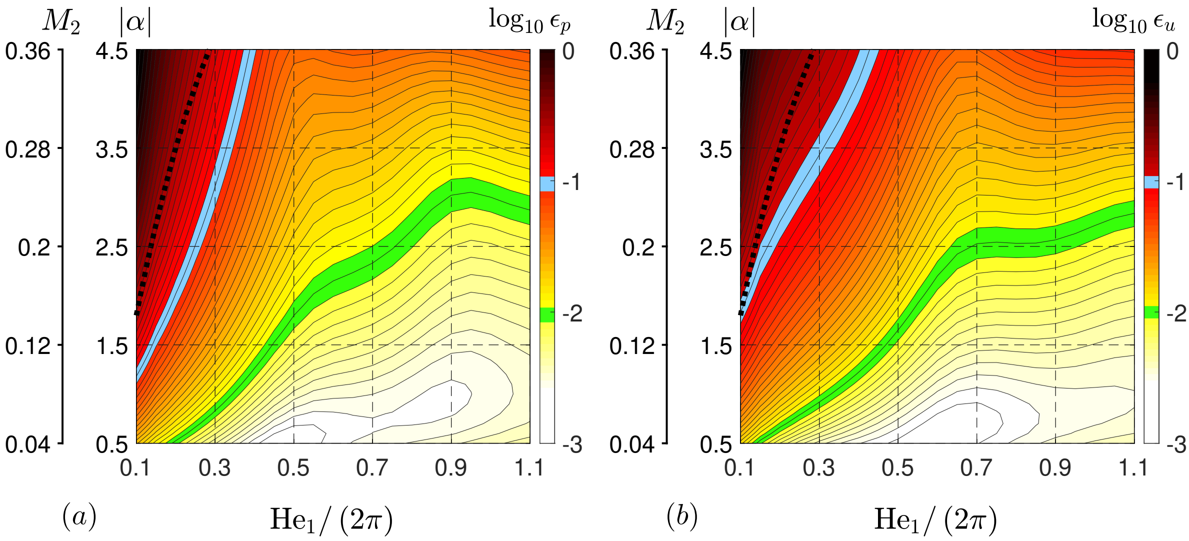

Figure 2.10: Contour maps of (a) ϵ_p and (b) ϵ_u using the proposed analytical model as functions of He_1 and α, in exponential test-case. The dashed line represents the lower frequency limit given by Eq. (2.75).

amplitudes for conical-shaped (Eq. (2.50)) and exponential-shaped (Eq. (2.66)) nozzles, respectively, sustaining a non-isentropic mean flow due to heat exchange with the surroundings. The wave amplitudes vary with position along the duct, x, and are only functions of inlet condition, Mach number, area and temperature variation parameters; they are straightforward, easy to compute. The computational cost of the WKB analytical solution was found to be significantly lower compared to the numerical LEEs solution, and the results are shown in Appendix D. Further to the assumptions outlined for deriving the general solution, it is also assumed that $M^2 \ll 1$, to facilitate using simplified Mach expressions for evaluating the integrals.

2.6 Analysis - isentropic flows

This section presents the acoustic solution of nozzles sustaining an isentropic mean flow, meaning the effects of fluid viscosity, thermal conductivity, and heat sources are negligible. As the steady (or mean) heat-flux from the system, $\bar{\dot{Q}}$ (Eq. (2.7)), is zero for an isentropic flow, the gradients of area and mean-temperature are related:

$$\bar{\dot{Q}} = 0 \quad \Rightarrow \quad \beta = \frac{\alpha M^2 (\gamma - 1)}{1 - M^2}. \tag{2.76}$$

The linearised Euler equations, governing the one-dimensional disturbance propagation in a nozzle with isentropic mean flow, are presented in Marble and Candel [76]. These equations are converted to the frequency domain, again by assuming a time-dependence of the form

$y' = \hat{y}\mathrm{e}^{i\omega t}$. This gives,

$$\left(\mathrm{i}\omega + \gamma M^2 \frac{\mathrm{d}\overline{u}}{\mathrm{d}x}\right)\hat{p} + \overline{u}\frac{\mathrm{d}\hat{p}}{\mathrm{d}x} + \frac{1}{M^2}\frac{\mathrm{d}\overline{p}}{\mathrm{d}x}\hat{u} + \gamma\overline{p}\frac{\mathrm{d}\hat{u}}{\mathrm{d}x} = 0, \tag{2.77}$$

$$\left(\mathrm{i}\omega + \frac{\mathrm{d}\overline{u}}{\mathrm{d}x}\right)\hat{u} + \overline{u}\frac{\mathrm{d}\hat{u}}{\mathrm{d}x} + \overline{u}\frac{\mathrm{d}\overline{u}}{\mathrm{d}x}\frac{\hat{p}}{\gamma\overline{p}} + \frac{1}{\overline{\rho}}\frac{\mathrm{d}\hat{p}}{\mathrm{d}x} = \cancelto{\sim 0}{\overline{u}\frac{\mathrm{d}\overline{u}}{\mathrm{d}x}\frac{\hat{s}}{c_p}}, \tag{2.78}$$

$$\mathrm{i}\omega\frac{\hat{s}}{c_p} + \overline{u}\frac{\mathrm{d}\hat{s}/c_p}{\mathrm{d}x} = 0. \tag{2.79}$$

As the source term of the linearised energy equation in Eq. (2.79) is zero, the entropy disturbance at the nozzle inlet advects with its magnitude unchanged. A second-order homogeneous ODE in $\hat{p}$ is again obtained using a similar procedure as for the non-isentropic flow and reads:

$$\left(1 - M^2 + \frac{2\alpha M}{\mathrm{i}k_o} - \frac{4\alpha^2 M^2}{k_o^2}\right)\frac{\mathrm{d}^2\hat{p}}{\mathrm{d}x^2} - \left(2\mathrm{i}Mk_o - \alpha + 2\alpha M^2 - \frac{2M}{\mathrm{i}k_o}\frac{\mathrm{d}\alpha}{\mathrm{d}x}\right)\frac{\mathrm{d}\hat{p}}{\mathrm{d}x} + \left({k_o}^2 + 3\alpha^2 M^2 d_a\right)\hat{p} = 0. \tag{2.80}$$

where $d_a = (1 - \kappa_\alpha)$. Applying the iterative WKB method gives the semi-analytical solution for acoustic pressure in terms of upstream (-) and downstream (+) propagating wave amplitudes by Eq. (2.37) with,

$$\mathcal{P}^{\pm} = \left(\frac{A_{s,1}}{A_s}\right)^{1/2}\left[\frac{\exp\left(M_1^2\left(\frac{\gamma-3}{8}\right) \pm M_1 \mp M_1^3\left(\frac{\gamma-1}{3}\right)\right)}{\exp\left(M^2\left(\frac{\gamma-3}{8}\right) \pm M \mp M^3\left(\frac{\gamma-1}{3}\right)\right)}\right]\exp\left(\int_{x_1}^{x}\mathrm{i}\left(\frac{\mp k_o}{1 \pm M} \pm \frac{\Phi_I^{\pm}}{2k_o}\right)\mathrm{d}\check{x}\right), \tag{2.81}$$

where,

$$\frac{\Phi_I^{\pm}}{k_o^2} = \frac{\delta_i^2}{4} \mp \delta_i^2 M + \kappa\delta_i^2\left(\frac{1}{2} \pm M\right) + \mathrm{O}(\delta_i^2 M^2), \quad \text{with } \delta_i = \frac{\alpha}{k_o}. \tag{2.82}$$

The corresponding velocity perturbation, $\hat{u}$, is determined using Eq. (2.39), where $\mathcal{B}^{\pm}$ is given by,

$$\mathcal{B}^{\pm} = \frac{1}{\mathrm{i}k_o\left(1 - M^2\right) - 2\alpha M}\left[\mathrm{i}k_o\left(1 - M^2\right) \pm \frac{\alpha}{2} - \alpha M \mp \frac{\alpha M^2\left(\gamma - 3\right)}{4} + \frac{\alpha M^3\left(\gamma + 1\right)}{2}\right]. \tag{2.83}$$

2.6.1 Analytical solution for a conical-shaped nozzle

An analytical solution can be further developed assuming a simplified Mach number dependence on the cross-sectional area, given as $M = M_1 A_{s,1}/A_s$. For the isentropic flow at low Mach numbers, the temperature variation (β) and thereby wave-number (k_o) variation, can be considered negligible in the nozzle. For example, for Fig. 2.2 (Left), geometry with an isentropic mean flow, the wave-number (k_o) changes by only 2% over the domain. This simplification leads to,

$$\mathcal{P}^{+} = \mathbf{O}^{+}\exp\left[-\mathrm{i}k_o\left(x - \frac{\sqrt{M_1}}{\breve{a}}\tan^{-1}\left(\frac{\breve{a}x\sqrt{M_1}}{1+\breve{a}x+M_1}\right) + \frac{\breve{a}M_1}{k_o^2}\left(1-\frac{1}{(1+\breve{a}x)^3}\right)\right)\right]$$
$$\mathcal{P}^{-} = \mathbf{O}^{-}\exp\left[\mathrm{i}k_o\left(x - \frac{\sqrt{M_1}}{2\breve{a}}\ln\left(\left(\frac{1-\sqrt{M_1}}{1+\sqrt{M_1}}\right)\left(\frac{1+\sqrt{M_1}+\breve{a}x}{1-\sqrt{M_1}+\breve{a}x}\right)\right) - \frac{\breve{a}M_1}{k_o^2}\left(1-\frac{1}{(1+\breve{a}x)^3}\right)\right)\right]$$

$$\text{where,} \quad \mathbf{O}^{\pm} = \left(\frac{A_{s,1}}{A_s}\right)^{1/2}\frac{\exp\left(M_1^2\left(\frac{\gamma-3}{8}\right) \pm M_1 \mp M_1^3\left(\frac{\gamma-1}{3}\right)\right)}{\exp\left(M^2\left(\frac{\gamma-3}{8}\right) \pm M \mp M^3\left(\frac{\gamma-1}{3}\right)\right)}. \tag{2.84}$$

2.6.2 Analytical solution for an exponentially-shaped nozzle

The simplified analytical solution when applied to the exponential-shaped nozzle with isentropic mean flow gives,

$$\mathcal{P}^{\pm} = \mathbf{O}^{\pm}\exp\left(\mp\frac{\mathrm{i}k_o}{\alpha}\ln\left(\frac{\exp(\alpha x) \pm M_1}{1 \pm M_1}\right) \pm \frac{\mathrm{i}\alpha^2 x}{8k_o} + \frac{\mathrm{i}\alpha M_1}{2k_o}\left(\exp(-\alpha x)-1\right)\right). \tag{2.85}$$

For the conical and exponentially shaped nozzles, the acoustic pressure in Eq. (2.37) is obtained by using $\mathcal{P}^{\pm}$ from Eq. (2.84) and Eq. (2.85), respectively. The velocity perturbation, $\hat{u}$, is determined using Eq. (2.39), with $\mathcal{B}^{\pm}$ now given by Eq. (2.83).

2.7 Effect of the entropy disturbance on the analytical model's accuracy

The analytical solutions developed in this work assume that the effect of the entropy disturbance on the acoustic field is negligible, with this assumption deemed justified by the low Mach assumption based on previous studies [44, 94]. This section compares the analytical model solutions to the numerical solution of the three linearised Euler equations, which fully account for acoustic-entropy coupling. This helps in understanding how the assumption holds for the considered geometries and flows. To investigate the effect of the entropy disturbance, a 1% normalised entropy or reduced temperature fluctuation ($s'/c_p \sim T'/\overline{T} = 0.01$ [32]) is applied at the inlet of the conical-shaped nozzle, and the acoustic field is studied for a range of Mach numbers and frequencies. (The qualitative behaviour of the acoustic-entropy coupling was observed to be similar for both the conical and exponential-shaped nozzles; hence only the former geometry is used for this investigation.)

- **Very low Mach numbers:** At low flow Mach numbers, with M varying from 0.005 at the inlet to 0.027 at the outlet, Fig. 2.11, compares the analytical model and numerical

3LEEs solution, for two different Helmholtz numbers. As observed, the analytical solution agrees very well with the numerical one, confirming that the effect of the entropy disturbance on the acoustic field is weak at these low Mach numbers.

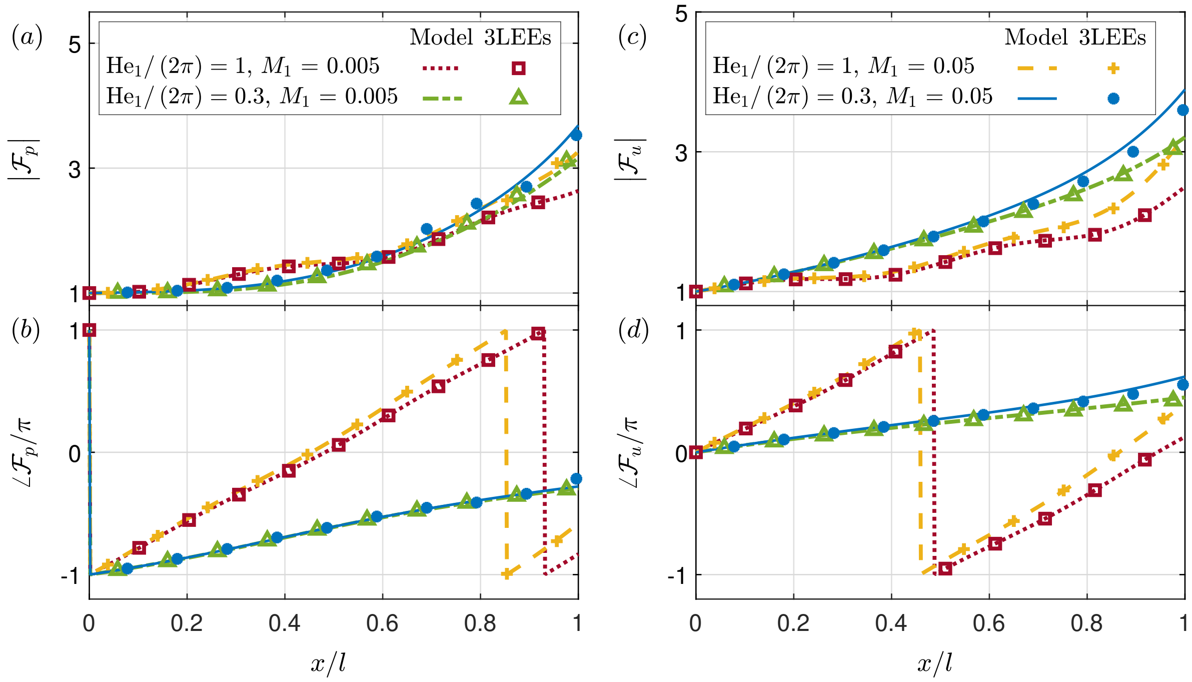

Figure 2.11: Evolution of F_p and F_u with x. $\overline{T}_1 = 1600$K, $\overline{T}_2 = 1200$K, $\hat{s}/c_p = 0.01$, $M_1 = 0.005$ & 0.05, $M_2 = 0.027$ & 0.27, $\mathrm{He}_1/(2\pi) = 1$ & 0.3, and $Z_1 =$ -1. (a): transfer function gain $|F_p|$. (b): transfer function phase $\angle F_p$. (c): transfer function gain $|F_u|$. (d): transfer function phase $\angle F_u$.

- **Increased low Mach numbers:** The analytical solution remains accurate with only small deviations (Fig. 2.11) when compared to 3LEEs at the higher flow Mach numbers (0.05 at inlet and 0.27 at outlet). This deviation was observed for both the Helmholtz numbers considered, implying only weak influence of the entropy disturbance on the acoustic field.

2.8 Application of the model for stability analysis

To investigate the applicability of the analytical model for stability analysis, the eigenmodes of the conical test-case shown in Figure 2.12 are predicted, assuming isentropic mean flow. Two different nozzle lengths of 0.5m and 1m are considered with inlet Mach numbers of 0.01 and 0.001. The obtained predictions are validated against the results of an in-house developed low-order network solver OSCILOS [53]. This network solver cannot directly account for the area variation of the nozzle. Therefore, the geometry shown in Figure 2.12 is represented as

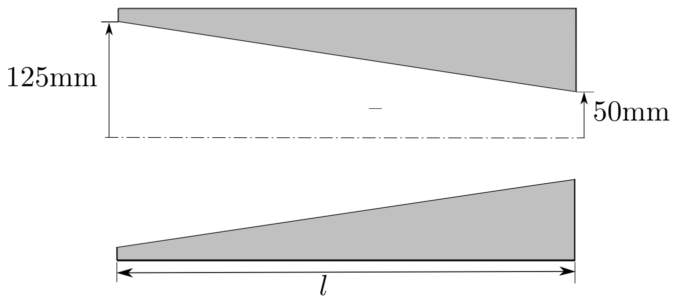

For $l = 0.5$m

	Inlet	Outlet
$M = \dfrac{\overline{u}}{\overline{c}}$	0.01	0.063
$\lvert\alpha\rvert$	2.5	6
$\overline{c}$	802m/s	801.5m/s
$f_{upper} = \dfrac{0.293\overline{c}}{r}$	1889Hz	4670Hz
$f_{lower} = \dfrac{\overline{c}}{2\pi}\sqrt{\dfrac{3\alpha^2 M}{2}}$	39Hz	229Hz

For $l = 1$m

	Inlet	Outlet
$M = \dfrac{\overline{u}}{\overline{c}}$	0.01	0.063
$\lvert\alpha\rvert$	1.2	3
$\overline{c}$	802m/s	801.5m/s
$f_{upper} = \dfrac{0.293\overline{c}}{r}$	1889Hz	4670Hz
$f_{lower} = \dfrac{\overline{c}}{2\pi}\sqrt{\dfrac{3\alpha^2 M}{2}}$	19Hz	118Hz

Figure 2.12: Schematic of the conical-shaped nozzle with the flow parameters and calculated frequency limits for isentropic mean flow.

a series of constant cross-sectional area cylindrical ducts, called segments. These are joined by applying the wave propagation and mean flow jump conditions at the interfaces. A spatial resolution of 100 segments for the 1m nozzle length was used and the convergence with number of segments was checked (error <0.5%). This axial segmentation approach within OSCILOS is similar to that used in [30, 131]. Simple boundary conditions - a closed end inlet and an open end outlet - are used for the present analysis. In many geometries, the premixed ducts upstream provide sufficient blockage near the combustor inlet and hence a boundary condition that is acoustically closed better represents the inlet [15]. Similarly, the outlet of the combustor rigs often discharges the flow into the atmosphere or a large plenum chamber. Therefore a open end boundary condition is employed for the outlet [15].

It is shown in Table 2.1 that the analytical model predicts the modes accurately, with minor errors in growth rate observed only at the lowest frequency fundamental mode. The frequency limits, outlined in Fig. 2.12, shows that the maximum of the lower frequency limit for nozzle with length 0.5m is $\sim$ 229Hz, while for the nozzle of length 1m it is $\sim$ 118Hz. Hence a deviation was observed for the fundamental modes as the frequencies lie close to this limit.

It can also be observed that the growth rate is negative for the considered modes. In nozzles/ducts carrying a mean flow the acoustic characteristics are altered; the damping of an

Table 2.1: Comparison of modal frequencies obtained from the analytical model and OSCILOS. f denotes the frequency (Hz), while ω_I denotes the growth rate (rad s^{-1}). **Top left table -** nozzle of length $l = 0.5$m, with $M_1 = 0.001$. **Top right table -** nozzle of length $l = 0.5$m, with $M_1 = 0.01$. **Bottom left table -** nozzle of length $l = 1$m, with $M_1 = 0.001$. **Bottom right table -** nozzle of length $l = 1$m, with $M_1 = 0.01$.

$l = 0.5$m, $M_1 = 0.001$, $M_2 = 0.006$			
Model		**OSCILOS**	
f **[Hz]**	ω_I **[rad s^{-1}]**	f **[Hz]**	ω_I **[rad s^{-1}]**
268.70	-12.91	268.76	-14.82
1169.50	-8.61	1169.60	-8.64
1984.83	-8.48	1985	-8.47

$l = 0.5$m, $M_1 = 0.01$, $M_2 = 0.063$			
Model		**OSCILOS**	
f **[Hz]**	ω_I **[rad s^{-1}]**	f **[Hz]**	ω_I **[rad s^{-1}]**
268.85	-128.95	267.24	-148.96
1168.40	-86.17	1168.20	-86.70
1983.06	-84.94	1983.10	-84.95

$l = 1$m, $M_1 = 0.001$, $M_2 = 0.006$			
Model		**OSCILOS**	
f **[Hz]**	ω_I **[rad s^{-1}]**	f **[Hz]**	ω_I **[rad s^{-1}]**
134.35	-6.45	134.38	-7.41
584.73	-4.30	584.79	-4.32
992.41	-4.24	992.51	-4.23
1396.14	-4.23	1396.30	-4.22
1798.60	-4.22	1798.80	-4.20

$l = 1$m, $M_1 = 0.01$, $M_2 = 0.063$			
Model		**OSCILOS**	
f **[Hz]**	ω_I **[rad s^{-1}]**	f **[Hz]**	ω_I **[rad s^{-1}]**
134.42	-64.47	133.62	-74.48
584.20	-43.10	584.11	-43.35
991.50	-42.47	991.55	-42.48
1394.91	-42.31	1395	-42.25
1797.02	-42.20	1797	-42.16

eigenmode (denoted by ω_I) will be increased. The convection of the acoustics by the mean flow and effect of flow on the reflection coefficients at the ends are the main reasons for the observed increase in dissipation [135]. Hence, the acoustic energy dissipation ($-|\omega_I|$) is higher for the case with a faster mean flow.

2.9 Summary

In summary, a computationally inexpensive semi-analytical solution for the planar acoustic field in quasi 1-D nozzles sustaining a mean flow that can be non-isentropic is developed. The heat exchange to the surroundings is considered as the source of non-isentropicity. The conservation equations are linearised and recast into a second-order homogeneous ordinary differential equation. This ODE is achieved by neglecting the effect of the entropy disturbance on the acoustic field, neglecting higher-order flow Mach number terms, and assuming that the length scale of the axial gradients are smaller than the wave-number of the acoustics. The resulting ODE is solved using an iterative WKB method, with the final solution expressed as a superposition of upstream and downstream propagating planar waves with varying amplitudes. These planar wave amplitudes depend on wave-number, upstream thermodynamic and mean flow properties and apply to arbitrary nozzle shapes and temperature profiles. Simplified analytical solutions are obtained for conical and exponentially-shaped nozzles with a linear mean temperature profile and validated by comparing them to numerical solutions of the linearised flow conservations.

Frequency limits of validity are proposed for the solutions, with frequencies needing to be low enough for the acoustic field to be planar, yet sufficiently high for the WKB assumptions to hold. The analytical solutions performed very well within (and even slightly beyond) the calculated frequency ranges of validity. Acoustic solutions are also presented for isentropic flows, having axial area and mean temperature variations directly related. The effect of neglecting the entropy disturbance effect on the acoustic field is investigated. It is found that the entropy disturbance effect remains negligible for sufficiently low flow Mach numbers and entropy disturbance amplitudes, consistent with previous findings. Finally, the model's applicability to stability analysis is shown by predicting the modal solutions and validating against the results of the lower order network solver (OSCILOS).

Chapter 3

Acoustic energy absorption and generation in nozzles with low subsonic, non-isentropic mean flow

In the previous chapter, we found that the axially varying flow conditions associated with axial area and temperature variations affect the acoustic response of nozzles. This effect potentially changes the acoustic energy balance of the system and therefore is important for understanding and controlling thermoacoustic phenomena in combustors. This chapter develops an analytical framework using the acoustic solutions from Chapter 2 to quantify the acoustic energy change in terms of an acoustic absorption coefficient Δ *[118]. Therefore,* $\Delta > 0$ *(*$\Delta < 0$*) corresponds to acoustic energy absorption (generation), with no acoustic energy change for* $\Delta = 0$*. For conical-shaped nozzles with linear mean temperature gradient, the effect of the mean flow conditions (area, temperature gradients and flow Mach number) and the disturbance conditions (frequency and inlet reflection coefficient) on* Δ *is studied. Parametric and optimisation studies are further carried out to determine the conditions that maximise or minimise the acoustic energy absorption in nozzles. The analysis revealed that a positive mean temperature gradient, representing a heated duct, caused acoustic energy absorption. Similarly, a negative mean temperature gradient, representing a cooled duct, caused acoustic energy generation. The simplified mathematical analysis also shows that the observations made are valid independently of the area profile when sufficiently high frequency and low flow Mach numbers criteria are met.*

3.1 Introduction

The existing acoustic energy balance studies [110–112, 114, 115] do not explicitly consider the nozzle flows with area and mean temperature variations. For such nozzles with non-isentropic mean flows, the characterisation of the energy balance with minimal parameters offers physical insights. It also reduces the computational effort in analysing many practical configurations to identify thermoacoustically stable conditions.

The acoustic absorption coefficient (Δ) is used to characterise the generation or dissipation of acoustic energy in nozzles sustaining mean flow [111]. It quantifies the loss of the acoustic energy flux across the duct, for instance $\Delta > 0$ ($\Delta < 0$) implies acoustic energy absorption (generation), while $\Delta = 0$ corresponds to no change in the acoustic energy, inside the duct. This characterisation of the acoustic energy balance for nozzle flows, in terms of Δ was investigated by Gaudron *et al.* [118, 119]. The final expression for Δ was shown to be a function of only a few mean flow parameters and the wave amplitudes at the nozzle ends. The acoustic wave amplitudes are obtained in this work using the WKB solution presented in Chapter 2, such that Δ can be estimated analytically.

The primary objective of the present work is therefore to develop a simplified analytical framework to estimate the acoustic absorption coefficient Δ, in nozzles with (i) varying cross-sectional area (ii) varying stream-wise mean temperature and (iii) low Mach number subsonic mean flow, which does not have to be isentropic. This is achieved by characterising the acoustic flow field variables using the analytical solution proposed in [93] and coupling it with the approach proposed in [118] for estimating Δ. This allows the exposure of direct linkage between nozzle heating/cooling and acoustic damping/generation, which is one of the main contributions of this analysis. This linkage is also investigated by utilising both the acoustic energy balance analysis, in line with [111], and a simplified mathematical analysis for a constant area duct with low Mach number flow.

The analytical framework developed in this chapter aims to estimate the acoustic absorption coefficient, Δ, in nozzles with a subsonic mean flow. This analysis uses the WKB solution to estimate the nozzle's acoustic response. Hence, the frequencies considered fall in the intermediate range (between the lower and upper frequency limits), as described in Section 2.3. These WKB solutions also require low flow Mach numbers and a negligible effect of the entropy disturbance on the acoustic field.

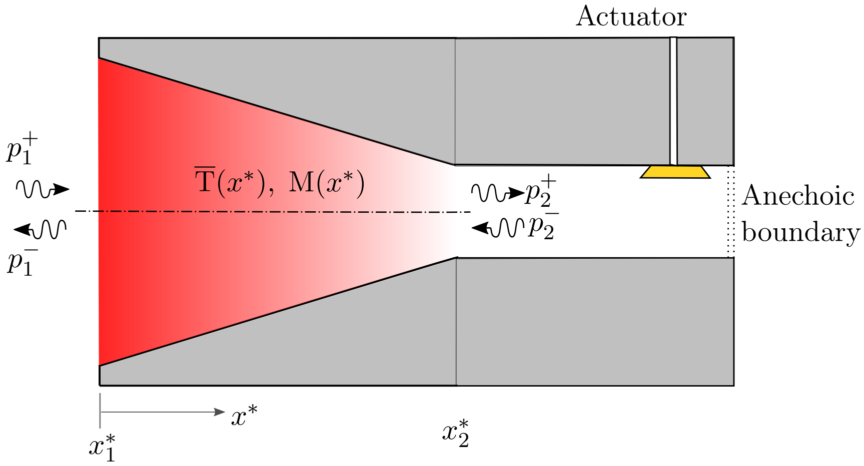

Figure 3.1: Conical-shaped nozzle sustaining mean temperature gradient and subsonic mean flow. $p^{\pm}$ represent the downstream (+) and upstream (-) propagating Riemann invariants. Subscript '1, 2' denote nozzle inlet and outlet and $x^* = x/l$. An actuator downstream of the nozzle is considered to impose inlet reflection coefficient.

3.2 Analysis

The linearised Euler equations (Eq. (2.8) - (2.9)) are presented in terms of a normalised spatial coordinate, x^*, ($x^* = x/l$) and local Helmholtz number $\mathrm{He} = 2\pi f l/\bar{c}$. The resulting equations can be expressed as,

$$A_1\hat{p} + \frac{\mathrm{d}\hat{p}}{\mathrm{d}x^*} + B_1\hat{u} + C_1\frac{\mathrm{d}\hat{u}}{\mathrm{d}x^*} = 0; \qquad D_1\hat{p} + \frac{\mathrm{d}\hat{p}}{\mathrm{d}x^*} + E_1\hat{u} + F_1\frac{\mathrm{d}\hat{u}}{\mathrm{d}x^*} = I_1\frac{\hat{s}}{c_p}, \tag{3.1, 3.2}$$

where the coefficients $A_1, B_1, C_1, D_1, E_1, F_1$, are similar to those in Eq. (2.18) but are now are functions of non-dimensional parameters (x^*, He, $\alpha^* = \alpha l$ and $\beta^* = \beta l$) and are slightly rearranged. They read:

$$A_1 = \left(\frac{\mathrm{iHe}}{M} + \gamma^2 M^2 \frac{1}{\bar{u}}\frac{\mathrm{d}\bar{u}}{\mathrm{d}x^*} + \gamma\beta^*\right),\ B_1 = \frac{\bar{\rho}\,\bar{c}}{M}\frac{1}{\gamma\bar{p}}\left(\frac{\mathrm{d}\bar{p}}{\mathrm{d}x^*}\left(\frac{1}{M^2} + 1 - \gamma\right) + \beta^*\right),\ C_1 = \frac{\bar{\rho}\,\bar{c}}{M}, \tag{3.3a-c}$$

$$D_1 = M^2\frac{1}{\bar{u}}\frac{\mathrm{d}\bar{u}}{\mathrm{d}x^*},\ E_1 = \bar{\rho}\,\bar{c}\left(\mathrm{iHe} + M\frac{1}{\bar{u}}\frac{\mathrm{d}\bar{u}}{\mathrm{d}x^*}\right),\ F_1 = \bar{\rho}\,\bar{c}M,\ I_1 = \bar{\rho}\,\bar{u}\frac{\mathrm{d}\bar{u}}{\mathrm{d}x^*}. \tag{3.4a-d}$$

The acoustic pressure and velocity fluctuations can be expressed in terms of the upstream (-) and downstream (+) propagating Riemann invariants ($\mathrm{P}^{\pm}$) as [43],

$$\hat{p}\,(x^*,\,\omega) = \mathrm{P}^+ + \mathrm{P}^-, \quad \hat{u}\,(x^*,\,\omega) = \frac{1}{\bar{\rho}\,\bar{c}}\left(\mathrm{P}^+ - \mathrm{P}^-\right), \tag{3.5}$$

and the entropy disturbance is represented in terms of $\hat{\psi} = \gamma\bar{p}\hat{s}/c_p$. Using Eq. (3.5) in Eqs. (3.1), (3.2) results in a first-order system of differential equations for the Riemann invariants ($\mathrm{P}^{\pm}$) and the entropy wave amplitude ($\hat{\psi}$) components, given by,

$$\frac{\mathrm{dP}^{\pm}}{\mathrm{d}x^*} = \mathrm{P}^+ \overbrace{\left[\frac{-1}{2\left(1 \pm M\right)}\left(\left(D \pm AM\right) + \frac{1}{\bar{\rho}\,\bar{c}}\left(E \pm BM\right) + \frac{\mathrm{d}}{\mathrm{d}x}\left(\frac{1}{\bar{\rho}\,\bar{c}}\right)\left(F \pm CM\right)\right)\right]}^{C_{11}\ (+)\ \text{or}\ C_{21}\ (-)}$$
$$+\,\mathrm{P}^- \overbrace{\left[\frac{-1}{2\left(1 \pm M\right)}\left(\left(D \pm AM\right) - \frac{1}{\overline{\rho c}}\left(E \pm BM\right) - \frac{\mathrm{d}}{\mathrm{d}x}\left(\frac{1}{\overline{\rho c}}\right)\left(F \pm CM\right)\right)\right]}^{C_{12}\ (+)\ \text{or}\ C_{22}\ (-)} + \hat{\psi}\overbrace{\left[\frac{M^2}{2\left(1 \pm M\right)}\frac{\beta^* - \alpha^*}{1 - \gamma M^2}\right]}^{C_{13}\ (+)\ \text{or}\ C_{23}\ (-)}, \tag{3.6}$$

$$\frac{\mathrm{d}\hat{\psi}}{\mathrm{d}x} = \mathrm{P}^+ \overbrace{\left[\Gamma\left(\gamma + \frac{1}{M}\right)\right]}^{C_{31}} + \mathrm{P}^- \overbrace{\left[\Gamma\left(\gamma - \frac{1}{M}\right)\right]}^{C_{32}} - \hat{\psi}\overbrace{\left[\frac{\mathrm{iHe}}{M} - \frac{1}{\overline{p}}\frac{\mathrm{d}\overline{p}}{\mathrm{d}x^*}\right]}^{C_{33}}; \tag{3.7}$$

where, $\Gamma = \left(\dfrac{\alpha^* M^2\left(\gamma - 1\right) - \beta^*\left(1 - M^2\right)}{1 - \gamma M^2}\right)$.

The above system of first-order differential equations govern the disturbance propagation in a nozzle with a non-isentropic mean flow due to steady heat transfer without neglecting any effect of the entropy disturbance on the acoustic field. Equations (3.6), (3.7) can be represented in matrix notation using a wave vector defined as $\mathbf{W}\left(x^*\right) = \begin{bmatrix}\mathrm{P}^+\left(x^*\right) & \mathrm{P}^-\left(x^*\right) & \hat{\psi}\left(x^*\right)\end{bmatrix}^T$. This gives,

$$\frac{\mathrm{d}}{\mathrm{d}x^*}\left[\mathbf{W}\left(x^*\right)\right] = \mathbf{C}\left(x^*\right)\mathbf{W}\left(x^*\right); \quad \text{with} \quad \mathbf{C}\left(x^*\right) = \begin{bmatrix} C_{11} & C_{12} & C_{13} \\ C_{21} & C_{22} & C_{23} \\ C_{31} & C_{32} & C_{33}\end{bmatrix}, \tag{3.8}$$

where the elements of the coefficient matrix, $\mathbf{C}\left(x^*\right)$, are as denoted in Eqs. (3.6), (3.7).

In Eq. (3.6), the entropy wave coefficient C_{13} or C_{23} is proportional to M^2. As well as the effects of shear dispersion, the low flow Mach numbers typically present in combustors makes the effect of the entropy disturbance on the acoustic field to be negligible, thus, decoupling Eq. (3.6) from Eq. (3.7). Therefore to obtain the acoustic response of the nozzle, only acoustic coefficients need to be retained, reducing $\mathbf{C}\left(x^*\right)$ from a 3×3 matrix to a 2×2 matrix. Thus, Eq. (3.8) reduces to,

$$\frac{\mathrm{d}}{\mathrm{d}x^*}\left[\mathbf{P}\left(x^*\right)\right] = \mathbf{C}\left(x^*\right)\mathbf{P}\left(x^*\right); \text{ with } \mathbf{C}\left(x^*\right) = \begin{bmatrix} C_{11} & C_{12} \\ C_{21} & C_{22}\end{bmatrix} \text{ and } \mathbf{P}\left(x^*\right) = \begin{bmatrix}\mathrm{P}^+\left(x^*\right) & \mathrm{P}^-\left(x^*\right)\end{bmatrix}^T. \tag{3.9}$$

Again, a fourth-order Runge-Kutta method is used to numerically solve the system of first-order ODEs in Eq. (3.9). The numerical implementation of the LEEs is discussed in Appendix A. On integrating Eq. (3.9), the transfer matrix $\mathbf{T}$ of the nozzle, relating the Riemann invariants at the inlet (x_1^*) and outlet (x_2^*) of the nozzle is obtained (shown in Fig. 3.1). This reads,

$$\mathbf{P}\left(x_2^*\right) = \left[\mathbf{T}\right]_{2\times 2}\mathbf{P}\left(x_1^*\right) \quad \text{where} \quad \mathbf{T} = \begin{bmatrix} T_{11} & T_{12} \\ T_{21} & T_{22}\end{bmatrix}. \tag{3.10}$$

The transfer matrix elements are obtained by applying two sets of independent acoustic boundary conditions at either end of the nozzle.

The variation of the acoustic energy flux across a nozzle with an arbitrary subsonic mean flow is characterised using the acoustic absorption coefficient (Δ), shown to be [118, 119],

$$\Delta = 1 - \frac{(1+M_2)^2\left|\mathrm{P}_2^+\right|^2 + \Theta\,\Xi\,\xi^{-1}(1-M_1)^2\left|\mathrm{P}_1^-\right|^2}{\Theta\,\Xi\,\xi^{-1}(1+M_1)^2\left|\mathrm{P}_1^+\right|^2 + (1-M_2)^2\left|\mathrm{P}_2^-\right|^2} \tag{3.11}$$

where,

$$\Theta = \frac{A_{s,\,1}}{A_{s,\,2}}, \quad \Xi = \sqrt{\overline{T}_1/\overline{T}_2}, \quad \text{and} \quad \xi = \overline{p}_1/\overline{p}_2. \tag{3.12 - 3.14}$$

with M_1 and M_2 as the flow Mach numbers at the inlet and outlet of the nozzle. The mean flow inside a nozzle with a given area and mean temperature profiles can be obtained by solving Eqs. (2.5) to obtain the flow Mach number distribution and the mean pressure ratio, ξ. The first-order system of differential equations given by Eq. (3.6) is solved numerically, and the elements of the transfer matrix (Eq. (3.10)) are determined. The Riemann invariants at the nozzle inlet and outlet are determined from Eq. (3.9) and used to compute Δ from Eq. (3.11). The numerical approach is computationally costly when a large sample space of area and temperature profiles, acoustic boundary conditions and frequencies, is investigated. Hence, the acoustic response is obtained using the WKB method based solution described in Chapter 2.

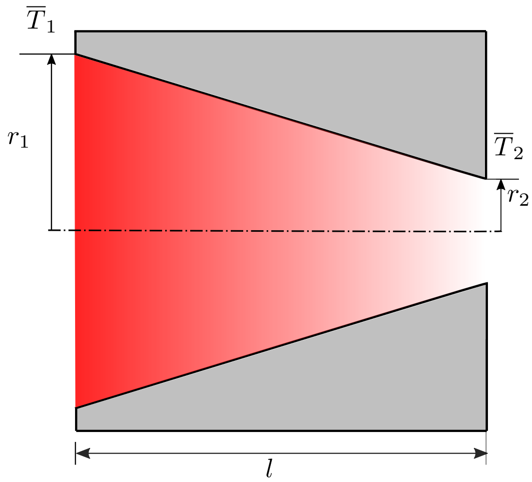

Mean flow	Inlet	Outlet
r	240 mm	168 mm
$\lvert\alpha^*\rvert$	1.2	1.71
$M = \dfrac{\overline{u}}{\overline{c}}$	0.15	0.273
$\overline{T}$	1600K	1120K
$\lvert\beta^*\rvert$	0.5	0.67
Frequency limits	He	f
Lower limit Eq. (3.17)	0.26	67Hz
Upper limit Eq. (3.18)	6.8	1735Hz

Figure 3.2: Schematic of a $l = 0.5$m long conical-shaped nozzle ($a^* = -0.3$) sustaining a non-isentropic mean flow ($b^* = -0.3$). $A_{s,\,1\,\text{or}\,2} = \pi r^2_{1\,\text{or}\,2}$. Other mean flow parameters and calculated frequency limits are also presented. Frequency limits are specified in terms of both Helmholtz numbers and frequencies.

3.3 Analytical model for the acoustic absorption coefficient

The semi-analytical solution is used to estimate the acoustic response, as it is computationally easy compared to numerical solutions and is applicable to arbitrary area and mean temperature variations. This solution as discussed in Chapter 2, however, requires the frequency to be "large" in one sense while also being low enough to ensure a planar acoustic field. For nozzles with non-isentropic mean flow, the final solution for the acoustic pressure and velocity are determined using Eq. (2.37) and Eq. (2.19), respectively.

On comparing Eqs. (2.37), (2.19) with Eqs. (3.5), and defining the inlet reflection coefficient as $R_1 = \mathrm{P}_1^+/\mathrm{P}_1^-$, the constants $C^\pm$ are obtained in terms of R_1 as,

$$\frac{\mathcal{C}^\pm}{\mathrm{P}_1^-} = \frac{\left(\mathcal{B}_1^\mp \pm 1\right) R_1 + \left(\mathcal{B}_1^\mp \mp 1\right)}{\left(\mathcal{B}_1^+ + \mathcal{B}_1^-\right)}, \quad \text{and} \quad \mathrm{P}_2^\pm = \frac{1}{2}\left[\mathcal{C}^+\,\mathcal{P}_2^+\left(1 \pm \mathcal{B}_2^+\right) + \mathcal{C}^-\,\mathcal{P}_2^-\left(1 \mp \mathcal{B}_2^-\right)\right], \tag{3.15, 3.16}$$

since using Eq. (2.38) gives $\mathcal{P}_1^\pm = 1$ at the nozzle inlet. The acoustic absorption coefficient Δ, given by Eq. (3.11), is estimated using the analytical expressions for $\mathrm{P}_2^\pm$, provided by Eq. (3.16). Note that while $\mathcal{P}^\pm$ denote the propagating plane wave amplitudes as defined in Eq. (2.37), $\mathrm{P}^\pm$ denote the Riemann invariants (Eq. (3.5)). To enforce a boundary condition at the inlet (x_1^*), the actuator in Fig. 3.1 is considered far downstream of the nozzle. Therefore, for any acoustic wave P_1^- impinging at the inlet, $\mathrm{P}_1^- \times R_1 = \mathrm{P}_1^+$ is reflected.

3.4 Conical-shaped nozzles with linear temperature gradient

The analysis described in Section 3.3 applies to nozzles with any area and mean temperature profiles, provided the frequency limit criteria set in Section 2.3 are satisfied. A conical-shaped nozzle with a linear stream-wise mean temperature gradient, shown in Fig. 3.1, is considered without loss of any generality. Therefore the acoustic response is determined using the simplified analytical solution presented in Section 2.4, further reducing the computational effort. The solution at any location now depends only on the local mean flow properties and frequency (He). These expressions can be used to estimate $\mathrm{P}_2^\pm$ analytically using Eq. (3.16) and thereby the acoustic absorption coefficient Δ (Eq. (3.11)). The corresponding lower frequency limit, given by Eq. (2.61), can be recast in terms of a critical Helmholtz number at the inlet,

$$\mathrm{He}_1 \gg \mathrm{He}_{\mathrm{cr}}^* = \max\left[\frac{l\bar{c}}{\bar{c}_1}\sqrt{\left|-\frac{b^{*2}}{16} + 2a^*b^*\right|},\ \frac{l\bar{c}}{\bar{c}_1}\sqrt{\left|\frac{-1}{16}\frac{b^{*2}}{(1+b^*)^2} + \frac{2a^*b^*}{(1+a^*)(1+b^*)}\right|}\right], \tag{3.17}$$

where $a^* = \breve{a}l$, $b^* = \breve{b}l$. Note that non-dimensional area and temperature variation parameters a^*, b^* are defined to remove any dependence of the solution on the nozzle length.

The upper frequency limit, requiring frequencies lower than He^*_{upper} reads,

$$\mathrm{He}_1 < \mathrm{He}^*_{upper} = \min\left[\frac{1.841\, l\, \bar{c}}{r\, \bar{c}_1}\right], \tag{3.18}$$

The "max" and the "min" functions in Eqs. (3.17), (3.18) gives the maximum and minimum values, respectively, for the limits of the frequency inside the nozzle.

To identify the frequency limits of validity, a conical nozzle of length 0.5m, with radii of 240mm and 168mm at the inlet and outlet, respectively, is considered (Fig. 3.2). The nozzle sustains a subsonic mean flow in the presence of a linear temperature gradient. From the inlet to the outlet the temperature varies from 1600K to 1120K, while the flow Mach number varies from 0.15 to 0.273. The schematic in Fig. 3.2 shows the nozzle geometry, mean flow parameters along with the corresponding frequency limits given by Eqs. (3.17), (3.18). It can be observed that there exists a range of frequencies (67Hz to 1735Hz) in which the model can be applied for acoustic field estimation without significant deviation from the numerical results. Therefore within these frequency ranges, the WKB model can be applied to estimate the acoustic response; this is further used to predict the acoustic absorption coefficient.

3.5 Results

3.5.1 Effect of frequency (He) and inlet reflection coefficient (R_1)

For different linear area and temperature profiles, governed by the parameters a^* and b^*, respectively, the acoustic absorption coefficient is compared as calculated with the numerical simulations for a range of average flow Mach numbers. Assuming an anechoic boundary condition at the inlet ($|R_1| = 0$), the results are shown in Fig. 3.3 for three different frequency values (in terms of Helmholtz number at the nozzle inlet, He_1),

The considered area profiles correspond to the converging, uniform and diverging nozzles with values of -0.3, 0, 0.3 for the area coefficient a^* (from top to bottom in Fig. 3.3). Similarly, three mean temperature coefficients (b^*), -0.3, 0, 0.3, are considered, representing negative, constant and positive temperature gradient in the nozzle, respectively. These variations in a^* and b^* are illustrated using a graphical representation of the nozzle's area profile and mean temperature distribution over each plot in Fig. 3.3. An average flow Mach number up to a maximum of 0.5 is considered to understand the analytical model behaviour at high subsonic flow Mach numbers.

The model predictions of the acoustic absorption coefficient, Δ, are in close agreement with the numerical results when M_{avg} is less than 0.25, as shown in Fig. 3.3. It can be observed that for an anechoic boundary at the inlet, the acoustic absorption coefficient Δ is independent of the Helmholtz number.

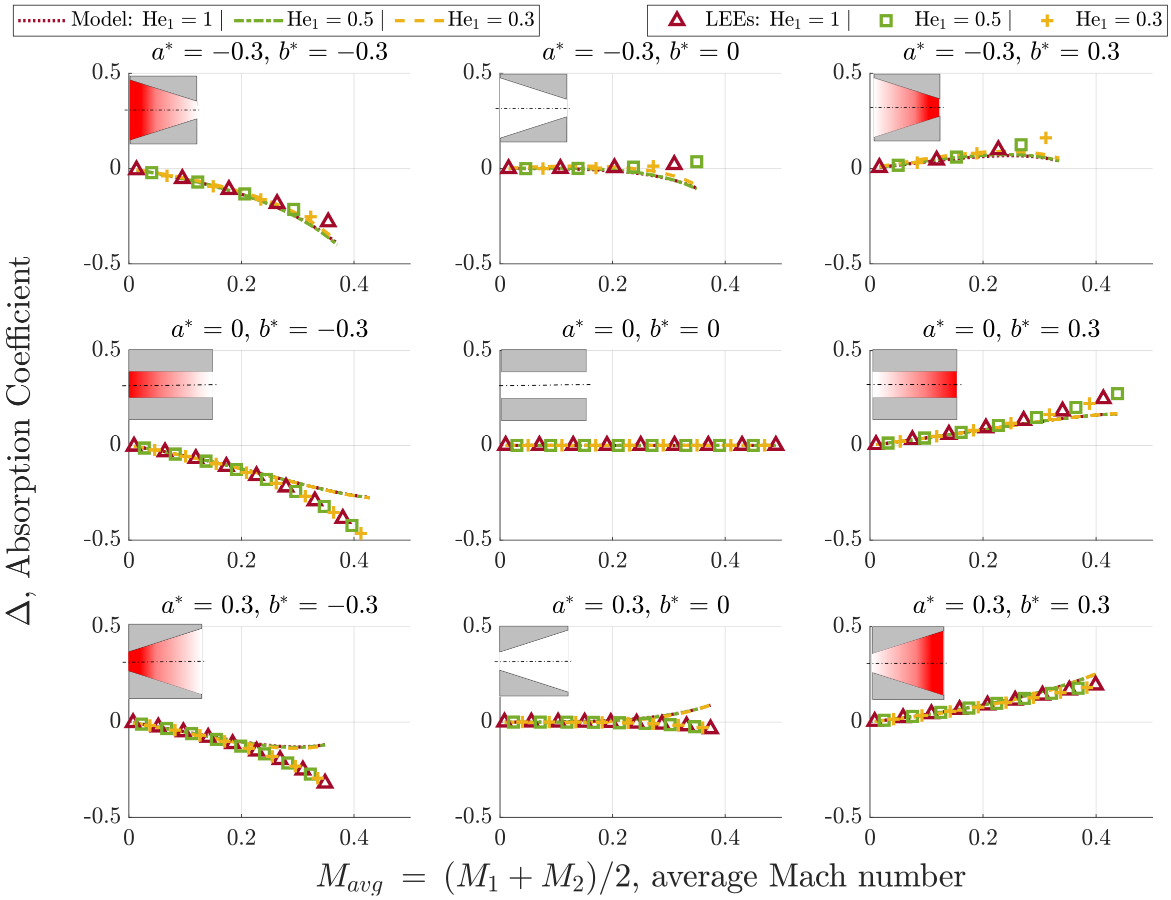

Figure 3.3: Comparison of Δ obtained using analytical model (represented by lines) and numerical LEEs (represented by markers) as a function of average Mach number $(M_1 + M_2)/2$, for a conical-shaped nozzle with linear mean temperature gradient and an anechoic boundary at the inlet ($|R_1| = 0$). Top row: $a^* = -0.3$, centre row: $a^* = 0$, bottom row: $a^* = 0.3$; left column: $b^* = -0.3$, middle column: $b^* = 0$, right column: $b^* = 0.3$.

For a non-anechoic inlet boundary condition with $|R_1| = 0.5$, Fig. 3.4 compares the model and numerical calculations of Δ. Notably, the expression for evaluating the acoustic absorption coefficient in Eq. (3.11) contains only the absolute value of the inlet reflection coefficient, without any influence of the phase ($\angle R_1$). At low flow Mach numbers, the model predictions again closely match with the validation simulations. While the numerical estimates remain independent of frequency, the model predictions deviate at low frequencies, attributed to the violation of lower frequency limit in Eq. (3.17) ($\mathrm{He}_1 > \mathrm{He}^*_{\mathrm{cr}} = 0.43$) for $a^* = |0.3|$, $b^* = |0.3|$.

Two key observations are made from Figs. 3.3 and 3.4: (i) the value of Δ remains independent of frequency, provided the lower frequency limit criterion, set by Eq. (3.17), is satisfied, (ii) for the mean flow parameters considered, the absolute value of Δ for the anechoic case in Fig. 3.3 is larger than its non-anechoic counterpart in Fig. 3.4, i. e., $|\Delta_{R_1=0}| > |\Delta_{R_1=0.5}|$.

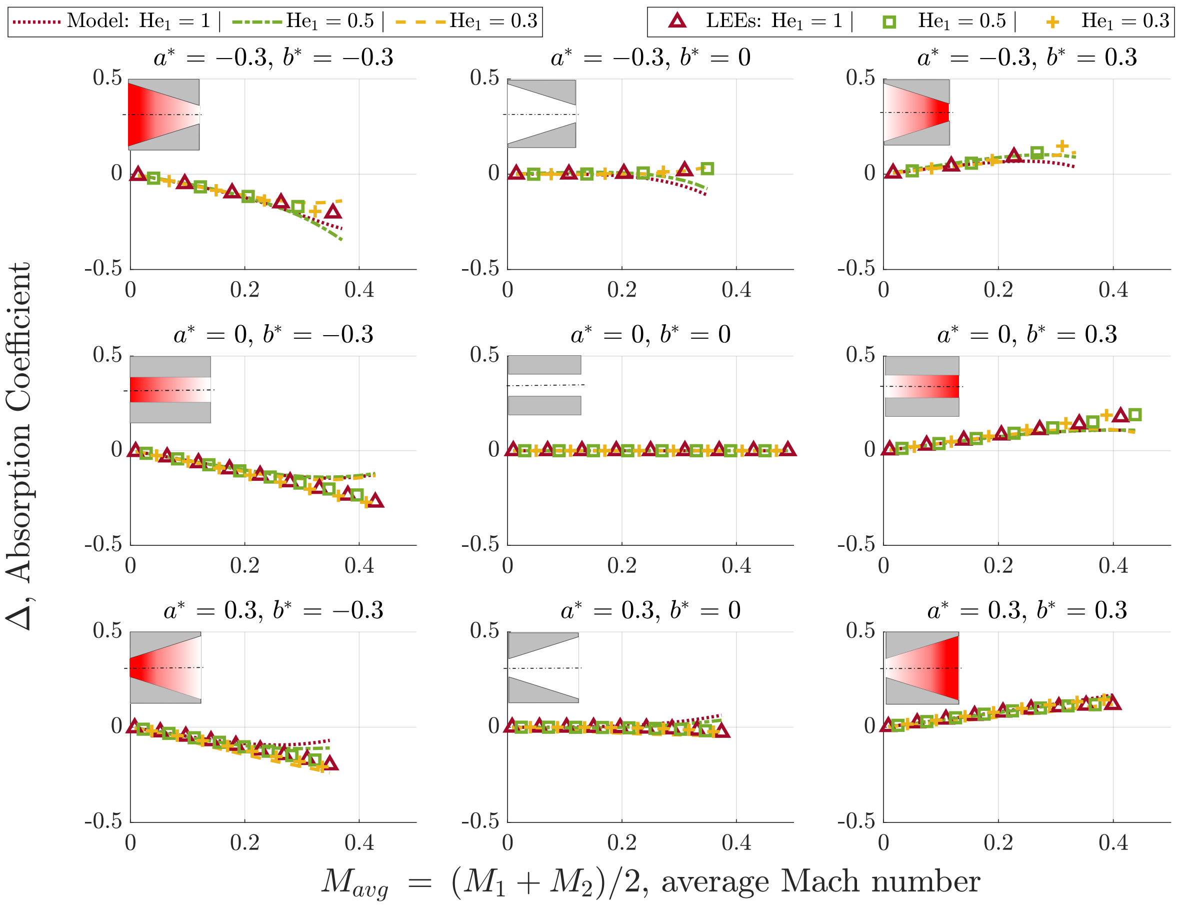

Figure 3.4: Comparison of Δ obtained using the model (represented by lines) and numerical LEEs (represented by markers) as a function of average flow Mach number $(M_1 + M_2)/2$, for a conical-shaped nozzle with linear mean temperature gradient and non-anechoic boundary at the inlet with $|R_1| = 0.5$. Top row: $a^* = -0.3$, centre row: $a^* = 0$, bottom row: $a^* = 0.3$; left column: $b^* = -0.3$, middle column: $b^* = 0$, right column: $b^* = 0.3$.

These observations were also confirmed by using a simplified mathematical analysis presented in 3.7. This simplified mathematical analysis is carried out assuming low flow Mach numbers (retaining only terms up to order $O(M)$) and the frequency criteria set by Eqs. (3.17), (3.18) to be satisfied.

Therefore to identify the conditions leading to the extrema of Δ, corresponding to maximum acoustic absorption or generation, an arbitrary frequency satisfying the limits set by Eqs. (3.17), (3.18), say $\text{He}_1 = 1$, and an anechoic boundary condition at the inlet ($|R_1| = 0$) are chosen. This eliminates the dependence of Δ on the acoustic parameters (He, R_1), and the study can be confined to analysing the effects of mean flow parameters on Δ.

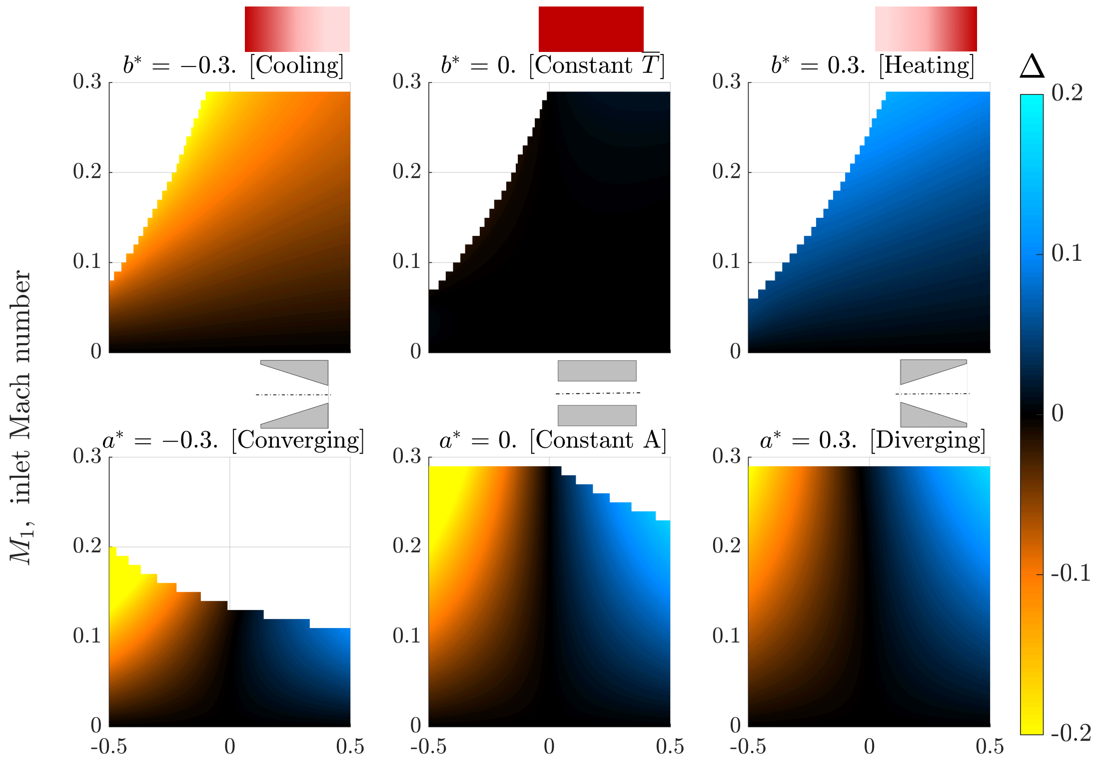

Figure 3.5: Contours of Δ obtained by the model (for $\mathrm{He}_1 = 1$) as a function of the inlet flow Mach number M_1, for a conical-shaped nozzle with an anechoic boundary at the inlet ($|R_1| = 0$) and a linear mean temperature profile. The top row plots are for a given b^* (top left: $b^* = -0.3$, top centre: $b^* = 0$, top right: $b^* = 0.3$) with varying a^*, while the bottom row plots are for a given a^* (bottom left: $a^* = -0.3$, bottom centre: $a^* = 0$, bottom right: $a^* = 0.3$) with varying b^*.

3.5.2 Effect of mean flow parameters

Fig. 3.5 shows the model's estimate of Δ as a function of the inlet flow Mach number, area variation (a^*) and mean temperature variation (b^*). The contour plots are shown for a given b^* (a^*) on the top row (bottom row), varying a^* (b^*) from -0.5 to 0.5. The acoustic absorption coefficient, Δ, is presented for flow Mach numbers up to 0.5, omitting regions with higher values as voids. The contour plots of Fig. 3.5 reveal an important finding: for a negative mean temperature gradient, the absorption coefficient is always negative, corresponding to acoustic energy generation inside the nozzle. Conversely, for a positive mean temperature gradient, the absorption coefficient remains positive, corresponding to acoustic energy absorption. For the case of a constant mean temperature maintained inside the nozzle, irrespective of the area variation parameter (a^*), Δ remains close to zero, i.e., there is a negligible generation or absorption of acoustic energy. For the low Mach number flow, the Mach number variation is negligible along the duct $\left(\frac{\mathrm{d}M}{\mathrm{d}x} \propto M\right)$ and remains a constant. However, for the heated duct the speed of sound increases due to increasing temperature. Therefore the local flow velocity $\overline{u}$ increases to keep the Mach number constant. The resulting high speed flow absorbs the acoustic energy provided at the inlet, consistent with the observations in [113, 135], and thereby results in $\Delta > 0$.

An energy analysis conducted along the lines of Morfey [111] (shown in Section 3.6) and a simplified mathematical analysis (presented in Section 3.7) confirms that acoustic energy generation and absorption occurs in cooled and heated nozzles, respectively, with negligible dependence on area variation parameter, a^*.

As observed in Fig. 3.5, regions with high acoustic energy absorption or generation are mostly confined to high flow Mach number regimes. The mean temperature variation parameter, b^*, has a stronger effect on Δ than the area variation parameter, a^*. For a given b^*, Fig. 3.5 confirms the existence of regions with a^* values that maximise $|\Delta|$. Hence, an optimisation search based on a genetic algorithm is performed to identify the global extrema, and the results are shown in Appendix B. These findings suggest that a set of mean flow parameters result in either significant acoustic energy damping ($\sim$ 60%) or significant acoustic energy generation ($\sim$ 110%).

Combustors often encounter a decreasing stream-wise mean temperature, owing to heat loss to the surroundings and mixing with the input cold dilution air. For a given combustor geometry with a fixed area profile, the acoustic behaviour can therefore be modified by adjusting the mean temperature profile. For example, for $a^* = -0.3$, by reducing b^* by 20% from -0.5 to -0.4, the acoustic energy generated can be reduced by 23% (Δ from -0.245 to -0.19). Using an energy analysis, this inverse linear dependence of Δ on the mean temperature gradient is further investigated in Section 3.6.

3.6 Energy analysis

To gain further insights into the effect of the mean temperature gradient on Δ, we analyse the acoustic energy balance inside the nozzle. For the case of a quasi 1-D nozzle with mean flow, Morfey [111] defines the acoustic energy flux $\mathbf{N}$ in terms of the total enthalpy fluctuations (J') and mass fluctuations (m') as,

$$\mathbf{N} = m'J'; \quad \text{with } m' = \overline{\rho}u' + \frac{M}{\overline{c}}p' \quad \text{and} \quad J' = \frac{p'}{\overline{\rho}} + \overline{u}u', \tag{3.19}$$

Multiplying Eq. (2.2) with $\overline{\rho}\, J'$, Eq. (2.3) with $\overline{u}\, m'$, adding the two equations and simplifying using Eqs. (2.5), we obtain,

$$\frac{\partial}{\partial t}\overbrace{\left[\frac{p'^2}{2\overline{\rho}\,\overline{c}^2}+p'u'\frac{M}{\overline{c}}+\frac{1}{2}\overline{\rho}u'^2\right]}^{\mathbf{E}}+\frac{\partial}{\partial x}\overbrace{\left[p'^2\frac{M}{\overline{\rho}\,\overline{c}}+p'u'\left(1+M^2\right)+\overline{\rho}\,\overline{u}u'^2\right]}^{\mathbf{N}}=\left[\frac{-p'^2\overline{u}}{\gamma\overline{p}}\left(\beta^*\left(\gamma-1\right)+\alpha^*\right)\right.$$
$$+\frac{p'M^2\overline{u}}{\gamma\overline{p}}\left(\beta^*\left(1-2\gamma\right)+\alpha^*\left(\gamma^2+\gamma-1\right)\right)+p'u'M^2\left(3\alpha^*\left(\gamma-1\right)+\beta^*\left(\frac{5}{2}-3\gamma+\gamma\frac{\alpha^*+\beta^*}{2}M^2\right)\right)$$
$$\left.-\,p'u'\alpha^*-\overline{\rho}\,\overline{u}u'^2\left(\frac{\beta^*}{2}\left(1-M^2\right)\left(2-\gamma\right)+\alpha^*\left(1-M^2\left(2\gamma-1\right)\right)\right)\right]\Big/\left(1-\gamma M^2\right). \tag{3.20}$$

The contribution of the entropy fluctuations to the total disturbance energy is neglected [117], consistent with the low flow Mach number [44, 94] and sufficiently high frequency assumptions [95]. Hence the relation $p' = \rho'\overline{c}^2$ is used. The resulting acoustic energy balance equation, Eq. (3.20), can be expressed as,

$$\frac{\partial \mathbf{E}}{\partial t}+\frac{\partial \mathbf{N}}{\partial x}=\mathbf{G}. \tag{3.21}$$

where $\mathbf{G}$, corresponding to the acoustic energy generation rate, is given by the right hand side of Eq. (3.20). $\mathbf{E}$ signifies the acoustic energy density of the nozzle. A value of $\mathbf{G} > 0$ signifies acoustic energy generation and $\mathbf{G} < 0$ corresponds to acoustic energy absorption inside the nozzle.

In the limit of very low Mach number flow inside nozzles with negligible area variation ($\alpha^* \sim 0$), the expression for $\mathbf{G}$ takes the form,

$$\mathbf{G} \sim -\beta^*\overline{u}\left[\frac{p'^2}{\gamma\overline{p}}\left(\gamma-1\right)+\overline{\rho}u'^2\right]. \tag{3.22}$$

In the above expression of Eq. (3.22), the term inside the square brackets is always positive. Hence the acoustic energy generation, $\mathbf{G}$, is proportional to the negative of the temperature gradient ($-\beta^*$). This dependence again shows that the acoustic energy absorption (generation) always occurs for ducts with positive (negative) mean temperature gradients, explaining the nature of the results observed in Section 3.5.

Most practical combustors, nozzles, after-burners, heat-exchangers and automotive exhaust systems exhibit a decreasing mean temperature profile due to heat loss to the surroundings, and Eq. (3.22) suggests a generation of the acoustic energy in these systems. This effect is particularly relevant to combustors as the temperature gradient can affect the system's propensity for thermoacoustic instabilities.

3.7 Simplified mathematical analysis

A simplified mathematical analysis is presented in this section to support further the conclusions drawn on the effects of (i) the mean flow, (ii) frequency and, (iii) reflection coefficient at the inlet boundary, on the acoustic absorption coefficient Δ. This analysis assumes low subsonic flow Mach numbers (only terms up to $\mathrm{O}(M)$ are retained) considering the frequency limits set by Eqs. (3.17), (3.18) to be satisfied. The effects of the frequency (He_1) and area variation (α^*) are firstly investigated using a nozzle sustaining isentropic mean flow ($\dot{\overline{Q}} = 0$) with an anechoic inlet boundary condition ($|R_1| = 0$), followed by analysing the effect of the non-isentropic mean flow and a non-anechoic inlet boundary condition ($|R_1| \neq 0$). Note that the area profile of the nozzle considered need not be conical and is more general.

3.7.1 Nozzles with isentropic mean flow

For a nozzle sustaining isentropic mean flow ($\dot{\overline{Q}} = 0$) with negligible flow Mach numbers ($M \sim 0$), the variation in temperature (β^*) and pressure can be obtained from Eq. (2.76) and Eqs. (2.5), respectively, and read,

$$\frac{1}{\overline{T}}\frac{\mathrm{d}\overline{T}}{\mathrm{d}x^*} = \frac{-\alpha^* M^2 (\gamma - 1)}{1 - \gamma M^2} \approx 0 \quad \Rightarrow \Xi \approx 1; \text{ also,} \quad \frac{1}{\overline{p}}\frac{\mathrm{d}\overline{p}}{\mathrm{d}x^*} = \frac{-(\beta^* - \alpha^*)\gamma M^2}{1 - \gamma M^2} \approx 0 \Rightarrow \xi \approx 1, \tag{3.23}$$

and therefore Δ (Eq. (3.11)) is given by,

$$\Delta_{|R_1|=0} = 1 - \frac{(1 - 2M_1)\,\Theta \; + (1 + 2M_2)\left|\mathrm{P}_2^+/\mathrm{P}_1^-\right|^2}{(1 - 2M_2)\left|\mathrm{P}_2^-/\mathrm{P}_1^-\right|^2}. \tag{3.24}$$

Using Eq. (3.16), explicit expressions are derived for $\left|\mathrm{P}_2^+/\mathrm{P}_1^-\right|^2$, $\left|\mathrm{P}_2^-/\mathrm{P}_1^-\right|^2$ that depend on the terms $\mathcal{P}_2^{\pm}$, $\mathcal{B}_{1,\,2}^{\pm}$, obtained using Eqs. (2.81), (2.83). Using the definition of $\delta_{1,\,2} = \dfrac{\alpha^*_{1,\,2}}{\mathrm{He}_{1,\,2}}$ and neglecting terms of order $\mathrm{O}(M^2)$, $\mathrm{O}(\delta^2)$ and higher, $\mathcal{P}_2^{\pm}$, $\mathcal{B}_{1,\,2}^{\pm}$ simplify to,

$$\mathcal{P}_2^{\pm} = \sqrt{\Theta}\exp\left(\pm S_a \mp \mathrm{i}\, S_b\right), \; \mathcal{B}_{1,\,2}^{\pm} = 1 \mp \frac{\mathrm{i}\delta_{1,\,2}}{2} + \mathrm{i}\delta_{1,\,2}M_{1,\,2}, \tag{3.25}$$

where $S_a = (M_1 - M_2)$, $S_b = \int_{x_1}^{x_2} (1 \mp M)\,\mathrm{d}\breve{x}$, noting again the subscripts 1, 2 correspond to the inlet and outlet of the nozzle, and $\breve{x}$ the dummy variable. This gives,

$$\left|\frac{\mathrm{P}_2^+}{\mathrm{P}_1^-}\right|^2 = \frac{\Theta}{4}\left[\delta_1^2\,\mathcal{M}_1^2\exp\left(2S_1\right) + \delta_2^2\,\mathcal{M}_2^2\exp\left(-2S_a\right) - 2\left(\delta_1\mathcal{M}_1\right)\,\left(\delta_2\mathcal{M}_2\right)\cos\left(2h_t\right)\right], \tag{3.26}$$

and,

$$\left|\frac{\mathrm{P}_2^-}{\mathrm{P}_1^-}\right|^2 = \Theta\exp\left(-2S_a\right)\left[1 + \left(\frac{\delta_1\mathcal{M}_1 - \delta_2\mathcal{M}_2}{2}\right)^2\right]. \tag{3.27}$$

where, $\mathcal{M}_{1,\,2} = 1 + 2M_{1,\,2}$, $h_t = \mathrm{He}_1\, S_b$. The acoustic absorption coefficient Δ is estimated using Eqs. (3.26), (3.27) in Eq. (3.24), neglecting terms of order $\mathrm{O}(\delta^2)$ and using the simplified Mach number-area relation, $M_2 = M_1\Theta$. This gives,

$$\Delta_{|R_1|=0} = 1 - \frac{(1-2M_1)}{(1-2M_1\,\Theta)\;\exp\left(-2M_1\,(1-\Theta)\right)}, \tag{3.28}$$

an expression for Δ that depends only on the mean flow and its gradients.

Eq. (3.28) shows that the acoustic absorption coefficient depends only on the mean flow, and hence any dependence on frequency (not captured by Eq. (3.28)) must be weak and negligible for small values of δ - a prerequisite for using the WKB solution. Therefore the mathematical analysis confirms that the acoustic absorption coefficient, Δ, behaves independent of frequency (He_1), when the frequency criteria (Eqs. (3.17), (3.18)) are satisfied and $|\delta| \ll 1$.

Using Taylor series, the exponential function in Eq. (3.28) is further expanded, neglecting terms of order $\mathrm{O}(M^2)$ and higher. This gives,

$$\Delta_{|R_1|=0} = 1 - \frac{(1-2M_1)}{(1-2M_1\,\Theta)\;(1-2M_1\,(1-\Theta))} = 1 - \frac{1-2M_1}{1-2M_1} = 0. \tag{3.29}$$

Thus, for nozzles with arbitrary area profile but isentropic mean flow, the acoustic absorption coefficient equals zero. However, at low flow Mach numbers, both isentropic and isothermal mean flows are associated with negligible and zero temperature variations respectively,

$$\beta_i^* = \frac{1}{\overline{T}}\frac{\mathrm{d}\overline{T}}{\mathrm{d}x^*} = \frac{-\alpha^* M^2\,(\gamma-1)}{1-\gamma M^2} \approx 0, \quad \text{while} \quad \beta^*_{\overline{T}=c} = 0. \tag{3.30}$$

This implies a more pronounced dependence of Δ on the temperature profile than on the area profile.

3.7.2 Nozzles with uniform area, sustaining non-isentropic mean flow

This section analyses the effect of the absolute value of the reflection coefficient at the inlet, $|R_1|$, and the temperature variation parameter, b^*, on the acoustic absorption coefficient Δ, assuming $a^* = 0$ to keep the procedure simple. Using a similar procedure as outlined in Section 3.7.1 and neglecting terms of order $\mathrm{O}(M^2)$, $\mathrm{O}(\delta^2)$ gives,

$$\Delta \approx 1 - \frac{(1-2M_1)\; + (1+2M_2)\exp\left(2S_c\right)|R_1|^2}{(1+2M_1)\,|R_1|^2 + (1-2M_2)\exp\;\left(-2S_c\right)}, \quad S_c = -M_1\left(\frac{1}{\Xi} + \gamma\sqrt{1+b^*} - (\gamma+1)\right). \tag{3.31}$$

Again on expanding the exponential function using Taylor series up to O(M) gives,

$$\Delta \approx \frac{\overbrace{2M_1\gamma\left(\sqrt{1+b^*}-1\right)|R_1|^2}^{\mathrm{F}_a} + 2M_1\gamma\left(\sqrt{1+b^*}-1\right)}{\underbrace{(1+2M_1)|R_1|^2}_{\mathrm{F}_b} + \left(1+2M_1\left(\gamma\sqrt{1+b^*}-(\gamma+1)\right)\right)}. \tag{3.32}$$

In Eq. (3.32), the terms F_a and F_b depend on the reflection coefficient at the inlet (R_1). When the temperature parameter b^* is positive ($b^*_+ > 0$), the condition $\Delta_{|R_1|=0} > \Delta$ requires,

$$b^*_+ \;<\; \frac{1+4M_1(1+\gamma)+4M_1^2\,(1+2\gamma)}{4M_1^2\gamma^2}. \tag{3.33}$$

In the limit of very low flow Mach numbers, the above inequality is satisfied due to the M_1^2 term in the denominator. Similarly for a negative value of the temperature parameter $b^*_- = -|b^*|$, the condition $\left|\Delta_{|R_u=0|}\right| > |\Delta|$ takes the form,

$$|b^*| > \frac{-\left(1+4M_1\,(1-\gamma)+\cancelto{0}{4M_1^2\,(1-2\gamma)}\right)}{4M_1^2\gamma^2} \quad \Rightarrow \quad M_1 < \frac{1}{4\,(\gamma-1)}. \tag{3.34}$$

For a value of $\gamma = 1.4$, inequality in Eq. (3.34) takes the form $M_1 < 0.625$, which is again satisfied given the analysis assumes low flow Mach numbers. Therefore, it can be generalised for both the cases of positive and negative values of b^* that $\left|\Delta_{|R_1|=0}\right| > \left|\Delta_{|R_1|\neq 0}\right|$ in the limit of low subsonic flow Mach numbers and sufficiently high frequencies.

It can also be noticed from the equation Eq. (3.32) that any positive value of the temperature profile (b^*_+) ensures $\Delta > 0$, while negative values (b^*_-) give $\Delta < 0$. This again shows that positive and negative values of the temperature gradient, b^*, correspond to acoustic energy absorption and generation, respectively.

3.8 Summary

An analytical framework has been developed in this chapter to estimate the acoustic absorption coefficient (Δ) in nozzles with a non-isentropic mean flow due to steady heat transfer using the WKB method based solutions developed in Chapter 2. This analysis exposed the direct linkage between heated/cooled nozzles and acoustic energy damping/generation. The model estimates for Δ are validated against the numerical predictions for conical-shaped nozzles with a linear temperature gradient. The results were found to match at low flow Mach numbers closely and when the frequency limits discussed in Section 2.3 are satisfied. It was further observed that the acoustic absorption coefficient depends very little on the frequency and maximises for an anechoic boundary condition at the inlet. Δ was also seen to depend more strongly on the mean temperature variation than on the area variation with acoustic energy generation for a negative temperature gradient and vice-versa. These observations were also explained by performing energy analysis and a simplified mathematical analysis, assuming very low Mach number flow. The results suggest that the acoustic energy generation can be reduced by altering the mean temperature profile in combustors and other practical systems.

Chapter 4

Acoustic response of non-isentropic nozzles using the Magnus expansion method

The WKB models so far discussed apply well at high frequencies; however, most unstable thermoacoustic modes occur at the fundamental modes of the system. These often occur at low enough frequencies ($\sim He < 0.3$*) that the effect of the shear dispersion on the entropy waves is minimal [95], and hence the effect of entropy disturbance on the acoustic field cannot be neglected. The WKB models are also restricted to low subsonic flow Mach numbers, but some practical applications, involving nozzles and afterburners, sustain super-critical (choked) flow configurations. Hence, a mathematical model that is accurate across a wide range of frequencies, applies to any nozzle shape, across a wide range of mean flow conditions and does not neglect the acoustic-entropy coupling, could be extremely useful. This chapter presents such a model for estimating the unsteady response of nozzles with heat transfer, excited by acoustic and/or entropy disturbances. The linearised Euler equations, represented as a first-order system of differential equations, are solved using the Magnus expansion based method [136], allowing the effects of frequency, heat transfer and acoustic-entropy coupling to be captured. The model was found to be accurate for converging-diverging nozzles operating in both sub-critical and super-critical (choked) configurations, showing good agreement with numerical predictions. This study revealed a strong effect of the heat transfer on the transfer functions of the nozzle, across the considered full spectrum of frequencies and high flow Mach numbers. It also revealed that steady heat transfer results in large generation of entropy perturbations which can increase the overall exhaust noise emissions in combustors and can also affect the thermoacoustic stability of the system [82, 92].*

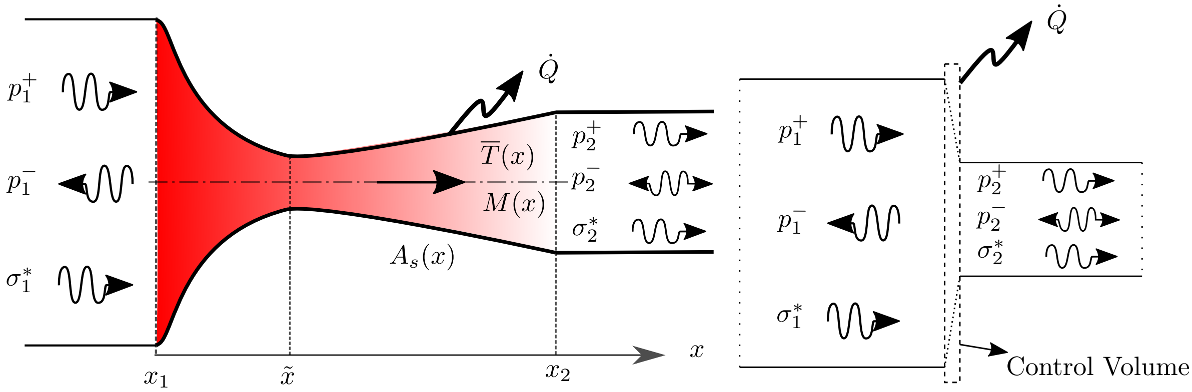

Figure 4.1: Sketch of a nozzle of length l exchanging heat ($\dot{Q}$) with the surroundings. (Left) Non-compact nozzle with $A_s(x)$, $M(x)$, and $\overline{T}(x)$ representing the nozzle cross-sectional area, flow Mach number and mean-temperature at any x varying from x_1 to x_2. (Right) Compact nozzle where the acoustic wavelength is assumed much longer than the nozzle length.

4.1 Introduction

The WKB method based solutions discussed in Chapter 2 are confined to low subsonic flow Mach numbers and neglect the effect of the entropy disturbance on the acoustic field [89, 93]. Hence WKB method based models are applicable to near flame regions of combustors and afterburners where low subsonic flow Mach numbers are encountered. However these models are inaccurate for nozzles and turbine blades, regions away from the flame in combustors/afterburner where high flow Mach numbers are encountered and indirect noise effects are important. The effect of the acoustic-entropy coupling is most relevant at the low-frequencies where most unstable thermoacoustic modes (fundamental modes) often exist. The WKB methods being high frequency asymptomatic methods have a poor low frequency behaviour.

4.1.1 Compact solutions

Analytical solutions for the acoustic and entropy transfer functions of a nozzle flow were firstly derived for "acoustically compact" geometries by Marble and Candel [76]. This compact analysis assumes the acoustic wavelength is significantly larger than the length scale of the nozzle area-change (as shown in Fig. 4.1 (Right)). It then follows that the normalised fluctuations of the mass flow rate ($I_A = \frac{\dot{m}'}{\overline{\dot{m}}}$), total or stagnation temperature ($I_B = \frac{T_t'}{\overline{T}_t}$), entropy ($I_C = \frac{s'}{c_p}$) remain unchanged and appear as jump conditions across the nozzle. Thus,

$$\left(\frac{\dot{m}'}{\overline{\dot{m}}}\right)_1 = \left(\frac{\dot{m}'}{\overline{\dot{m}}}\right)_2, \quad \left(\frac{T_t'}{\overline{T}_t}\right)_1 = \left(\frac{T_t'}{\overline{T}_t}\right)_2, \quad \left(\frac{s'}{c_p}\right)_1 = \left(\frac{s'}{c_p}\right)_2. \tag{4.1}$$

The vector $\mathbf{I} = [I_A \ \ I_B \ \ I_C]^{\mathrm{T}}$, corresponding to the flow invariants (as defined in [77]), remains constant across the nozzle at the compact limit. In terms of the normalised primitive variables, $p^* = \dfrac{p'}{\gamma\bar{p}}, u^* = \dfrac{u'}{\bar{u}}$ and $\sigma^* = \dfrac{s'}{c_p}$, these invariants read:

$$I_A = p^* + u^* - \sigma^*, \quad I_B = (\gamma - 1)\frac{M^2 u^* + p^* + \dfrac{\sigma^*}{\gamma - 1}}{1 + \dfrac{\gamma - 1}{2}M^2}, \quad I_C = \sigma^*. \qquad (4.2a - c)$$

The normalised primitive variables are also related to the non-dimensional Riemann invariants $p^{\pm}$ as, $p^+ = p^* + u^* M$ and $p^- = p^* - u^* M$. Therefore the flow invariants can be related to the wave vector $\mathbf{W}^* = [p^+ \ \ p^- \ \ \sigma^*]^{\mathrm{T}}$ using the matrix $\mathbf{D}$ as follows,

$$\overbrace{\begin{bmatrix} I_A \\ I_B \\ I_C \end{bmatrix}}^{\mathbf{I}} = \overbrace{\begin{bmatrix} \dfrac{1}{2M}(1+M) & \dfrac{1}{2M}(1-M) & -1 \\ \dfrac{\gamma-1}{2\zeta}(1+M) & \dfrac{\gamma-1}{2\zeta}(1-M) & \dfrac{1}{\zeta} \\ 0 & 0 & 1 \end{bmatrix}}^{\mathbf{D}} \overbrace{\begin{bmatrix} p^+ \\ p^- \\ \sigma^* \end{bmatrix}}^{\mathbf{W}^*}, \qquad (4.3)$$

where $\zeta = 1 + \dfrac{\gamma - 1}{2}M^2$.

Equations (4.1), (4.3) apply to compact isentropic nozzles with both sub-critical and super-critical flows. For a nozzle sustaining subsonic flow Mach numbers, three different incoming waves that correspond to the acoustic waves at either end of the nozzle ($p^+_{1,\,f}$, $p^-_{2,\,f}$) and an entropy wave at the inlet ($\sigma^*_{1,\,f}$) are applied, where the subscript 'f' denotes that the waves are externally forced. These incoming waves result in three outgoing waves, namely, an upstream propagating wave acoustic at the inlet (p^-_1), downstream propagating acoustic wave at the outlet (p^+_2) and an entropy wave at the outlet (σ^*_2). A transfer function relates the outgoing wave to the incoming externally forced wave, for example, $\mathcal{F} = p^+_2/p^+_{1,\,f}$ relates the outgoing acoustic wave at the outlet to the incoming acoustic wave at the inlet. Considering unitary incoming acoustic waves and no entropy waves, the transfer functions are obtained from Eq. (4.1), these denoting the acoustic reflection and transmission by the nozzle. Similarly, the acoustic response to an incoming entropy wave is also calculated. Together these acoustic transfer functions are summarised in Table 4.1.

For nozzles sustaining super-critical flow without any shock-waves inside, only two incoming waves, $p^+_{1,\,f}$ and $\sigma^*_{1,\,f}$, can be applied, with fast and slow propagating acoustic waves at the outlet ($p^{\pm}_2$), an entropy wave at the outlet (σ^*_2) and an upstream propagating acoustic wave at the inlet (p^-_1) as the outgoing waves. The requirement that mass fluctuations cannot occur at

Table 4.1: Transfer functions of a compact sub-critical nozzle with isentropic mean flow. 'In' represents the externally excited incoming waves while 'Out' denotes the outgoing waves.

In \ Out	p_1^-	p_2^+
p_1^+	$\dfrac{M_2-M_1}{1-M_1}\dfrac{1+M_1}{M_1+M_2}\dfrac{1-\frac{1}{2}(\gamma-1)M_1M_2}{1+\frac{1}{2}(\gamma-1)M_1M_2}$	$\dfrac{2M_2}{1+M_2}\dfrac{1+M_1}{M_1+M_2}\dfrac{1+\frac{1}{2}(\gamma-1)M_2^2}{1+\frac{1}{2}(\gamma-1)M_1M_2}$
σ_1^*	$-\dfrac{M_2-M_1}{1-M_1}\dfrac{M_1}{1+\frac{1}{2}(\gamma-1)M_1M_2}$	$\dfrac{M_2-M_1}{1+M_2}\dfrac{M_2}{1+\frac{1}{2}(\gamma-1)M_1M_2}$
p_2^-	$\dfrac{2M_1}{1-M_1}\dfrac{1-M_2}{M_1+M_2}\dfrac{1+\frac{1}{2}(\gamma-1)M_1^2}{1+\frac{1}{2}(\gamma-1)M_1M_2}$	$-\dfrac{M_2-M_1}{1+M_2}\dfrac{1-M_2}{M_1+M_2}\dfrac{1-\frac{1}{2}(\gamma-1)M_1M_2}{1+\frac{1}{2}(\gamma-1)M_1M_2}$

Table 4.2: Transfer functions of a compact super-critical nozzle with isentropic mean flow. 'In' represents the externally excited incoming waves while 'Out' denotes the outgoing waves.

In \ Out	p_1^-	p_2^+	p_2^-
p_1^+	$\dfrac{1-\frac{1}{2}(\gamma-1)M_1}{1+\frac{1}{2}(\gamma-1)M_1}$	$\dfrac{1+\frac{1}{2}(\gamma-1)M_2}{1+\frac{1}{2}(\gamma-1)M_1}$	$\dfrac{1-\frac{1}{2}(\gamma-1)M_2}{1+\frac{1}{2}(\gamma-1)M_1}$
σ_1^*	$\dfrac{-M_1}{1+\frac{1}{2}(\gamma-1)M_1}$	$\dfrac{M_2-M_1}{2\left(1+\frac{1}{2}(\gamma-1)M_1\right)}$	$\dfrac{-(M_2+M_1)}{2\left(1+\frac{1}{2}(\gamma-1)M_1\right)}$

the choked throat ($\tilde{x}$) is specified as a boundary condition [76] taking the form,

$$\frac{M'}{M} = u^* - \frac{\gamma-1}{2}p^* - \frac{\sigma^*}{2} = 0. \tag{4.4}$$

In terms of the acoustic waves ($p^\pm$) and the entropy wave (σ^*), the above boundary condition becomes,

$$p_u^- = R_u p_u^+ + R_s \sigma_u^*, \quad \text{with} \quad R_u = \frac{3-\gamma}{1+\gamma}, R_s = \frac{-2}{1+\gamma}, \tag{4.5}$$

with the subscript 'u' representing the location $\tilde{x}_u$, infinitesimally upstream of the throat.

We note that the solutions for the acoustic and entropy transfer functions, provided in Tables 4.1 and 4.2, are confined to nozzles sustaining isentropic mean flow. This compact solution was further extended to non-compact geometries by Duran and Moreau [77]. A semi-analytical solution derived from truncation of an infinite series expansion, called the Magnus expansion based method was used to obtain the acoustic response of the nozzle in their work. This method was applicable over a wide range of frequencies and can fully account for acoustic-entropy coupling. Hence these models are of interest to the thermoacoustic research communities due to their excellent low-frequency behaviour. However, the methodology presented in Duran and Moreau [77] applies only to nozzles with an isentropic mean flow and cannot account for flows with steady heat transfer. Many practical applications encounter non-isentropic mean flows due to wall friction or heat transfer. De Domenico *et al.* [107] and Yang *et al.* [132] have recently showed that, in the diverging portion of realistic nozzles, the flow can separate creating recirculation regions and, hence, turbulence both leading to mean flow non-isentropicity affecting the acoustic behavior. The isentropic acoustic theories found to result in strong deviations for such nozzles. Another source of non-isentropicity can be heat transfer, as happens in combustors and heat exchangers. Chapter 3 of this thesis already showed that the steady heat transfer can significantly affect the acoustics of the nozzle. An analytical solution for the acoustic response of nozzles to incoming acoustic and/or entropy disturbances when the nozzle mean flow is non-isentropic does not exist, even in the compact limit. This chapter presents a model based on the Magnus expansion to estimate the transfer functions of a nozzle exchanging heat with the surroundings for both compact and non-compact nozzle geometries in the presence of a mean flow. All the other sources of non-isentropicity, for example, through wall friction and flow separation, are neglected, and only steady heat transfer is considered in this analysis.

The key aspects of this chapter are therefore to propose a Magnus expansion based solution for the 1-D acoustic field sustained in nozzles with non-isentropic mean flow due to steady heat transfer, as shown diagrammatically in Fig. 4.1. This solution: (i) applies to nozzles with both sub-critical and super-critical flow configurations, (ii) accurately accounts for the acoustic-entropy coupling, (iii) captures the frequency response over a wide range of frequencies. Therefore we describe the first semi-analytical model proposing compact and non-compact acoustic solutions for such nozzles.

4.2 Analysis

The linearised form of the Euler equations (Eqs. (2.2) - (2.4)), are written in terms of the normalised fluctuating flow variables p^*, u^* and σ^*. This gives,

$$\frac{\partial p^*}{\partial t} + \overline{u}\frac{\partial}{\partial x}\left(p^* + u^*\right) = -\overline{\dot{Q}}\frac{\gamma - 1}{\gamma \overline{p}}\left(u^* + \gamma p^*\right), \tag{4.6}$$

$$\frac{\partial u^*}{\partial t} + \overline{u}\frac{\partial u^*}{\partial x} + \frac{\overline{c}^2}{\overline{u}}\frac{\partial p^*}{\partial x} + \frac{\mathrm{d}\overline{u}}{\mathrm{d}x}\left[2u^* - \left(\gamma - 1\right)p^* - \sigma^*\right] = 0, \tag{4.7}$$

$$\frac{\partial \sigma^*}{\partial t} + \overline{u}\frac{\partial \sigma^*}{\partial x} = -\overline{\dot{Q}}\frac{\gamma - 1}{\gamma \overline{p}}\left(u^* + \gamma p^*\right). \tag{4.8}$$

The above linearised Euler equations (LEEs), Eqs. (4.6) - (4.8), govern the unsteady flow in a nozzle sustaining mean flow with steady heat transfer (the source of non-isentropicity).

The definitions of the flow invariants (Eq. (4.2)) allow us to express the LEEs in Eqs. (4.6) - (4.8) in a matrix form as:

$$\frac{\partial}{\partial t}\mathbf{I} + \overline{u}\mathbf{E}_x\frac{\partial}{\partial x}\mathbf{I} + \frac{(\gamma-1)\,\overline{\dot{Q}}}{2\zeta\gamma\overline{p}}\mathbf{E}_s\mathbf{I} = 0, \quad \text{where} \quad \mathbf{E}_x = \begin{bmatrix} 1 & \dfrac{\zeta}{(\gamma-1)M^2} & -\dfrac{1}{(\gamma-1)M^2} \\ \dfrac{\gamma-1}{\zeta} & 1 & \dfrac{\gamma-1}{\zeta} \\ 0 & 0 & 1 \end{bmatrix}, \tag{4.9a – b}$$

$$\mathbf{E}_s = \frac{1}{M^2-1}\begin{bmatrix} M^2(1-\gamma)-2 & \zeta\dfrac{\gamma+1}{\gamma-1} & -\gamma M^2 - \dfrac{2\gamma}{\gamma-1} \\ 2\gamma(\gamma-1) + \dfrac{M^2(1-\gamma^2)}{\zeta} & -2\zeta\gamma + \dfrac{\gamma^2 M^2}{\gamma-1} & 2\gamma\left(\gamma - \dfrac{M^2}{\zeta}\right) - \dfrac{\gamma(\gamma-1)}{\zeta}M^4 \\ 2\zeta(\gamma M^2-1) & -2\zeta^2 & 2\zeta\gamma M^2 \end{bmatrix}. \tag{4.10}$$

It can be observed from Eqs. (4.9 b) and (4.10) that the coefficients in the system of ODEs (Eq. 4.9 a) are only functions of the axial mean flow and the steady heat transfer rate per unit volume, $\overline{\dot{Q}}$.

On assuming a harmonic time-dependence for the fluctuating quantities in the form $y = \hat{y}e^{i\omega t}$, Eq. (4.9 a) is recast in the frequency domain as,

$$\frac{\mathrm{d}}{\mathrm{d}x}\hat{\mathbf{I}} = \mathbf{A}\left(x,\,\omega,\,\overline{\dot{Q}}\right)\hat{\mathbf{I}} \quad \text{with} \quad \mathbf{A} = -[\mathbf{E}_x]^{-1}\left(\frac{i\omega}{\overline{u}}\mathcal{I} + \frac{(\gamma-1)\,\overline{\dot{Q}}}{2\zeta\gamma\overline{p}\overline{u}}\mathbf{E}_s\right)\hat{\mathbf{I}}, \tag{4.11}$$

where $\mathcal{I}$ is an identity matrix of order 3.

The frequency and the heat transfer rate are specified in terms of the non-dimensional parameters $\mathrm{He} = \omega l/\overline{c}$ (axial Helmholtz number) and $\tilde{Q} = \dfrac{\overline{\dot{Q}}l}{\overline{p}_{t,\,1}\overline{c}_{t,\,1}}$, respectively, where $\overline{p}_{t,\,1}$ and $\overline{c}_{t,\,1}$ correspond to the stagnation pressure and stagnation speed of sound at the inlet, respectively. The subscript 't' denotes the stagnation (or total) quantities.

The first-order system of differential equations in Eq. (4.11) is solved using a Magnus expansion based method. In this method, the solution is expressed as an infinite expansion around the axial Helmholtz number (He) and the non-dimensional heat transfer ($\tilde{Q}$). This infinite series expansion is truncated to a certain order that guarantees reasonable accuracy for the model under given conditions. The final solution is expressed as a relation between the flow invariants at any location (x^*) to those at the inlet using,

$$\hat{\mathbf{I}}(x^*,\, \mathrm{He},\, \tilde{Q}) = [\exp[\mathbf{B}(x^*,\, \mathrm{He},\, \tilde{Q})]]\hat{\mathbf{I}}_1, \quad \text{with} \quad \mathbf{B}(x^*,\, \mathrm{He},\, \tilde{Q}) = \sum_{k=0}^{\infty} \mathbf{B}^{(k)}(x^*,\, \mathrm{He},\, \tilde{Q}), \tag{4.12}$$

where $x^* = x/l$ denotes the dimensionless axial coordinate. $\mathbf{B}^{(k)}(x^*,\, \mathrm{He},\, \tilde{Q})$ represents the terms of the Magnus expansion each of order $O(\mathrm{He},\, \tilde{Q})^k$ with k being the order of Magnus expansion. These terms are obtained recursively using the matrix $\mathbf{F}_n^{(k)}$, as discussed in [77, 136]:

$$\begin{aligned} \mathbf{F}_q^{(j)} &= \sum_{m=1}^{q-j} \left[\mathbf{B}^{(m)},\, \mathbf{F}_{q-m}^{(j-1)}\right], \quad 2 \leqslant j \leqslant q-1, \\ \mathbf{F}_q^{(1)} &= \left[\mathbf{B}^{(q-1)},\, \mathbf{A}\right], \quad \mathbf{F}_q^{(q-1)} = ad_{\mathbf{B}^{(1)}}^{(q-1)}(\mathbf{A}) \end{aligned} \tag{4.13}$$

where $ad_B^{(k)}(\mathbf{A})$ is an iterated commutator given by,

$$ad_B^{(0)}(\mathbf{A}) = \mathbf{A}, \quad ad_{\mathbf{B}}^{(k+1)}(\mathbf{A}) = \left[\mathbf{B},\, ad_{\mathbf{B}}^{(k)}(\mathbf{A})\right] \tag{4.14}$$

Thus, $\mathbf{B}^{(k)}$ is finally given by,

$$\mathbf{B}^{(1)}(x^*) = \int_0^{x^*} \mathrm{d}\breve{x}\mathbf{A}\left(\breve{x}\right), \quad \text{and} \quad \mathbf{B}^{(q)}(x^*) = \sum_{j=1}^{q-1} \frac{b_j}{j!} \int_0^{x^*} \mathbf{F}_q^{(j)}\left(\breve{x}\right) \mathrm{d}\breve{x}. \tag{4.15}$$

with $\breve{x}$ as the dummy variable. The exponential of the matrix $\mathbf{B}$ in Eq. (4.12) can be expanded using Taylor series up to an order k to obtain the invariant transfer matrix at the same accuracy of the truncated Magnus series. To ensure convergence, the series may require computing the transfer matrices separately for different sections of the nozzle which are subsequently multiplied for the final result [136].

Using Eqs. (4.12) and (4.3), we obtain a transfer matrix, $\mathbf{T}$, relating the wave-vectors at the inlet to any location x^*, which reads,

$$\mathbf{W}_{x^*}^* = \mathbf{T}\mathbf{W}_1^*, \quad \text{where} \quad \mathbf{T} = \left[\mathbf{D}_{x^*}\right]^{-1} \mathbf{C}\, \mathbf{D}_1, \tag{4.16}$$

where $\mathbf{C} = [\exp[\mathbf{B}(x^*,\, \mathrm{He},\, \tilde{Q})]]$ and $\mathbf{D}$ is given in Eq. (4.3).

4.3 Acoustic and entropy transfer functions of the nozzle

In this section, the acoustic transfer functions of nozzles sustaining sub-critical and super-critical flows are determined for acoustic and entropy disturbance forcing at the inlet. For a nozzle sustaining subsonic flow Mach numbers, the incoming, $\mathcal{W}_{in}^* = \left[p_1^+\; p_2^-\; \sigma_1^*\right]^{\mathrm{T}}$ and the outgoing, $\mathcal{W}^*_{out} = \left[p_2^+ \; p_1^- \; \sigma_2^*\right]^{\mathrm{T}}$, waves are related using a scattering matrix $\mathbf{S}$ as,

$$\mathcal{W}^*_{out} = \mathbf{S}\mathcal{W}^*_{in}, \tag{4.17}$$

which is obtained by rearranging Eq. (4.16). Note that while $\mathbf{W}^*_{x^*}$ denotes wave vector at any normalised spatial location x^*, $\mathcal{W}^*_{in,\,out}$ denotes the directional wave vectors - either incoming or outgoing.

For a nozzle sustaining super-critical flow without any shock-waves inside, the acoustic and entropy forcing inputs at the inlet ($p^+_{1,\,f}$ and $\sigma^*_{1,\,f}$) along with Eq. (4.5) give the three input conditions. Eq. (4.16) for the subsonic portion of the super-critical nozzle then takes the form,

$$\begin{bmatrix} p_u^+ \\ p^-_{f,\,u} \\ \sigma^*_u \end{bmatrix} = \underbrace{\left[\mathbf{D}_2^{'}\right]^{-1} \mathbf{C}\, \mathbf{D}_1}_{\mathbf{T}'} \begin{bmatrix} p^+_{1,\,f} \\ p_1^- \\ \sigma^*_{1,\,f} \end{bmatrix}. \tag{4.18}$$

The above equation can be rearranged again by collecting the forcing inputs on one side and the unknowns on the other. This gives, $\mathbf{W}^*_u = \mathbf{S}_s\mathcal{W}^*_{in}$ since the upstream propagating wave near the throat (x^*_u), $p^-_{u,\,f} = 0$, for the super-critical case and thus $\mathcal{W}^*_{in} = \left[p^+_{1,\,f} \quad 0 \quad \sigma^*_{1,\,f}\right]^T$. Also we define $\mathbf{S}_s$ as the scattering matrix of the subsonic portion given in terms of the elements of $\mathbf{T}^{'}$. The wave vector infinitesimally upstream of the throat ($\mathbf{W}^*_u$) propagates unaltered at the throat and hence $\mathbf{W}^*_u = \mathbf{W}^*_d$, with subscript 'd' denoting a location infinitesimally downstream of the throat. The transfer matrix in the supersonic portion of the nozzle is denoted by $\mathbf{T}_{su}$, and relates the wave vectors as $\mathbf{W}^*_2 = \mathbf{T}_{su}\mathbf{W}^*_d$, with $\mathbf{T}_{su} = [\mathbf{D}_2]^{-1}\mathbf{C}\,\mathbf{D}_d$. This gives,

$$\mathbf{W}^*_2 = \mathbf{T}_{su}\mathbf{S}_s\mathcal{W}^*_{in}. \tag{4.19}$$

Equation (4.19) expresses the fast (p_2^+) and slow (p_2^-) propagating acoustic waves and the entropy wave (σ_2^*) at the outlet as a function of the acoustic ($p^+_{1,\,f}$) and entropy ($\sigma^*_{1,\,f}$) forcing at the nozzle inlet. The upstream propagating wave at the inlet (p_1^-) in the subsonic portion is given by the second element of the vector $\mathcal{W}^*_{out}$.

4.4 Validation results

The Magnus expansion-based semi-analytical solution is validated by comparing its predictions against the numerical solutions of the linearised Euler equations (LEEs) Eqs. (4.6) - (4.8), and a Magnus order of $k = 5$ is considered for this case. Note that these linearised Euler equations are for a nozzle with a known distribution of heat transfer rate per unit volume, while Eqs. (2.8) - (2.10) are applicable for a given temperature profile but are both inter-convertible. It should also be noted that these LEEs fully account for the acoustic entropy coupling unlike the 2LEEs used for validation in Chapter 2 and 3.

A converging-diverging nozzle of the type shown in Fig. 4.1 is considered for the validation, with an area variation profile given as,

$$\frac{A_s(x)}{\tilde{A}_s} = \begin{cases} \frac{1}{2}\left(\frac{A_{s,\,1}}{\tilde{A}_s} - 1\right)\left[\cos\left(\frac{x}{\tilde{x}}\right) + 1\right] + 1 & \text{if } x \in [0,\ \tilde{x}] \\ 1 + \left(\frac{A_{s,\,2}}{\tilde{A}_s} - 1\right)\frac{x - \tilde{x}}{l - \tilde{x}} & \text{if } x \in [\tilde{x},\ l] \end{cases} \tag{4.20}$$

where $\tilde{x} = 0.15$m is the location of the throat, $\tilde{A}_s = 0.002\text{m}^2$ corresponds to the throat area, $A_{s,\,1}/\tilde{A}_s = 2.1$ and $A_{s,\,2}/\tilde{A}_s = 1.18$.

Two different inlet conditions are considered that correspond to (i) sub-critical and (ii) super-critical flows (without shocks). For the sub-critical case, an inlet flow Mach number of $M_1 = 0.2$ is considered with an inlet temperature of 1600 K and a pressure of 1 bar. The mean flow is obtained by solving Eqs. (2.5), (2.7) using a Runge-Kutta fourth-order implicit scheme for different levels of heat transfer set by $\tilde{Q}$. Although a constant heat transfer $\tilde{Q}$ is assumed along the walls of the nozzle for both cases for simplicity, the approach can assume any spatial distribution $\tilde{Q}(x^*)$. The mean flow for the super-critical case is obtained using a modified finite-difference based MacCormack scheme [137]. An inlet flow Mach number of $M_1 = 0.29$ is considered for the isentropic case with $\overline{T}_1 = 1600$K, $\overline{p}_1 = 1$bar. When heat is added ($\tilde{Q} > 0$) or removed ($\tilde{Q} < 0$), the inlet Mach number for the given geometry differs and ranges from $M_1 = 0.28$ to $M_1 = 0.30$, for $\tilde{Q} = 0.3$ to $\tilde{Q} = -0.5$, respectively. The evolution of the Mach number and the mean temperature inside the nozzle is presented in Fig. 4.2. As expected, the temperature at the outlet is higher when heat is added than for the isentropic case. For the Mach number distribution, we observe different trends for the sub-critical and super-critical cases. For the subsonic flow, the Mach numbers are higher when heat is added. This can be attributed to the decrease of the density and subsequent increase of the velocity of the flow to satisfy continuity. For the super-critical nozzle, adding heat reduces the flow Mach numbers, explained by the increase of the speed of sound due to the temperature rise.

4.4.1 Effect of heat transfer on the acoustic and entropy response at zero frequencies

The heat transfer effect on the acoustic response of nozzles at zero-frequencies ($\text{He}_1 = 0$) is presented in this section. The heat transfer rate $\tilde{Q}$ is varied in the range $\in [-0.5, 0.5]$ for the sub-critical flow and $\tilde{Q} \in [-0.5, 0.3]$ for the super-critical one. For $\tilde{Q} > 0.3$ in the super-critical regime, a normal shock appears and such flow cases are not considered for validation in this chapter. The results compare the transfer functions calculated by the model, assuming a Magnus expansion order, $k = 5$, alongside the numerical solutions of LEEs (Eqs. (4.6) - (4.8)).

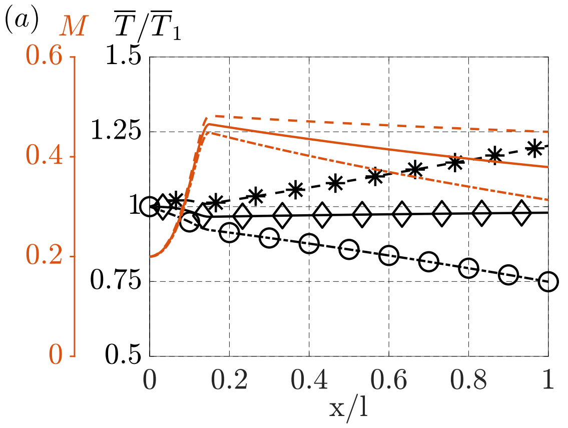

Figure 4.2: Mach number, M, (lines) and mean-temperature, $\overline{T}$, (lines with markers) for: (a) sub-critical case with $\tilde{Q}$ values of -0.5 (-···-), 0 (——), 0.5 (- - -); (b) super-critical case for $\tilde{Q}$ values of -0.5 (-···-), 0 (——), 0.3 (- - -).

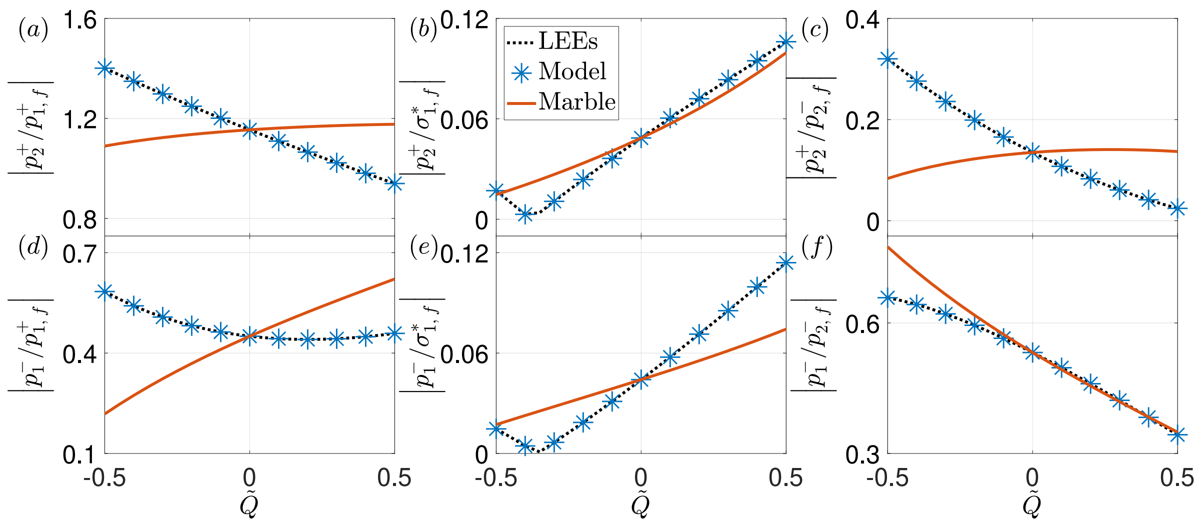

Figure 4.3: Transfer functions for the sub-critical nozzle flow at zero-frequency predicted by the present model ($*$), the compact isentropic model of [76] (——), and numerical solutions (······).

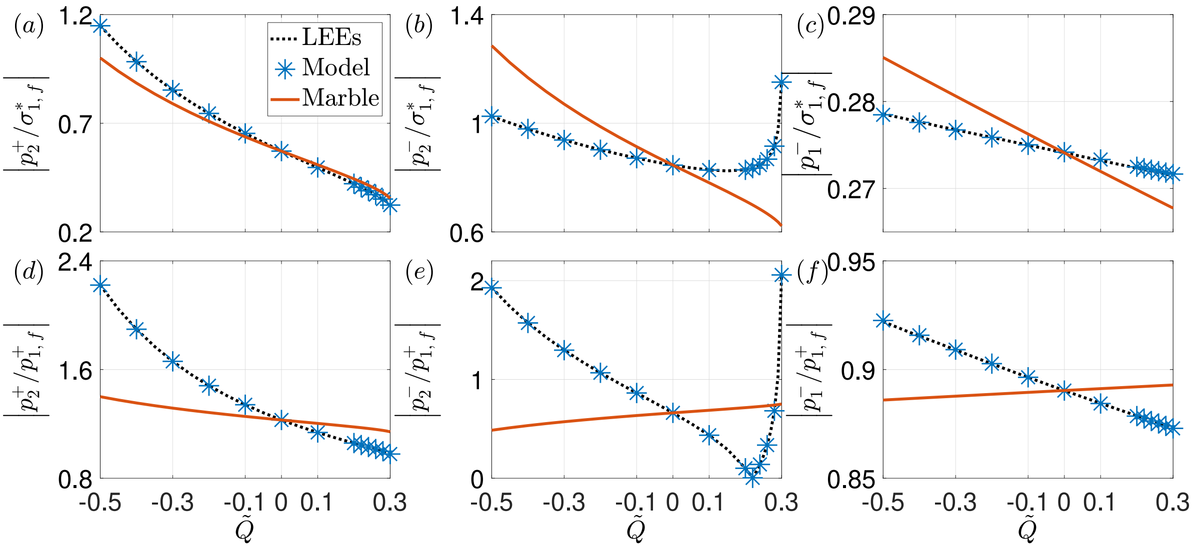

Figure 4.4: Transfer functions for the super-critical nozzle flow at zero-frequency predicted by the present model ($*$), the compact isentropic model of [76] (——), and numerical LEEs (······).

The compact, isentropic theory results of Marble and Candel [76] presented in Section 4.1.1 are also plotted to assess the importance of the heat transfer on the acoustic solution. As shown in Table 4.1, these transfer functions are functions of only the flow Mach numbers at the inlet and the outlet. Hence, corrected Mach numbers based on the non-isentropic mean flow results are used in estimating these compact, isentropic transfer functions.

Figures 4.3 and 4.4 show the coefficients of the transfer functions for the sub-critical and super-critical nozzle flow cases, respectively. The model predictions are compared with numerical solutions, and an excellent agreement is observed. The effect of heat transfer on the results is revealed to be important and cannot be accurately captured using isentropic compact theory results of [76], outlined in Tables 4.1 and 4.2, even with corrected mean flow. Strong sensitivity of the entropy transfer function was observed for the super-critical case where the flow Mach numbers in the diverging portion get close to 1. A finer resolution was adapted to capture the trend reversal in these regions.

4.4.2 Effect of heat transfer on the acoustic and entropy response at non-zero frequencies

Figure 4.5 shows the variation of magnitude and phase of the acoustic transfer functions for the sub-critical nozzle flow as a function of the frequency, for both isentropic ($\tilde{Q} = 0$) and non-isentropic ($\tilde{Q} = -0.5$) cases. It can again be observed that the model estimates are accurate. The magnitudes of the reflected acoustic wave at the inlet, p_1^-, initially peaked before exhibiting a low pass like behaviour for both acoustic ($p_{1,f}^+$) and entropic ($\sigma_{1,f}^*$) forcing. This behaviour was also observed for the acoustic transmission transfer function (p_2^+) for an entropy forcing

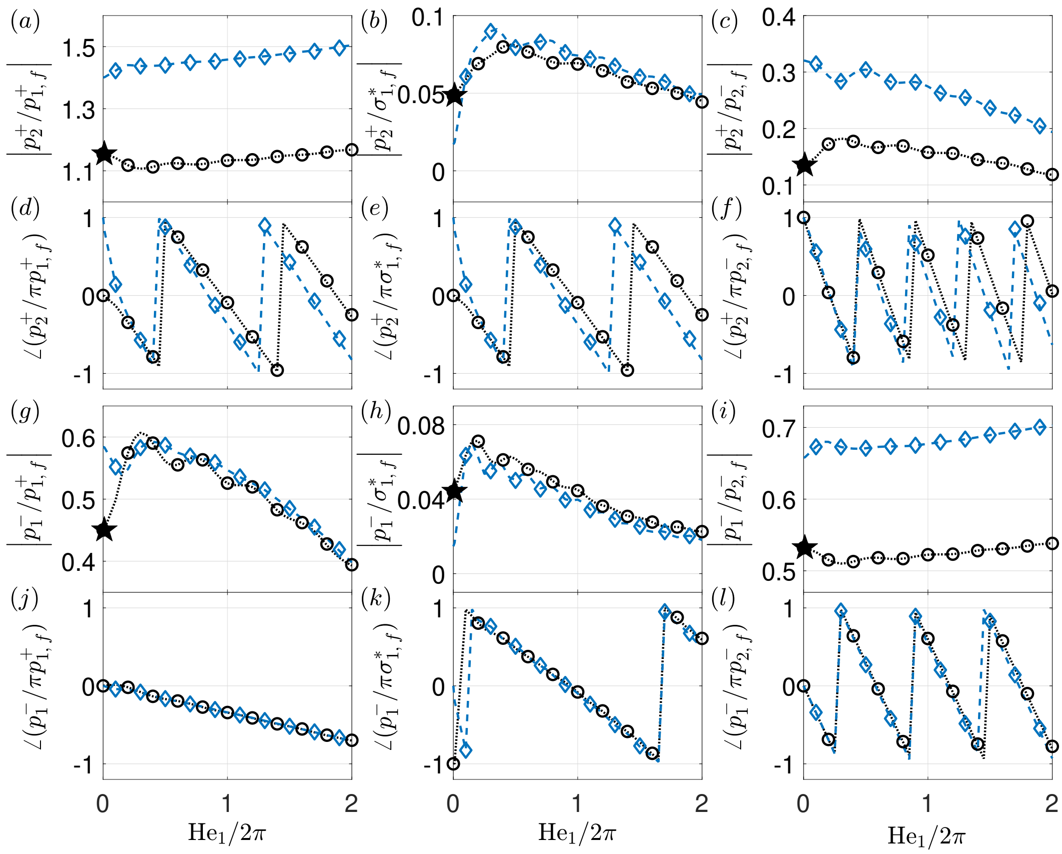

Figure 4.5: Transfer functions for nozzle with sub-critical flow as a function of the frequency He_1. Numerical (······) and model solutions (◯) for $\tilde{Q} = 0$. Numerical (- - -) and model solutions (◇) for $\tilde{Q} = -0.5$. [76] compact solution (★).

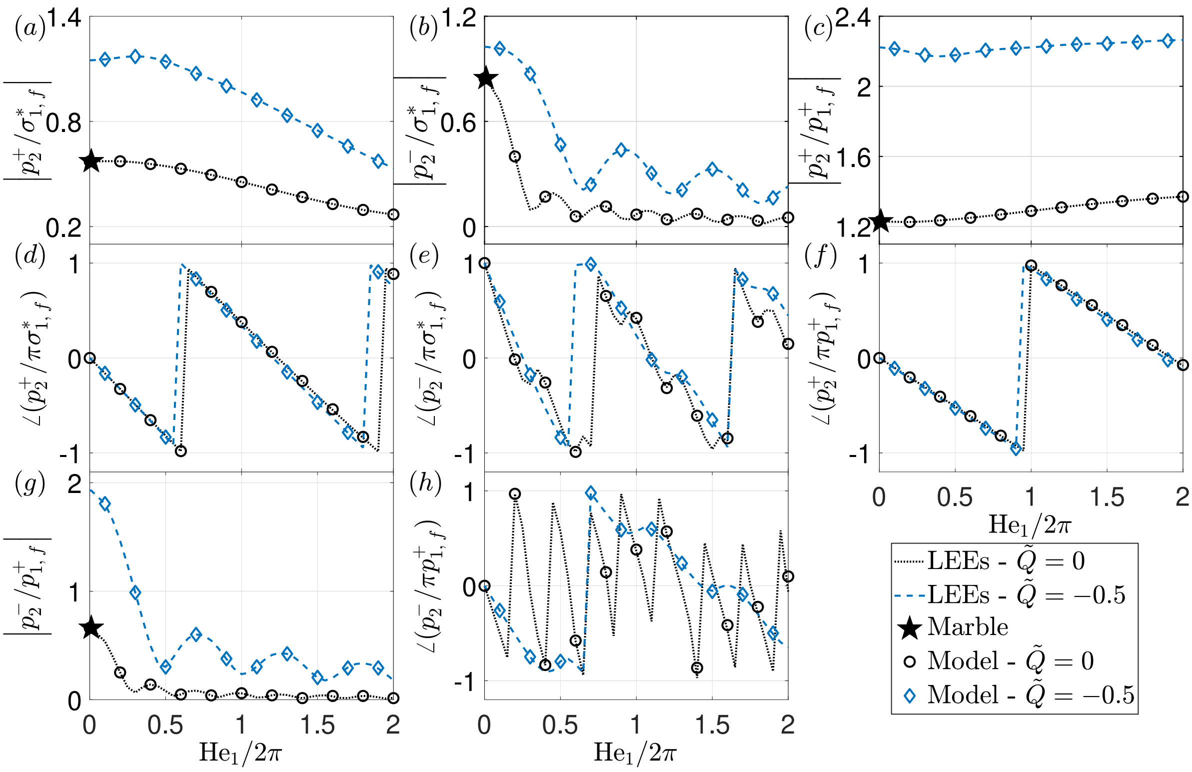

Figure 4.6: Transfer functions for nozzle with super-critical flow as a function of the frequency He$_1$. [76] compact solution (★).

($\sigma^*_{1,f}$) at the inlet. The phase of the transfer functions is observed to be only mildly affected by the heat transfer.

Fig. 4.6 shows the variation of the transfer functions as a function of the frequency for the super-critical nozzle flow with $\tilde{Q} = -0.5$ and 0. The upstream propagating wave at the inlet (p_1^-) is not plotted as this is calculated using the scattering matrix of the subsonic portion alone and behaved similar to p_1^- of the sub-critical flow case. The model estimates for the transfer functions are again accurate for both cases. The slow propagating wave at the outlet (p_2^-) has a low pass like behaviour for both entropy ($\sigma^*_{1,f}$) and acoustic ($p^+_{1,f}$) forcing at the inlet. The phase variation is again observed to be minimal with heat transfer except for the slow propagating wave (p_2^-) when forced with entropy ($\sigma^*_{1,f}$).

4.4.3 Effect of heat transfer on the entropy generation at zero frequencies

For nozzles sustaining isentropic mean flow, as noted from Eq. (2.79), the entropy wave advects without any amplification or attenuation. However, for nozzles sustaining heat transfer, the amplitude of the entropy wave changes. The indirect noise thereby produced can be higher than anticipated using the isentropic relations and must be accurately modelled; this is achieved using the Magnus expansion method.

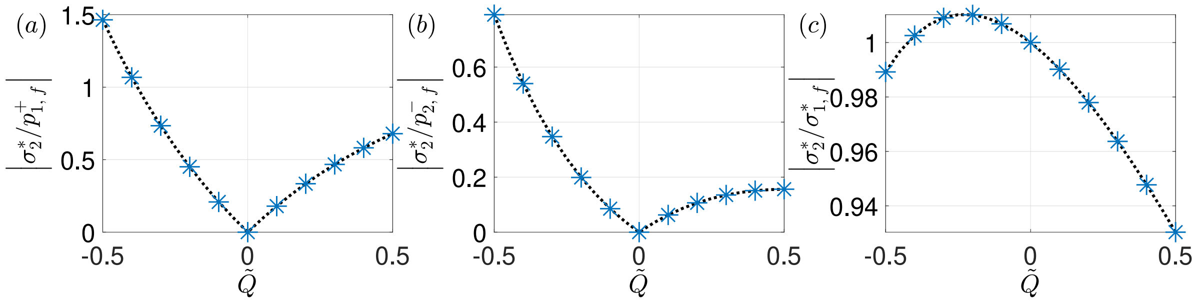

Figure 4.7: Entropy generation and amplification in sub-critical nozzle flow at zero-frequency predicted by the present model ($*$) and numerical LEEs (······).

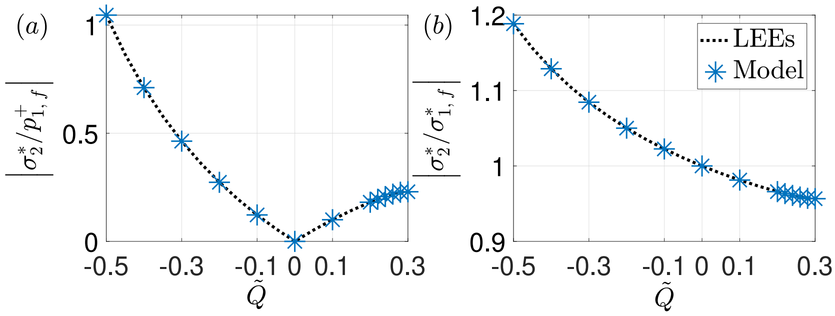

Figure 4.8: Entropy generation and amplification in super-critical nozzle flow at zero-frequency predicted by the present model ($*$) and numerical LEEs (······).

Figures 4.7 and 4.8 present the entropy generation and amplification in nozzles sustaining sub-critical and super-critical flows, respectively, as a function of the $\tilde{Q}$ at zero frequencies. The model estimates are accurate and as observed, heat exchange in the form of heat added ($\tilde{Q} > 0$) or removed ($\tilde{Q} < 0$) can result in significant levels of entropy generation for given input acoustic disturbances. For the isentropic case ($\tilde{Q} = 0$), however, the entropy generation due to these incoming acoustic wave forcing is zero (Fig. 4.7 (a), (b) and Fig. 4.8 (a)). For this case of acoustic forcing, nozzles losing heat ($\tilde{Q} < 0$) are subjected to higher levels of entropy generation than nozzles gaining heat for the same $\left|\tilde{Q}\right|$. Hence practical combustors which generally sustain a heat loss to the cold dilution air or due to the presence of heat exchangers [10] are susceptible to higher exhaust noise due to indirect noise generation mechanisms. The upstream propagating acoustic component of the generated indirect noise also affects the thermoacoustic stability of the system [92].

The entropy wave amplification ($\sigma_2^*/\sigma_{1,\,f}^*$) is less sensitive to $\tilde{Q}$ for nozzles with sub-critical flow (Fig. 4.7 (c)) than super-critical flow (Fig. 4.7 (b)). A maximum of 6% attenuation occurs for $\tilde{Q} = 0.5$ for the sub-critical case while a 20% amplification occurs for the super-critical case at $\tilde{Q} = -0.5$. As expected, the entropy wave advects unaltered ($\sigma_2^*/\sigma_{1,\,f}^* = 1$) for the isentropic case ($\tilde{Q} = 0$).

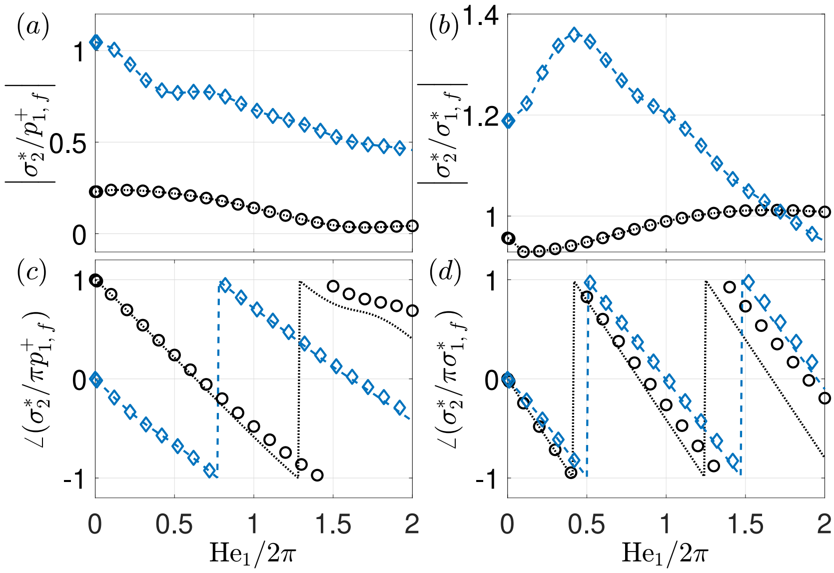

Figure 4.9: Entropy generation and amplification for the super-critical nozzle flow as a function of the frequency He_1. Numerical (······) and model solutions (◯) for $\tilde{Q} = -0.5$. Numerical (- - -) and model solutions (◇) for $\tilde{Q} = 0.3$.

4.4.4 Effect of heat transfer on the entropy generation at non-zero frequencies

We now turn our attention to study the effect of $\tilde{Q}$ for non-zero frequencies. Figs. 4.9 and 4.10 show that for the considered $\tilde{Q}$, the magnitude of the transfer functions is accurately captured with small deviations in the phase at high frequencies, for sub-critical and super-critical flows, respectively. This deviation is attributed to the truncation of the Magnus expansion to the fifth order in frequency ($k = 5$). Note that the results in this case are presented for $\tilde{Q} = -0.5$ and 0.5 for the sub-critical case, $\tilde{Q} = -0.5$ and 0.3 for the super-critical case. Negative values of $\tilde{Q}$ can be again observed to result in larger levels of entropy generation ($|\sigma_2^*|$). This difference as a function of $\tilde{Q}$ is appreciable for low frequencies and diminishes at high frequencies.

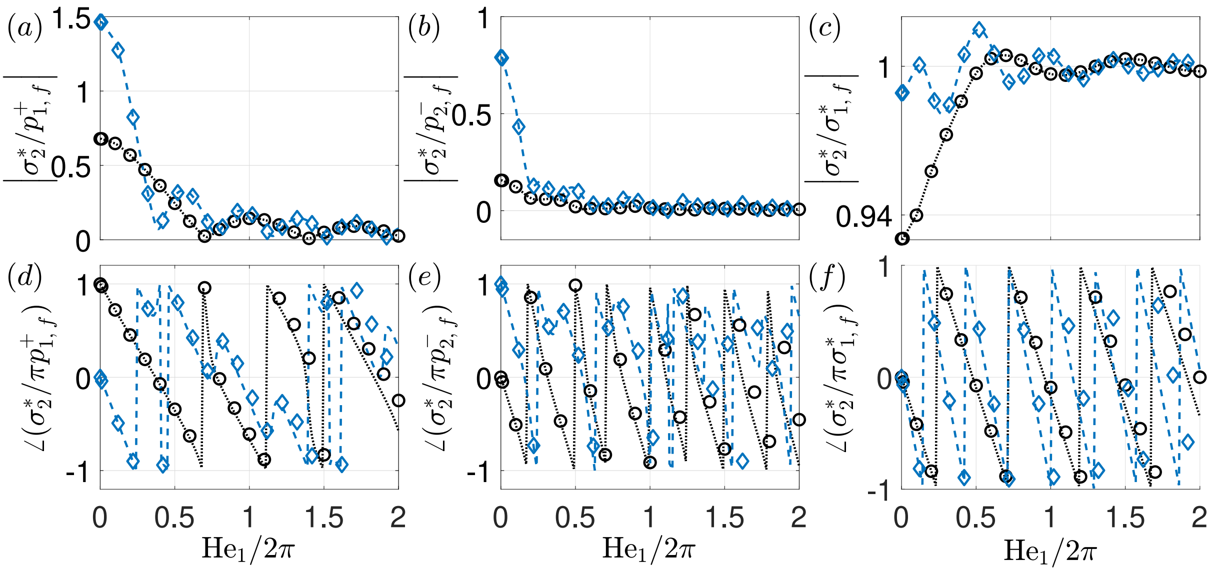

Figure 4.10: Entropy generation and amplification for the sub-critical nozzle flow as a function of the frequency He_1. Numerical (······) and model solutions (◯) for $\tilde{Q} = 0.5$. Numerical (- - -) and model solutions (◊) for $\tilde{Q} = -0.5$.

4.5 Summary

To summarise, this chapter introduces a mathematical model to determine the acoustic and entropy transfer functions of a quasi 1-D nozzle sustaining non-isentropic mean flows, with heat transfer as the source of non-isentropicity. The model is applied to nozzles with both sub-critical and super-critical flow configurations for different levels of heat transfer and frequency, and the predictions are successfully validated against numerical solutions of the LEEs. The computational cost of the Magnus expansion model is significantly lower compared to the numerical LEEs solution and the detailed comparison is given in Appendix D. The model results are also compared with the isentropic compact transfer functions presented by [76], and it is observed that neglecting the heat transfer can lead to large deviations. Certain acoustic transfer functions are amplified with increasing $\tilde{Q}$, while some are found to be attenuated. For both the sub-critical and super-critical cases, the magnitude of the transfer functions was found to be more strongly affected in the presence of heat transfer than the phase. For nozzles with heat transfer, entropy generation was observed to occur in response to incident acoustic disturbances, with stronger entropy waves for the case of nozzles sustaining heat loss.

Although this analysis considers the steady heat-transfer as the main source of non-isentropicity, other sources are also possible. For example, De Domenico *et al.* [107, 108] analysed the effects of flow separation and friction on the acoustics. The effect of dissipation (flow re-circulation and wall friction) was modelled from conservation laws by Jain and Magri [109], who computed acoustic transfer functions for any Helmholtz number and Mach-number regime and analysed the effect that dissipation has on thermoacoustic stability. Also, the effect of shear dispersion and local turbulent mixing on the entropy wave [100, 101] were found to significantly affect thermoacoustic behaviour in nozzles. Emmanuelli *et al.* [103, 104] and Huet *et al.* [105, 106] developed acoustic models that accurately account for these the non-planar entropy wave effects.

Chapter 5

Semi-analytical solutions for the 2-D acoustic field in annular nozzles with mean flow

In this chapter, the WKB and the Magnus expansion based solutions, presented in chapters 2 and 4, are extended to estimate the two-dimensional acoustic field in an annular nozzle flow. The annular nozzle is assumed to have a thin gap, such that only axial and azimuthal flow perturbations are significant. The mean radius of the annulus as well as its flow width can vary in the axial direction, and the mean flow passing through it can have axial and azimuthal components. The WKB solution can consider the mean flow to be non-isentropic with arbitrary axial temperature variation, while, the Magnus expansion based analysis is limited to isentropic annular nozzle flows in this study. The governing flow conservation equations, the mean flow equations and the linearised Euler equations (LEEs) for both the isentropic and non-isentropic annular nozzle flows are presented. The LEEs thus achieved are solved using both the WKB based and Magnus expansion based methods. While the WKB based method neglects entropy disturbance effects and requires sufficiently high frequencies and low subsonic flow Mach numbers, the Magnus expansion based model presented in this chapter is limited by the isentropic mean flow ($\dot{Q} = 0$) assumption. The model solutions are validated against numerical solutions by applying them to an annular nozzle with a quarter sinusoid like area variation. The WKB model's applicability to stability analysis is further shown by accurately predicting ($< 2\%$ deviation) the acoustic modes for an axially varying annular nozzle, validated using a 2-D low-order network model solver based on modal expansions.

5.1 Introduction

An acoustic model that accurately captures the two-dimensional acoustic field in a thin annular geometry, accounting for geometric complexities in the form of varying mean radius and flow width, and mean flow complexities in the form of an azimuthal mean flow component and non-isentropic mean flow, has so far been lacking. This chapter presents such a two-dimensional acoustic model.

The main contribution is to derive semi-analytical model solutions, based on the iterative WKB method and the Magnus expansion method, for the 2-D acoustic field in an annular nozzle which (i) has a varying mean radius and flow width, (ii) sustains a subsonic mean flow which may have components in both the axial and azimuthal directions, and (iii) exhibits an axial temperature variation (only for the WKB solution), as shown diagrammatically in Fig. 5.1. The general case of a non-isentropic mean flow will be considered for the WKB solution, for which the axial temperature and cross-sectional area gradients can be prescribed independently. However, the Magnus solution is limited to isentropic mean flows without any heat exchange with the surroundings in this study. The capabilities of the two models are summarised in Table 5.1.

Table 5.1: Modelling for thin annular nozzle flows

Model	Isentropic flow with axial and azimuthal components	Low subsonic mean flows	Sub-critical and super-critical flows	Heat transfer effects
WKB based	✓	✓	✖	✓
Magnus expansion based	✓	✓	✓	✖

In the context of a narrow gap annular nozzle, the two-dimensional conservation equations are derived and presented by neglecting any effects of diffusion and flow variations in the radial direction. The conservation equations are linearised, assuming the perturbations to be small compared to the mean flow properties. The analysis makes the narrow annular gap assumption [125], using which the radial modes are assumed to be cut off for the considered frequencies. Acoustic variations in both the axial and azimuthal directions are accounted for. The LEEs obtained for the isentropic and non-isentropic flows are also then presented, these being an important contribution of this work.

The analysis is first applied to annular nozzles with non-isentropic mean flow due to steady heat transfer, and the acoustic solution is obtained using the iterative WKB method. Similar to the assumptions of the one-dimensional WKB acoustic solution, sufficiently high frequencies and low subsonic flow Mach numbers in the nozzle are assumed. The effect of the entropy disturbance on the acoustic field is also neglected, again citing low flow Mach numbers [44] and

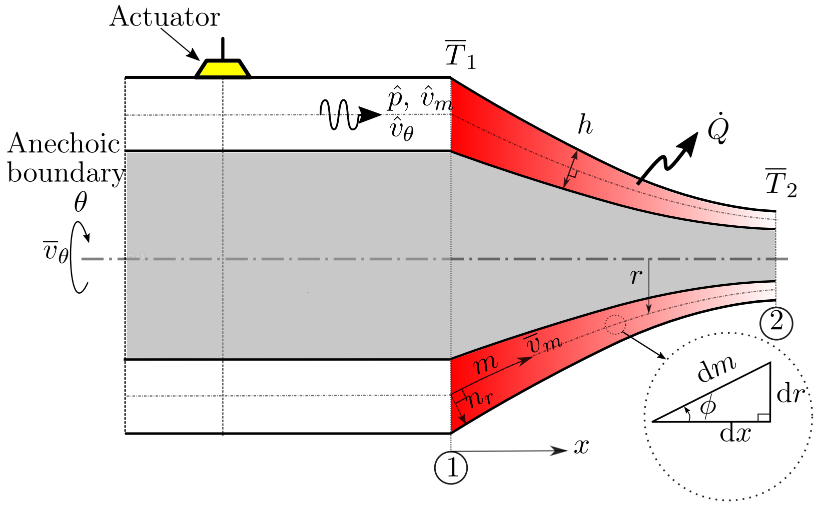

Figure 5.1: Sketch of an annular nozzle with varying mean radius (r) and flow width (h), in between the inlet plane, denoted 1, and the outlet plane, denoted 2. m, n_r and θ correspond to the meridional, normal and azimuthal directions respectively. For the validation test-cases, actuation upstream of the area variation, and an anechoic boundary upstream of actuation are considered.

enhanced shear dispersion of the entropy waves at these high frequencies [95, 101].

The Magnus expansion based solution is then presented for the 2-D acoustic field sustained in annular nozzles with isentropic mean flow. As shown for the 1-D acoustic field in Chapter 4, this solution can be applied to both sub-critical and super-critical configurations and is accurate over a wide range of frequencies. The effect of the entropy disturbance on the acoustic field is also accurately captured.

5.2 Analysis using the iterative WKB method

In an annular nozzle, as shown in Fig. 5.1, the axial (x) and the radial (r) coordinates are not independent as the nozzle radius varies as a function of x, that is $r = r(x)$. Hence, the axial and the radial coordinates are mapped into independent meridional (denoted by m) and normal (denoted by n_r) coordinates as shown in Fig. 5.1. The flow variations in the normal direction (n_r) are assumed negligible for this analysis assuming a thin annular gap [125], therefore variations in both mean flow and perturbations along the normal direction are neglected. This transformation leads to the following conservation equations, consistent with [138], given by,

- **Mass conservation**

$$\frac{\partial \rho}{\partial t} + \frac{1}{rh}\frac{\partial(\rho r h v_m)}{\partial m} + \frac{1}{r}\frac{\partial(\rho v_\theta)}{\partial \theta} = 0, \tag{5.1}$$

- **Meridional momentum conservation**

$$\frac{\partial v_m}{\partial t} + v_m \frac{\partial v_m}{\partial m} + \frac{v_\theta}{r}\frac{\partial v_m}{\partial \theta} - \frac{v_\theta^2}{r}\sin\phi = -\frac{1}{\rho}\frac{\partial p}{\partial m}, \tag{5.2}$$

- **Azimuthal momentum conservation**

$$\frac{\partial v_\theta}{\partial t} + v_m \frac{\partial v_\theta}{\partial m} + \frac{v_\theta}{r}\frac{\partial v_\theta}{\partial \theta} + \frac{v_m v_\theta}{r}\sin\phi = -\frac{1}{\rho r}\frac{\partial p}{\partial \theta} \tag{5.3}$$

- **Energy conservation**

$$\frac{\partial s}{\partial t} + v_m \frac{\partial s}{\partial m} + \frac{v_\theta}{r}\frac{\partial s}{\partial \theta} = \frac{R_g}{p}\dot{Q} \tag{5.4}$$

where v_m, v_θ, r denote the meridional velocity, azimuthal velocity, and the mean radius of the annular nozzle respectively, while $\phi = \sin^{-1}(\mathrm{d}r/\mathrm{d}m)$. As shown in Fig. 5.1, h represents the flow width, measured along the normal direction n_r. The effects of the steady heat interaction per unit volume to the surroundings, denoted $\overline{\dot{Q}}$, is accounted for, assuming no heat perturbations inside the nozzle ($\dot{Q}' = 0$). The area and mean-temperature variations in the meridional direction are also characterised by the variables α and β using:

$$\alpha = \frac{1}{A_f}\frac{\mathrm{d}A_f}{\mathrm{d}m} = \overbrace{\frac{1}{r}\frac{\mathrm{d}r}{\mathrm{d}m}}^{\Delta_r} + \frac{1}{h}\frac{\mathrm{d}h}{\mathrm{d}m}; \qquad \beta = \frac{1}{\overline{T}}\frac{\mathrm{d}\overline{T}}{\mathrm{d}m}, \tag{5.5, 5.6}$$

where A_f corresponds to the meridional flow area, thus $A_f = 2\pi r \dfrac{h}{\cos\phi}$. Note that the gradients are defined with respect to the meridional axis. Using the thermodynamic relation $\mathrm{d}\overline{H} = \overline{T}\mathrm{d}\overline{s} + \mathrm{d}\overline{p}/\overline{\rho}$, time-averaged form of Eq. (5.4) and assuming no mean flow variations in the azimuthal direction, i.e., $\dfrac{\partial}{\partial\theta}(\,) = 0$, the steady heat-transfer rate of the annular nozzle in terms of mean flow gradients reads:

$$\overline{\dot{Q}} = \overline{\rho}\,\overline{v}_m \left(c_p \frac{\mathrm{d}\overline{T}}{\mathrm{d}m} + \overline{v}_m \frac{\mathrm{d}\overline{v}_m}{\mathrm{d}m} + \overline{v}_\theta \frac{\mathrm{d}\overline{v}_\theta}{\mathrm{d}m} \right). \tag{5.7}$$

Similarly, the time-averaged components of the annular nozzle conservation equations (Eqs. (5.1) - (5.3)) can be expressed in terms of α, β, M_m, M_θ and r as,

$$\frac{1}{\overline{v}_m}\frac{\mathrm{d}\overline{v}_m}{\mathrm{d}m} = \frac{\beta - \alpha - \gamma M_\theta^2 \Delta_r}{1 - \gamma M_m^2}, \quad \frac{1}{\overline{v}_\theta}\frac{\mathrm{d}\overline{v}_\theta}{\mathrm{d}m} = -\Delta_r, \quad \frac{1}{\overline{p}}\frac{\mathrm{d}\overline{p}}{\mathrm{d}m} = \frac{-\gamma M_m^2(\beta - \alpha) + \gamma M_\theta^2 \Delta_r}{1 - \gamma M_m^2},$$
$$\frac{1}{\overline{\rho}}\frac{\mathrm{d}\overline{\rho}}{\mathrm{d}m} = \frac{\alpha\gamma M_m^2 - \beta + \gamma M_\theta^2 \Delta_r}{1 - \gamma M_m^2}; \tag{5.8 - 5.11}$$

where, $M_m = \overline{v}_m/\overline{c}$ and $M_\theta = \overline{v}_\theta/\overline{c}$ are the meridional and azimuthal flow Mach numbers, and

$\Delta_r = \dfrac{1}{r}\dfrac{\mathrm{d}r}{\mathrm{d}m}$.

On equating the first order perturbation components, the linearised Euler equations in the time domain can be obtained. These are converted to the frequency domain, assuming a harmonic time dependence of the form $y' = \hat{y}\mathrm{e}^{\mathrm{i}\omega t + \mathrm{i}n\theta}$ for the flow perturbations, where ω represents the complex angular frequency and n denotes the azimuthal mode number - an integer. This gives,

$$\begin{aligned}&\frac{1}{\overline{\rho}\,\overline{c}}\left[\frac{\mathrm{i}\omega}{\overline{c}} + \beta\gamma M_m + \frac{\mathrm{i}n}{r}M_\theta + \gamma^2 M_m^3\left((\beta-\alpha) - \frac{M_\theta^2}{M_m^2}\Delta_r\right)\right]\hat{p} + \quad \frac{M_m}{\overline{\rho}\,\overline{c}}\frac{\mathrm{d}\hat{p}}{\mathrm{d}m} + \\ &\left(\alpha - (\beta-\alpha)M_m^2 + M_\theta^2\Delta_r\right)\hat{v}_m + \frac{\mathrm{d}\hat{v}_m}{\mathrm{d}m} + \frac{\mathrm{i}n}{r}\hat{v}_\theta = 0,\end{aligned} \tag{5.12}$$

$$\left(\mathrm{i}\omega + \frac{\mathrm{d}\overline{v}_m}{\mathrm{d}m} + \frac{\mathrm{i}n}{r}\overline{v}_\theta\right)\frac{\hat{v}_m}{\overline{v}_m} + \frac{\mathrm{d}\hat{v}_m}{\mathrm{d}m} + \frac{\mathrm{d}\overline{v}_m}{\mathrm{d}m}\frac{\hat{p}}{\gamma\overline{p}} + \frac{1}{\overline{\rho}\,\overline{v}_m}\frac{\mathrm{d}\hat{p}}{\mathrm{d}m} - 2\frac{M_\theta}{M_m}\Delta_r\hat{v}_\theta = \frac{1}{\overline{v}_m}\left(\overbrace{\overline{v}_m\frac{\mathrm{d}\overline{v}_m}{\mathrm{d}m}}^{\textbf{Term 1}} + \overbrace{\overline{v}_\theta\frac{\mathrm{d}\overline{v}_\theta}{\mathrm{d}m}}^{\textbf{Term 2}}\right)\frac{\hat{s}}{c_p}, \tag{5.13}$$

$$\left(\mathrm{i}\omega + \frac{\mathrm{i}n}{r}\overline{v}_\theta + \overline{v}_m\Delta_r\right)\hat{v}_\theta + \overline{v}_m\frac{\mathrm{d}\hat{v}_\theta}{\mathrm{d}m} + \frac{\mathrm{i}n}{r}\frac{\hat{p}}{\overline{\rho}} = 0, \tag{5.14}$$

$$\left(\mathrm{i}\omega + \frac{\mathrm{i}n}{r}\overline{v}_\theta\right)\frac{\hat{s}}{c_p} + \overline{v}_m\frac{\mathrm{d}\hat{s}/c_p}{\mathrm{d}m} = -\overline{v}_m\left(\frac{\beta\left(1-M_m^2\right) + (1-\gamma)\left(\alpha M_m^2 + M_\theta^2\Delta_r\right)}{1-\gamma M_m^2}\right)\left(\frac{\hat{v}_m}{\overline{v}_m} + \frac{\hat{p}}{\overline{p}}\right). \tag{5.15}$$

The above linearised Euler equations (LEEs), Eqs. (5.12) - (5.15), apply to a thin annular nozzle sustaining a mean flow with both meridional and azimuthal components, and arbitrary mean radius, flow width and temperature variations in the meridional direction. These LEEs (Eqs. (5.12) - (5.15)), apart from the assumptions for the mean flow, assume the flow perturbations in the normal direction (n_r) to be negligible and assume a linear framework for the fluctuations. The LEEs thus achieved are applicable for any frequency, azimuthal mode number and mean flow in an annular nozzle.

The effect of the entropy disturbance on the acoustic field is governed by the source term in the meridional momentum equation, Eq. (5.13). An important observation here is that the gradients of both the meridional (Term 1) and azimuthal (Term 2) velocities in Eq. (5.13) affect the communication between the acoustics and the entropy. As stated earlier, owing to the high-frequency approximation of the WKB method and low flow Mach number assumption considered for the final solutions, the effect of the entropy perturbations on the acoustic field is neglected. Therefore the right hand side of Eq. (5.13) is assumed negligible, allowing Eqs. (5.12) and (5.13) to be written in the form,

$$A_2\hat{p} + B_2\frac{\mathrm{d}\hat{p}}{\mathrm{d}m} + C_2\hat{v}_m + \frac{\mathrm{d}\hat{v}_m}{\mathrm{d}m} + X_1\hat{v}_\theta = 0; \qquad D_2\hat{p} + E_2\frac{\mathrm{d}\hat{p}}{\mathrm{d}m} + F_2\hat{v}_m + \frac{\mathrm{d}\hat{v}_m}{\mathrm{d}m} + X_2\hat{v}_\theta \approx 0, \quad (5.16,\ 5.17)$$

where the coefficients $A_2, B_2, C_2, D_2, E_2, F_2, X_1$ and X_2 correspond to the coefficients of the perturbation terms in Eqs. (5.12) and (5.13) and read,

$$
\begin{aligned}
A_2 =& \frac{1}{\overline{\rho}\,\overline{c}}\left[\frac{\mathrm{i}\omega}{\overline{c}} + \beta\gamma M_m + \frac{\mathrm{i}n}{r}M_\theta + \gamma^2 M_m^3\left((\beta-\alpha) - \frac{M_\theta^2}{M_m^2}\Delta_r\right)\right],\ B_2 = \frac{M_m}{\overline{\rho}\,\overline{c}},\\
C_2 =& \left(\alpha - (\beta-\alpha)\,M_m^2 + M_\theta^2\Delta_r\right),\ D_2 = \frac{\mathrm{d}\overline{v}_m}{\mathrm{d}m}\frac{1}{\gamma\overline{p}},\ E_2 = \frac{1}{\overline{\rho}\,\overline{v}_m},\\
F_2 =& \left(\mathrm{i}\omega + \frac{\mathrm{d}\overline{v}_m}{\mathrm{d}m} + \frac{\mathrm{i}n}{r}\overline{v}_\theta\right)\frac{1}{\overline{v}_m},\ X_1 = \frac{\mathrm{i}n}{r},\ X_2 = -2\frac{M_\theta}{M_m}\Delta_r. \qquad (5.18\text{a - f})
\end{aligned}
$$

These coefficients are functions of the meridional coordinate m (axial and radial), meridional wave-number $k_o = \omega/\overline{c}$ and azimuthal mode number n. Note that the axially varying mean or fluctuating variables can be expressed as functions of the meridional coordinate (m) once the mapping $m = m(x,\, r)$ is obtained from the nozzle geometry profile.

Again, we use Eqs. (5.16) and (5.17) to eliminate $\mathrm{d}\hat{v}_m/\mathrm{d}m$, and express $\hat{v}_m$ in terms of $\hat{p}$, $\mathrm{d}\hat{p}/\mathrm{d}m$ and $\hat{v}_\theta$ as,

$$
\hat{v}_m = G_2\hat{p} + H_2\frac{\mathrm{d}\hat{p}}{\mathrm{d}m} + I_2\hat{v}_\theta; \quad \text{with } G_2 = \left(\frac{A_2 - D_2}{F_2 - C_2}\right),\ H_2 = \left(\frac{B_2 - E_2}{F_2 - C_2}\right) \text{ and } I_2 = \left(\frac{X_1 - X_2}{F_2 - C_2}\right). \qquad (5.19)
$$

Eq. (5.19) and its differential with respect to m then replace $\hat{v}_m$ and $\mathrm{d}\hat{v}_m/\mathrm{d}m$ in Eq. (5.16), leading to a second order differential equation (ODE) for $\hat{p}$:

$$
H_2\frac{\mathrm{d}^2\hat{p}}{\mathrm{d}m^2} + \left(G_2 + \frac{\mathrm{d}H_2}{\mathrm{d}m} + C_2H_2 + B_2\right)\frac{\mathrm{d}\hat{p}}{\mathrm{d}m} + \left(C_2G_2 + \frac{\mathrm{d}G_2}{\mathrm{d}m} + A_2\right)\hat{p} = -I_2\frac{\mathrm{d}\hat{v}_\theta}{\mathrm{d}m} - \overbrace{(C_2I_2 + \frac{\mathrm{d}I_2}{\mathrm{d}m} + X_1)}^{K_1}\hat{v}_\theta. \qquad (5.20)
$$

On using Eq. (5.14), and expressing $\hat{v}_\theta$ in terms of $\hat{p}$ and $\mathrm{d}\hat{v}_\theta/\mathrm{d}m$, we obtain,

$$
H_2\frac{\mathrm{d}^2\hat{p}}{\mathrm{d}m^2} + \left(G_2 + \frac{\mathrm{d}H_2}{\mathrm{d}m} + C_2H_2 + B_2\right)\frac{\mathrm{d}\hat{p}}{\mathrm{d}m} + \left(C_2G_2 + \frac{\mathrm{d}G_2}{\mathrm{d}m} + A_2 - \frac{J_2}{J_1}K_1\right)\hat{p} = \left(\frac{K_1}{J_1} - I\right)\frac{\mathrm{d}\hat{v}_\theta}{\mathrm{d}m}. \qquad (5.21)
$$

with $J_1 = \dfrac{1}{\overline{v}_m}\left(\mathrm{i}\omega + \dfrac{\mathrm{i}n}{r}\overline{v}_\theta + \overline{v}_m\Delta_r\right)$, $J_2 = \dfrac{\mathrm{i}n}{\overline{\rho}r}$.

Using Eqs. (5.8) - (5.11), any mean flow gradient terms in the coefficients of the second order differential equation (Eq. (5.21)) are expressed in terms of α, β, M_m, M_θ and r. Again using the definitions of $\delta \sim \dfrac{\mathrm{O}(\alpha)}{k_o}$ or $\dfrac{\mathrm{O}(\beta)}{k_o}$ or $\dfrac{\mathrm{O}(\Delta_r)}{k_o}$ and the ratio $\kappa_\alpha = \dfrac{1}{\alpha^2}\dfrac{\mathrm{d}\alpha}{\mathrm{d}m}, \kappa_\beta = \dfrac{1}{\beta^2}\dfrac{\mathrm{d}\beta}{\mathrm{d}m} \sim \mathrm{O}(1)$

and retaining only terms up to order $\mathrm{O}(\delta^2)$, $\mathrm{O}(M^2,\, M_\theta^2)$, the ODE takes the following form:

$$
\begin{aligned}
&\left[(1-\mu M_\theta)^2 - M_m^2 - (\beta - 2\alpha)\,\frac{M_m}{\mathrm{i}k_o}\,(1-2\mu M_\theta)\right]\frac{\mathrm{d}^2\hat{p}}{\mathrm{d}m^2}\frac{1}{k_o^2} \\
&-\left[2\mathrm{i}M_m - \frac{\alpha+\beta}{k_o}\,(1-\mu M_\theta)^2 + \frac{\alpha\,(1+\gamma)+\beta}{k_o}M_m^2 - M_\theta\frac{\Delta_r}{k_o}\,(2\mu + M_\theta) + \frac{2\mu^2 M_\theta^2}{r k_o}\,(1+r\Delta_r)\right. \\
&\left.-\frac{M_m}{\mathrm{i}k_o^2}\left(2\alpha\beta\,(2+\mu M_\theta) - 2\beta^2 - 4\alpha^2\mu M_\theta - \left(\frac{\mathrm{d}\beta}{\mathrm{d}m} - 2\frac{\mathrm{d}\alpha}{\mathrm{d}m}\right)(1-2\mu M_\theta)\right)\right]\frac{\mathrm{d}\hat{p}}{\mathrm{d}m}\frac{1}{k_o} \\
&+\left[1-\mu^2\left(1-\mu M_\theta + \frac{M_m}{\mathrm{i}k_o}\,(\beta - 2\Delta_r)\right) - \frac{\mathrm{i}\beta M_m\,(1+\gamma)}{k_o} - \frac{2\mu M_\theta}{k_o^2}\Delta_r\left(\alpha - 2\Delta_r + \frac{\cot\phi}{R_c}\right)\right]\hat{p} \\
&= \cancelto{0}{\overbrace{\frac{\overline{\rho c}}{k_o^2}\left[-\mu M_m^2\,(2\,(\beta-\alpha) - \Delta_r) - 2M_\theta\Delta_r\,(1+\mu M_\theta)\right]}^{\textbf{Terms higher than order} \sim \mathbf{O}(\delta^2)}}\,\frac{\mathrm{d}\hat{v}_\theta}{\mathrm{d}m},
\end{aligned}
\tag{5.22}
$$

where, $\mu = n/k_o r$ is the ratio of azimuthal wave-number (n/r) to the meridional wave-number (k_o) and R_c is the local radius of curvature of the duct. In the above equation, the azimuthal wave-number is assumed to be less than the meridional wave-number, $n/r < k_o$, and terms of order $\mathrm{O}(\mu^3)$ and higher are hence neglected.

As indicated by the crossed out arrow, the coefficient of $\mathrm{d}\hat{v}_\theta/\mathrm{d}m$ in Eq. (5.22) is neglected owing to its multiplication factor $1/k_o^2$. Eq. (5.22) then takes the form of a homogeneous second order ordinary differential equation (ODE), this governing the acoustic field in an annular nozzle with arbitrary meridional temperature gradient predominantly due to heat transfer and mean flow (the latter with both meridional and azimuthal components). The main assumptions underpinning it are: (*i*) the narrow annular gap assumption that the acoustic field is two-dimensional, (*ii*) $|\delta| \ll 1$ and $\kappa \sim \mathrm{O}(1)$, (*iii*) constant gas properties γ, R_g, (*iv*) negligible effect of the entropy disturbance on the acoustic field, (*v*) low Mach number flow such that terms of $\mathrm{O}(\delta^2 M^2)$, $\mathrm{O}(M^3)$, $\mathrm{O}(M_\theta^3)$ and higher are negligible, (*vi*) azimuthal wave-number is less than meridional wave-number such that terms of order $\mathrm{O}(\mu^3)$ and higher are negligible.

The ODE in Eq. (5.22) is consistent with our previous derivation for plane waves (Eq. (2.21)) when the two-dimensional effects on both the mean flow and acoustic field are negligible, i.e., $\mu = 0$, $M_\theta = 0$, $m \equiv x$.

5.2.1 Semi-analytical solution using the iterative WKB method

The iterative WKB method is now applied to solve the ODE in Eq. (5.22) by expressing the two-dimensional pressure perturbation as,

$$\hat{p}\left(m,\omega,n\right) = I \exp \int_{m_1}^{m} \left(a^{\pm}\left(\breve{m}\right) + \mathrm{i} b^{\pm}\left(\breve{m}\right)\right) \mathrm{d}\breve{m}, \tag{5.23}$$

with $\breve{m}$ as a dummy variable, and m_1 corresponding to the nozzle inlet shown in Fig. 5.1. The positive (+) and negative (-) signs correspond to the downstream and the upstream propagating wave amplitudes, respectively. The two real variables, a and b, for the first iteration take the values $a_1 \approx \mathrm{O}(\alpha,\ \beta)$ while $b_1 \approx \mathrm{O}(k_o)$ [88, 93]. The wave-number is assumed to be real, and the imaginary part is neglected. For the test-case considered in Fig. 5.2 (right), it is later shown in Section 5.3.2 that the fundamental mode's imaginary part is less than 1% of its real counterpart, justifying this assumption. The mathematical analysis (presented in Appendix C) also shows that assuming ω to be either real or complex for the WKB analysis resulted in a difference of less than 0.01% for the modal solution estimates of the annular nozzle test-case in Fig. 5.2 (Right).

On substituting Eq. (5.23) into Eq. (5.22) and equating the real part to zero, a quadratic equation for b is obtained,

$$-b^2\left[\left(1-\mu M_\theta\right)^2 - M_m^2\right] + 2k_o M_m b + k_o^2\left[1-\mu^2\left(1-\mu M_\theta\right)\right] + \mathrm{O}(\delta^2) \approx 0. \tag{5.24}$$

Solutions for Eq. (5.24) yield improved estimates for b:

$$\frac{b^{\pm}}{k_o} = \frac{M_m \mp \lambda}{\left(1-\mu M_\theta\right)^2 - M_m^2}, \quad \text{where } \lambda = \sqrt{\left(1-\mu M_\theta\right)^2 - \mu^2\left(1-M_m^2\right)}. \tag{5.25}$$

Similarly, on equating the imaginary part to zero and neglecting terms of order $\mathrm{O}\left(\delta^3\right)$, $\mathrm{O}\left(\delta^3 M\right)$ and higher relative to the leading term of order $\mathrm{O}(\delta)$, an updated result for $a^{\pm}$ is obtained,

$$\begin{aligned} a^{\pm} = -\frac{\alpha}{2} - \frac{\beta}{4} - \frac{1}{2\lambda}\frac{d\lambda}{\mathrm{d}m} &+ \overbrace{\left[\frac{\alpha\gamma M_m^2}{2} \pm \frac{\mu^2 M_m}{2\lambda}\left(\beta - \Delta_r\right) + \frac{\mu^2 M_\theta^2}{r} - \frac{\Delta_r M_\theta^2}{2} \pm \frac{3\Delta_r \mu M_m M_\theta}{\lambda}\right]}^{\textbf{Terms 1}} \\ &+ \overbrace{\left[\left(\frac{\beta}{2} - \alpha\right)\left(M_m^2 \mp \lambda M_m\left(1+2\mu M_\theta\right)\right) - \Delta_r \mu M_\theta\left(3+2\mu M_\theta\right) \mp \frac{\beta\gamma M_m}{2\lambda}\right]}^{\textbf{Terms 2}}. \end{aligned} \tag{5.26}$$

Using the definition of acoustic pressure given by Eq. (5.23) along with the final expressions for $a^{\pm}$, $b^{\pm}$, the principle of superposition allows the overall solution for the acoustic pressure to be expressed as,

$$\hat{p}\left(m,\omega,n\right)=\mathcal{C}^{+}\mathcal{P}^{+}\left(m,\omega,n\right)+\mathcal{C}^{-}\mathcal{P}^{-}\left(m,\omega,n\right), \tag{5.27}$$

with $\mathcal{C}^{+}$ and $\mathcal{C}^{-}$ being constants that are determined using boundary conditions and,

$$\begin{aligned}\mathcal{P}^{\pm}=\left(\frac{A_{f,1}}{A_f}\right)^{1/2}\left(\frac{\overline{T}_1}{\overline{T}}\right)^{1/4}\left(\frac{\lambda_1}{\lambda}\right)^{1/2}&\exp\left(\int_{m_1}^{m}\left[\textbf{sum of Terms 1 \& 2}\text{ in Eq. (5.26)}\right]\mathrm{d}\breve{m}\right)\\ &\times\exp\left(\int_{m_1}^{m}\mathrm{i}k_o\left(\frac{M_m\mp\lambda}{\left(1-\mu M_\theta\right)^2-M_m^2}\right)\mathrm{d}\breve{m}\right),\end{aligned} \tag{5.28}$$

where subscript 1 denotes the values at the inlet and $\breve{m}$ is again a dummy variable. The explicit dependence of the acoustic field solution on the area, mean temperature profile and meridional and azimuthal mean flow components can be observed in Eq. (5.28). The amplitude part of the wave-like solution in $\mathcal{P}^{\pm}$, given by Eq. (5.28), contains Terms 1 and 2 from Eq. (5.26) under the integral sign. This implies the final solution requires numerical integration, and at any location m, it depends on the mean flow properties upstream. Hence this general solution, applicable to arbitrary area and temperature profiles, is considered to be semi-analytical.

The meridional velocity perturbation, $\hat{v}_m$, is determined from Eq. (5.19) and can be written as,

$$\hat{v}_m\left(m,\omega,n\right)=\frac{1}{S}\left[\frac{1}{\overline{\rho}\,\overline{c}\mathrm{i}k_o}\left(\mathcal{B}^{+}\mathcal{C}^{+}\mathcal{P}^{+}-\mathcal{B}^{-}\mathcal{C}^{-}\mathcal{P}^{-}\right)+\frac{M_m}{\mathrm{i}k_o}\left(X_1-X_2\right)\hat{v}_\theta\right], \tag{5.29}$$

where $S=1+\mu M_\theta+\left(\beta-2\alpha\right)M_m/\mathrm{i}k_o$, and,

$$\begin{aligned}\mathcal{B}^{\pm}=&\pm\frac{\alpha}{2}\pm\frac{\beta}{4}\pm\frac{1}{2\lambda}\frac{\mathrm{d}\lambda}{\mathrm{d}m}\left(1-M_m^2\right)+\mathrm{i}k_o\lambda\left(1+2\mu M_\theta+3\mu^2M_\theta^2\right)\mp\mathrm{i}k_o\mu M_mM_\theta\\ &\pm\mu M_\theta\Delta_r\left(3+2\mu M_\theta\right)+M_m\left(\frac{\beta}{2\lambda}\left(\gamma+\lambda^2\right)-\alpha\lambda\right)-\frac{\mu^2M_m\left(\beta-\Delta_r\right)}{2\lambda}\pm\frac{\beta M_m^2}{4}\left(2\gamma-7\right)\\ &\pm\frac{\alpha M_m^2\left(3-\gamma\right)}{2}\mp\frac{\mu^2M_\theta^2}{r}\left(1-r\Delta_r\right)\pm\frac{\Delta_rM_\theta^2}{2}+2\lambda\mu M_mM_\theta\left(\frac{\beta}{2}-\alpha\right)-\frac{3\Delta_r\mu M_mM_\theta}{\lambda}.\end{aligned} \tag{5.30}$$

The azimuthal velocity perturbation solution $\hat{v}_\theta$ in Eq. (5.29), for a given $\hat{v}_{\theta,1}$ at the inlet, is obtained from the solution of the non-homogeneous first order differential equation given by Eq. (5.14), and reads,

$$\hat{v}_\theta=\frac{\hat{v}_{\theta,1}+\displaystyle\int_{m_1}^{m}\frac{-\hat{p}}{\overline{\rho}\,\overline{v}_m}\frac{\mathrm{i}n}{r}\left[\exp\left(\int_{m_1}^{m}\left(\frac{\mathrm{i}\omega}{\overline{v}_m}+\frac{M_\theta}{M_m}\frac{\mathrm{i}n}{r}-\Delta_r\right)\mathrm{d}\breve{m}\right)\right]\mathrm{d}\tilde{m}}{\exp\left(\displaystyle\int_{m_1}^{m}\left(\frac{\mathrm{i}\omega}{\overline{v}_m}+\frac{M_\theta}{M_m}\frac{\mathrm{i}n}{r}+\Delta_r\right)\mathrm{d}\breve{m}\right)}, \tag{5.31}$$

with $\breve{m}$ and $\tilde{m}$ as dummy variables.

5.2.2 Frequency range of validity for semi-analytical solution

- **Cut-on frequency limit:** The presence of non-decaying waves in the circumferential direction requires the frequency to be larger than the cut-on frequency of the necessary azimuthal mode sustained in the duct. Evanescent waves in the azimuthal direction occur for any frequency lower than this. The azimuthal cut-on frequency limit is obtained by finding the frequency for which the determinant of the quadratic equation (Eq. (5.24)) becomes greater than zero. This condition is expressed in terms of Helmholtz number at the inlet, He_1, thus requiring $\mathrm{He}_1 > \mathrm{He}_{1,\,c}$, where,

$$\mathrm{He}_{1,\,c} = \mathbf{max}\left[\frac{nl}{r}\frac{\bar{c}}{\bar{c}_1}\left(M_\theta + \sqrt{1-M_m^2}\right)\right] \tag{5.32}$$

  and the "max" function gives the maximum limiting value at any location for the term inside the square braces. A frequency above this limit is required to ensure the azimuthal mode is cut-on inside the annular nozzle.

- **Lower frequency limit:** The analytical solution derived using the WKB method assumes high frequency. Based on the terms neglected in deriving the final solution of the acoustic variables, Eqs. (5.27) - (5.31) can be used to obtain an expression for the frequency above which the WKB solution guarantees accurate results, given in terms of Helmholtz number, $\mathrm{He} = \omega l/\bar{c}$. The lower frequency limit for the analytical solution will then be given by either this or the azimuthal mode cut-on limit in Eq. (5.32):

$$\mathrm{He}_{lower} = \mathbf{max}\left[\mathrm{He}_{1,\,c},\, \frac{l\bar{c}}{\bar{c}_1}\sqrt{\delta^2 + \delta^2 M_m}\right], \quad \text{where} \quad \delta = \mathbf{max}\left[\frac{|\alpha|}{k_o}, \frac{|\beta|}{k_o}\right]. \tag{5.33}$$

  Except for the fundamental plane wave mode, the lower frequency limit is generally governed by the azimuthal cut-on limit. For example, for the test-case considered in Fig. 5.2 (Left), the WKB limit given by the second term in the bracket of Eq. (5.33) requires $\mathrm{He}_1/(2\pi) > 0.224$, which is satisfied by all azimuthal modes beyond the fundamental plane wave mode for which $n = 0$.

- **Upper frequency limit:** The WKB solution in this chapter is valid for systems where the higher-order acoustic radial modes are cut-off, which sets an upper limit on the frequency that can be considered. The frequency at which the radial modes are cut-on depends on the radial gap, and is given [125] as,

$$\mathrm{He}_{upper} = \mathbf{min}\left[\frac{\pi l}{(r_o - r_i)}\frac{\bar{c}}{\bar{c}_1}\sqrt{1-M_m^2}\right], \tag{5.34}$$

  where, r_o and r_i correspond to the outer and inner radii of the annular nozzle respectively. It is assumed that the source of acoustic waves is far upstream, as shown in Fig. 5.1, and any evanescent radial modes fully decay before they reach the nozzle inlet at m_1.

To summarise, Eqs. (5.27) - (5.31) estimate the two-dimensional acoustic field in an annular nozzle with both meridional (or axial) and azimuthal mean flows, sustaining any meridional (or axial) temperature gradient due to heat exchange with the surroundings. These, along with the linearised Euler equations Eqs. (5.12) - (5.15) are important results of this work. It should be noted that the variations in the meridional direction can always be mathematically expressed in terms of axial variations once the mapping function $m = m(x,\, r)$ is known from the nozzle geometry. Beyond the assumptions stated in the derivation of the governing ODE for acoustic pressure, (i) terms of order $\mathrm{O}(\delta^2)$ and higher are further neglected, (ii) the imaginary part of wave-number (k_o) is assumed very small compared to the real part, and (iii) the considered frequency and azimuthal mode requires to satisfy both the lower and upper frequency limits set by Eqs. (5.33) and (5.34), respectively.

5.3 Validation

The WKB method based semi-analytical model described in Section 5.2 can be applied to any annular nozzle area variation, temperature profile, low subsonic mean flow and azimuthal mode number, as long as the perturbation frequency conforms to the limits presented in Section 5.2.2. For validation, the model is initially applied to an annular nozzle whose shape varies axially as a quarter sinusoid, as shown in Fig. 5.2, with the outer, r_o, and inner, r_i, radii prescribed by,

$$\begin{aligned}
\frac{r_{o,\,x}^2}{r_{o,\,2}^2} &= \frac{1}{2}\left(\frac{r_{o,\,1}^2}{r_{o,\,2}^2} - 1\right)\left[\cos\left(\pi\frac{x - x_1}{x_2 - x_1}\right) + 1\right] + 1, \text{ with } \pi r_{o,\,1}^2 = 3\mathrm{m}^2 \text{ and } \pi r_{o,\,2}^2 = 1\mathrm{m}^2; \\
\frac{r_{i,\,x}^2}{r_{i,\,2}^2} &= \frac{1}{2}\left(\frac{r_{i,\,1}^2}{r_{i,\,2}^2} - 1\right)\left[\cos\left(\pi\frac{x - x_1}{x_2 - x_1}\right) + 1\right] + 1, \text{ with } \pi r_{i,\,1}^2 = 2.5\mathrm{m}^2 \text{ and } \pi r_{o,\,2}^2 = 0.8\mathrm{m}^2;
\end{aligned} \tag{5.35}$$

and subscripts 1 and 2 represent the inlet and outlet planes respectively (shown in Fig. 5.1). A linear axial temperature gradient, varying from 1600K at the inlet to 800K at the outlet is considered. The inlet acoustic impedance $Z_1 = \dfrac{\hat{p}}{\bar{\rho}_1 \bar{c}_1 \hat{v}_{m,\,1}}$ is assumed to be equal to -1. Other mean flow and geometrical parameters, along with the frequency limits defined in Section 5.2.2, are presented in Fig. 5.2 (Left).

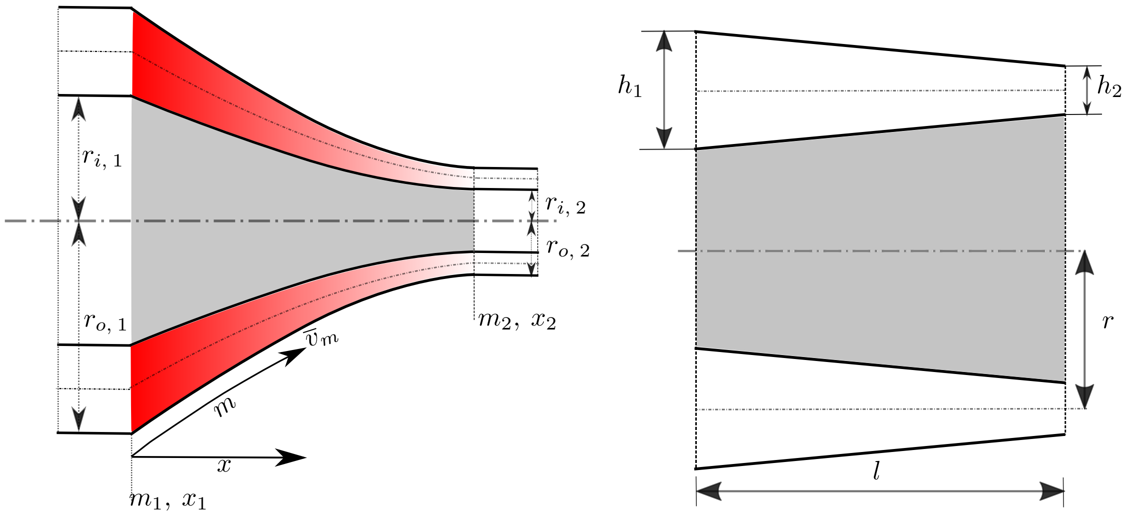

Mean flow	Inlet	Outlet
$M_m = \dfrac{\overline{v}_m}{\overline{c}}$	0.2	0.236
$\overline{T}$	1600K	800K
M_θ	0.012	0.03
Frequency limits	He/ (2π)	f
Lower limit for n = 0	0.224	168Hz
Lower limit for n = 2	1.02	766Hz
Upper limit	9.8	7363Hz

Mean flow	Inlet	Outlet
$M_m = \dfrac{\overline{v}_m}{\overline{c}}$	0.03	0.06
$\overline{T}$	1600K	1598K
M_θ	0	0
Frequency limits	He/ (2π)	f
Lower limit for n = 0	0.16	120Hz
Lower limit for n = 2	0.91	684Hz
Upper limit	5	3756Hz

Figure 5.2: (Left) Schematic of the first annular nozzle used for validation. It has length $l = 1$m and its shape varies axially as a quarter sinusoid, with the corresponding inlet and outlet radii given in Eq. (5.35). The nozzle sustains a non-isentropic mean flow whose parameters, along with the calculated frequency limits, are shown in the table. (Right) Schematic of the second annular nozzle used for validation. It has a conical shape with constant mean radius ($l = 0.5$m, $h_1 = 0.05$m, $h_2 = 0.025$m, $r = 0.175$m). It sustains an isentropic mean flow whose parameters, along with the calculated frequency limits are shown in the table. (For both the cases, the lower frequency limit, He_{lower}, is given by Eq. (5.33), while the upper frequency limit, He_{upper}, is given by Eq. (5.34)).

The semi-analytical model solutions obtained using Eqs. (5.27) - (5.31), are compared with the numerical solutions of the linearised Euler equations, Eqs. (5.12) - (5.15), assuming negligible effect of the entropy disturbance on the acoustic field. Dowling's [134] approach of a semi-infinite boundary is considered in the meridional direction, facilitating validation over a wide range of frequencies and azimuthal mode numbers. For a particular frequency and azimuthal mode number, the resulting initial value problem of the LEEs is solved using a fourth order Runge-Kutta method by discretising the duct into 1000 equal domains (N) of 1mm each.

The definitions of the transfer functions for the acoustic pressure, meridional velocity and the error function (calculated as an L^2 norm) remain as defined in Chapter 1 (Eqs. (2.62), (2.63) and (2.64)).

5.3.1 Results

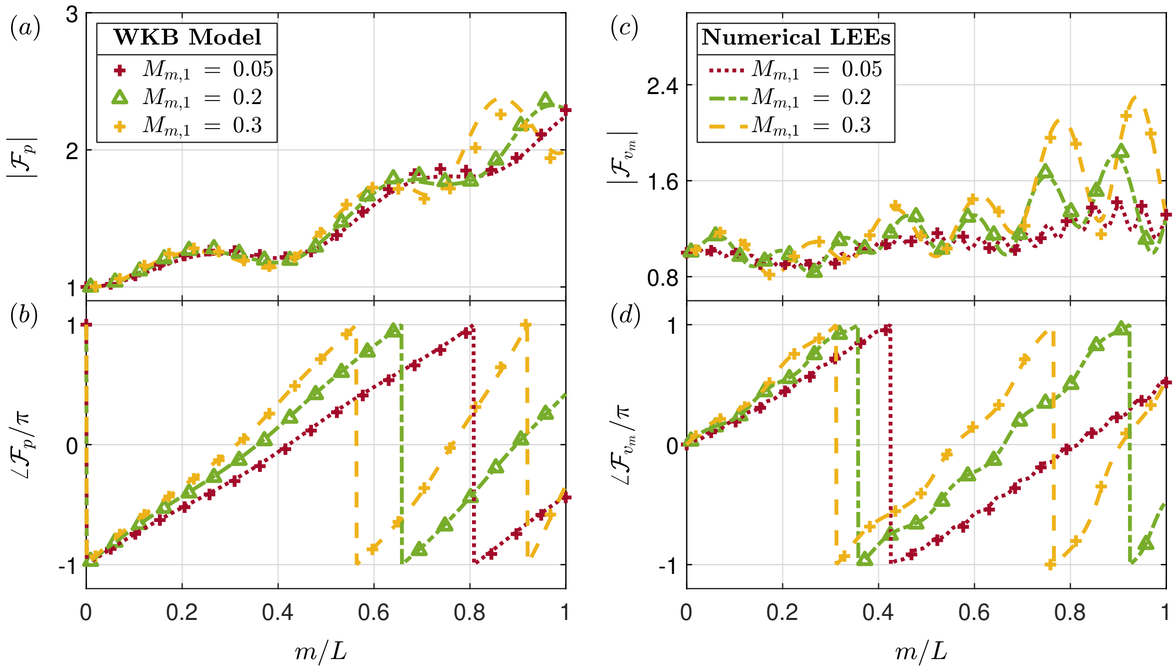

Figure 5.3: Evolution of F_p and F_{v_m} with meridional coordinate, m. $\overline{T}_1 = 1600$ K, $\overline{T}_2 = 800$ K; $M_{m,1} = 0.05,\ 0.2\ \&\ 0.3$, $M_{m,2} = 0.09\ \&\ 0.36\ \&\ 0.56$; $\overline{v}_{\theta,1} = 10\text{ms}^{-1}$; $\hat{v}_{\theta,1} = 1\text{ms}^{-1}$; $\text{He}_1/(2\pi) = 1.2$, n = 1 and Z_1 = -1. (a): transfer function gain $|F_p|$. (b): transfer function phase $\angle F_p$. (c): transfer function gain $|F_{v_m}|$. (d): transfer function phase $\angle F_{v_m}$.

The quarter sinusoidal shaped nozzle in Fig. 5.2 (Left) is initially considered across three different meridional inlet flow Mach numbers and three azimuthal mode numbers. The considered frequency of $\text{He}_1/(2\pi) = 1.2$, satisfies both the lower and upper frequency limits set by Eqs. (5.33) and (5.34) for the considered azimuthal mode numbers.

- **Low subsonic flow Mach numbers:** Figure 5.3 compares the semi-analytical model and numerical LEEs solutions for the acoustic pressure and velocity for different meridional flow Mach numbers and an azimuthal mode number of $n = 1$. For the case of low flow Mach numbers ($M_{m,1} = 0.05$ and 0.2 at the inlet, and $M_{m,2} = 0.09$ and 0.36 at the outlet), in the presence of a strong axial temperature gradient 800Km^{-1}, the model predictions closely match with the numerical solutions. Also the model prediction for azimuthal velocity perturbation $\hat{v}_\theta$, shown in Fig. 5.4 (a) and (b) for an inlet flow Mach number of $M_{m,1} = 0.05$ and $\hat{v}_{\theta,1} = 1$ ms^{-1}, is accurate.

- **High subsonic flow Mach numbers:** Figures 5.3, 5.4 (c) and (d), compare model and numerical predictions for the case where the inlet meridional Mach number is 0.3 (and the corresponding outlet meridional Mach number 0.56, with the maximum flow Mach number inside the nozzle being 0.6). As the derivation of the semi-analytical model assumes low flow Mach numbers, a deviation is observed in the model solutions for this higher flow Mach number case. However, the model error ϵ (using Eq. (2.64)) was observed to be less than 7% for both acoustic pressure and velocity ($\epsilon_p = 0.07$ and $\epsilon_{v_m} = 0.063$). Similarly, the error for the azimuthal velocity perturbation (Fig. 5.4 (c) and (d)) estimate was observed to be less than 8% ($\epsilon_{v_\theta} = 0.076$), compared to the numerical solution. Although a separate first-order ODE is solved for $\hat{v}_\theta$, the error is manifested from using the acoustic pressure ($\hat{p}$) solution given by Eq. (5.27) in the estimation of $\hat{v}_\theta$ (Eq. (5.31)). Hence the errors are of the same order.

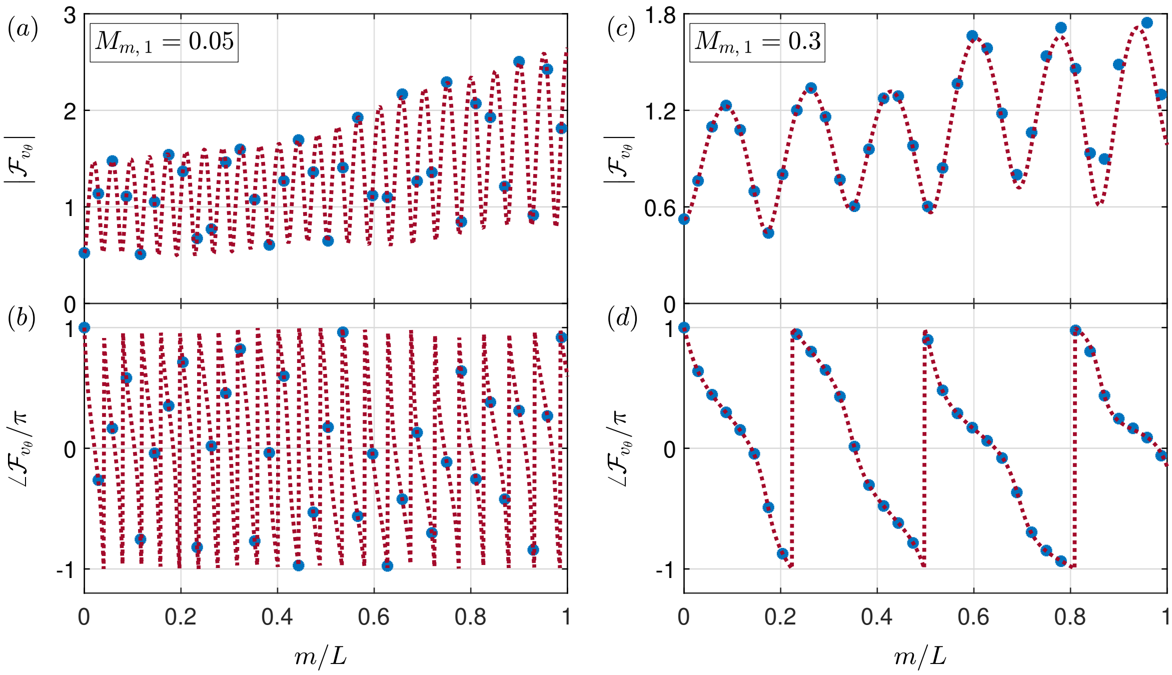

Figure 5.4: Evolution of F_{v_θ} with meridional coordinate, m. Numerical LEEs (lines) and WKB model (markers). $\overline{T}_1 = 1600$ K, $\overline{T}_2 = 800$ K; $\overline{v}_{\theta,1} = 10\text{ms}^{-1}$; $\hat{v}_{\theta,1} = 1\text{ms}^{-1}$; $\text{He}_1/(2\pi) = 1.2$, and $n = 1$. (Left) $M_{m,1} = 0.05$, $M_{m,2} = 0.09$, (a): transfer function gain $|F_{v_\theta}|$, (b): transfer function phase $\angle F_{v_\theta}$. (Right) $M_{m,1} = 0.3$, $M_{m,2} = 0.56$, (c): transfer function gain $|F_{v_\theta}|$, (d): transfer function phase $\angle F_{v_\theta}$.

- **Effect of the azimuthal mode number:** The semi-analytical model is applied to the quarter sinusoid shaped nozzle (Fig. 5.2 (Left)) for three different azimuthal mode numbers $n = 0$, 1 and 2, all for the same mean flow and meridional wave-number ($\text{He}_1/(2\pi) = 1.2$). As shown in Fig. 5.5, the model predictions are accurate for all three mode numbers, n. The increased effect of the higher order circumferential modes

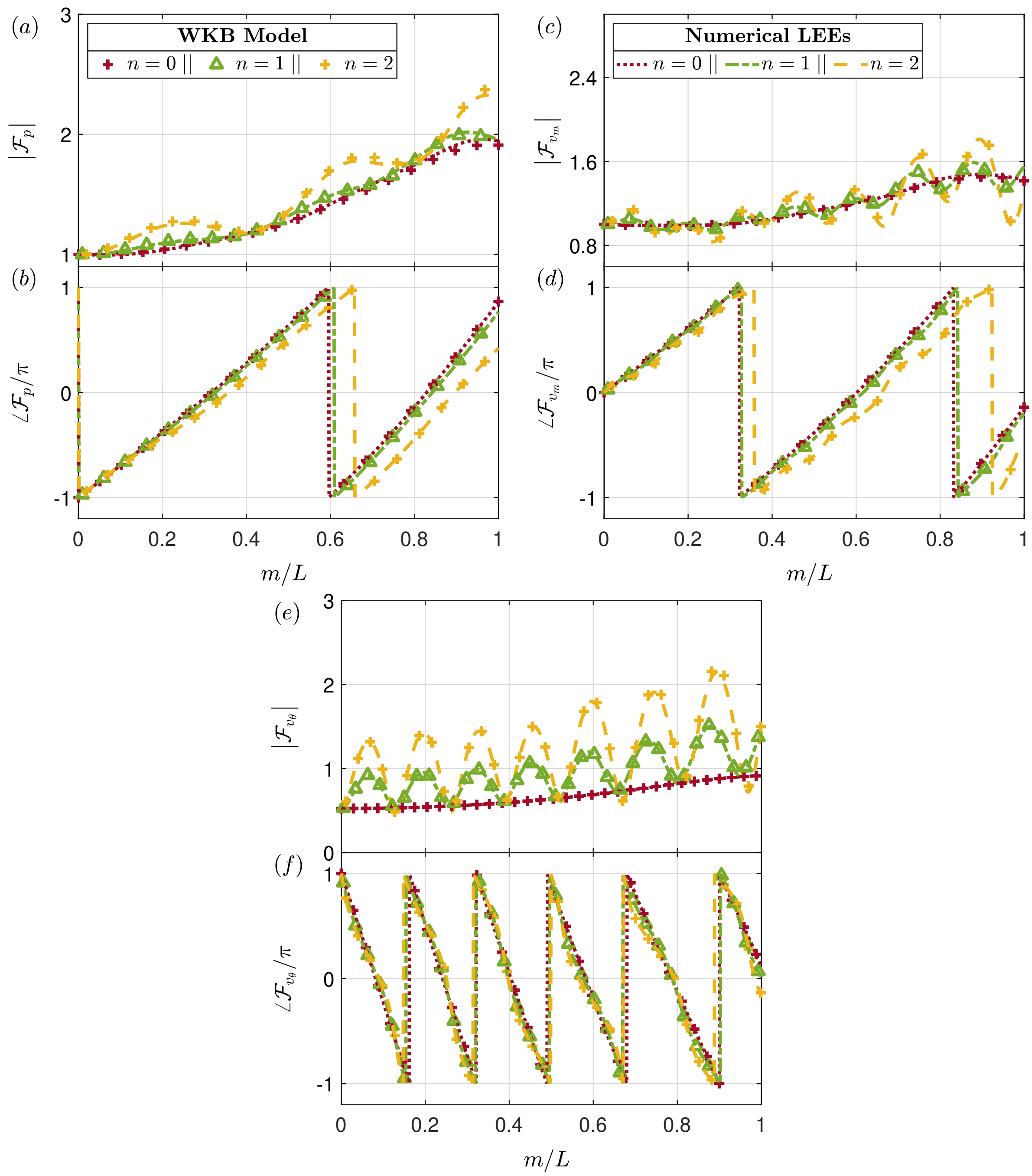

Figure 5.5: Evolution of F_p, F_{v_m}, and F_{v_θ} with m for n = 0, 1, and 2. $\mathrm{He}_1/(2\pi) = 1.2$; $\overline{T}_1 = 1600$ K, $\overline{T}_2 = 800$ K; $M_{m,1} = 0.2$, $M_{m,2} = 0.36$; $\overline{v}_{\theta,1} = 10\mathrm{ms}^{-1}$ and $\hat{v}_{\theta,1} = 1\mathrm{ms}^{-1}$. (a): transfer function gain $|F_p|$, (b): transfer function phase $\angle F_p$. (c): transfer function gain $|F_{v_m}|$, (d): transfer function phase $\angle F_{v_m}$, (e): transfer function gain $|F_{v_\theta}|$, (b): transfer function phase $\angle F_{v_\theta}$.

(n = 1, 2) on the meridional acoustic field is apparent from Fig. 5.5.

- **Effect of flow Mach number:** The semi-analytical model's applicability limits further demonstrated in Fig. 5.6 for $n = 0$ and Fig. 5.7 for $n = 2$ using contour plots for the error calculated using Eq. (2.64). The dotted (······) and the chain (-··-) lines correspond to the lower and upper frequency limits Eqs. (5.33) and (5.34) respectively. Thus, the intermediate region between the lines represents the regimes where the model is applicable. The acoustic pressure and velocity errors illustrate that the model can be employed over a wide range of flow Mach numbers and frequencies while keeping the error below 10% (enveloped by the blue contour). The model applicability limits are slightly wider for the case with no azimuthal modes ($n = 0$), given in Fig. 5.7, but low frequency performance is limited by the high frequency requirements of the WKB method.

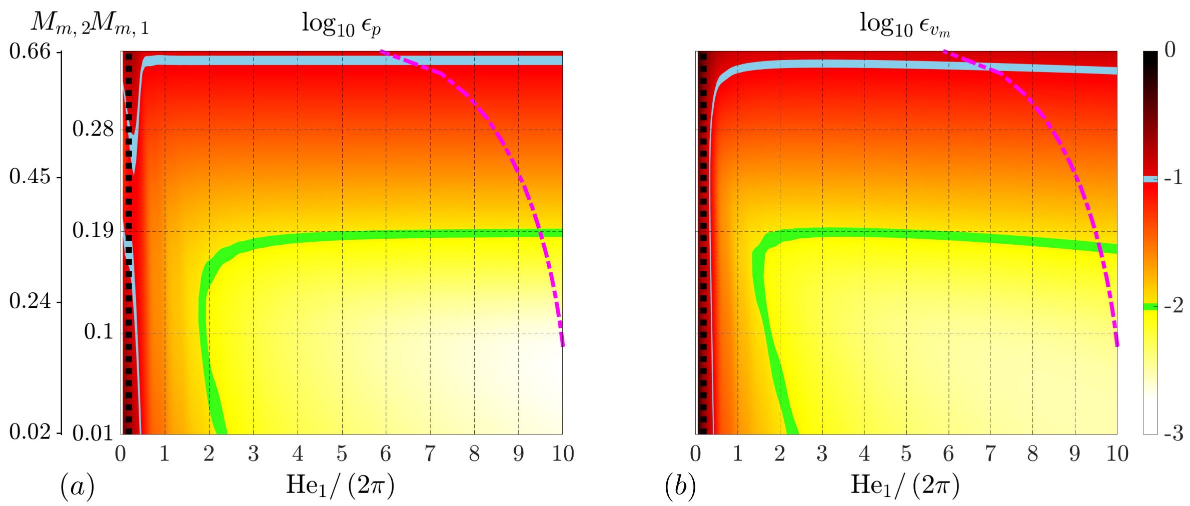

Figure 5.6: Contour maps of (a) ϵ_p and (b) ϵ_{v_m} as functions of He_1 and $M_{m,1}$, for nozzle with shape varying axially as a quarter sinusoid, $n = 0$, $\overline{v}_\theta = 10\mathrm{ms}^{-1}$, $\overline{T}_1 = 1600$ K, $\overline{T}_2 = 800$ K, and $\hat{v}_{\theta,1} = 1\mathrm{ms}^{-1}$. The (······) and (-··-) lines represents the lower and upper frequency limits given by Eqs. (5.33) and (5.34) respectively.

5.3.2 Application of the WKB model for modal stability analysis

To assess whether the developed semi-analytical model can be used to predict the acoustic modes (or, for geometries supporting unsteady heat release rate, thermoacoustic modes) of a system, the acoustic modes are predicted for the simpler test case on the right of Fig. 5.2, allowing validation against the in-house 2-D low-order network solver, OSCILOS$_{\mathrm{ann}}$ [52]. The mean flow is assumed to be along the axial direction and isentropic, with no azimuthal flow ($\overline{v}_\theta = 0$ and $\hat{v}_{\theta,1} = 0\ \mathrm{ms}^{-1}$). The eigenmodes of this conical shaped annular nozzle are predicted using the semi-analytical model. Two different azimuthal mode numbers of $n = 0$ and $n = 2$ are considered with the nozzle inlet and outlet flow Mach numbers as 0.03 and 0.06, respectively. OSCILOS$_{ann}$ is able to deal with a network of annular geometries, each with a fixed flow cross-

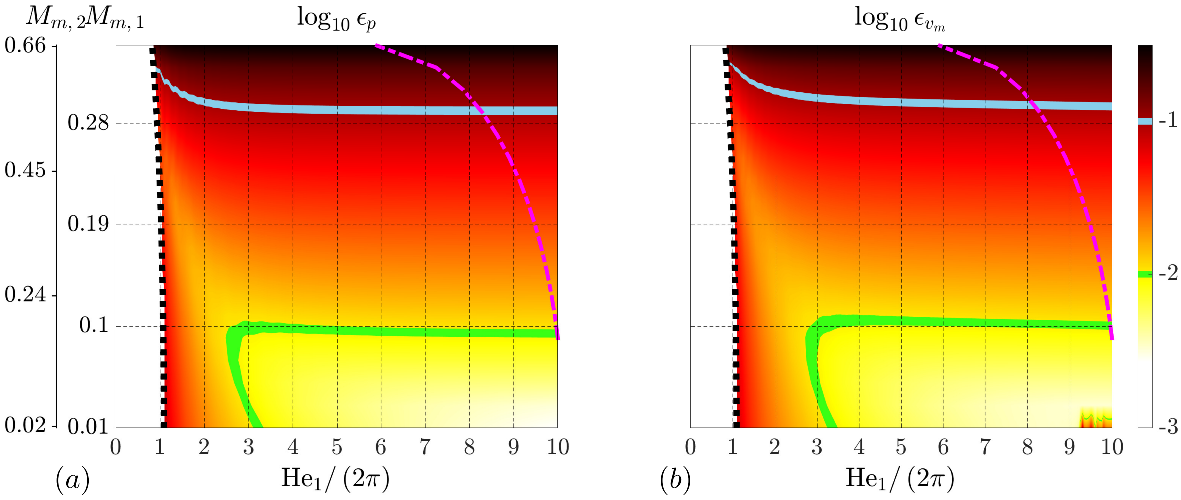

Figure 5.7: Contour maps of (a) ϵ_p and (b) ϵ_{v_m} as functions of He_1 and $M_{m,1}$, for nozzle with shape varying axially as a quarter sinusoid, $n = 2$, $\overline{v}_\theta = 1\mathrm{ms}^{-1}$, $\overline{T}_1 = 1600$ K, $\overline{T}_2 = 800$ K, and $\hat{v}_{\theta,1} = 1\mathrm{ms}^{-1}$. The (⋯⋯) and (-·-·-) lines represents the lower and upper frequency limits given by Eqs. (5.33) and (5.34) respectively.

sectional area. The axially-conical geometry is therefore segmented into 50 segments along its 0.5m length. Convergence with the number of segments was checked, giving an error of $< 0.01\%$ for the frequency and $< 0.7\%$ for the growth rate. Simple boundary conditions - an open-end condition for both nozzle inlet ($\hat{p}_1 = 0$) and outlet ($\hat{p}_2 = 0$) - are used. The dispersion relation in terms of the semi-analytical model solution can then be written as,

$$\text{Determinant} = \begin{vmatrix} 1 & 1 \\ \mathcal{P}^+(L,\omega,n) & \mathcal{P}^-(L,\omega,n) \end{vmatrix} = 0 \quad \Rightarrow \mathcal{P}^-(L,\omega,n) - \mathcal{P}^+(L,\omega,n) = 0 \qquad (5.36)$$

Table 5.2: Comparison of modal frequencies, growth rates obtained from the semi-analytical model and $\mathrm{OSCILOS_{ann}}$ for the annular nozzle with isentropic axial mean flow, shown in Fig. 5.2 (Right). **Left table -** for azimuthal mode number $n = 0$. **Right table -** for azimuthal mode number $n = 2$.

$n = 0$, $M_{m,1} = 0.03$, $M_{m,2} = 0.06$			
OSCILOS_ann		**WKB Model**	
f **[Hz]**	ω_I **[rad s^{-1}]**	f **[Hz]**	ω_I **[rad s^{-1}]**
745.51	-46.19	749.90	-44.20
1497.62	-45.39	1499.90	-44.20
2248.38	-45.22	2249.90	-44.20
2998.75	-45.17	2999.90	-44.20
3748.98	-45.14	3749.90	-44.20

$n = 2$, $M_{m,1} = 0.03$, $M_{m,2} = 0.06$			
OSCILOS_ann		**WKB Model**	
f **in [Hz]**	ω_I **[rad s^{-1}]**	f **in [Hz]**	ω_I **[rad s^{-1}]**
1555.71	-10.66	1557.70	-10.25
2026.60	-24.81	2028.30	-24.17
2630.47	-33.05	2631.80	-32.30
3294.94	-37.42	3296	-36.61
3989.86	-39.86	3990.70	-39.02

The modal predictions are shown in Table 5.2 for the two azimuthal wavenumbers. It can be seen that the modes are accurately predicted using the semi-analytical model (Eq. (5.36)) with minor errors, $< 0.5\%$ for the frequency and $< 2\%$ for the growth rate. This confirms that the semi-analytical solution for the annular nozzle can also be readily applied to calculate acoustic modes. Hence it could be incorporated in lower order network models used for stability analysis of annular combustors ([45–47, 50, 122–124]). Notably, for a purely meridional acoustic mode ($n = 0$) in the constant mean radius nozzle, the growth rate (ω_I) predicted by the model remains the same for different modes, as shown in Table 5.2. This behavior was observed across different mean flow conditions.

5.4 Analysis using the Magnus expansion method

The above WKB method-based solution applies to annular nozzles sustaining mean flow (both axial and azimuthal) and an axial temperature variation. However, the analysis is limited to low subsonic flow Mach numbers and sufficiently high frequencies. The unstable modes in thermoacoustically sensitive systems typically occur near the fundamental frequency, which maybe at such low frequencies that the effect of the entropy disturbance on the acoustic field cannot be neglected. Therefore, a semi-analytical solution based on the Magnus expansion method is considered to capture the 2-D acoustic field in annular nozzles with varying mean radius. The solution thus achieved is accurate across a wide range of frequencies, applies for both sub-critical and super-critical flow configurations, fully accounts for acoustic-entropy coupling; however, the mean flow is assumed isentropic to make the analysis simple.

This section presents such a model based on the Magnus expansion solution to estimate the 2-D acoustic field in annular geometries that sustain the effects of axial variations in both the mean radius and the width of the annular duct. This is also an important contribution being reported in this chapter. The linearised Euler equations presented in Section 5.2 are recast for an isentropic flow, and the resulting LEEs are solved using the Magnus expansion method outlined in Chapter 4.

This analysis also assumes that the variations in the normal direction are negligible, and the mean flow is assumed isentropic, involving no heat exchange with the surroundings. The conservation equations for mass, meridional and azimuthal momentum, and energy, in such quasi 2-D perfect inviscid, isentropic remains similar to Eqs. (5.1) - (5.4), except that the heat transfer rate per unit volume, $\overline{\dot{Q}} = 0$. In addition to the non-dimensional fluctuating flow variables p^*, σ^*, $v_m^* = \dfrac{v'_m}{\overline{v}_m}$ and $v_\theta^* = \dfrac{v'_\theta}{\overline{c}_t}$ are defined. The azimuthal velocity fluctuation v_θ^* is normalised with $\overline{c}_t$ to avoid singularity for the case of zero azimuthal mean flow ($\overline{v}_\theta = 0$).

The time-averaged steady conservation equations, Eqs. (5.8) - (5.11) along with the requirement that $\overline{\dot{Q}} = 0$ (from Eq. (5.7)) gives the mean flow solution sustained in the isentropic annular nozzle. Similarly, the linearised form of the Euler equations are obtained by equating the first order fluctuating quantities. This gives,

$$\frac{\overline{\mathrm{D}}p^*}{\mathrm{D}t} + \overline{v}_m \frac{\partial}{\partial m} v_m^* + \overline{c}_t \frac{\partial v_\theta^*}{r\partial\theta} = 0. \tag{5.37}$$

$$\frac{\overline{\mathrm{D}}v_m^*}{\mathrm{D}t} + \frac{\overline{c}^2}{\overline{v}_m}\frac{\partial p^*}{\partial m} + \frac{\mathrm{d}\overline{v}_m}{\mathrm{d}m}\left[2v_m^* - (\gamma-1)\,p^* - \sigma^*\right] + \frac{\overline{v}_\theta}{\overline{v}_m}\frac{\mathrm{d}\overline{v}_\theta}{\mathrm{d}m}\left[2\frac{\overline{c}_t}{\overline{v}_\theta}v_\theta^* - (\gamma-1)\,p^* - \sigma^*\right] = 0, \tag{5.38}$$

$$\frac{\overline{\mathrm{D}}v_\theta^*}{\mathrm{D}t} + \frac{\overline{c}^2}{\overline{c}_t}\frac{\partial p^*}{r\partial\theta} = \frac{\overline{v}_m}{\overline{v}_\theta}\frac{\mathrm{d}\overline{v}_\theta}{\mathrm{d}m}v_\theta^*, \quad \frac{\overline{\mathrm{D}}\sigma^*}{\mathrm{D}t} = 0. \tag{5.39 - 5.40}$$

where the material derivative is defined as $\frac{\overline{\mathrm{D}}}{\mathrm{D}t}(\,) = \frac{\partial(\,)}{\partial t} + \overline{v}_m\frac{\partial(\,)}{\partial m} + \overline{v}_\theta\frac{\partial(\,)}{r\partial\theta}$. The above linearised Euler equations, Eqs. (5.37) - (5.40), govern the unsteady flow inside a thin annular nozzle with both varying mean-radius and flow width, in the presence of both axial and azimuthal mean isentropic flow .

To employ the Magnus expansion, the linearised Euler equations are recast using the flow invariants of fluctuating mass (I_A), stagnation temperature (I_B), entropy (I_C). In addition to these flow invariants, defined in Eq. (4.2), the fluctuating angular momentum of the fluid is considered [128]. While the fourth invariant is defined as $I_{D,\,old} = v_\theta^*$ in Duran and Morgans [128], it is defined as, $I_D = rv_\theta^*$ in this work as the effect of the mean radius (r) variation is also considered. Using this definition of I_D and other flow invariants from Eq. (4.2), a relation with the primitive variables is obtained:

$$\overbrace{\begin{bmatrix} I_A \\ I_B \\ I_C \\ I_D \end{bmatrix}}^{\mathbf{I}} = \overbrace{\begin{bmatrix} 1 & 1 & -1 & 0 \\ F_1 & F_1 M_m^2 & \frac{1}{\zeta} & \frac{F_1F_2}{r} \\ 0 & 0 & 1 & 0 \\ 0 & 0 & 0 & 1 \end{bmatrix}}^{\mathbf{D}_I^P} \overbrace{\begin{bmatrix} p^* \\ v_m^* \\ s^* \\ rv_\theta^* \end{bmatrix}}^{\mathbf{IP}}, \quad \Rightarrow \mathbf{IP} = \left[\mathbf{D}_I^P\right]^{-1} I. \tag{5.41}$$

with $F_1 = (\gamma-1)/\zeta$, $\zeta = 1 + \frac{\gamma-1}{2}M^2$ and $F_2 = M_\theta\overline{c}_t/\overline{c}$. The linearised Euler equations (Eqs. (5.37) - (5.40)) are now recast in terms of invariants, and are compactly written using matrix notation as,

$$\frac{\partial}{\partial t}\mathbf{I} + \overline{v}_m\mathbf{E}_m\frac{\partial}{\partial m}\mathbf{I} + \left[\overline{v}_\theta\mathbf{I} + \overline{c}_t\mathbf{E}_\theta\right]\frac{\partial}{r\partial\theta}\mathbf{I} = 0 \tag{5.42}$$

where now $\mathbf{I} = [I_A \;\; I_B \;\; I_C \;\; I_D]^T$ and $\mathcal{I}$ represents a fourth order identity matrix,

$$\mathbf{E}_m(m) = \begin{bmatrix} 1 & \dfrac{\zeta}{(\gamma-1)M_m^2} & -\dfrac{1}{(\gamma-1)M_m^2} & -\dfrac{\bar{c}_t}{r}\dfrac{\bar{v}_\theta}{\bar{v}_m^2} \\ \dfrac{\gamma-1}{\zeta} & 1 & \dfrac{\gamma-1}{\zeta} & 0 \\ 0 & 0 & 1 & 0 \\ 0 & 0 & 0 & 1 \end{bmatrix}, \tag{5.43}$$

$$\mathbf{E}_\theta(m) = \begin{bmatrix} 0 & 0 & 0 & 1/r \\ \dfrac{\gamma-1}{\zeta}\dfrac{\bar{v}_\theta}{\bar{c}_t}\dfrac{M_m^2}{M_m^2-1} & -\dfrac{\bar{v}_\theta}{\bar{c}_t}\dfrac{1}{M_m^2-1} & \dfrac{\bar{v}_\theta}{\bar{c}_t}\dfrac{1+(\gamma-1)M_m^2}{\zeta\left(M_m^2-1\right)} & \dfrac{\gamma-1}{\zeta}\dfrac{M^2-1}{M_m^2-1}\dfrac{1}{r} \\ 0 & 0 & 0 & 0 \\ \dfrac{rM_m^2}{\zeta\left(M_m^2-1\right)} & \dfrac{-r}{(\gamma-1)\left(M_m^2-1\right)} & \dfrac{r\left(1+(\gamma-1)M_m^2\right)}{\zeta(\gamma-1)\left(M_m^2-1\right)} & \dfrac{\bar{v}_\theta}{\bar{c}_t}\dfrac{1}{M_m^2-1} \end{bmatrix}, \tag{5.44}$$

The effects of the mean radius variation are captured by the coefficients $\mathbf{E}_m$ and $\mathbf{E}_\theta$; these being different from the invariant system of ODEs presented in Duran and Morgans [128]. The matrix coefficients of Eq. (5.42) are only functions of the meridional and azimuthal components of the mean flow. Assuming a harmonic time-dependence for the fluctuating quantities, $y^* = \hat{y}\mathrm{e}^{\mathrm{i}\omega t + \mathrm{i}n\theta}$, the above equations are written in the frequency domain. Using the definition of axial and azimuthal Helmholtz numbers as $\mathrm{He} = \omega l/\bar{c}$ and $\Omega = nl/r$, with the dimensionless meridional coordinate $m^* = m/l_m$ (where l_m is the meridional length of the nozzle), Eq. (5.42) becomes,

$$\frac{\mathrm{d}}{\mathrm{d}m^*}\hat{\mathbf{I}} = \mathbf{A}_{\mathrm{ann}}\hat{\mathbf{I}}, \quad \text{with } \mathbf{A}_{\mathrm{ann}} = \frac{-\mathrm{i}\bar{c}_t}{\bar{v}_m}\left[\mathbf{E}_m\right]^{-1}\left[\mathrm{He}\frac{\bar{c}}{\bar{c}_t}\mathcal{I} + \Omega\left(\mathbf{E}_\theta + \frac{\bar{v}_\theta}{\bar{c}_t}\mathcal{I}\right)\right], \tag{5.45}$$

The above equation is of the form Eq. (4.12) and can be solved using Magnus expansion where we seek a solution of the form,

$$\hat{\mathbf{I}}(m^*,\, \mathrm{He},\, \Omega) = [\exp[\mathbf{B}(m^*,\, \mathrm{He},\, \Omega)]]\hat{\mathbf{I}}_1, \quad \text{with, } \mathbf{B}(m^*,\, \mathrm{He},\, \Omega) = \sum_{k=0}^{\infty}\mathbf{B}^{(k)}(m^*,\, \mathrm{He},\, \Omega) \tag{5.46}$$

$\mathbf{B}^{(k)}(\xi)$ now represent the terms of the Magnus expansion each of order $O(\mathrm{He},\, \Omega)^k$. For initial conditions specified at the inlet in terms of the primitive variables $\mathbf{IP}_1$, using Eq. (5.41) in Eq. (5.46), we get the acoustic solution at any given m^* for a particular He, Ω as,

$$\mathbf{IP}(m^*,\, \mathrm{He},\, \Omega) = \mathbf{D}_P^I.\left[[\exp[\mathbf{B}(m^*,\, \mathrm{He},\, \Omega)]].\left[\left[\mathbf{D}_P^I\right]_1^{-1}.\mathbf{IP}_1\right]\right] \tag{5.47}$$

.

5.5 Validation

To validate the proposed solution based on Magnus expansion, the model is applied to the quarter sinusoid test-case shown in Fig. 5.2 (Left) assuming isentropic mean flow. The results are compared with numerical simulations of the LEEs (Eqs. (5.37) - (5.40)) under the acoustic forcing and boundary conditions summarised in Fig. 5.1. The linearised Euler equations are simulated for a given value of entropy and azimuthal velocity perturbation levels at the inlet. The boundary condition at the nozzle inlet (m_1) is specified in terms of the acoustic impedance, Z_1 (with $Z_1 = \hat{p}_1/\left(\overline{\rho}_1\overline{c}_1\hat{v}_{m,\,1}\right)$). A semi-infinite outlet boundary condition is again used and the resulting initial value problem is numerically solved using the 4th order Runge-Kutta method. The variations of the acoustic pressure and velocity in the nozzle are related to the velocity forcing at the inlet using the definition of the transfer functions defined in Eqs. (2.62), (2.63). Note that the acoustic pressure and velocity are presented in dimensional form for the results such that it facilitates comparison with the WKB results. This is achieved using the definitions, $\hat{p} = p^*\gamma\overline{p}$, $\hat{v}_m = v_m^*\overline{v}_m$, $\hat{v}_\theta = v_\theta^*\overline{c}_t$. Magnus expansion order of $k = 5$ is considered.

5.5.1 Results

The annular nozzle shown in Fig. 5.2 (Left) is considered across both sub-critical and super-critical configurations assuming isentropic mean flow. Inlet Mach numbers of $M_{m,\,1} = 0.02$ and 0.2 (with $M_{m,\,2} = 0.05$ and 0.56 at the outlet, respectively) are considered for the sub-critical case while an inlet flow Mach number of 2.5 (with $M_{m,\,2} = 1.27$) is considered for the super-critical case. Two different inlet axial Helmholtz numbers, $\mathrm{He}_1/\left(2\pi\right) = 0.01$ and 1 are considered.

- **Sub-critical flow:** The analytical model estimates are compared to the numerical results in Fig. 5.8 and 5.9 for Helmholtz numbers of $\mathrm{He}_1/\left(2\pi\right) = 1$ and $\mathrm{He}_1/\left(2\pi\right) = 0.01$, respectively. Inlet entropy disturbances of $\sigma_1^* = 0.01$ and 0.1 (1% and 10% temperature fluctuations, respectively) and an inlet azimuthal velocity disturbance $\hat{v}_{\theta,\,m,\,1} = 1\ \mathrm{ms}^{-1}$, in the presence of a strong azimuthal mean flow ($\overline{v}_{\theta,\,1} = 40\mathrm{m\,s}^{-1}$) is considered for this sub-critical flow configuration. It is noted that the analytical and numerical solutions are in close agreement for the considered axial Helmholtz numbers and flow Mach numbers.

  Figure 5.10 compares the model estimates to the numerical solutions of the acoustic field in nozzles with higher levels of inlet entropy disturbances of 0.1 and 0.3 for two azimuthal mode numbers of n = 1, 2. The considered azimuthal mode numbers are required to satisfy the upper frequency limit given by Eq. (5.34), and hence frequency values of $\mathrm{He}_1/\left(2\pi\right) = 1$ and 3, are chosen for n = 1 and n = 2, respectively. The model performs accurately even for these high levels of entropy disturbance and azimuthal mode numbers considered. A deviation, however, was observed in predicting $\hat{v}_\theta$ at high frequencies ($\mathrm{He}_1/\left(2\pi\right) = 3$).

This deviation can be attributed to truncating the Magnus expansion series to the first five terms.

- **Super-critical flow:** Fig. 5.11 compares the analytical model estimates to the numerical results for the annular nozzle (Fig. 5.2 (Left)) sustaining a super-critical mean flow with an inlet flow Mach number of 2.5 and outlet flow Mach number of 1.27. Across the frequencies ($\mathrm{He}_1/(2\pi) = 0.01$ & 1) and entropy disturbances ($\sigma_1^* = 0.001$ & 0.01) considered, the model was found to be accurate.

These results suggest that the model based on the Magnus expansion method applies over a wider frequency range for nozzles sustaining isentropic mean flow (both sub-critical and super-critical flows), with an excellent match with numerical LEEs over the low frequency regime, which is important for thermoacoustic studies. The model was also shown to accurately capture the effects of the entropy disturbance on the acoustic field.

- **Comparison with the WKB model solution:** Figures 5.12 and 5.13 compare the Magnus expansion and WKB method based solutions for frequencies $\mathrm{He}_1/(2\pi) = 1$ and 0.01, respectively, for the nozzle shown in Fig. 5.2 (Left) sustaining an isentropic mean flow. It can be observed that at high frequencies ($\mathrm{He}_1/(2\pi) = 1$), the WKB solution remains close to the Magnus solution for lower levels of entropy disturbance ($\sigma_1^* = 0.01$) and flow Mach numbers ($M_{m,1} = 0.02$). As the WKB solution assumes high frequencies, a large deviation is observed in the low frequency regimes ($\mathrm{He}_1/(2\pi) = 0.01$), as shown in Fig. 5.13. These observations again show that the acoustic-entropy coupling effect is not accurately captured by the WKB solution and it is limited to high frequencies.

- **Applicability of Magnus expansion based solution for non-isentropic flows:** The applicability of the Magnus expansion based model for nozzles sustaining non-isentropic mean flow due to steady heat transfer is investigated by predicting the acoustic field sustained in the annular nozzle shown in Fig. 5.2 (Left) using the Magnus expansion based model, WKB solution and numerical LEEs. The results are presented in Fig. 5.14 for two different azimuthal mode numbers of $\mathrm{n} = 0$ & 1. As the Magnus expansion model assumes isentropic mean flow in its derivation, corrected Mach numbers based on the non-isentropic mean flow results are used in estimating the acoustic field. It can be observed from Fig. 5.14 that applying Magnus expansion based solution for nozzles sustaining non-isentropic mean flow due to steady heat transfer leads to large deviations (>20%), while the WKB model closely matches to the numerical LEEs.

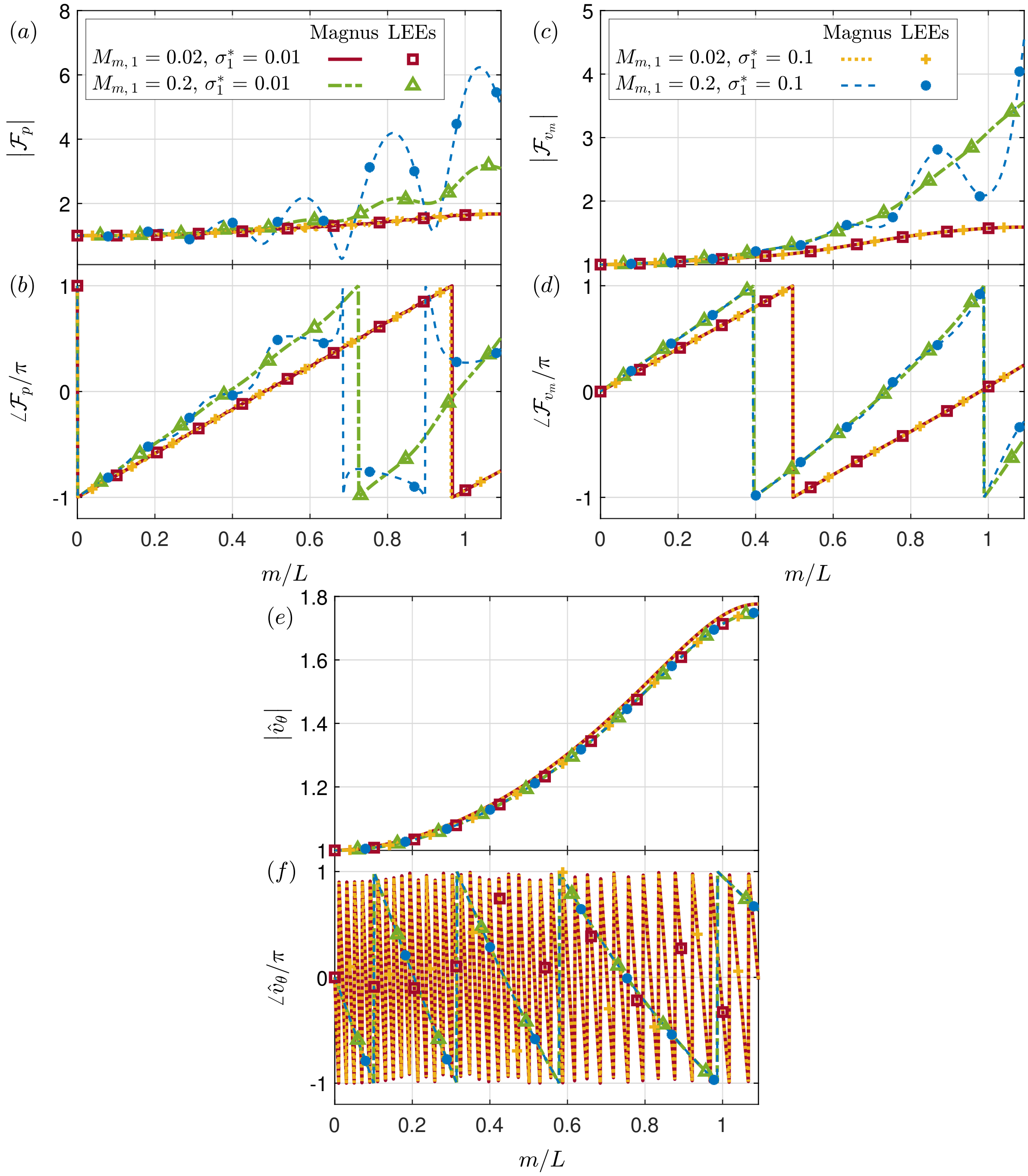

Figure 5.8: Evolution of F_p, F_{v_m} and $\hat{v}_\theta$ with m/L. $M_{m,1} = 0.02$ & 0.2, $M_{m,2} = 0.056$ & 0.56, for $\mathrm{He}_1/(2\pi) = 1$ (n = 0), and $Z_1 =$ -1. (a): transfer function gain $|F_p|$. (b): transfer function phase $\angle F_p$. (c): transfer function gain $|F_{v_m}|$. (d): transfer function phase $\angle F_{v_m}$. (e): gain of $|\hat{v}_\theta|$. (f): phase of $\angle\hat{v}_\theta$.

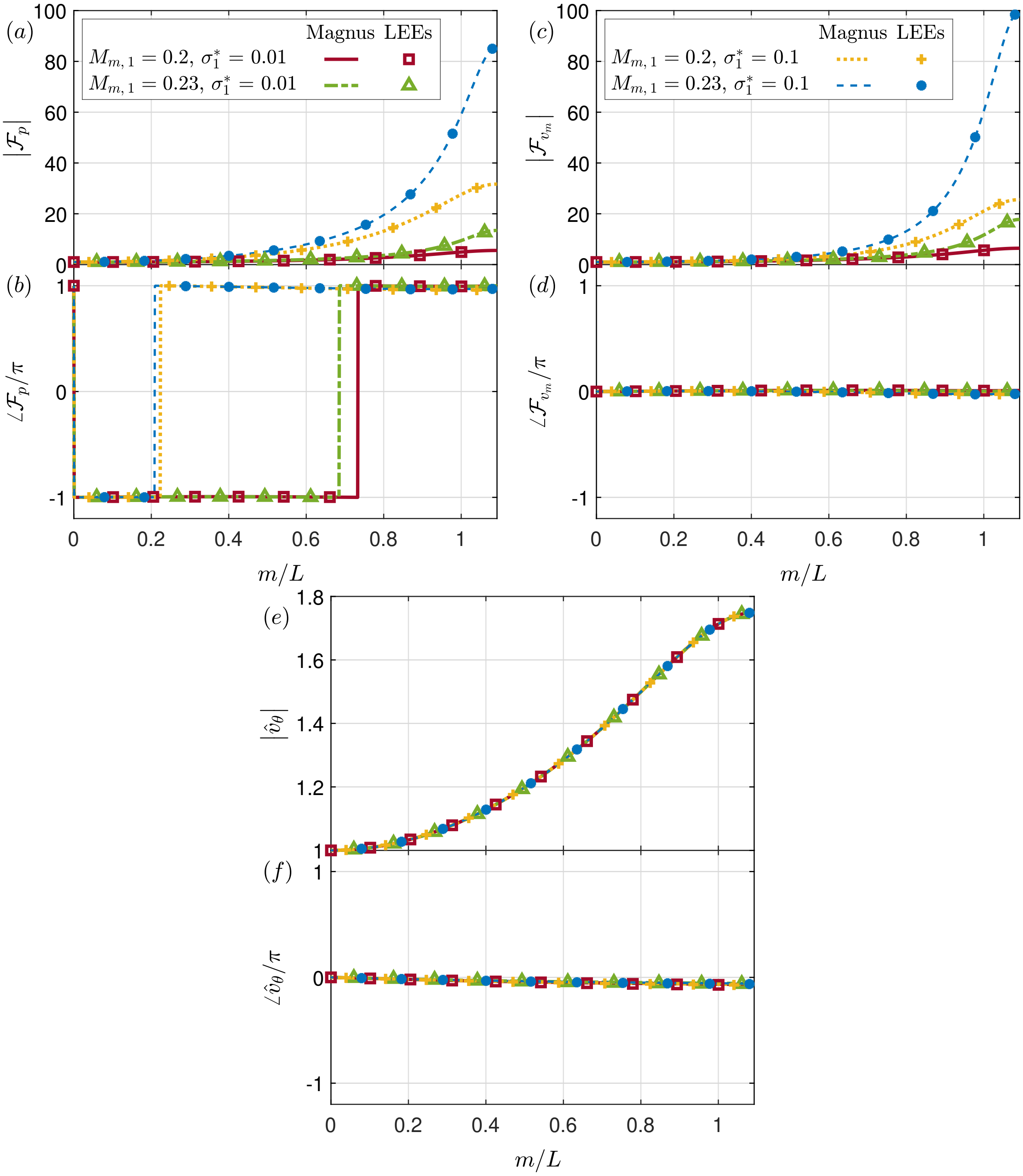

Figure 5.9: Evolution of F_p, F_{v_m} and $\hat{v}_\theta$ with m/L. $M_{m,1} = 0.2$ & 0.23, $M_{m,2} = 0.56$ & 0.72, for $\mathrm{He}_1/(2\pi) = 0.01$ (n = 0), and Z_1 = -1. (a): transfer function gain $|F_p|$. (b): transfer function phase $\angle F_p$. (c): transfer function gain $|F_{v_m}|$. (d): transfer function phase $\angle F_{v_m}$. (e): gain of $|\hat{v}_\theta|$. (f): phase of $\angle\hat{v}_\theta$.

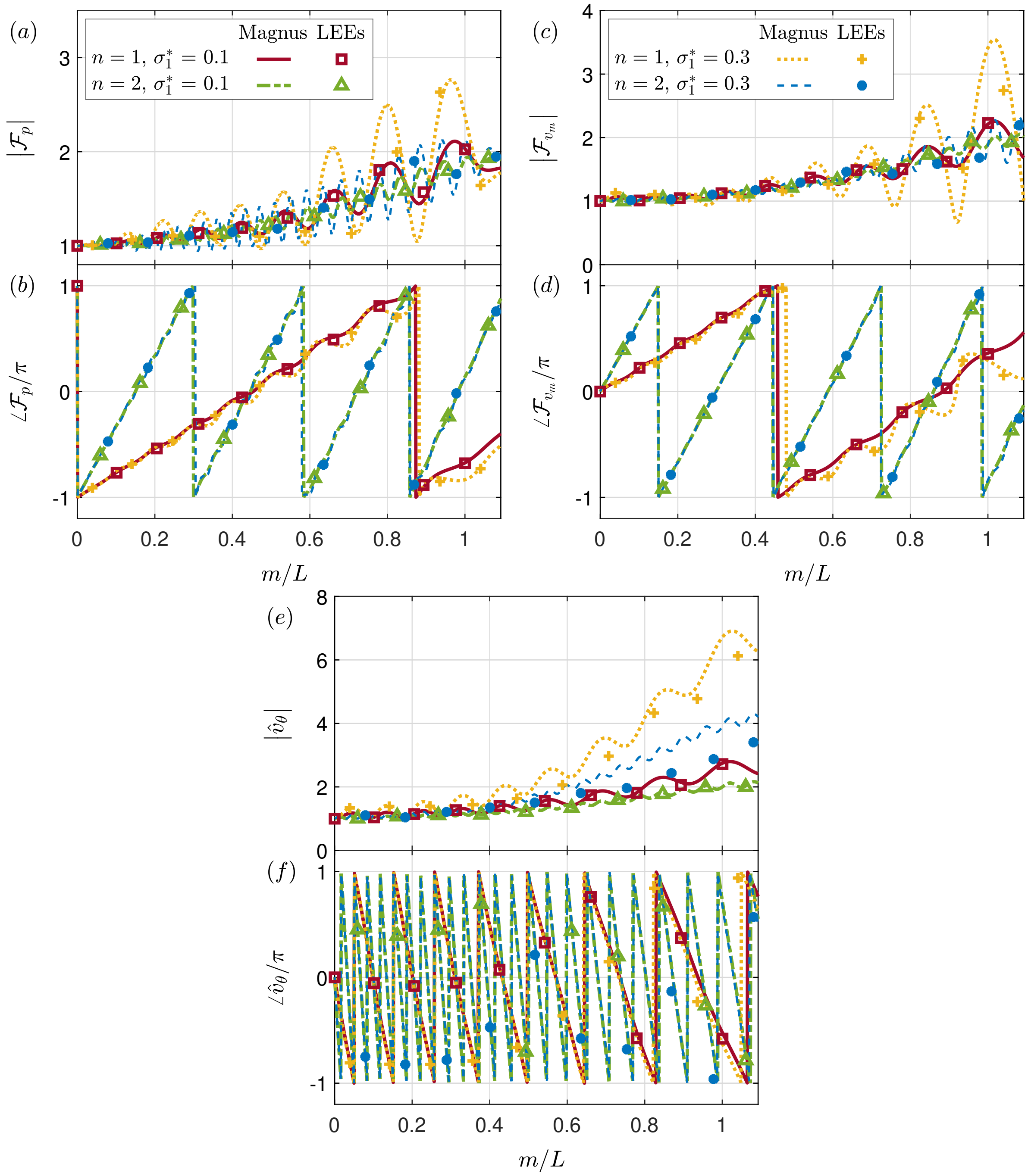

Figure 5.10: Evolution of F_p, F_{v_m} and $\hat{v}_\theta$ with m/L. $M_{m,1} = 0.02$, $M_{m,2} = 0.05$, for $\mathrm{He}_1/(2\pi)$ $= 1$ (n = 1) & 3 (n = 2), σ^* of 0.1 and 0.3, and Z_1 = -1. (a): transfer function gain $|F_p|$. (b): transfer function phase $\angle F_p$. (c): transfer function gain $|F_{v_m}|$. (d): transfer function phase $\angle F_{v_m}$. (e): gain of $|\hat{v}_\theta|$. (f): phase of $\angle\hat{v}_\theta$.

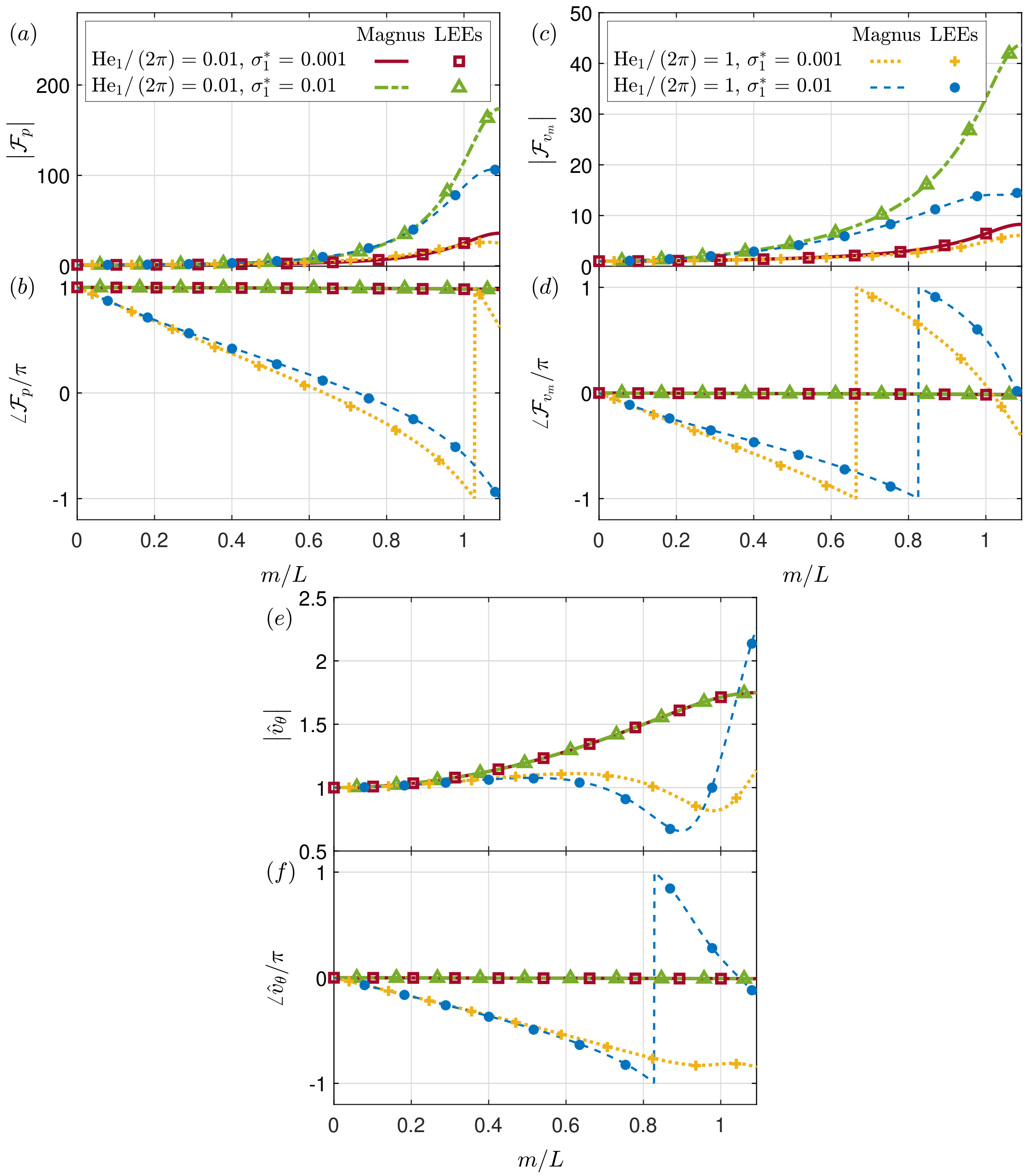

Figure 5.11: Evolution of F_p, F_{v_m} and $\hat{v}_\theta$ with m/L. $M_{m,1} = 2.5$, $M_{m,2} = 1.27$, for He$_1$/ (2π) = 0.01 (n = 0) & 1 (n = 1), σ^* of 0.001 and 0.01, and Z_1 = -1. (a): transfer function gain $|F_p|$. (b): transfer function phase $\angle F_p$. (c): transfer function gain $|F_{v_m}|$. (d): transfer function phase $\angle F_{v_m}$. (e): gain of $|\hat{v}_\theta|$. (f): phase of $\angle\hat{v}_\theta$.

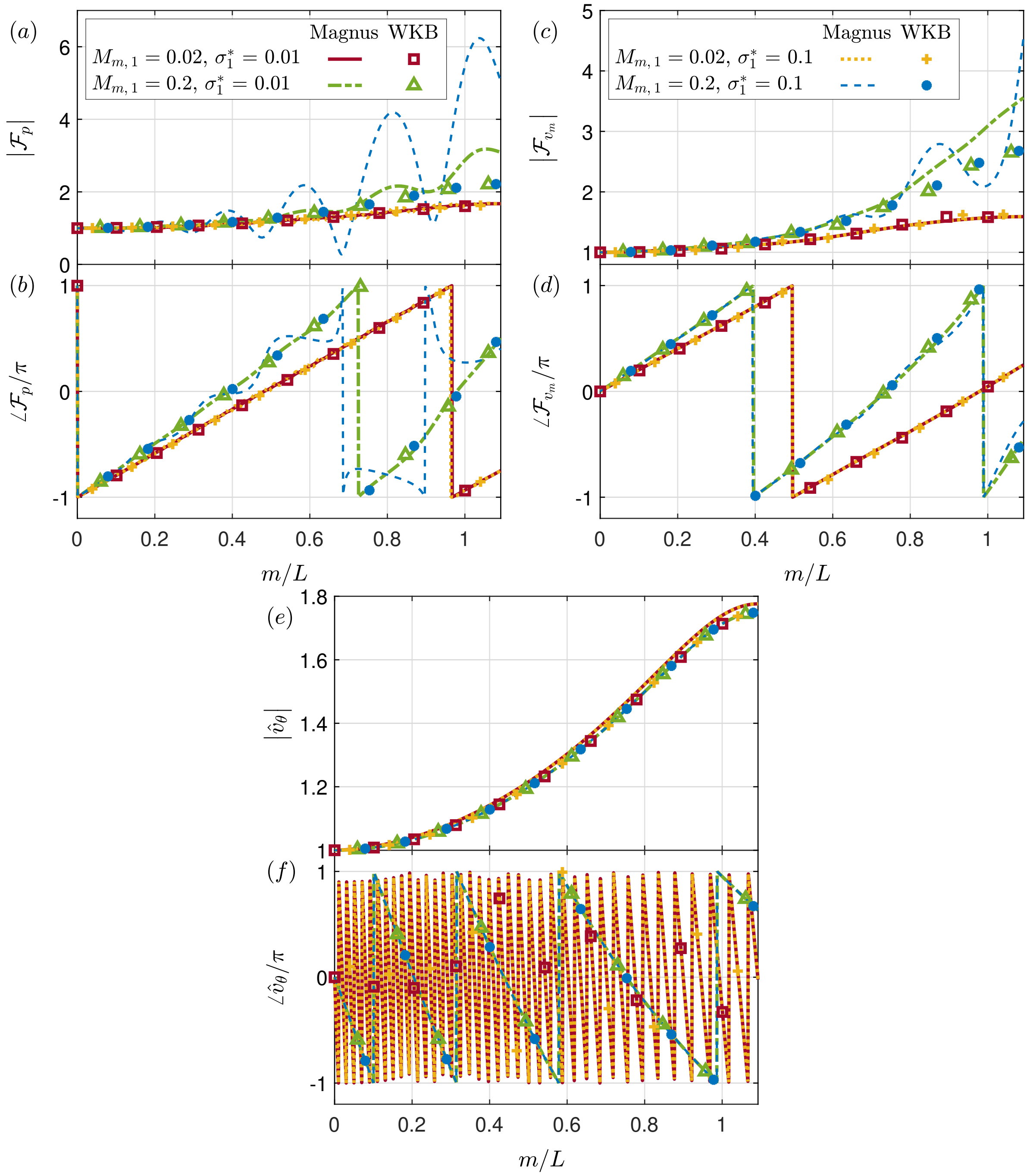

Figure 5.12: Evolution of F_p, F_{vm} and $\hat{v}_\theta$ with m/L. $M_{m,1}$ = 0.02 & 0.2, $M_{m,2}$ = 0.056 & 0.56, for $\mathrm{He}_1/(2\pi) = 1$ (n = 0), $\sigma_1^* = 0.01$ & 0.1, and Z_1 = -1. (a): transfer function gain $|F_p|$. (b): transfer function phase $\angle F_p$. (c): transfer function gain $|F_{v_m}|$. (d): transfer function phase $\angle F_{v_m}$. (e): gain of $|\hat{v}_\theta|$. (f): phase of $\angle \hat{v}_\theta$.

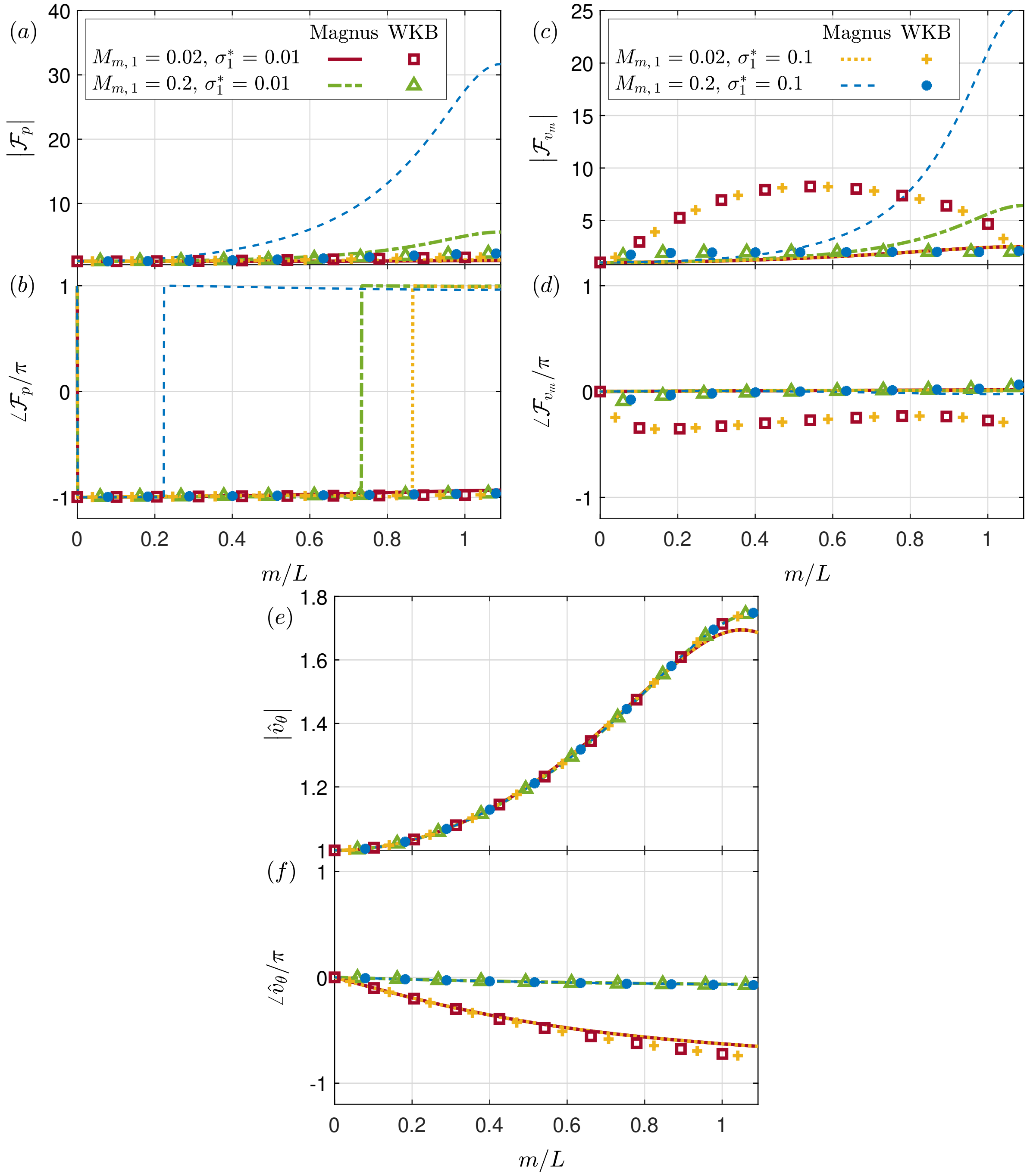

Figure 5.13: Evolution of F_p, F_{v_m} and $\hat{v}_\theta$ with m/L. $M_{m,1} = 0.02$ & 0.2, $M_{m,2} = 0.056$ & 0.56, for $\mathrm{He}_1/(2\pi) = 0.01$ (n = 0), $\sigma_1^* = 0.01$ & 0.1, and Z_1 = -1. (a): transfer function gain $|F_p|$. (b): transfer function phase $\angle F_p$. (c): transfer function gain $|F_{v_m}|$. (d): transfer function phase $\angle F_{v_m}$. (e): gain of $|\hat{v}_\theta|$. (f): phase of $\angle\hat{v}_\theta$.

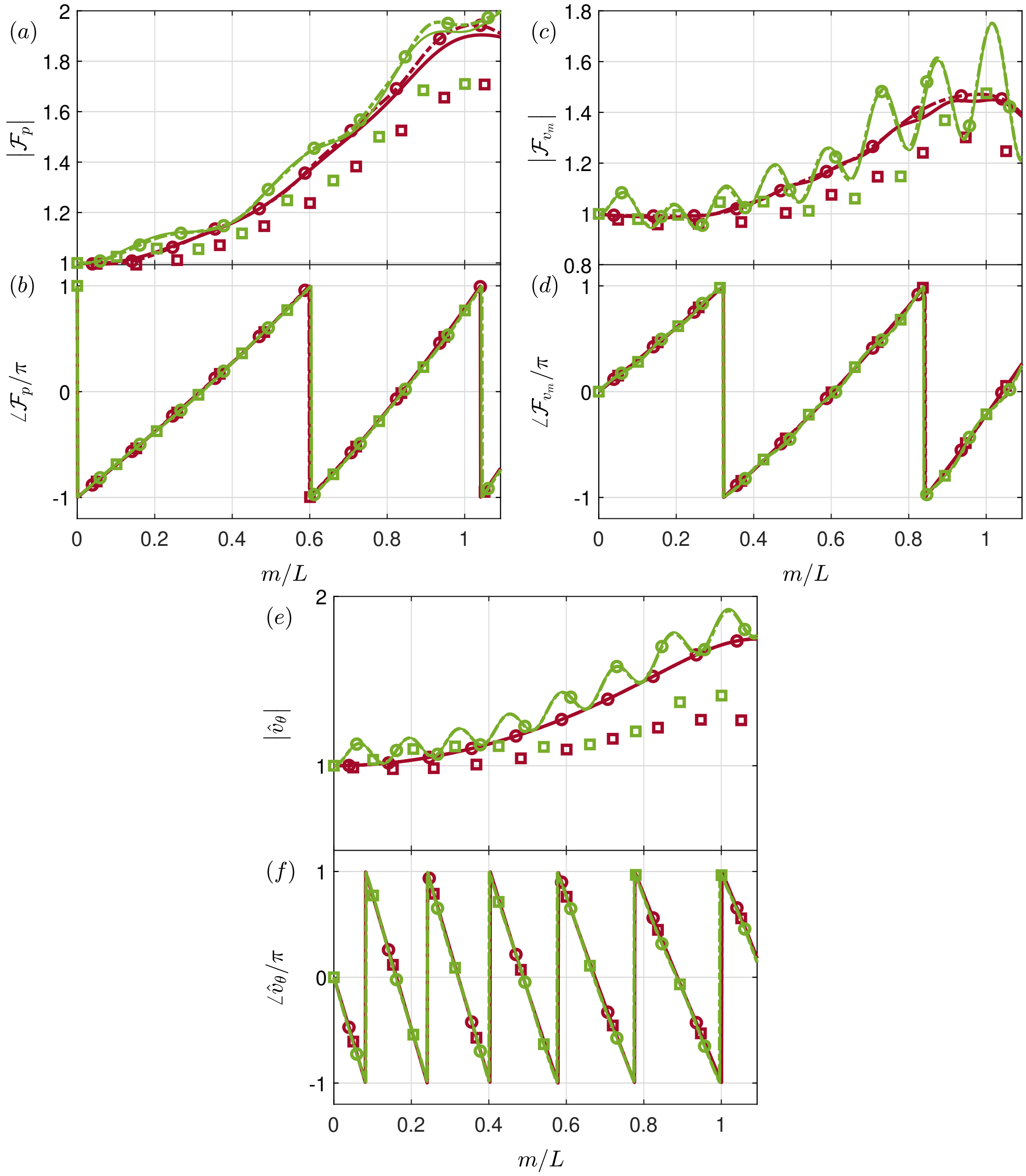

Figure 5.14: Evolution of F_p, F_{v_m} and $\hat{v}_\theta$ with m/L. $M_{m,1} = 0.2$, $M_{m,2} = 0.56$; $M_{\theta,1} = 0.0125$, $M_{m,2} = 0.03$; $\overline{T}_1 = 1600\text{K}$, $\overline{T}_2 = 800\text{K}$, for $\text{He}_1/(2\pi) = 1.2$ with n = 0 (denoted by green) and n = 1 (denoted by red), Z_1 = -1. (a): transfer function gain $|F_p|$. (b): transfer function phase $\angle F_p$. (c): transfer function gain $|F_{v_m}|$. (d): transfer function phase $\angle F_{v_m}$. (e): gain of $|\hat{v}_\theta|$. (f): phase of $\angle\hat{v}_\theta$. The lines (—) represent the WKB based solution, markers (□) represent the Magnus expansion based solution, while the lines with markers (-·○-·) represent the numerical LEEs solution.

5.6 Summary

In summary, semi-analytical model solutions for the two-dimensional acoustic field in a thin annular nozzle, sustaining a mean flow with both axial and azimuthal components, are presented using the iterative WKB and the Magnus expansion methods. The annular nozzle is considered to have both mean radius and flow width variations, and hence the model allows for more general geometries than previous studies. While the WKB model applies to nozzles exchanging heat and exhibiting an axial temperature variation, the Magnus expansion model applies to isentropic nozzles in this study. A coordinate transformation facilitated the derivation of a new set of mean flow equations and linearised Euler equations (LEEs), these being an important contribution of this thesis. In deriving these equations, the variations normal to the nozzle walls are neglected in both mean and fluctuations, assuming a thin annular gap.

Firstly, the obtained LEEs are solved using the WKB method which requires, (i) neglecting the effect of entropy perturbations on the acoustic field, (ii) neglecting higher-order flow Mach number terms, and (iii) assuming that the mean flow variations occur slowly in some sense, compared to the wave-number of the acoustics. The acoustic field predictions are validated against the numerical solutions of the LEEs by applying them to an annular nozzle whose shape varies as a quarter sinusoid for different frequencies and flow Mach numbers. The WKB model predictions performed very well within the calculated frequency ranges of validity for Mach numbers as high as 0.6 inside the nozzle. The model's applicability for studying thermoacoustic instabilities is further shown by accurately predicting the acoustic modes for an axially varying annular nozzle and comparing with the in-house developed numerical low order network solver ($\text{OSCILOS}_{\text{ann}}$).

In the second approach, the linearised Euler equations governing the acoustic field in the thin annular nozzle are solved using the Magnus expansion method, assuming an isentropic mean flow. This method is applicable over a wide range of frequencies, flow Mach numbers (both sub-critical and super-critical flows) and accurately accounts for the acoustic-entropy coupling. By applying the model to the quarter sinusoid shaped annular nozzle, it has been observed the obtained results are accurate even at large frequencies and flow Mach numbers.

While the WKB model was found to be accurate in predicting the acoustic field in annular nozzles with non-isentropic mean flow due to steady heat transfer, the solution is limited to low subsonic flow Mach numbers, sufficiently high frequencies and negligible effect of the entropy disturbance on the acoustic field. The Magnus expansion based solution led to deviations for nozzles sustaining non-isentropic mean flow but was accurate for isentropic mean flows across a wide range of frequencies and flow Mach numbers, accurately accounting for the acoustic-entropy coupling. The solutions from both these semi-analytical models are computationally easy to evaluate and can be readily employed in lower order thermoacoustic solvers.

Chapter 6

Conclusions

6.1 Summary of the contributions of this PhD work

In this thesis we developed simplified analytical frameworks for estimating the one-dimensional and two-dimensional acoustic fields established in axial and annular nozzles, respectively. These nozzles feature (i) varying cross-sectional area, (ii) varying axial mean temperature predominantly due to heat transfer, and (iii) sub-critical/super-critical[1] mean flow, which does not have to be isentropic. Heat exchange to the surroundings is considered as the only source of non-isentropicity, and any effects of flow separation, fluid viscosity and wall friction are neglected. Asymptotic methods such as WKB and Magnus expansion methods are used for predicting the acoustic field, and the resulting model estimates are validated using numerical simulations. The applicability of some of the developed models for stability analysis is shown by comparing the obtained modal solutions to in-house developed low-order network model solvers based on modal expansions. The analytical models thus developed can be of great interest to both thermoacoustic and acoustic communities.

The first contribution of this thesis has been to develop WKB method based semi-analytical solutions to estimate the planar acoustic field in quasi 1-D nozzles with a mean flow that can be non-isentropic due to steady heat transfer. The WKB models require high frequencies and neglect the effect of the entropy disturbance on the acoustic field. The general semi-analytical solution allows arbitrary area and temperature profiles but comes at the expense of marginally increased computational effort. The general solution can be further simplified for specific area and temperature profiles; for example, for the case of conical and exponentially shaped nozzles with a linear temperature gradient, simplified analytical solutions are presented for both isentropic and non-isentropic flows. These simplified solutions only depend on the

[1] By applying the Rankine-Hugoniot jump conditions, acoustic solution in the presence of any shock waves can also be obtained [77].

local mean flow and thermodynamic properties and the wave-number. They provide a simpler, physically more insightful solution but are confined to low subsonic flow Mach numbers. Explicit expressions are obtained for the frequency ranges in which the model is applicable. Within the frequency range of validity, the model accurately predicts the nozzles' acoustic field and eigenmodes.

The second contribution has been to investigate the effect of steady heat transfer on the acoustic energy balance in nozzles sustaining mean flow. This is achieved by quantifying the acoustic energy change in terms of the acoustic absorption coefficient Δ, with $\Delta > 0$ ($\Delta < 0$) signifying acoustic energy absorption (generation). The acoustic response for determining Δ is obtained using the WKB solution, and the considered frequencies, therefore, fall within the WKB validity limits. The effect of the mean flow conditions, frequency and inlet reflection coefficient on Δ is investigated. The analytical model predictions and the simplified mathematical analysis revealed that at sufficiently high frequencies Δ is not dependent upon frequency and shows a maximum for an anechoic inlet boundary. The analysis revealed that the temperature gradient significantly affects the acoustic behaviour, with a positive gradient causing acoustic absorption and a negative gradient resulting in acoustic generation. It is also reported that the effect of the area gradient on Δ is minimal compared to the temperature gradient. This result suggested that practical combustors, afterburners and automotive exhaust systems, which exhibit axial temperature drops due to heat loss, may be especially prone to thermoacoustic instabilities due to acoustic energy generation. It is observed that by altering the temperature variation, a proportional decrease in acoustic energy generation can be obtained in the nozzles.

The WKB solutions are confined to sufficiently high frequencies and low subsonic flow Mach numbers and neglect the effect of the entropy disturbance on the acoustic field. A semi-analytical solution based on the Magnus expansion method was therefore developed in this thesis to account for the main drawbacks of the WKB method. For the first time, a Magnus expansion solution is developed for flows exhibiting heat transfer and thus which are not isentropic. The linearised Euler equations are recast as a first-order system of ODEs in terms of the flow invariants. This system of ODEs is expanded around the non-dimensional frequency and heat-transfer terms and truncated to the first five terms of the expansion. The model accurately determines the acoustic and entropy transfer functions for both sub-critical and super-critical flow configurations and is applicable over a wide range of frequencies, with small deviations at very high frequencies. It was observed that the steady heat transfer significantly affects the acoustic response even at the acoustically compact limit. Hence, the compact isentropic nozzle solutions of Marble and Candel [76] cannot be applied to nozzles with non-isentropic mean flows. This thesis, therefore, presents the first compact (and non-compact) solution for nozzles exchanging heat to the surroundings. The results also show that heat transfer profoundly affects the entropy generation in a nozzle with the potential of significantly increasing indirect

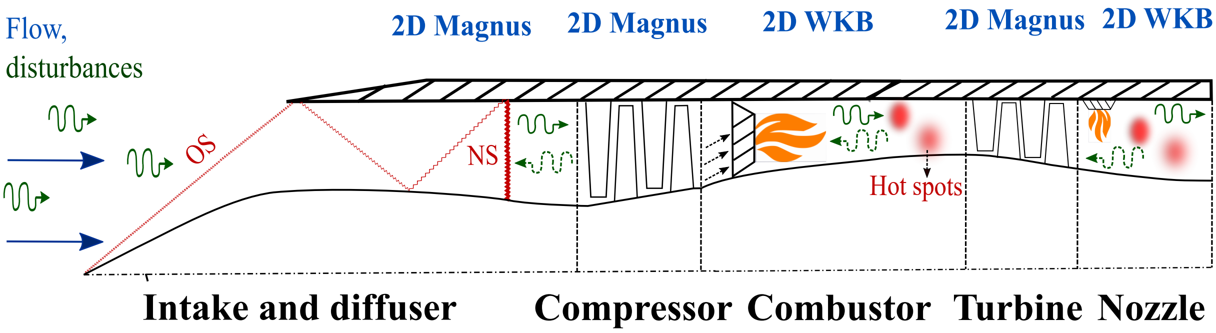

Figure 6.1: Schematic of a jet engine with annular combustor describing the applicability of the 2D acoustic models in different domains. OS and NS represent the oblique and normal shocks sustained in the intake.

noise emissions. A nozzle losing heat led to stronger entropy generation compared to nozzles gaining heat. Again as most practical systems sustain heat loss, they encounter larger levels of entropy generated noise. Therefore nozzles losing heat are prone to higher levels of acoustic energy generation at sufficiently high frequencies and generate strong entropy waves at low frequencies.

It should be noted that compared to WKB solutions, the Magnus expansion method based acoustic solutions require higher computational cost (Appendix D), and they cannot be expressed as a superposition of upstream and downstream propagating wave amplitudes. Also, the high-frequency behaviour of the WKB solution is better than for the Magnus solution. Therefore, in regions near the flame where the flow Mach numbers are low, and area/temperature gradients are not too strong, WKB solutions can be applied given their advantages of reduced complexity and computational cost. In regimes involving high flow Mach numbers, for example, nozzles or turbine blades, Magnus expansion based models can be used.

The last contribution of the thesis is to extend the WKB and Magnus expansion based methods to capture the two-dimensional acoustic field in annular nozzles sustaining a mean flow. For the first time, the effects of both the mean radius and the flow width variations are accounted for. While the WKB solution developed can be applied to nozzles with non-isentropic mean flow, the Magnus solution is limited to the isentropic case in this study. The WKB solution's frequency limits are presented, and its applicability to stability analysis is shown. As the higher-order azimuthal modes of the annular nozzles occur at high frequencies, the WKB predictions are accurate with a negligible effect of the entropy disturbance due to shear dispersion. When the mean flow sustains high flow Mach numbers with negligible changes in the temperature, the Magnus expansion based model can be applied.

Figure 6.1 shows a use-case of a jet engine with an annular combustor and regions where the developed 2-D acoustic models can be applied. The Magnus expansion-based model can be applied for intakes and diffusers involving super-critical flows with or without shocks. For this case, the acoustic propagation is separately solved in the sub-sonic and super-sonic portions, as described in [128]. This 2-D model can also be applied to estimate acoustic propagation through compressor or turbine blades, assuming the mean flow to be isentropic. For combustor/afterburner regions involving steady heat transfer and low flow Mach numbers to keep the flame stable, the WKB model can be applied. Therefore, the models thus developed can be used to study the thermoacoustic behaviour in various domains of the GT engine. Similarly, the 1-D models would be useful in GT engines using can-combustors.

6.2 Future work

- The present work developed several analytical models for the acoustic field solutions in nozzles with axially varying flows. Implementing these solutions in lower-order thermoacoustic solvers could improve their accuracy for complex geometries at reasonable computational cost.
- Steady heat transfer is considered as the prime source of non-isentropicity for the models developed in this thesis. However, combustors and diverging portions of the nozzles encounter flow separation and wall friction [109]. Yang *et al.* [132], De Domenico *et al.*, [107] that the presence of recirculation zones strongly affect the entropy field and thereby the acoustic response of the nozzles. A model which can also account for these effects would be more accurate for many flows.
- Only the effects of the acoustic-entropy coupling is discussed in this work neglecting any compositional or vortical disturbances which can also act as sources of indirect noise. The acoustic-vorticity coupling of acoustics with vorticity waves [139] can affect the acoustic field and the acoustic energy balance of the system. The vortical structures are triggered by the acoustic fluctuations at the flow separation edges, and as these structures convect downstream they may continuously interact with the acoustic field, leading to attenuation or amplification of the acoustic energy. Hence, acoustic-entropy [26] as well as acoustic-vorticity coupling [113, 140, 141] may lead to net absorption or generation of acoustic energy due to acoustical energy transfer to the entropy and vorticity mode or vice versa.
- Compositional inhomogeneities [78, 142, 143] can also lead to the generation of indirect combustion noise and it was shown that this compositional noise depends on the local mixture composition and can exceed entropy noise for fuel-lean conditions and supercritical nozzle flows. This suggests that the compositional indirect noise also requires due consideration in modelling the thermoacoustic behavior inside low-emission combustors.
- The Magnus expansion based model in Chapter 5 is limited to annular nozzles with isentropic mean flows. Further developing the model to account for steady heat transfer

- a crucial effect - would facilitate it being employed in determining the acoustic response of more complex components such as the stator blades (or nozzles) of the turbine. These blades encounter heat transfer due to blade cooling and often sustain super-critical flow configurations, and hence the WKB models cannot be applied.

- The effects of viscosity (momentum diffusion) and the boundary layer are neglected in this analysis for both the mean flow and perturbed flow. However, the viscous effects become important at higher frequencies, and linearised Navier-Stokes equations (LNSEs) can estimate the acoustic field better than LEEs. Further extension of the models to account for the viscous effects would be useful.

- Finally, the non-linear response of the normal shock, present in the intake diffuser and turbine blades to incoming disturbances can be better determined using a weakly non-linear analysis than a linear framework described in this thesis.

Bibliography

[1] *Ambient air pollution: a global assessment of exposure and burden of disease.* Tech. rep. 2016, 121 p.

[2] M. Basner, W. Babisch, A. Davis, M. Brink, C. Clark, S. Janssen, and S. Stansfeld. "Auditory and non-auditory effects of noise on health". In: *The Lancet* 383.9925 (2014), pp. 1325–1332.

[3] *A C A R E. Flightpath 2050: Europe's vision for aviation.* Tech. rep. 2011.

[4] *European Union Emission Inventory Report 1990–2011 Under the UNECE Convention on Long-Range Transboundary Air Pollution (LRTAP).* Tech. rep. 2013.

[5] J. B. Heywood. *Internal Combustion Engine Fundamentals, Second Edition.* en. 2nd edition. New York: McGraw-Hill Education, 2018.

[6] S. M. Correa. "Power generation and aeropropulsion gas turbines: from combustion science to combustion technology". In: *Symposium (International) on Combustion.* Vol. 27. 2. Elsevier. 1998, pp. 1793–1807.

[7] J. W. S. Rayleigh. "The explanation of certain acoustical phenomena". In: *Nature* 18.455 (1878), pp. 319–321.

[8] T. C. Lieuwen. *Unsteady Combustor Physics.* Cambridge University Press, 2012.

[9] D. Durox, T. Schuller, N. Noiray, A. Birbaud, and S. Candel. "Rayleigh criterion and acoustic energy balance in unconfined self-sustained oscillating flames". In: *Combustion and Flame* 156.1 (2009), pp. 106–119.

[10] M. Hempsell. "Progress on the SKYLON and SABRE". In: vol. 11. Proceedings of the International Astronautical Congress, 2013, pp. 8427–8440.

[11] J. Beita, M. Talibi, S. Sadasivuni, and R. Balachandran. "Thermoacoustic Instability Considerations for High Hydrogen Combustion in Lean Premixed Gas Turbine Combustors: A Review". In: *Hydrogen* 2.1 (2021), pp. 33–57.

[12] Z. Lim, J. Li, and A. S. Morgans. “The effect of hydrogen enrichment on the forced response of CH4/H2/Air laminar flames”. In: *International Journal of Hydrogen Energy* 46.46 (2021), pp. 23943–23953.

[13] D. G. Crighton, A. P. Dowling, J. E. Ffowcs-Williams, M. Heckl, F. G. Leppington, and J. F. Bartram. “Modern Methods in Analytical Acoustics Lecture Notes”. In: *The Journal of the Acoustical Society of America* 92.5 (1992), pp. 3023–3023.

[14] T. Lieuwen. “Modeling premixed combustion-acoustic wave interactions: A review”. In: *Journal of Propulsion and Power* 19.5 (2003), pp. 765–781.

[15] A. P. Dowling and S. R. Stow. “Acoustic Analysis of Gas Turbine Combustors”. In: *Journal of Propulsion and Power* 19.5 (2003), pp. 751–764.

[16] T. Poinsot. “Prediction and control of combustion instabilities in real engines”. In: *Proceedings of the Combustion Institute* (2016).

[17] C. J. Goy, S. R. James, and S. Rea. “Monitoring combustion instabilities: E. ON UK’s experience. Chapter 8 In: Lieuwen T, Yang V, editors. Combustion instabilities in gas turbine engines: operational experience, fundamental mechanisms, and modeling.” In: *Progress in Astronautics and Aeronautics* 210 (2005), p. 163.

[18] *Prediction of Aerodynamic Frequencies in a Gas Turbine Combustor Using Transient CFD*. Vol. Volume 2: Combustion, Fuels and Emissions. Turbo Expo: Power for Land, Sea, and Air. June 2009, pp. 585–594.

[19] S. Roux, G. Lartigue, T. Poinsot, U. Meier, and C. Bérat. “Studies of mean and unsteady flow in a swirled combustor using experiments, acoustic analysis, and large eddy simulations”. In: *Combustion and Flame* 141.1 (2005), pp. 40–54.

[20] I. Hernández, G. Staffelbach, T. Poinsot, J. C. Román Casado, and J. B. Kok. “LES and acoustic analysis of thermo-acoustic instabilities in a partially premixed model combustor”. In: *Comptes Rendus Mécanique* 341.1 (2013). Combustion, spray and flow dynamics for aerospace propulsion, pp. 121–130.

[21] G. Staffelbach, L. Gicquel, G. Boudier, and T. Poinsot. “Large Eddy Simulation of self excited azimuthal modes in annular combustors”. In: *Proceedings of the Combustion Institute* 32.2 (2009), pp. 2909–2916.

[22] O. Schulz, U. Doll, D. Ebi, J. Droujko, C. Bourquard, and N. Noiray. “Thermoacoustic instability in a sequential combustor: Large eddy simulation and experiments”. In: *Proceedings of the Combustion Institute* 37.4 (2019), pp. 5325–5332.

[23] M. Ihme. “Combustion and engine-core noise”. In: *Annu. Rev. Fluid Mech.* 49 (2017), pp. 277–310.

[24] M. A. Heckl. "Active Control of the Noise from a Rijke Tube". In: *Aero- and Hydro-Acoustics*. Ed. by G. Comte-Bellot and J. E. F. Williams. Berlin, Heidelberg: Springer Berlin Heidelberg, 1986, pp. 211–216.

[25] S. M. Candel. "Combustion instabilities coupled by pressure waves and their active control". In: *Symposium (International) on Combustion* 24.1 (1992). Twenty-Fourth Symposium on Combustion, pp. 1277–1296.

[26] A. Dowling. "The calculation of thermoacoustic oscillations". In: *Journal of Sound and Vibration* 180.4 (1995), pp. 557–581.

[27] J. Keller, W. Egli, and J. Hellat. "Thermally induced low-frequency oscillations". In: *Zeitschrift für angewandte Mathematik und Physik ZAMP* 36.2 (1985), pp. 250–274.

[28] J. J. Keller. "Thermoacoustic oscillations in combustion chambers of gas turbines". In: *AIAA Journal* 33.12 (1995), pp. 2280–2287.

[29] S. Candel. "Combustion dynamics and control: Progress and challenges". In: *Proceedings of the Combustion Institute* 29.1 (2002). Proceedings of the Combustion Institute, pp. 1–28.

[30] X. Han, J. Li, and A. S. Morgans. "Prediction of combustion instability limit cycle oscillations by combining flame describing function simulations with a thermoacoustic network model". In: *Combustion and Flame* 162.10 (2015), pp. 3632–3647.

[31] D. Laera, T. Schuller, K. Prieur, D. Durox, S. M. Camporeale, and S. Candel. "Flame Describing Function analysis of spinning and standing modes in an annular combustor and comparison with experiments". In: *Combustion and Flame* 184 (2017), pp. 136–152.

[32] Y. Xia, D. Laera, W. P. Jones, and A. S. Morgans. "Numerical prediction of the Flame Describing Function and thermoacoustic limit cycle for a pressurised gas turbine combustor". In: *Combustion Science and Technology* 191.5-6 (2019), pp. 979–1002.

[33] F. E. Marble and S. M. Candel. "An analytical study of the non-steady behavior of large combustors". In: *Symposium (International) on Combustion* 17.1 (1979). Seventeenth Symposium (International) on Combustion, pp. 761–769.

[34] A. P. Dowling and J. E. Ffowcs Williams. *Sound and sources of sound.* John Wiley & Sons, Inc. New York, USA, 1983. Chap. 6.

[35] F. E. C. Culick. "Combustion Instabilities in Propulsion Systems". In: *Unsteady Combustion.* Ed. by F. Culick, M. V. Heitor, and J. H. Whitelaw. Dordrecht: Springer Netherlands, 1996, pp. 173–241.

[36] B. T. Zinn and M. E. Lores. "Application of the Galerkin Method in the Solution of Non-linear Axial Combustion Instability Problems in Liquid Rockets". In: *Combustion Science and Technology* 4.1 (1971), pp. 269–278.

[37] I. Waugh, M. Geuß, and M. Juniper. “Triggering, bypass transition and the effect of noise on a linearly stable thermoacoustic system”. In: *Proceedings of the Combustion Institute* 33.2 (2011), pp. 2945–2952.

[38] L. Magri and M. P. Juniper. “Sensitivity analysis of a time-delayed thermo-acoustic system via an adjoint-based approach”. In: *Journal of Fluid Mechanics* 719 (2013), pp. 183–202.

[39] F. Nicoud, L. Benoit, C. Sensiau, and T. Poinsot. “Acoustic Modes in Combustors with Complex Impedances and Multidimensional Active Flames”. In: *AIAA Journal* 45.2 (2007), pp. 426–441.

[40] S. M. Camporeale, B. Fortunato, and G. Campa. “A Finite Element Method for Three-Dimensional Analysis of Thermo-acoustic Combustion Instability”. In: *Journal of Engineering for Gas Turbines and Power* 133.1 (Sept. 2011). 011506.

[41] C. F. Silva, F. Nicoud, T. Schuller, D. Durox, and S. Candel. “Combining a Helmholtz solver with the flame describing function to assess combustion instability in a premixed swirled combustor”. In: *Combustion and Flame* 160.9 (2013), pp. 1743–1754.

[42] F. Ni, M. Miguel-Brebion, F. Nicoud, and T. Poinsot. “Accounting for Acoustic Damping in a Helmholtz Solver”. In: *AIAA Journal* 55.4 (2017), pp. 1205–1220.

[43] E. Dokumaci. “An approximate analytical solution for plane sound wave transmission in inhomogeneous ducts”. In: *Journal of Sound and Vibration* 217.5 (1998), pp. 853–867.

[44] J. Li, D. Yang, and A. S. Morgans. “The effect of an axial mean temperature gradient on communication between one-dimensional acoustic and entropy waves”. In: *International Journal of Spray and Combustion Dynamics* 10.2 (2018), pp. 131–153.

[45] S. Evesque and W. Polifke. “Low-Order Acoustic Modelling for Annular Combustors: Validation and Inclusion of Modal Coupling”. In: vol. Volume 1: Turbo Expo 2002. Turbo Expo: Power for Land, Sea, and Air. June 2002, pp. 321–331.

[46] S. Evesque, W. Polifke, and C. Pankiewitz. “Spinning and Azimuthally Standing Acoustic Modes in Annular Combustors”. In: vol. 3182. Aeroacoustics Conferences. American Institute of Aeronautics and Astronautics, May 2003.

[47] S. R. Stow and A. P. Dowling. “A Time-Domain Network Model for Nonlinear Thermoacoustic Oscillations”. In: *Journal of Engineering for Gas Turbines and Power* 131.3 (Feb. 2009). 031502.

[48] J. Li and A. S. Morgans. “Time domain simulations of nonlinear thermoacoustic behaviour in a simple combustor using a wave-based approach”. In: *Journal of Sound and Vibration* 346 (2015), pp. 345–360.

[49] M. Bauerheim, F. Nicoud, and T. Poinsot. “Progress in analytical methods to predict and control azimuthal combustion instability modes in annular chambers”. In: *Physics of Fluids* 28.2 (2016), p. 021303.

[50] D. Yang, D. Laera, and A. S. Morgans. “A systematic study of nonlinear coupling of thermoacoustic modes in annular combustors”. In: *Journal of Sound and Vibration* 456 (2019), pp. 137–161.

[51] F. Schaefer and W. Polifke. “Low-order Network Model of a Duct with Non-Uniform Cross-Section and Varying Mean Temperature in the Presence of Mean Flow”. In: *AIAA Propulsion and Energy 2019 Forum*.

[52] D. Yang, D. Laera, and A. S. Morgans. *Open Source Combustion Instability Low Order Simulator for Annular Combustors (OSCILOS_ann)*. Tech. rep.

[53] J. Li, D. Yang, C. Luzzato, and A. S. Morgans. *Open Source Combustion Instability Low Order Simulator (OSCILOS–Long) Technical report*. Tech. rep.

[54] L. Crocco. “Aspects of Combustion Stability in Liquid Propellant Rocket Motors Part I: Fundamentals. Low Frequency Instability With Monopropellants”. In: *Journal of the American Rocket Society* 21.6 (1951), pp. 163–178.

[55] L. Crocco. “Aspects of Combustion Stability in Liquid Propellant Rocket Motors Part II: Low Frequency Instability with Bipropellants. High Frequency Instability”. In: *Journal of the American Rocket Society* 22.1 (1952), pp. 7–16.

[56] *Influence of the Interaction of Equivalence Ratio and Mass Flow Fluctuations on Flame Dynamics*. Vol. Volume 2: Turbo Expo 2005. Turbo Expo: Power for Land, Sea, and Air. June 2005, pp. 249–257.

[57] T. Lieuwen and B. T. Zinn. “The role of equivalence ratio oscillations in driving combustion instabilities in low NOx gas turbines”. In: *Symposium (International) on Combustion* 27.2 (1998), pp. 1809–1816.

[58] R. Balachandran, B. Ayoola, C. Kaminski, A. Dowling, and E. Mastorakos. “Experimental investigation of the nonlinear response of turbulent premixed flames to imposed inlet velocity oscillations”. In: *Combustion and Flame* 143.1 (2005), pp. 37–55.

[59] N. Noiray, D. Durox, T. Schuller, and S. Candel. “A unified framework for nonlinear combustion instability analysis based on the flame describing function”. In: *Journal of Fluid Mechanics* 615 (2008), pp. 139–167.

[60] A. Giauque, L. Selle, L. Gicquel, T. Poinsot, H. Buechner, P. Kaufmann, and W. Krebs. “System identification of a large-scale swirled partially premixed combustor using LES and measurements”. In: *Journal of Turbulence* 6 (2005), N21.

[61] H. J. Krediet, C. H. Beck, W. Krebs, S. Schimek, C. O. Paschereit, and J. B. W. Kok. "Identification of the Flame Describing Function of a Premixed Swirl Flame from LES". In: *Combustion Science and Technology* 184.7-8 (2012), pp. 888–900.

[62] P. Wolf, G. Staffelbach, L. Y. Gicquel, J.-D. Müller, and T. Poinsot. "Acoustic and Large Eddy Simulation studies of azimuthal modes in annular combustion chambers". In: *Combustion and Flame* 159.11 (2012), pp. 3398–3413.

[63] L. Tay-Wo-Chong and W. Polifke. "Large Eddy Simulation-Based Study of the Influence of Thermal Boundary Condition and Combustor Confinement on Premix Flame Transfer Functions". In: *Journal of Engineering for Gas Turbines and Power* 135.2 (Jan. 2013). 021502.

[64] S. Wysocki, G. Di-Chiaro, and F. Biagioli. "Effect of fuel mixture fraction and velocity perturbations on the flame transfer function of swirl stabilized flames". In: *Combustion Theory and Modelling* 19.6 (2015), pp. 714–743.

[65] S. Hermeth, G. Staffelbach, L. Gicquel, and T. Poinsot. "LES evaluation of the effects of equivalence ratio fluctuations on the dynamic flame response in a real gas turbine combustion chamber". In: *Proceedings of the Combustion Institute* 34.2 (2013), pp. 3165–3173.

[66] X. Han and A. S. Morgans. "Simulation of the flame describing function of a turbulent premixed flame using an open-source LES solver". In: *Combustion and Flame* 162.5 (2015), pp. 1778–1792.

[67] S. Ruan, T. D. Dunstan, N. Swaminathan, and R. Balachandran. "Computation of Forced Premixed Flames Dynamics". In: *Combustion Science and Technology* 188.7 (2016), pp. 1115–1135.

[68] C. Y. Lee and S. Cant. "LES of Nonlinear Saturation in Forced Turbulent Premixed Flames". In: *Flow, Turbulence and Combustion* 99.2 (Sept. 2017), pp. 461–486.

[69] D. Durox, T. Schuller, N. Noiray, and S. Candel. "Experimental analysis of nonlinear flame transfer functions for different flame geometries". In: *Proceedings of the Combustion Institute* 32.1 (2009), pp. 1391–1398.

[70] J. Kopitz, A. Huber, T. Sattelmayer, and W. Polifke. "Thermoacoustic Stability Analysis of an Annular Combustion Chamber With Acoustic Low Order Modeling and Validation Against Experiment". In: vol. Volume 2: Turbo Expo 2005. Turbo Expo: Power for Land, Sea, and Air. June 2005, pp. 583–593.

[71] P. Palies, D. Durox, T. Schuller, and S. Candel. "Nonlinear combustion instability analysis based on the flame describing function applied to turbulent premixed swirling flames". In: *Combustion and Flame* 158.10 (2011), pp. 1980–1991.

[72] B. Schuermans, F. Guethe, D. Pennell, D. Guyot, and C. O. Paschereit. “Thermoacoustic Modeling of a Gas Turbine Using Transfer Functions Measured Under Full Engine Pressure”. In: *Journal of Engineering for Gas Turbines and Power* 132.11 (Aug. 2010). 111503.

[73] F. Di Sabatino, T. F. Guiberti, W. R. Boyette, W. L. Roberts, J. P. Moeck, and D. A. Lacoste. “Effect of pressure on the transfer functions of premixed methane and propane swirl flames”. In: *Combustion and Flame* 193 (2018), pp. 272–282.

[74] A. P. Dowling. “Nonlinear self-excited oscillations of a ducted flame”. In: *Journal of Fluid Mechanics* 346 (1997), pp. 271–290.

[75] G. Campa and S. M. Camporeale. “Prediction of the Thermoacoustic Combustion Instabilities in Practical Annular Combustors”. In: *Journal of Engineering for Gas Turbines and Power* 136.9 (Mar. 2014). 091504.

[76] F. Marble and S. Candel. “Acoustic disturbance from gas non-uniformities convected through a nozzle”. In: *Journal of Sound and Vibration* 55.2 (1977), pp. 225–243.

[77] I. Duran and S. Moreau. “Solution of the quasi-one-dimensional linearized Euler equations using flow invariants and the Magnus expansion”. In: *Journal of Fluid Mechanics* 723 (2013), pp. 190–231.

[78] L. Magri. “On indirect noise in multicomponent nozzle flows”. In: *Journal of Fluid Mechanics* 828 (2017), R2.

[79] S. W. Rienstra and A. Hirschberg. “An introduction to acoustics”. In: *Eindhoven University of Technology* 18 (2004), p. 19.

[80] N. A. Eisenberg and T. W. Kao. “Propagation of Sound through a Variable-Area Duct with a Steady Compressible Flow”. In: *The Journal of the Acoustical Society of America* 49.1B (1971), pp. 169–175.

[81] V. Easwaran and M. Munjal. “Plane wave analysis of conical and exponential pipes with incompressible mean flow”. In: *Journal of Sound and Vibration* 152.1 (1992), pp. 73–93.

[82] O. M. Umurhan. “Exploration of fundamental matters of acoustic instabilities in combustion chambers”. In: *Center for Turbulence Research, Annual Briefs* (1999), pp. 99–108.

[83] M. L. Munjal and M. G. Prasad. “On plane-wave propagation in a uniform pipe in the presence of a mean flow and a temperature gradient”. In: *The Journal of the Acoustical Society of America* 80.5 (1986), pp. 1501–1506.

[84] R. Sujith, G. Waldherr, and B. Zinn. “An exact solution for one-dimensional acoustic fields in ducts with an axial temperature gradient”. In: *Journal of Sound and Vibration* 184.3 (1995), pp. 389–402.

[85] B. Karthik, B. M. Kumar, and R. I. Sujith. “Exact solutions to one-dimensional acoustic fields with temperature gradient and mean flow”. In: *The Journal of the Acoustical Society of America* 108.1 (2000), pp. 38–43.

[86] P. Subrahmanyam, R. Sujith, and T. C. Lieuwen. “A family of exact transient solutions for acoustiv wave propagation in inhomogeneous, non-uniform area ducts”. In: *Journal of Sound and Vibration* 240.4 (2001), pp. 705–715.

[87] A. Schlissel. “The initial development of the WKB solutions of linear second order ordinary differential equations and their use in the connection problem”. In: *Historia Mathematica* 4.2 (1977), pp. 183–204.

[88] A. Cummings. “Ducts with axial temperature gradients: An approximate solution for sound transmission and generation”. In: *Journal of Sound and Vibration* 51.1 (1977), pp. 55–67.

[89] J. Li and A. S. Morgans. “The one-dimensional acoustic field in a duct with arbitrary mean axial temperature gradient and mean flow”. In: *Journal of Sound and Vibration* 400 (2017), pp. 248–269.

[90] E. Dokumaci. “Comment on “the one dimensional acoustic field with arbitrary mean axial temperature gradient and mean flow” (J.Li and A.S.Morgans, Journal of Sound and Vibration 400 (2017) 248-269)”. In: *Journal of Sound Vibration* 410 (Dec. 2017), pp. 485–487.

[91] V. K. Rani and S. L. Rani. “WKB solutions to the quasi 1-D acoustic wave equation in ducts with non-uniform cross-section and inhomogeneous mean flow properties – Acoustic field and combustion instability”. In: *Journal of Sound and Vibration* 436 (2018), pp. 183–219.

[92] A. S. Morgans and I. Duran. “Entropy noise: A review of theory, progress and challenges”. In: *International Journal of Spray and Combustion Dynamics* 8.4 (2016), pp. 285–298.

[93] S. R. Yeddula and A. S. Morgans. “A semi-analytical solution for acoustic wave propagation in varying area ducts with mean flow”. In: *Journal of Sound and Vibration* 492 (2021), p. 115770.

[94] E. Dokumaci. “On transmission of sound in a non-unofrm duct carrying a subsonic compressinle flow”. In: *Journal of Sound and Vibration* 210.3 (1998), pp. 391–401.

[95] A. Giusti, N. A. Worth, E. Mastorakos, and A. P. Dowling. “Experimental and Numerical Investigation into the Propagation of Entropy Waves”. In: *AIAA Journal* 55.2 (2017), pp. 446–458.

[96] A. S. Morgans, C. S. Goh, and J. A. Dahan. “The dissipation and shear dispersion of entropy waves in combustor thermoacoustics”. In: *Journal of Fluid Mechanics* 733 (2013), R2.

[97] Y. Xia, I. Duran, A. S. Morgans, and X. Han. “Dispersion of Entropy Perturbations Transporting through an Industrial Gas Turbine Combustor”. In: *Flow, Turbulence and Combustion* 100.2 (Mar. 2018), pp. 481–502.

[98] A. P. Dowling and S. Hubbard. “Instability in lean premixed combustors”. In: *Proceedings of the Institution of Mechanical Engineers, Part A: Journal of Power and Energy* 214.4 (2000), pp. 317–332.

[99] T. Sattelmayer. “Influence of the Combustor Aerodynamics on Combustion Instabilities From Equivalence Ratio Fluctuations ”. In: *Journal of Engineering for Gas Turbines and Power* 125.1 (Dec. 2002), pp. 11–19.

[100] M. Weilenmann, Y. Xiong, and N. Noiray. “On the dispersion of entropy waves in turbulent flows”. In: *Journal of Fluid Mechanics* 903 (2020), R1.

[101] M. Weilenmann and N. Noiray. “Experiments on sound reflection and production by choked nozzle flows subject to acoustic and entropy waves”. In: *Journal of Sound and Vibration* 492 (2021), p. 115799.

[102] J. Rodrigues, A. Busseti, and S. Hochgreb. “Numerical investigation on the generation, mixing and convection of entropic and compositional waves in a flow duct”. In: *Journal of Sound and Vibration* 472 (2020), p. 115155.

[103] A. Emmanuelli, J. Zheng, M. Huet, A. Giauque, T. Le Garrec, and S. Ducruix. “Description and application of a 2D-axisymmetric model for entropy noise in nozzle flows”. In: *Journal of Sound and Vibration* 472 (2020), p. 115163.

[104] A. B. Emmanuelli, M. Huet, T. Le Garrec, and S. Ducruix. “Study of Entropy Noise through a 2D Stator using CAA”. In: AIAA AVIATION Forum. 0. American Institute of Aeronautics and Astronautics, June 2018.

[105] M. Huet, A. Emmanuelli, and T. Le Garrec. “Entropy noise modelling in 2D choked nozzle flows”. In: *Journal of Sound and Vibration* 488 (2020), p. 115637.

[106] M. Huet, A. Emmanuelli, and S. Ducruix. “Influence of viscosity on entropy noise generation through a nozzle”. In: *Journal of Sound and Vibration* 510 (2021), p. 116293.

[107] F. De Domenico, E. O. Rolland, and S. Hochgreb. “A generalised model for acoustic and entropic transfer function of nozzles with losses”. In: *Journal of Sound and Vibration* 440 (2019), pp. 212–230.

[108] F. De Domenico, E. O. Rolland, J. Rodrigues, L. Magri, and S. Hochgreb. “Compositional and entropy indirect noise generated in subsonic non-isentropic nozzles”. In: *J. Fluid Mech.* 910 (2021).

[109] A. Jain and L. Magri. “A physical model for indirect noise in non-isentropic nozzles: Transfer functions and stability”. In: *arXiv preprint arXiv:2106.10469* (2021).

[110] R. H. Cantrell and R. W. Hart. "Interaction between Sound and Flow in Acoustic Cavities: Mass, Momentum, and Energy Considerations". In: *The Journal of the Acoustical Society of America* 36.4 (1964), pp. 697–706.

[111] C. Morfey. "Acoustic energy in non-uniform flows". In: *Journal of Sound and Vibration* 14.2 (1971), pp. 159–170.

[112] G. J. Bloxsidge, A. P. Dowling, N. Hooper, and P. J. Langhorne. "Active control of reheat buzz". In: *AIAA Journal* 26.7 (1988), pp. 783–790.

[113] D. Bechert. "Sound absorption caused by vorticity shedding, demonstrated with a jet flow". In: *Journal of Sound and Vibration* 70.3 (1980), pp. 389–405.

[114] M. K. Myers. "Transport of energy by disturbances in arbitrary steady flows". In: *Journal of Fluid Mechanics* 226 (1991), pp. 383–400.

[115] A. Giauque, T. Poinsot, M. Brear, and F. Nicoud. "Budget of disturbance energy in gaseous reacting flows". In: *Proc. of the Summer Program.* Center for Turbulence Research, NASA Ames/Stanford Univ. 2006, pp. 285–297.

[116] M. J. Brear, F. Nicoud, M. Talei, A. Giauque, and E. R. Hawkes. "Disturbance energy transport and sound production in gaseous combustion". In: *Journal of Fluid Mechanics* 707 (2012), pp. 53–73.

[117] N. Karimi, M. J. Brear, and W. H. Moase. "Acoustic and disturbance energy analysis of a flow with heat communication". In: *Journal of Fluid Mechanics* 597 (2008), pp. 67–89.

[118] R. Gaudron and A. S. Morgans. "Acoustic absorption in a subsonic mean flow at a sudden cross section area change". In: *Proceedings of ICSV 26–International Congress on Sound and Vibration.* 2019, pp. 1–8.

[119] R. Gaudron, D. Yang, and A. S. Morgans. "Acoustic Energy Balance During the Onset, Growth, and Saturation of Thermoacoustic Instabilities". In: *Journal of Engineering for Gas Turbines and Power* 143.4 (Mar. 2021). 041026.

[120] R. Royce. *The jet engine.* John Wiley & Sons, 2015.

[121] C. P. Mark and A. Selwyn. "Design and analysis of annular combustion chamber of a low bypass turbofan engine in a jet trainer aircraft". In: *Propulsion and Power Research* 5.2 (2016), pp. 97–107.

[122] S. R. Stow and A. P. Dowling. "Thermoacoustic Oscillations in an Annular Combustor". In: vol. Volume 2: Coal, Biomass and Alternative Fuels; Combustion and Fuels; Oil and Gas Applications; Cycle Innovations. Turbo Expo: Power for Land, Sea, and Air. V002T02A004. June 2001.

[123] M. Bauerheim, J.-F. Parmentier, P. Salas, F. Nicoud, and T. Poinsot. “An analytical model for azimuthal thermoacoustic modes in an annular chamber fed by an annular plenum”. In: *Combustion and Flame* 161.5 (2014), pp. 1374–1389.

[124] J. G. Aguilar and M. P. Juniper. “Adjoint Methods for Elimination of Thermoacoustic Oscillations in a Model Annular Combustor via Small Geometry Modifications”. In: vol. Volume 4A: Combustion, Fuels, and Emissions. Turbo Expo: Power for Land, Sea, and Air. V04AT04A054. June 2018.

[125] S. R. Stow, A. P. Dowling, and T. P. Hynes. “Reflection of circumferential modes in a choked nozzle”. In: *Journal of Fluid Mechanics* 467 (2002), pp. 215–239.

[126] J. Li, J. Nan, and L. Yang. “Analytical solutions for the acoustic field in a thin annular duct with temperature gradient and mean flow”. In: *Journal of Sound and Vibration* 467 (2020), p. 115043.

[127] J. Li, D. Wang, A. S. Morgans, and L. Yang. “Analytical solutions of acoustic field in annular combustion chambers with non-uniform cross-sectional surface area and mean flow”. In: *Journal of Sound and Vibration* 506 (2021), p. 116175.

[128] I. Duran and A. S. Morgans. “On the reflection and transmission of circumferential waves through nozzles”. In: *Journal of Fluid Mechanics* 773 (2015), pp. 137–153.

[129] S. R. Stow. *LOTAN: low-order thermo-acoustic network model.* Tech. rep. Tech. Rep., Cambridge University, Cambridge, 2005.

[130] G. Campa, S. M. Camporeale, A. Guaus, J. Favier, M. Bargiacchi, A. Bottaro, E. Cosatto, and G. Mori. “A Quantitative Comparison Between a Low Order Model and a 3D FEM Code for the Study of Thermoacoustic Combustion Instabilities”. In: vol. Volume 2: Combustion, Fuels and Emissions, Parts A and B. Turbo Expo: Power for Land, Sea, and Air. June 2011, pp. 859–869.

[131] J. Li, Y. Xia, A. S. Morgans, and X. Han. “Numerical prediction of combustion instability limit cycle oscillations for a combustor with a long flame”. In: *Combustion and Flame* 185 (2017), pp. 28–43.

[132] D. Yang, J. Guzmán-Iñigo, and A. S. Morgans. “Sound generation by entropy perturbations passing through a sudden flow expansion”. In: *Journal of Fluid Mechanics* 905 (2020), R2.

[133] U. Ingard and V. K. Singhal. “Upstream and downstream sound radiation into a moving fluid”. In: *The Journal of the Acoustical Society of America* 54.5 (1973), pp. 1343–1346.

[134] A. P. Dowling and Y. Mahmoudi. “Combustion noise”. In: *Proceedings of the Combustion Institute* 35.1 (2015), pp. 65–100.

[135] U. Ingard and V. K. Singhal. “Effect of flow on the acoustic resonances of an open-ended duct”. In: *The Journal of the Acoustical Society of America* 58.4 (1975), pp. 788–793.

[136] S. Blanes, F. Casas, J. A. Oteo, and J. Ros. “The Magnus expansion and some of its applications”. In: *Phys. Rep.* 470.5-6 (2009), pp. 151–238.

[137] J. D. Anderson. *Modern compressible flow: with historical perspective.* Vol. 12. McGraw-Hill New York, 1990.

[138] J. D. Stanitz. *One-dimensional compressible flow in vaneless diffusers of radial-and mixed-flow centrifugal compressors, including effects of friction, heat transfer and area change.* Tech. rep. Tech. Rep., National Advisory Committee for Aeronautics., 1952.

[139] S. Boij and B. Nilsson. “Scattering and absorption of sound at flow duct expansions”. In: *Journal of Sound and Vibration* 289.3 (2006), pp. 577–594.

[140] Y. Fukumoto and M. Takayama. “Vorticity production at the edge of a slit by sound waves in the presence of a low-Mach-number bias flow”. In: *Physics of Fluids A: Fluid Dynamics* 3.12 (1991), pp. 3080–3082.

[141] J. C. Wendoloski. “Sound absorption by an orifice plate in a flow duct”. In: *The Journal of the Acoustical Society of America* 104.1 (1998), pp. 122–132.

[142] L. Magri, J. O’Brien, and M. Ihme. “Compositional inhomogeneities as a source of indirect combustion noise”. In: *Journal of Fluid Mechanics* 799 (2016), R4.

[143] J. G. Inigo, P. J. Baddoo, L. J. Ayton, and A. S. Morgans. “Noise generated by entropic and compositional inhomogeneities interacting with a cascade of airfoils”. In: *25th AIAA/CEAS Aeroacoustics Conference.*

Appendix A

Numerical procedure for solving the linearised Euler equations

The linearised Euler equations given by Eq. (3.6) are solved assuming a semi-infinite boundary condition at $x^* = 1$ [134]. This results in an initial value problem which is solved using a fourth-order Runge-Kutta method. The first-order system of ODEs are as follows,

$$\frac{\mathrm{dP}^+}{\mathrm{d}x^*} = C_{11}\mathrm{P}^+ + C_{12}\mathrm{P}^-, \;\; \& \;\; \frac{\mathrm{dP}^-}{\mathrm{d}x^*} = C_{21}\mathrm{P}^+ + C_{22}\mathrm{P}^-, \quad \text{subjected to } \mathrm{P}_1^+ \text{ and } \mathrm{P}_1^- \text{ at the inlet.} \tag{A.1}$$

with R_1 as the reflection coefficient at the inlet, $R_1 = \frac{\mathrm{P}_1^+}{\mathrm{P}_1^-}$.

In a linear framework, the elements of the transfer function, defined in Eq. (3.10), can be obtained by subjecting the system of ODEs in Eq. (A.1) to any two different conditions. For examples, $\mathrm{P}_1^+ = 0$, $\mathrm{P}_1^- = 1$ and $\mathrm{P}_1^+ = 1$, $\mathrm{P}_1^- = 0$ are chosen here. The acoustic response of the nozzle, expressed in terms of $\frac{\mathrm{P}_2^+}{\mathrm{P}_1^-}$ and $\frac{\mathrm{P}_2^-}{\mathrm{P}_1^-}$ is given by,

$$\frac{\mathrm{P}_2^+}{\mathrm{P}_1^-} = T_{11}R_1 + T_{12}; \quad \frac{\mathrm{P}_2^-}{\mathrm{P}_1^-} = T_{21}R_1 + T_{22}; \tag{A.2}$$

where the T_{11}, T_{12}, T_{21}, T_{22} are the elements of the transfer matrix shown in Eq. (3.10). These expressions are finally used in the estimation of Δ using Eq. (3.11).

Appendix B

Optimisation search

The global extrema of Δ as a function of mean flow parameters (a^*, b^* and M_1), are found using an optimisation search based on a genetic algorithm. The constraints applied to the parameters are as follows,

$$-0.8 \leq a^* \leq 2; \quad -0.8 \leq b^* \leq 5; \quad 0 \leq M_1 \leq 0.3. \tag{B.1}$$

Although the theoretical limits for a^* and b^* range from -1 to ∞, these area and temperature profiles are practically infeasible. For example, $a^* > 2$ indicates a diverging nozzle with significant area change and hence prone to flow separation. Thus, the area variation (a^*) is limited by nominal levels of flow acceleration for converging ducts and flow separation for diverging ducts. The mean temperature variation (b^*) is limited by the combustion process, and the practical temperature gradients encountered. The value of M_1 is limited by the low Mach number flow assumption, typical for combustor flows. The flow conditions for maximum acoustic absorption and generation are presented in Table D.1, along with their corresponding values.

Table B.1: The flow conditions and corresponding extrema for $|\Delta|$.

Acoustic generation	**Acoustic absorption**
$a^* = -0.373$	$a^* = -0.72$
$b^* = -0.8$	$b^* = 5$
$M_1 = 0.25$	$M_1 = 0.262$
$\Delta_{\text{min}} = -1.335$	$\Delta_{\text{max}} = 0.611$

As seen in Table D.1, maximum acoustic generation (Δ = -1.335) occurs when the non-dimensional mean temperature variation b^* assumes the lowest possible negative value constrained by the limit. Similarly, the maximum acoustic absorption ($\Delta = 0.611$) corresponds to $b^* = 5$, constrained by the maximum positive value set by the limits.

Appendix C

WKB analysis by assuming wave-number k_o to be complex

The effect of neglecting the imaginary part of wave-number is evaluated mathematically in this section. A new real parameter ν is defined as the ratio of the imaginary part of angular frequency (ω_I) to the real part (ω_R). Thus we have,

$$\nu = \frac{\omega_I}{\omega_R} \qquad \Longrightarrow \omega = \omega_R\,(1 + \mathrm{i}\nu) \quad \text{or} \quad k_o = k_{o,\,R}\,(1 + \mathrm{i}\nu)\,, \tag{C.1}$$

For the modes of interest in thermoacosutic applications, $\omega_I \ll \omega_R$, and hence $|\nu| \ll 1$, as stated earlier. It should also be noted that, δ is at-least an order larger in magnitude than ν. For example, in the annular test-case considered in Fig. 5.2 (Right), $|\delta|$ is observed to be is ≈ 0.17 while $|\nu| \approx 0.009$, corresponding to the first harmonic mode with $n = 0$. It is assumed that the parameters, δ, μ are of the same order, that is,

$$\delta = \mathrm{O}\left(\frac{\alpha,\, \beta,\, \Delta_r}{k_o}\right), \quad \text{and} \quad \mu = \frac{n}{k_o r}, \quad \text{with} \quad \mathrm{O}(\delta) \sim \mathrm{O}(\mu) \gg \mathrm{O}(\nu). \tag{C.2}$$

Also,

$$\mu = \frac{n}{k_{o,\,R}\,(1+\mathrm{i}\nu)\,r} \approx \frac{n}{k_{o,\,R}\,r}\left(1 - \mathrm{i}\nu - \nu^2 + ...\right) \approx \mu_R\,(1 - \mathrm{i}\nu) \tag{C.3}$$

Now Eq. (5.23) is again substituted into Eq. (5.22) and the real part of the equation is equated to zero. However, the wave-number k_o is considered complex. This results in,

$$-b^2\left[(1-\mu M_\theta)^2 - M_m^2\right] + 2k_{o,\,R} M_m b + k_{o,\,R}^2\left[1 - \mu_R^2\,(1 - \mu_R M_\theta)\right] + \mathrm{O}(\delta^2,\, \delta^2 M_m,\, \delta\nu M_m,) \approx 0. \tag{C.4}$$

The contribution of the terms involving ν are still negligible (since $|\nu| \ll |\delta|$). The 'new' quadratic equation thus obtained has real number $k_{o,\,R}$ in place of k_o. Thus,

$$\frac{{b_{new}}^{\pm}}{k_{o,\,R}} = \frac{M_m \mp \lambda_R}{\left(1-\mu_R M_\theta\right)^2 - M_m^2}; \quad \text{where } \lambda_R = \sqrt{\left(1-\mu_R M_\theta\right)^2 - \mu_R^2\left(1-M_m^2\right)}. \tag{C.5}$$

Similarly on equating the imaginary part, we arrive at,

$$\begin{aligned}{a_{new}}^{\pm} = &-\frac{\alpha}{2} - \frac{\beta}{4} - \frac{1}{2\lambda_R}\frac{d\lambda_R}{\mathrm{d}m} + \left[\frac{\alpha\gamma M_m^2}{2} \pm \frac{\mu_R^2 M_m}{2\lambda_R}\left(\beta-\Delta_r\right) + \frac{\mu_R^2 M_\theta^2}{r} - \frac{\Delta_r M_\theta^2}{2} \pm \frac{3\Delta_r \mu_R M_m M_\theta}{\lambda_R}\right] \\ &+ \left[\left(\frac{\beta}{2}-\alpha\right)\left(M_m^2 \mp \lambda_R M_m\left(1+2\mu_R M_\theta\right)\right) - \Delta_r \mu_R M_\theta\left(3+2\mu_R M_\theta\right) \mp \frac{\beta\gamma M_m}{2\lambda_R}\right] \\ &\pm \overbrace{\frac{\nu k_R}{\lambda_R}\left(1 + \frac{b_{new}^{\pm}}{k_r}M_m - \left(\frac{b_{new}^{\pm}}{k_r}\right)^2 \mu_R M_\theta\right)}^{\textbf{Extra term}}.\end{aligned} \tag{C.6}$$

The final model solution for acoustic pressure is obtained by substituting for $a_{new}^{\pm}$, $b_{new}^{\pm}$ in place of $a^{\pm}$, $b^{\pm}$ in Eq. (5.23). This solution was further used to solve for the eigenmodes of the annular nozzle shown in Fig. 5.2 (Right), using Eq. (5.36). However, assuming k_o to be real or complex for the WKB analysis resulted in a difference of less than 0.01% for the modal solutions.

For the special case of a quasi 1-D nozzle sustaining a planar acoustic field, Eqs. (C.5) and (C.6) simplify as,

$$a^{\pm} = -\frac{\alpha}{2} - \frac{\beta}{4} \mp \left(\frac{\beta}{2}-\alpha\right)M + \left(\frac{\beta}{2}-\alpha\right)M^2 + \frac{\alpha\gamma M^2}{2} \mp \frac{\beta\gamma M}{2} \pm \overbrace{\frac{\nu k_{o,\,R}}{1\pm M}}^{\textbf{Term 1}}; \quad {b_{1,\,r}}^{\pm} = \frac{\mp k_{o,\,R}}{1\pm M}. \tag{C.7}$$

Based on the definition of WKB (Eq. (2.25)), we evaluate $a^{\pm} + \mathrm{i}b^{\pm}$ for the general solution of acoustic pressure, $\hat{p}$. The addition of Term 1 in $a^{\pm}$ and $\mathrm{i}b_{1,\,r}^{\pm}$ (Eq. (C.7)), results in,

$$\frac{\pm\nu k_{o,\,R}}{1\pm M} + \mathrm{i}\frac{\mp k_{o,\,R}}{1\pm M} \;=\; \mathrm{i}\frac{\mp\left(k_{o,\,R}+\mathrm{i}k_{o,\,I}\right)}{1\pm M} \;=\; \mathrm{i}b_1^{\pm}. \tag{C.8}$$

Therefore on writing the final solution for $\hat{p}$ using the definition in Eq. (2.25), we again get $\hat{p} = \exp\left(a^{\pm} + \mathrm{i}b_1^{\pm} \pm \mathrm{i}\Phi_{NI}/2k_o\right)$. Thus, when $|\nu| \ll 1$, assuming the wave-number to be real for the initial WKB analysis still gives a complex wave-number in the final expression for the planar acoustic field estimation.

Appendix D

Computational cost comparison of models

To evaluate the computational cost of the WKB, Magnus expansion and numerical LEEs solutions, the conical test case in Fig. 2.12 is considered across 1000 different frequencies ranging from 0.3 to 1.1. It should be noted that in this frequency range the estimates of the WKB models are also accurate at low levels of entropy disturbance magnitudes. Although a Magnus expansion order of $k = 5$ is used in the analysis, we here compare the computational performance of models from $k = 2$ to $k = 5$. The calculations are produced using MATLAB (Windows version) installed on a HP Z4 G4 workstation with 10 physical cores, 3.7GHz clock speed and 64GB RAM, and the results are as follows, As seen in Table D.1, the analytical solution computation requires minimal effort as it does not require any numerical integration in evaluating the wave propagation.

Table D.1: Computational performance of the analytical and numerical solutions.

Model	**Computational time in [s]**
Numerical LEEs	4122.55
2^{nd} order Magnus, $k = 2$	71.50
3^{rd} order Magnus, $k = 3$	112.23
4^{th} order Magnus, $k = 4$	163.06
5^{th} order Magnus, $k = 5$	250.12
WKB	0.02

Appendix E

Figure Usage Permission

Fig. No.	Fig. Source	Copyright Holder	Permission Granted
1.2	[16]	PCI (Elsevier)	Yes - Elsevier (Purchase copy attached)

Table E.1: Permission for Figure Reproduction from Copyright Holder

ELSEVIER LICENSE
TERMS AND CONDITIONS

Sep 25, 2021

This Agreement between Imperial College London -- Saikumar Reddy Yeddula ("You") and Elsevier ("Elsevier") consists of your license details and the terms and conditions provided by Elsevier and Copyright Clearance Center.

License Number	5156270142037
License date	Sep 25, 2021
Licensed Content Publisher	Elsevier
Licensed Content Publication	Proceedings of the Combustion Institute
Licensed Content Title	Prediction and control of combustion instabilities in real engines
Licensed Content Author	T. Poinsot
Licensed Content Date	Jan 1, 2017
Licensed Content Volume	36
Licensed Content Issue	1
Licensed Content Pages	28
Start Page	1
End Page	28
Type of Use	reuse in a thesis/dissertation
Portion	figures/tables/illustrations

Number of figures/tables/illustrations	1
Format	electronic
Are you the author of this Elsevier article?	No
Will you be translating?	No
Title	Analytical models for thermo-acoustic interactions in axially varying flows
Institution name	Imperial College London
Expected presentation date	Nov 2021
Portions	Figure 1 (left).
Requestor Location	Imperial College London Flat 5, Nansen Village, 21 Woodside Avenue, Barnet London, N128AQ United Kingdom Attn: Imperial College London
Publisher Tax ID	GB 494 6272 12
Total	0.00 USD

Terms and Conditions

INTRODUCTION

1. The publisher for this copyrighted material is Elsevier. By clicking "accept" in connection with completing this licensing transaction, you agree that the following terms and conditions apply to this transaction (along with the Billing and Payment terms and conditions established by Copyright Clearance Center, Inc. ("CCC"), at the time that you opened your Rightslink account and that are available at any time at http://myaccount.copyright.com).

GENERAL TERMS

2. Elsevier hereby grants you permission to reproduce the aforementioned material subject to the terms and conditions indicated.